

CHIPPING AND BREAKAGE OF CARBIDE TOOLS

CHIPPING AND BREAKAGE OF CARBIDE TOOLS

by

ZAHER A. M. MASOOD, B.Sc. (Eng.)

A Thesis

Submitted to the School of Graduate Studies
in Partial Fulfilment of the Requirements

for the Degree

Master of Engineering

McMaster University

May, 1976

TO MY MOTHER

MASTER OF ENGINEERING (1976)
(Mechanical Engineering)

McMaster University
Hamilton, Ontario

TITLE: Chipping and Breakage of Carbide Tools

AUTHOR: Zaher Abdel Meged Masood,
B.Sc. (Production Eng.)
(Alexandria University, Alexandria,
Egypt)

SUPERVISOR: Professor J. Tlusty

NUMBER OF PAGES: xv, 201

SCOPE AND CONTENTS:

The purpose of this project was to study the failure mechanisms of carbide tools in turning operations due to fracture of the cutting edge. The study consisted of a combination of turning tests, examination of fracture surfaces and an analysis of the stresses in the tool as produced by the cutting force. Thermal stresses are so far not considered. It is concluded that chipping is a ductile failure due to high shear stresses at the cutting edge and breakage is brittle fracture originating at the rake face at a local maximum of tensile stress.

For the finite element stress analysis a new method of successively refining mesh while diminishing the analysed area is introduced which is rather effective and economical in that all computation except for the final field is done only once for various loading cases.

ACKNOWLEDGEMENTS

My sincere gratitude and thanks are due to Dr. J. Tlusty for providing constant guidance and inspiration throughout the study.

The author also expresses his appreciation to Ms. BettyAnne Bedell and Ms. Barbara Eastman for typing the manuscript.

I gratefully acknowledge the financial assistance from the National Research Council of Canada and McMaster University.

TABLE OF CONTENTS,

	<u>Page</u>
CHAPTER 1 INTRODUCTION	1
CHAPTER 2 BASIC CHARACTERISTICS OF SINTERED CARBIDES AND SUMMARY OF KNOWLEDGE FOUND IN BIBLIOGRAPHY ON BREAKAGE OF CARBIDE TOOLS	4
2.1 Basic Characteristics of Sintered Carbide Tool Materials	4
2.1.1 Introduction	4
2.1.2 Method of Manufacturing Carbides	5
2.2 Failure of Carbide Tools	16
2.2.1 Tool Wear and Tool Failure Mechanisms	16
2.2.2 Parameters Affecting the Stresses in a Tool a) Thermally induced stresses	19
b) Stresses generated by the cutting force	19
2.3 Parameters Significant for Failure of Cemented Carbides	24
2.3.1 Introduction	26
2.3.2 The Relation Between Fracture Toughness and the Material Parameters	27
2.3.3 Structural Parameters and their Influence on the Stress Dis- tribution in the Binder Phase of Cemented Carbides	29
2.3.4 Standard Test Method for Measuring Material Properties	34
2.3.5 The Development of Test Method	36

2.3.6	Introduction of Tool Fracture Classification System-	38
CHAPTER 3	EXPERIMENTAL RESULTS	46
3.1	Introduction	46
3.2	Test Equipment and Materials	46
3.2.1	Machine Tool	46
3.2.2	Tool	46
3.2.3	Workpiece	47
3.3	Cutting Tests	50
3.4	Fractography	75
3.5	Fracture Mechanisms for Sintered Carbides	75
3.5.1	Transgranular Fracture	75
3.5.2	Intergranular Fracture	75
3.6	Evaluation of Test Results	79
3.6.1	Type of Fracture	79
3.6.2	Chipping	79
3.6.3	Breakage	82
CHAPTER 4	ANALYSIS OF STRESSES	95
4.1	Introduction	95
4.2	Definition of the Problem	95
4.3	Stress Analysis of the Tool	112
4.3.1	Solution Using Elementary Beam Theory (Cantilever Beam in Bending)	112
4.3.2	Solutions Using the Finite Element Technique	118
	A - Single step method	118
	B - Stepwise sub-dividing and refining method	146
CHAPTER 5	CONCLUSIONS	156

REFERENCES		159
APPENDIX A	Analysis of Stresses Using the Single Step Method	161
APPENDIX B	Resulting Stresses in the Case of Zero Rake Angle and No Flank Wear ($a = 0.0$ inch)	168
APPENDIX C	Derivation of the Replacement Matrix Used in the Method Suggested by Tlusty	178
APPENDIX D	Computer Program Used for Calculation of the Replacement Matrix in the First Step	182
APPENDIX E	Computer Program for Calculation of the Stresses in the Fifth Step	189

LIST OF TABLES

	<u>Page</u>
Table 1 Key properties of hard metal carbides	6
Table 2 Solubility of carbides in iron	8
Table 3 Chemical composition and hardness of wickaloy grades	47
Table 4 Chemical composition and hardness of steels 4340, 1040	50
Table 5 Test results in case of continuous cutting using tool number 1-a	51
Table 6 Test results in case of continuous cutting using tool number 1-b	53
Table 7 Test results in case of continuous cutting using tool number 1-c	54
Table 8 Test results in case of continuous cutting using tool number 2-a,b	55
Table 9 Test results in case of continuous cutting using tool number 3	56
Table 10 Test results in case of continuous cutting using tool number 4-a	57
Table 11 Test results in case of continuous cutting using tool number 4-b,c	58
Table 12 Test results in case of continuous cutting using tool number 5	59
Table 13 Test results in case of continuous cutting using tool number 6	60
Table 14 Test results in case of continuous cutting using tool number 7-a	61
Table 15 Test results in case of continuous cutting using tool number 7-b	62
Table 16 Test results in case of continuous cutting using tool number 8	63
Table 17 Test results in case of continuous cutting using tool number 9-a,b,c	65

Table 18	Test results in case of continuous cutting using tool number 10-a,b,c, 11	66
Table 19	Test results in case of interrupted cutting using tool number 1	67
Table 20	Test results in case of interrupted cutting using tool number 2-a,b	68
Table 21	Test results in case of interrupted cutting using tool number 3, 4	69
Table 22	Summary of tests results in case of continuous cutting	71
Table 23	Summary of tests results in case of interrupted cutting	73
Table 24	Chemical composition of the etcher used for removing the iron	82

LIST OF FIGURES

	<u>Page</u>
Figure 1. Structure of WC-Co Combination	10
Figure 2. The frequency of occurrence of narrow and wide particle size distribution as a function of spherical diameter in microns.	10
Figure 3. Transverse rupture strength of sintered carbide as a function of mean grain size for various types of distributions.	11
Figure 4. Hardness of straight tungsten carbide-cobalt grades (Adamas grades) as a function of cobalt content and grain size.	13
Figure 5. Transverse rupture strength of straight tungsten carbide-cobalt grades as a function of cobalt content and grain size.	14
Figure 6. Transverse rupture strength of sintered carbides at elevated temperature, according to Kreimer.	15
Figure 7. Tool wear features	17
Figure 8. Temperatures in the workpiece in the chip	21
Figure 9a,b Tensile stresses in the tool	25
Figure 10. The mean free path λ versus fracture toughness after results from Gurland and Pairkh	28
Figure 11. The mean free path λ versus fracture toughness ϵ_{fr} for a number of carbide tool materials.	30
Figure 12. Transverse rupture strength (σ_{ft}) as a function of mean free path for various compositions.	31
Figure 13. The influence of grain size on tensile strength (σ_{ft}) and fracture strain (ϵ_{ft}) for straight carbides.	31
Figure 14. a) Geometry of the Bridgman model b) Analogue for the structure of cemented carbides.	33

Figure 15.	The ultimate uniaxial strain (ϵ_{ft} , tensile test) as a function of d_{av}/λ_{av}	35
Figure 16.	The ultimate uniaxial strain (ϵ_{ft} , bending test) vs. the ratio d_{av}/λ_{av} for a number of commercial grades	35
Figure 17.	Distribution of stresses of a diametrical loaded circular disc.	37
Figure 18.	Stress distribution across the diagonals of a diagonally loaded square specimen.	39
Figure 19.	Safety chart of the chipping at low cutting speed.	41
Figure 20.	Typical location and appearance of various types of fatigue cracks.	43
Figure 21.	Fatigue tool life of P20 tungsten carbide determined by the chipping starting on the flank and or the chipping starting on the rake face.	44
Figure 22.	Example of breakage (Tool grade K7H)	45
Figure 23.	Dimensions of the tool	48
Figure 24.	Microstructure of K7H carbide grade	48
Figure 25.	Microstructure of K45 carbide grade	49
Figure 26.	Microstructure of WP5 carbide grade	49
Figure 27.	Microstructure of WP6 carbide grade	49
Figure 28.	Optical micrograph showing a trans-granular crack	76
Figure 29.	Types of intergranular fracture	78
Figure 30.	Optical micrograph showing an inter-granular crack	78
Figure 31.	Chipping of the edge (K45 tool grade)	80
Figure 32-a	Stereo picture of chipping area at the nose of the tool, WP6	81

Figure 32-b	Chipping area near to the tool nose WP6	81
Figure 33-a	Chipping area after etching, WP6	83
Figure 33-b	Chipping area after etching, K45	83
Figure 34-a	Crack on the rake face of K7H carbide grade	84
Figure 34-b	End of the same crack as figure 34-a with high magnification	84
Figure 35-a	Microcrack on the rake face of K45 carbide grade tool	86
Figure 35-b	Stereo view of the same microcrack as figure 35-a	86
Figure 36-a	Microcrack on the rake face of the same tool as figure 35	87
Figure 36-b	Microcrack with high magnification, K45, tool grade	87
Figure 37.	Fracture surface at K7H carbide grade tool	88
Figure 38.	Fracture surface of the same tool as figure 37 taken from another view	88
Figure 39.	Fracture surface of K7H carbide grade tool	89
Figure 40.	Fracture surface of K45 carbide grade tool	89
Figure 41.	Stereo picture of fracture surface of K45 carbide grade tool	90
Figure 42.	Fracture surface of K45 carbide grade tool	90
Figure 43.	Stereo picture of fracture surface WP6	91
Figure 44.	Stereo picture of fracture surface WP6	92
Figure 45.	Stereo picture of fracture surface WP5	93
Figure 46-a	The load distribution (normal and shear loads) on the rake face and on the flank	97

Figure 46-b	Mesh used in the Finite Element Computation (single step method)	98
Figure 47.	Diagrammatical representation of the problem	100
Figure 48.	The area of interest (B) with refined mesh and imposed the displacement boundary conditions (δ_b)	103
Figure 49.	The area of interest (B) with refined mesh and imposed a very stiff springs (K_b) and external force (F_b) on boundary b	106
Figure 50.	Substructures A and B	108
Figure 51.	Stepwise and subdividing and refining method (Tlusty's approach)	111
Figure 52-a	Normal stress contours using the classical solution	113
Figure 52-b	Maximum principal stress contours using the classical solution	114
Figure 52-c	Minimum principal stress contours using the classical solution	115
Figure 52-d	Maximum shear stress contours using the classical solution	116
Figure 52-e	Direction of maximum principal stresses and maximum shear stresses using the classical solution	117
Figure 53-a	Computed maximum principal stress in the loading region	119
Figure 53-b	Computed maximum principal stress in the tool and tool holder	120
Figure 54..	Computed minimum principal stress in the loading region	121
Figure 55.	Computed maximum shear stress in the loading region	122
Figure 56-a	Directions at maximum principal stress and at maximum shear stress in the loading region	126

Figure 56-b	Directions of maximum principal stress and at maximum shear stress in the tool	127
Figure 57.	Computed maximum principal stress in the loading region	131
Figure 58.	Computed minimum principal stress in the loading region	132
Figure 59.	Computed maximum shear stress in the loading region	133
Figure 60.	Computed maximum principal stress in the loading region	134
Figure 61.	Computed minimum principal stress in the loading region	135
Figure 62.	Computed maximum shear stress in the loading region	136
Figure 63-a	Computed maximum principal stress in the loading region	138
Figure 63-b	Computed maximum principal stress in the tool and tool holder	139
Figure 64.	Computed minimum principal stress in the loading region	140
Figure 65.	Computed maximum shear stress in the loading region	141
Figure 66-a	Computed maximum principal stress in the loading region	142
Figure 66-b	Computed maximum principal stress in the tool and tool holder	143
Figure 67.	Computed minimum principal stress in the loading region	144
Figure 68.	Computed maximum shear stress in the loading region	145
Figure 69.	Dimensions of the fifth step (loading region)	147
Figure 70.	Computed maximum principal stress in the loading region	148

Figure 71.	Computed minimum principal stress in the loading region	149
Figure 72.	Computed maximum shear stress in the loading region	150
Figure 73.	Computed maximum principal stress in the loading region	152
Figure 74.	Computed minimum principal stress in the loading region	153
Figure 75.	Computed maximum shear stress in the loading region	154

CHAPTER 1

INTRODUCTION

Tool wear in metal cutting is characterized by a number of various features. Flank wear and crater wear are accepted as a regular phenomenon. They grow rather uniformly with the time of cutting. Chipping of the edge and breakage are both irregular phenomena and their development is difficult to predict and they should be avoided completely if possible. Breakage is the most dangerous of all the various tool wear features because it may lead to damage of the work-piece and/or of the machine.

Sintered carbides are one of the most important cutting tool materials. They offer an unsurpassed combination of hardness and strength. Therefore, many attempts have been made to evaluate the significant parameters resulting in failure of sintered carbides.

In the present work an attempt has been made to study the mechanisms of chipping and breakage of carbide tools.

Failure of steel cutting grade carbide tools due to the fracture of the cutting edge was investigated in turning operations. Three types of work material were used (steel 1040, steel 4340 and steel 4340 hardened and tempered to 380 BHN. The purpose was to try and correlate tool failure with an analysis of the stresses in the tool caused by the

cutting force. Thermal effects have so far been neglected. The study consisted of metal cutting tests (continuous and interrupted) in which tools were tested until they failed due to fracture.

The study of fracture in sintered carbides on a microscopic scale has been limited mainly to the optical examination of surface cracks on the intersection of fracture surfaces with polished surfaces. The large depth of focus of the Scanning Electron Microscope has permitted the examination of fractured surfaces. The fractured surfaces of the carbide tools were examined and a stereo picture for both chipping and breakage were obtained and examined to investigate the fracture phenomena of each. The stress distribution on the tool and on a special area of interest (tool wedge) was carried out using the Finite Element Method. The method is especially useful for stress analysis problems which cannot be solved by classical theory. The problem is mainly the analysis of local stresses in the tool wedge. The computations were carried out using two different methods of mesh generation. The first method was named "The Single Step Method" in which the computation work was carried out in one step. Also, a stepwise subdividing and refining method was used for investigating the stresses in the tool wedge. Using this method the computation work was carried out in a number of steps ending with the area of interest with a very fine mesh in which stresses could be obtained in great detail.

A new algorithm was developed which makes it possible

to investigate stresses at various loads without repeating these successive steps of computation.

By comparing the cutting test results, analysis of fractures surfaces and the stress fields, it was concluded that chipping is a ductile failure due to shear stresses close to the cutting edge while breakage is a brittle fracture phenomenon originating at a certain distance from the cutting edge. It is assumed that the work will be continued to include the temperature effects.

CHAPTER 2

BASIC CHARACTERISTICS OF SINTERED CARBIDES AND SUMMARY OF KNOWLEDGE FOUND IN BIBLIOGRAPHY ON BREAKAGE OF CARBIDE TOOLS

2.1 Basic Characteristics of Sintered Carbide Tool Materials

2.1.1 Introduction

Tungsten carbide was discovered by Moissan in about 1890. However, at that time it was of no value as a cutting tool material, since fabrication into cutting tools was not possible due to decomposition at the high temperatures required for sintering. A solution to this problem was found by Schroter in 1923 when he mixed tungsten carbide with cobalt powder, the mixture being sintered at about 1320°C (melting point of cobalt). The actual cutting tool material was introduced around 1933 by Krupp in Germany under the name of Widia. The name implies "like diamond". Although it actually is by far not as hard as diamond, the sintered WC with Co binder offered and practically offers still today an unsurpassed combination of hardness and strength. It was its ability to retain high hardness up to temperatures of 800°C to 1000°C compared to high speed steels which lose substantially their hardness at temperatures in the range of 500°C to 700°C which made it an instant success in machining non-ferrous materials and cast iron. However, it was soon discovered that in machining steel it suffered from severe

cratering on the rake face. This was remedied by the introduction, almost a decade later, of the complex tungsten carbide and titanium carbide (WC + TiC). In spite of some recent developments in tool materials sintered carbides are still the most important cutting tool materials.

2.1.2 Method of Manufacturing Carbides

Based on powder metallurgy techniques, the procedures to manufacture sintered carbides for tools are:

1. Tungsten oxide reduced by hydrogen results in tungsten powder.
2. Milling of tungsten with carbon (lamp black), blending in fine mixture in a ball mill, heating and carburizing.
3. Ball milling (several days) together with cobalt.
4. Waxing to impart some cohesion and lubrication.
5. Cold compacting at pressures up to 60,000 psi using dies of alloy steel. Dies must be larger to account for shrinkage during subsequent sintering.
6. Presintering (816°C) in hydrogen, removing the lubricant, shaping, and machining if necessary. —
7. Sintering (at temperatures in the range of 1370°C to 1593°C) in hydrogen or in a vacuum, so the cobalt melts and tungsten carbide dissolves partly in cobalt, diffuses and forms a strong matrix.

In items 1 to 7 any oxidation should be prevented.

Densification occurs by liquid phase sintering above the melting point of the binder phase (1320°C) [1]. The process takes place in three overlapping stages:

1. Rearrangement of the particles into a dense packing by particle transport under the influence of the surface tension of the liquid.
2. Solution and reprecipitation of WC in and out of the liquid resulting in further densification and particle growth.
3. Coalescence and welding of carbide particles, which may interfere with further densification.

Various types of hard metallic carbides have been considered for cutting tools. The hardness and melting point values for a number of them are assembled in Table 1, in a sequence of decreasing hardness.

TABLE 1. KEY PROPERTIES OF HARD METAL CARBIDES

Material		Microhardness (kg/sq.mm)	Melting Point (F)	Melting Point (C)	Theoretical Density (g/cm ³)
TiC	Titanium carbide	3200	5790	3200	4.94
VC	Vanadium carbide	2950	5125	2830	5.71
HfC	Hafnium carbide	2700	7030	3890	12.76
ZrC	Zirconium carbide	2560	6380	3530	6.56
CbC	Columbium carbide	2400	6330	3500	7.80
Cr ₃ C ₂	Chromium carbide	2280	3440	1895	6.66
WC	Tungsten carbide	2080	4710	2600	15.67
Mo ₂ C	Molybdenum carbide	1950	4850	2400	9.18
TaC	Tantalum carbide	1790	6835	3780	14.50

Brief comments can be made regarding their individual practical usefulness [2].

- Titanium Carbide (TiC) is essential to be added to tungsten carbide to impart crater resistance for machining steel as cutting speed increases.
- Vanadium Carbide (VC) has never been properly cemented together to form a strong body and is used only, to a small extent, as an additive to control grain growth.
- Hafnium Carbide (HfC) is expensive and has only recently become available in quantity conditions. This applies also to Zirconium Carbide (ZrC). Neither of these appears to be suitable as a cemented carbide except as an additive.
- Columbium Carbide (CbC), which also has been used as an additive to control grain growth and to improve crater resistance in steel machining grades, is generally associated with Tantalum Carbide (TaC).
- Chromium Carbide (Cr_3C_2) cannot be properly bonded or cemented and, therefore, is used only, to a limited extent, as an additive for grain growth control.

Thus the two most important classes remain to be the "straight" grades of WC-Co combination and the "steel cutting" grades of (WC + TiC, WC) - Co combination. In order to understand their properties, Table 2 shows the affinity of the various carbides to iron [3].

TABLE 2. SOLUBILITY OF CARBIDES IN IRON

<u>Carbide</u>	<u>Solubility in Iron at 1250°C</u>
Tungsten Carbide (WC)	7%
Titanium Carbide (TiC)	Less than $\frac{1}{2}\%$
50/50 TiC/WC solid solution	$\frac{1}{2}\%$
Tantalum Carbide	$\frac{1}{2}\%$

Tungsten Carbide easily dissolves in iron. Therefore, when machining steel rather extensive diffusion occurs on the rake face of the tool over which the hot chip is sliding. The underside of the chip is freshly generated non-contaminated steel and the tool material readily dissolves in it and a crater is generated on the face of the tool. Because the chip slides away and continuously a new chip surface is created no saturation by the diffusing WC can occur and the diffusion rate is kept high. In machining cast iron this does not occur because cast iron is already rather saturated with carbon. This would not occur with TiC which, therefore, would be very crater resistant.

However, similarly as with iron, WC is rather well soluble in cobalt while TiC is not. In the structure of the WC-Co combination the WC grains are bonded together by a thin intermediate layer of, actually, solid solution of WC in Co (Fig. 1).

This is what makes the bond so strong. There is an ideally thin layer of the (WC + Co) bond which gives the best

strength. A thick layer would be in the middle almost pure Co with much less strength.

Actually, in order to obtain a good uniformly thin uninterrupted layer it is important that high uniformity of grain size be maintained. Graphs in Figures 2 and 3 illustrate this, reproduced from [1].

In Figure 2, two types of grain size distributions are shown, one wide and one narrow, both centered on 4 microns diameter. In Figure 3 the transverse rupture strength of sintered carbide is shown as a function of mean grain size for various types of distributions. It is seen that the narrow distribution gives up to 400,000 psi strength and exceeds that of the wider distribution by about 15%.

It is understood that a bond layer which is too thin leads to harder, however, more brittle grades. A thicker layer of Co, which is more ductile than WC imparts the material better impact resistance.

Because of the bad solubility of TiC in Co a sintered material of a TiC-Co combination would have very little strength. Therefore the steel cutting grades are made either as a combination of complex (WC + TiC) carbides with up to 50% TiC content and Co, or complex (WC + TiC) carbides, simple WC carbides and Co (the three-phase carbide).

In both the basic classes of straight and steel cutting grades the amount of cobalt content influences both hardness and strength. Actually, in general, the hardness of a sintered carbide is determined by the carbide grains while its strength is determined by the strength of the binder.

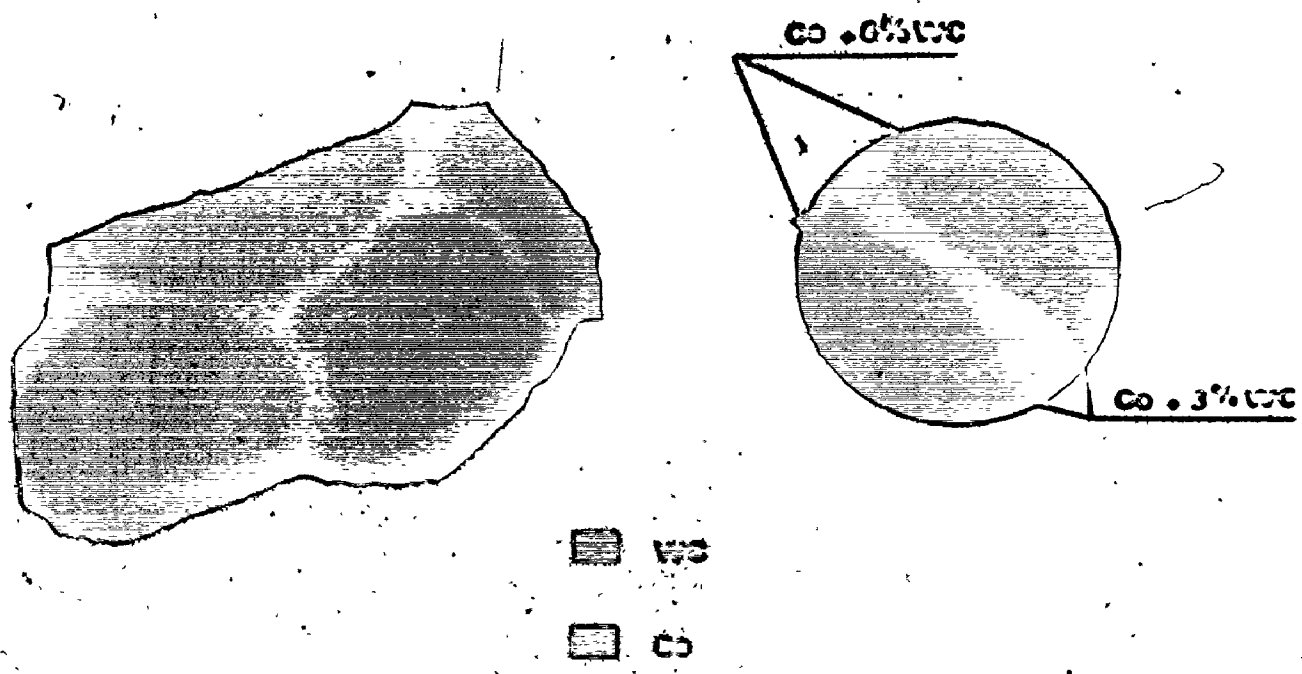


Figure 1. Structure of WC-Co Combination.

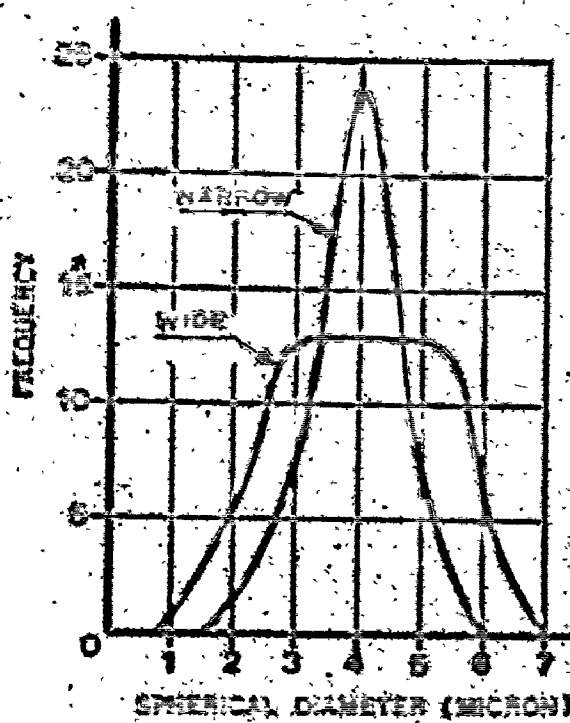


Figure 2. The Frequency of Occurrence of Narrow and Wide Particle Size Distril a Fi of

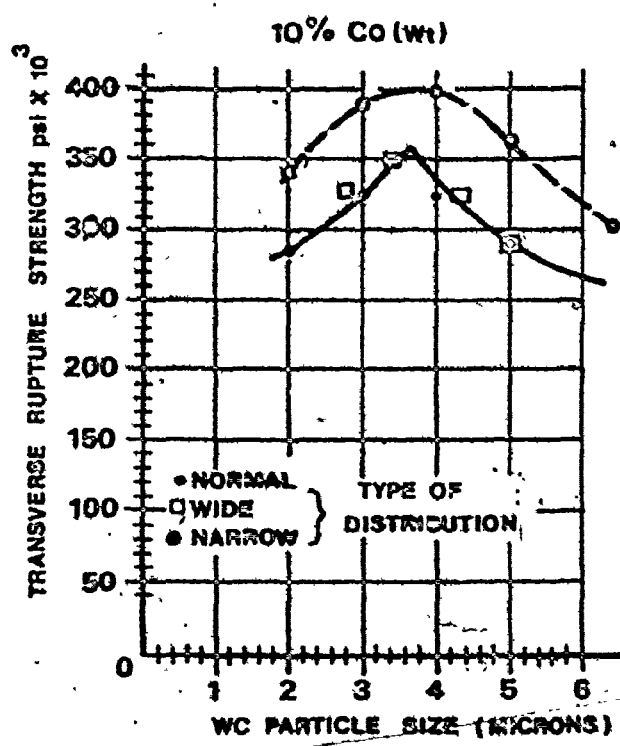


Figure 3. Transverse Rupture Strength of Sintered Carbide as a Function of Mean Grain Size for Various Types of Distributions.

Therefore, naturally, with the increase of cobalt content hardness decreases and strength increases (the latter up to a certain percentage, 15 to 20 wt.%). The grain size has an influence too.

The effect of cobalt content on hardness is shown in Figure 4 and on transverse rupture strength in Figure 5 [2]. In this respect it is fair to include also the effect of temperature. Thus, the comparison of strength of the various classes of sintered carbides inclusive effect of temperature is shown in Figure 6 reproduced from [4], based on [5].

It is seen that in general, and especially so at room temperature, the straight grades are the strongest ones and they are about 1.5 times stronger than the three-phase carbides. With temperature the straight grades lose hardness faster than the complex grades and they are equally strong at 500°C . At higher temperatures the straight grades are again much better.

Thus, while the addition of TiC strongly improves crater resistance it leads to some loss of strength. Therefore, recently new developments were based on:

- a) Coating a thin layer (5 microns) of purely TiC on a strong WC-Co combination base.
- b) Developing sintered carbide of TiC and MoC with Ni as a binder.

The solution a) is being rather widely accepted while the material b) is still rather limited in practical

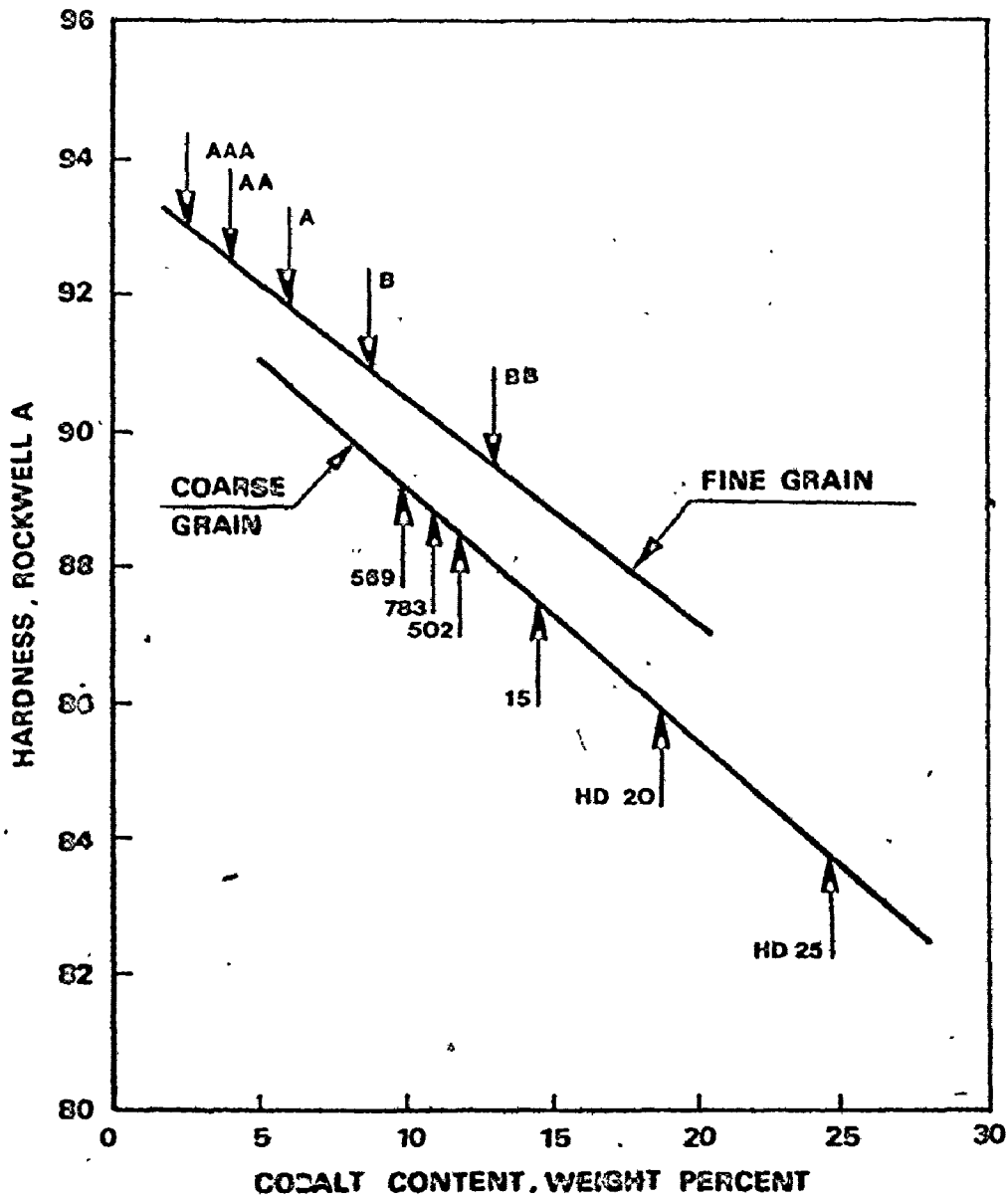


Figure 4. Hardness of Straight Tungsten Carbide-Cobalt Grades (Adamas Grades) as a Function of Cobalt Content and Grain Size.

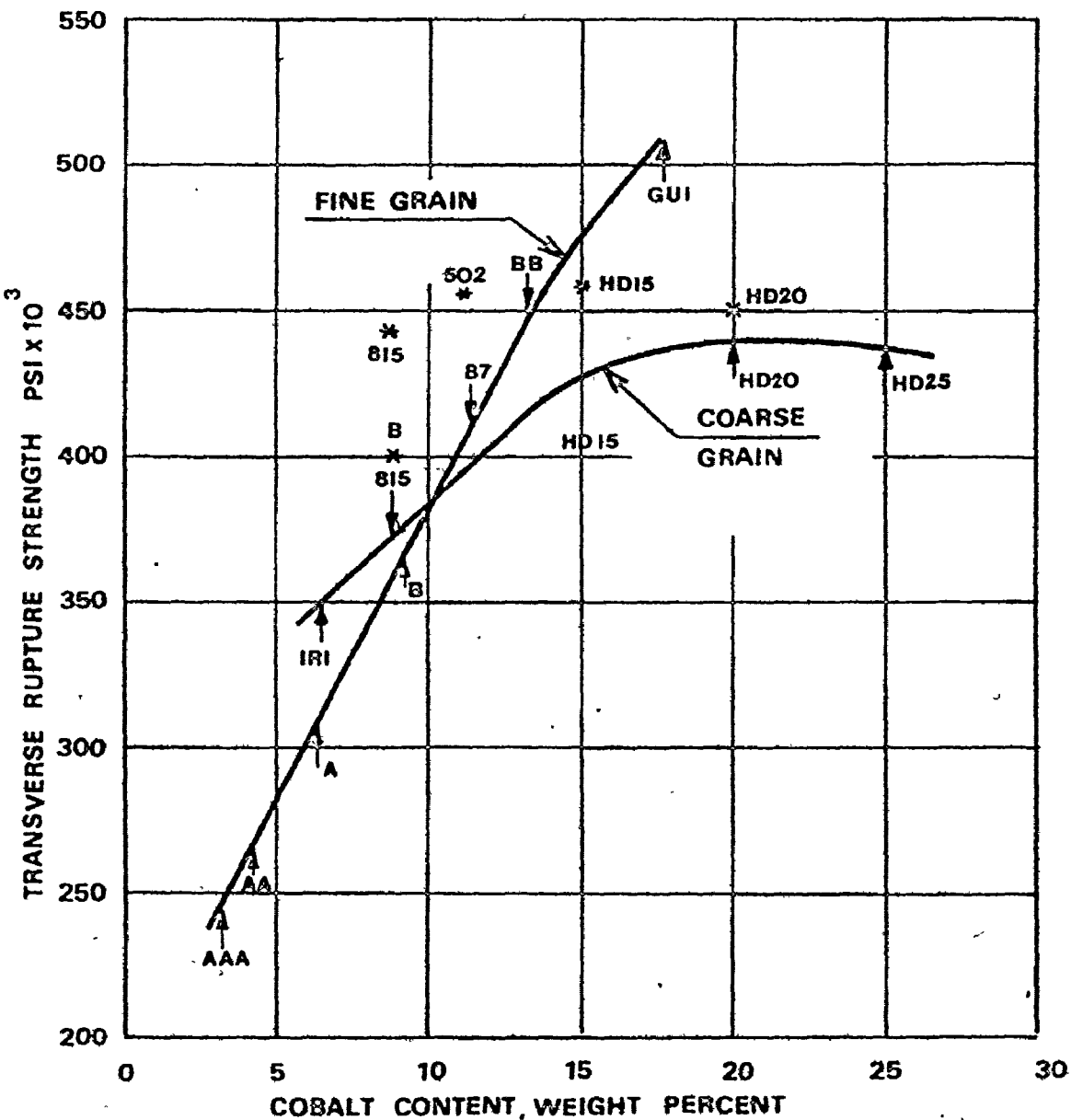


Figure 5. Transverse Rupture Strength of Straight Tungsten Carbide-Cobalt Grades as a Function of Cobalt Content and Grain Size.

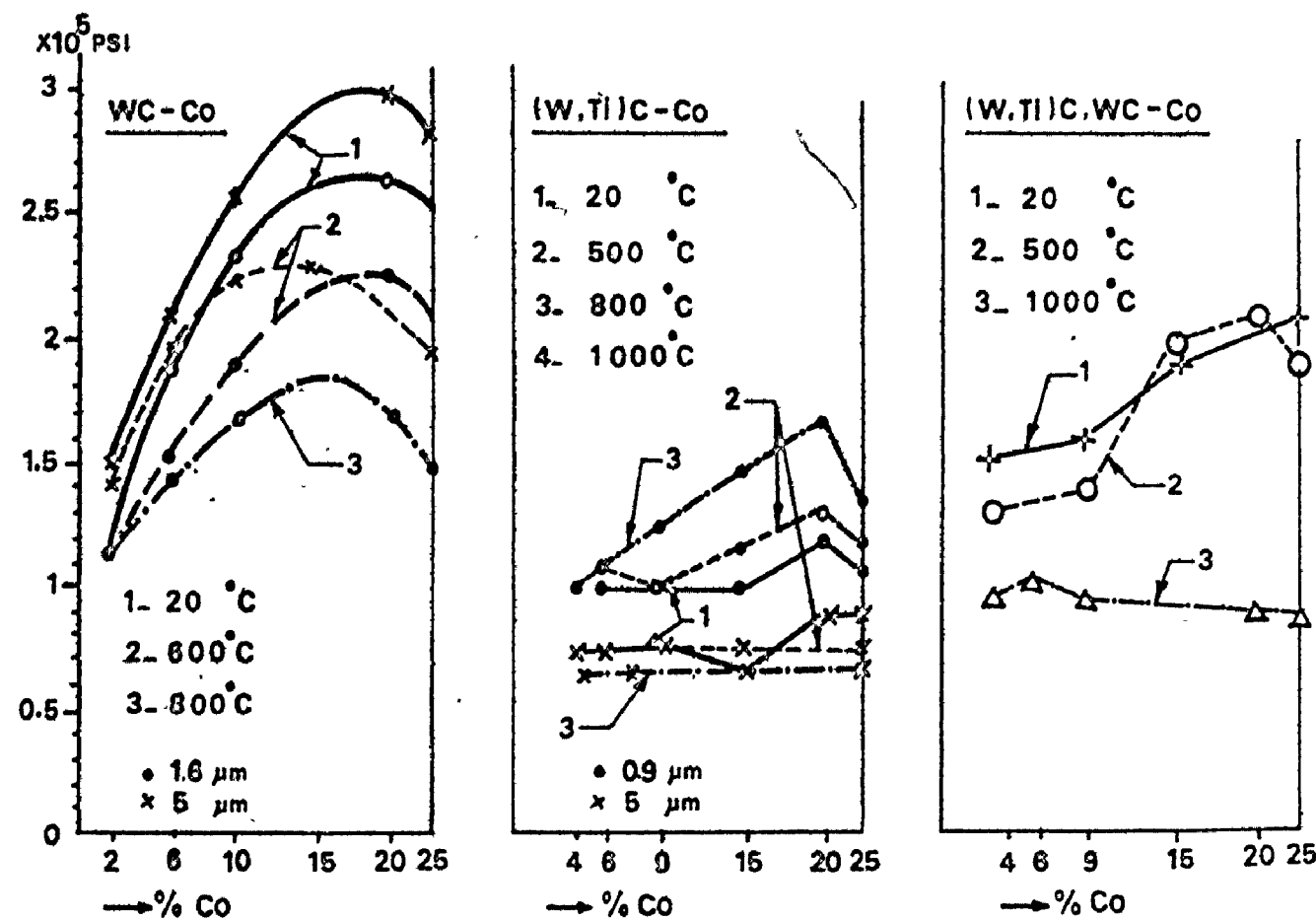


Figure 6. Transverse Rupture Strength of Sintered Carbides at Elevated Temperature, According to Kreimer.

applications.

Other recent developments in cutting tool materials were non-carbides like Borazon (cubic boron nitride) and UCON (an alloy of Columbium (Cb), Titanium (Ti) and Tungsten (W); nitrided at its surface.)

2.2 Failure of Carbide Tools

2.2.1 Tool Wear and Tool Failure Mechanisms

Tool wear in metal cutting is characterized by a number of various features which are diagrammatically summarized in Figure 7 [4].

There the flank wear FW may be distinguished which is caused by the rubbing of the workpiece material on the flank, i.e., on the relief side of the main cutting edge, of the nose radius and of a part of the secondary edge, crater wear CW which is due to the sliding of the chip on the rake face of the tool, the notch N which develops on the main cutting edge at the point which cuts the surface of the work-piece, chipping CH of the edge, cracks CR which may be parallel with or transversal to the cutting edge, breakage BR of the tool nose, plastic deformation PD of the tool nose.

Of all these forms of wear the flank wear FW is always present and it is accepted as the regular phenomenon. The flank wear width increases rather regularly with the time of cutting. Flank wear is usually accepted as the criterion for tool life which is considered terminated when flank wear width reaches a certain limit value. The crater wear CW is another rather regular phenomenon. It does not occur always but

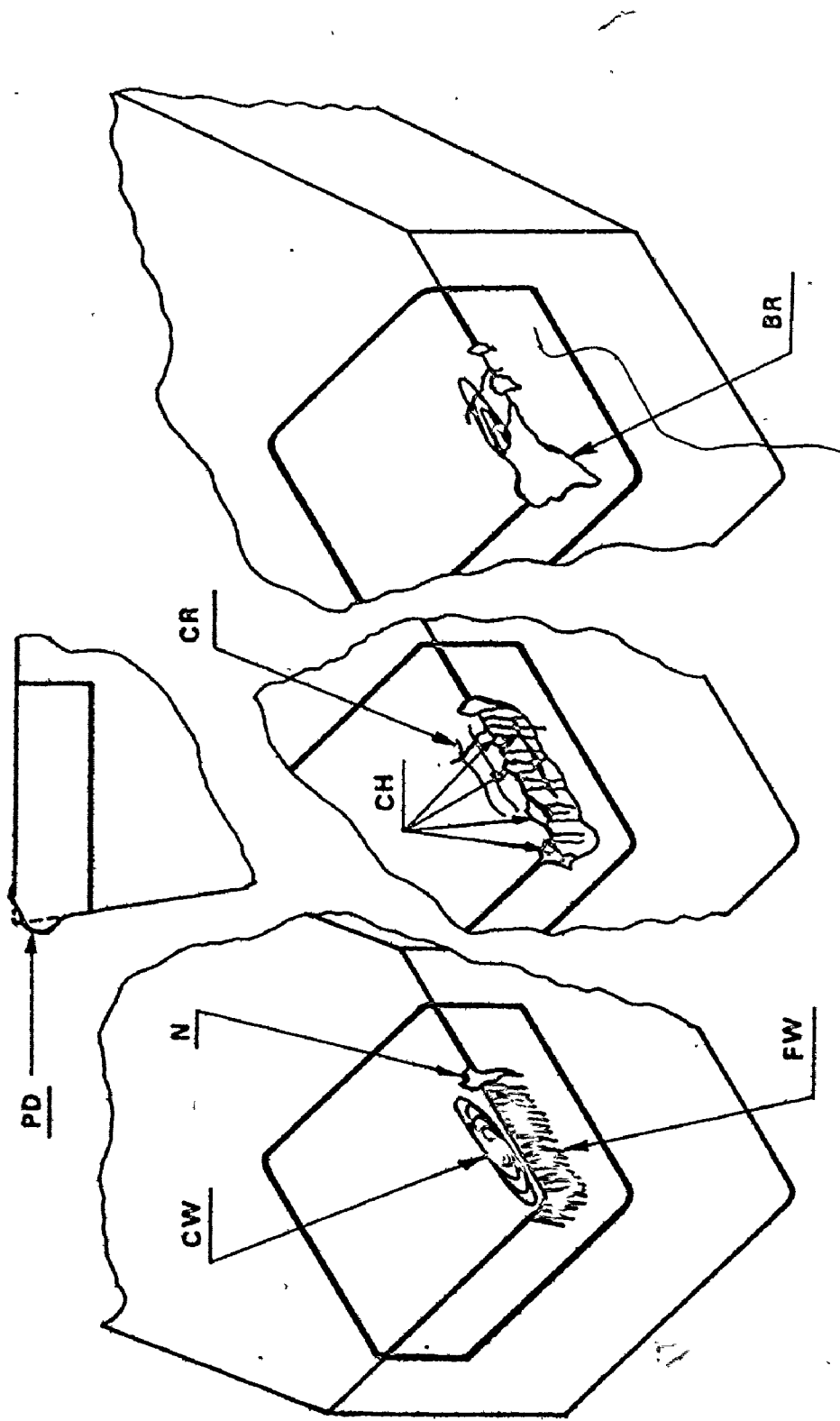


Figure 7. Tool Wear Features.

whenever it does it also grows rather uniformly with time. The time of cutting during which both FW and CW will not exceed an unwanted value can be fairly well predicted.

All the other mentioned phenomena are rather irregular and their development is difficult to predict and they should be avoided completely if possible by a suitable choice of tool material, tool geometry and cutting conditions, mainly of cutting speed and feed (chip thickness). Chipping of the edge and breakage might be considered both to be phenomena of primarily brittle fracture and differ mainly by their magnitude and they are related to the phenomenon of cracks. On the contrary, plastic deformation is mainly associated with the loss of compressive strength of the tool material at high cutting temperatures. Breakage is the most dangerous of all the various tool wear features because it may lead to damage of the workpiece and/or of the machine. Breakage and chipping as brittle fractures develop from macrocracks which result from interlinking of microcracks originating in points where the tensile stress exceeds the tensile strength. More precisely, it is recently recognized that the limit is imposed on tensile strain rather than on tensile stress which, of course, involves the modulus of elasticity of the material concerned. An ultimate admissible tensile stress value could be obtained once the modulus of elasticity is given.

Brittle fracture is a rather probabilistic phenomenon and it depends very much on the existence of cracks and voids in the material prior to its stressing. In this instance it

very often depends strongly on the surface quality of the stressed specimen. However, it is found that breakage of carbide tools is also affected by fatigue and consequently the specimens fail at lower stress values if the stress is of a periodically variable nature as, for example, in interrupted cutting. This shows that breakage is not purely brittle in character.

Chipping occurs close to the cutting edge where a very high temperature is developed. The binder (cobalt) would lose its strength and becomes ductile to a certain degree due to the high temperature generated during the cut. The results obtained using the finite element technique agreed rather well with those of Loladze [6]. Both of them showed compressive stresses near the cutting edge contact area between chip and tool and almost no tensile stresses responsible for the brittle fracture are found. Chipping is thus considered as being more of a ductile than brittle fracture phenomenon.

2.2.2 Parameters Affecting the Stresses in a Tool

As mentioned earlier, brittle fracture fundamentally is associated with tensile stresses. In a tool these may be due to two basically different causes:

- a) The thermal load
- b) The load by the cutting force

a) Thermally induced stresses

When the tool starts cutting a high temperature

develops very quickly on the rake face due to the contact with the chip which has been heated as a result of plastic work in the shear zone and also due additionally to the friction work (or, more precisely due to the plastic flow in the layer of the chip which is close to the rake face of the tool) and the flank of the tool heats up as well due to friction between the machined surface and the tool.

Subsequently, as part of the heat is conducted away through the insert and, further through the holder, the temperature inside the insert increases too. In a short time the temperature field in the insert reaches a steady balanced state. A typical example of temperatures in the chip and workpiece as are obtained in machining steel with carbide tools is given in Figure 8. In this example the maximum temperature on the rake face of the tool reached 750°C . During the heating up period of the tool when the outer parts of the insert expand more than the inside, compression stresses only are produced in the insert.

However, when the tool stops cutting its outside is cooled first by air or by cutting fluid, and the cooling of the interior follows later. The outer parts are shrinking and tensile stresses are created. These are greater when cooling is efficient. Therefore, use of coolants is not recommended in high speed machining with carbides.

Tlusty [4] shows that the important parameters which influence the resistance to thermal shock are the Coefficient of Thermal Expansion α and Thermal Conductivity K . It is

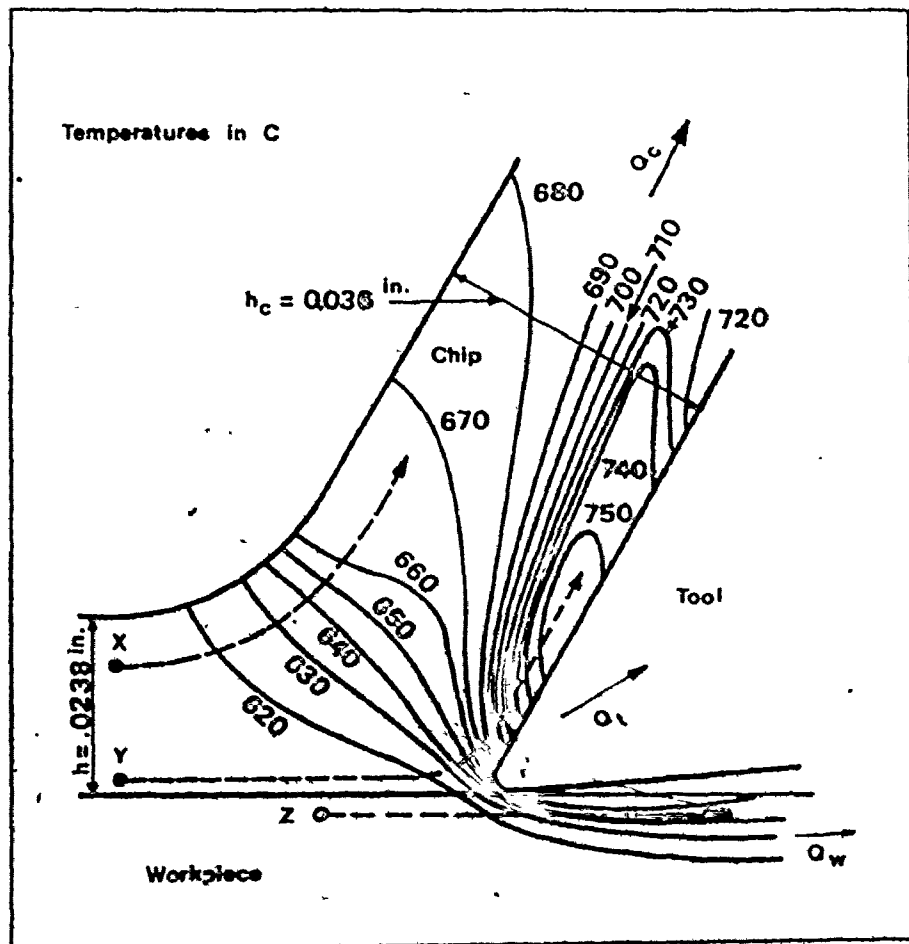


Figure 8. Temperatures in the Workpiece and in the Chip.

obvious that the greater is α , the greater stress is induced by a given temperature gradient because of greater differences of expansion of the corresponding layers of the tool. For a given heat flux the temperature gradients in the tool will be smaller for materials with better conductivity K .

Various authors define then the resistance to thermal shock in various ways but always it is proportional to the ratio of K/α .

The formula of Kals [7] is:

$$R_t = \epsilon_f \frac{K}{\alpha} \quad , \quad \epsilon_f = \alpha \Delta \theta \quad (2.1)$$

where ϵ_f is the ultimate tensile strain of the given material.

The thermal stress of a clamped tool-bit can be expressed by:

$$\sigma_\theta = \alpha \Delta \theta \cdot E \quad (2.2)$$

So, let the thermal load be characterized by a heat flux ϕ per unit area then:

$$\frac{\Delta \theta}{L} = \frac{\phi}{K} \quad (2.3)$$

where L = length of thermal path

ϕ = heat flux

$$\therefore \sigma_\theta = \frac{\alpha E}{K} \phi L \quad (2.4)$$

In this equation the thermal stress sensitivity s_t is

represented by $\frac{\alpha E}{K}$ which is not just simply the inverse of R_t because it involves also the modulus of elasticity E.

The parameter which is of greatest importance for breakage either due to the cutting force or due to the thermal stress is the tensile strength or the ultimate tensile strain. This parameter is generally measured by means of a bending test and the values of maximum tensile stress induced in this test at the fracture load are called the Transverse Rupture Strength, TRS.

Data on Transverse Rupture Strength of various types of carbides at various temperatures may be found in the book of Kreimer [5]. From this reference the graphs given in Figure 6 are compiled. In these graphs the values of TRS are plotted with respect to the Co content in the sintered carbide and the various curves apply to different temperatures in the range of room temperature of 20°C up to 800°C and 1000°C respectively. In the two first graphs also, the effect of carbide grain size is shown using very fine grain and rather coarse grain types.

Briefly, the TRS of all kinds of carbide grades depends strongly on the content of cobalt, the best percentage of which is between 15 and 20 wt. %. The "straight" grades are much stronger than the steel cutting grades at room temperature but they start losing the strength with increasing temperature above about 500°C .

The steel cutting grades are less sensitive to increased temperature and the strength of certain of these grades actually improves and attains a maximum at about 500°C .

to 800°C and is almost equal to the strength of the straight grades in this temperature range.

b) Stresses generated by the cutting force

There have been attempts to experimentally determine the distribution of stresses in the tool loaded by the cutting force. Several authors used a method where photoelastic analysis was applied to a tool made of transparent plastic which was used to cut lead at rather low cutting speeds (at higher speeds the plastic would lose its strength due to the temperature generated during the cut). One of these investigators was Loladze [6].

In Figure 9-a a typical example is shown of the distribution of stress on the rake face of a tool with 10° positive rake angle. The stress is plotted in relation to the distance y from the cutting edge and C is the length of contact between the chip and the rake face. For $y < C$ the stress is compressive with a maximum value at the distance $y = 0.4C$. For $y > C$ the stress is tensile with a maximum at $y = 2C$. Loladze investigated the effect of the rake angle on the value of maximum tensile stress which in general was found proportional to the chip thickness a .

In Figure 9-b the relative value of the maximum tensile stress as measured in photoelastic fringe orders is plotted versus chip thickness a (inch) for rake angles:
1) $+ 20^{\circ}$, 2) 0° , 3) -20° .

It is seen that the maximum tensile stress was found to be about seven times lower for $\alpha = -20^{\circ}$ than for $\alpha = 20^{\circ}$.

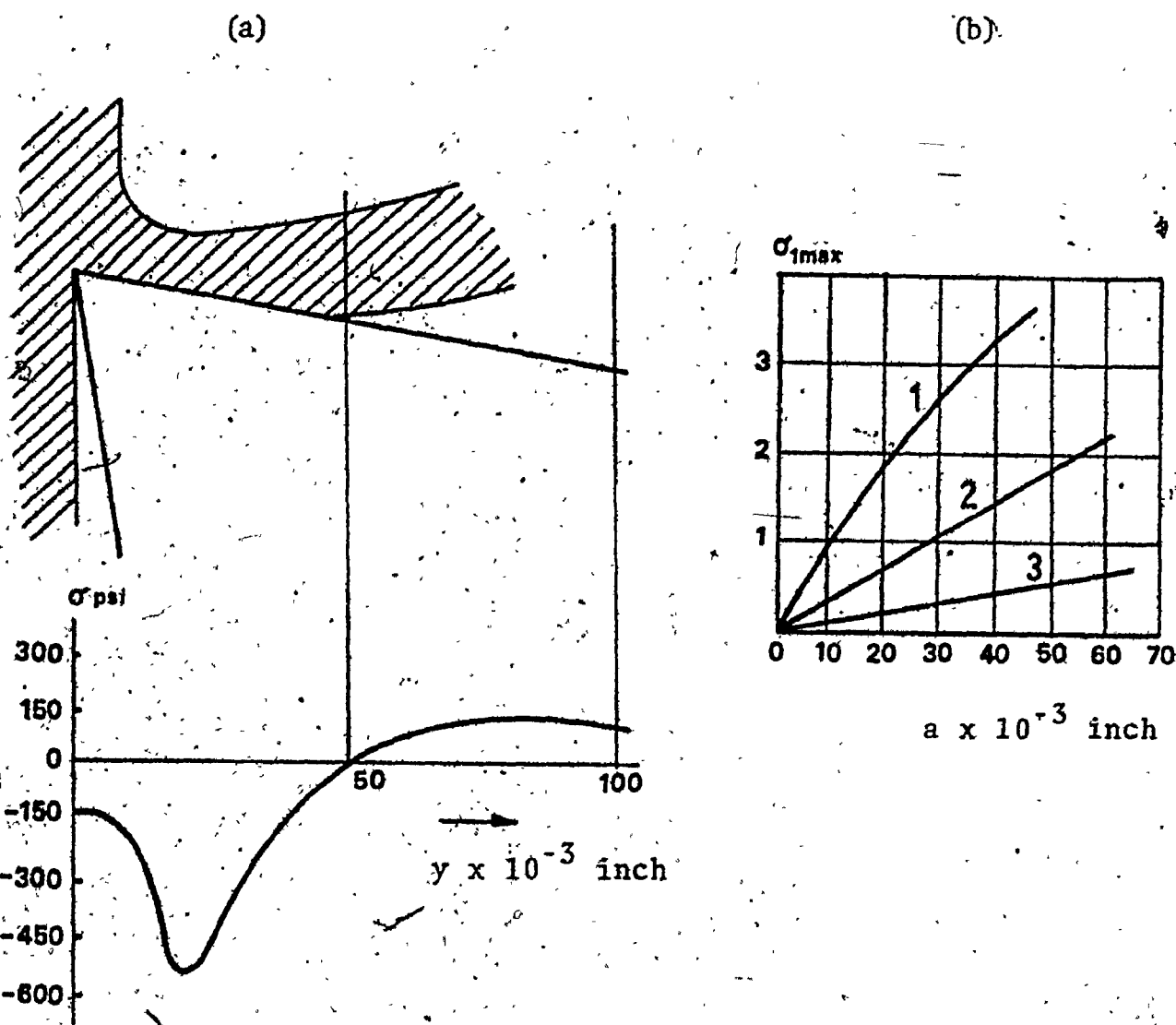


Figure 9(a), (b). Tensile Stresses in the Tool.

A very systematic work in this area was carried out by Primus, [8]. He used glass tools to machine aluminum and a diamond tool to machine various steels and, again, applied photoelastic analysis. He did not evaluate stresses in the tool but concentrated on determining the distribution of the cutting load on the rake and flank faces.

2.3 Parameters Significant for Failure of Cemented Carbides

2.3.1 Introduction

Brittle fracture of cemented carbides is an important factor in cutting tool performance. It has been observed that the strength and toughness of cemented carbides are predominantly influenced by grain size and the thickness of the binder layer. Some investigators have determined a significant dependence of strength on the isostatic stress component. This dependence was found to increase with a decreasing percentage of the binder content.

An attempt has been made by Kals [9] to evaluate the ratio of the effective stress (σ) and the maximum tensile stress (σ) component within the binder ($C = \bar{\sigma}/\sigma$) in relation to strength.

It has been shown that the ultimate tensile strain can be related to C. In turn, the parameter C is dependent on structural parameters.

Recently, Shaw et al. [10] came to the conclusion that the maximum tensile strain criterion is a reliable tool for predicting brittle fracture. However, measurement of

small strain is substantially more difficult than the measurement of load. Subsequently the ultimate strain is preferentially derived from $\epsilon_f = \frac{\sigma_f}{E}$. There is more evidence that ϵ_f is an adequate parameter for brittle material.

From the results of Gurland and Parikh [11] it appears that ϵ_f may satisfy as a criterion for fracture toughness of cemented carbides when the carbide contents exceed 60%.

Hatano [12] and Brands [13], who examined the influence of the deformation rate and the isostatic stress component on brittle fracture respectively, concluded that the ultimate uniaxial strain (ϵ_f) rather than the fracture strength (σ_f) is the reliable brittle failure criterion. Brands showed that brittle failure occurs irrespective of the state of stress when the maximum elastic strain

$$\epsilon_1 = \frac{1}{E} \{ \sigma_1 - \nu(\sigma_2 + \sigma_3) \} \quad (2.5)$$

reaches a critical value.

This would mean that the combined principal stresses rather than the maximum uniaxial stress determines failure.

2.3.2 The Relation between Fracture Toughness and the Material Parameters

Examining experimental results obtained by Gurland and Parikh, it has been observed that a pure exponential relationship exists between fracture toughness in bending ϵ_{FT} and the mean free path between the carbides, i.e., the average value of the thickness of the binder layer (Figure 10).

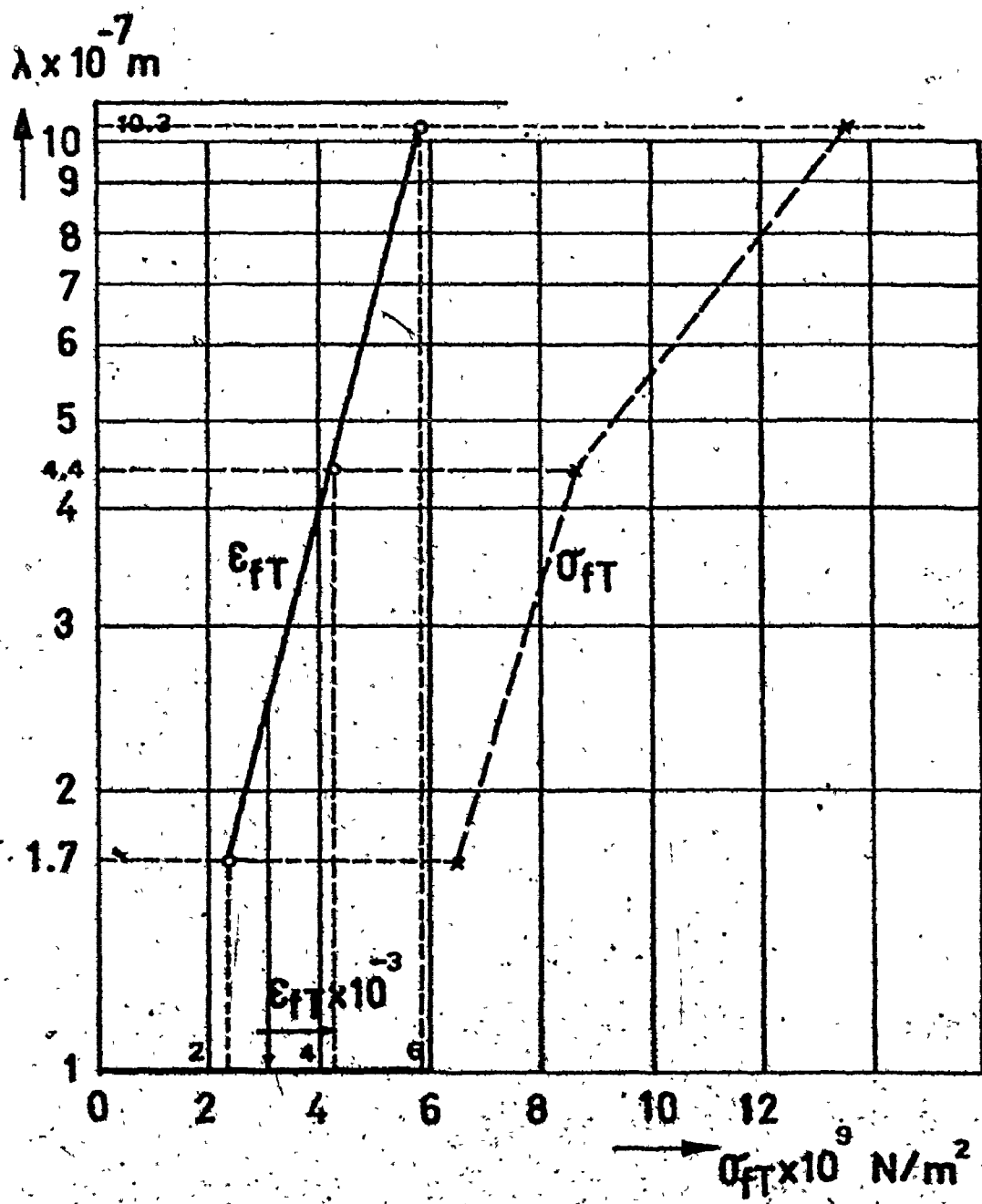


Figure 10. The Mean Free Path λ Versus Fracture Toughness after Results from Guyland and Parikh.

$16 \text{ J/m}^2 = 6895 \text{ N/m}^2$

Figure 11 taken from Liebowitz [11] shows that this behaviour can be confirmed for various sintered carbide grades quoted by their corresponding ISO denotations. The values of mean free paths have been calculated from the average particle size d_1 and the composition of the material G , assuming cubic grains

$$\lambda = d_1 \left(\sqrt[3]{\frac{1}{G}} - 1 \right)$$

2.6)

The author concludes that:

- a) Fracture toughness is mainly controlled by the mechanical properties of the binder and by the mean free path between grains.
- b) The mechanical properties of the carbides (TiC, TaC, NbC, CrC₂, WC) do not have any significant influence on fracture toughness.

Gurland and Parikh [11] have shown that strength increases with increasing values of the mean free path λ . However, beyond $\lambda = 0.45 \mu$ when the influence of plastic deformation becomes important, the trend is reversed (Figure 12).

From the work of Doi et al. [14], Figure 13, it appears that there is a systematic increase in rupture strength with a decrease in grain size.

2.3.3 Structural Parameters and their Influence on the Stress Distribution in the Binder Phase of Cemented Carbides

Although a relationship between structural and

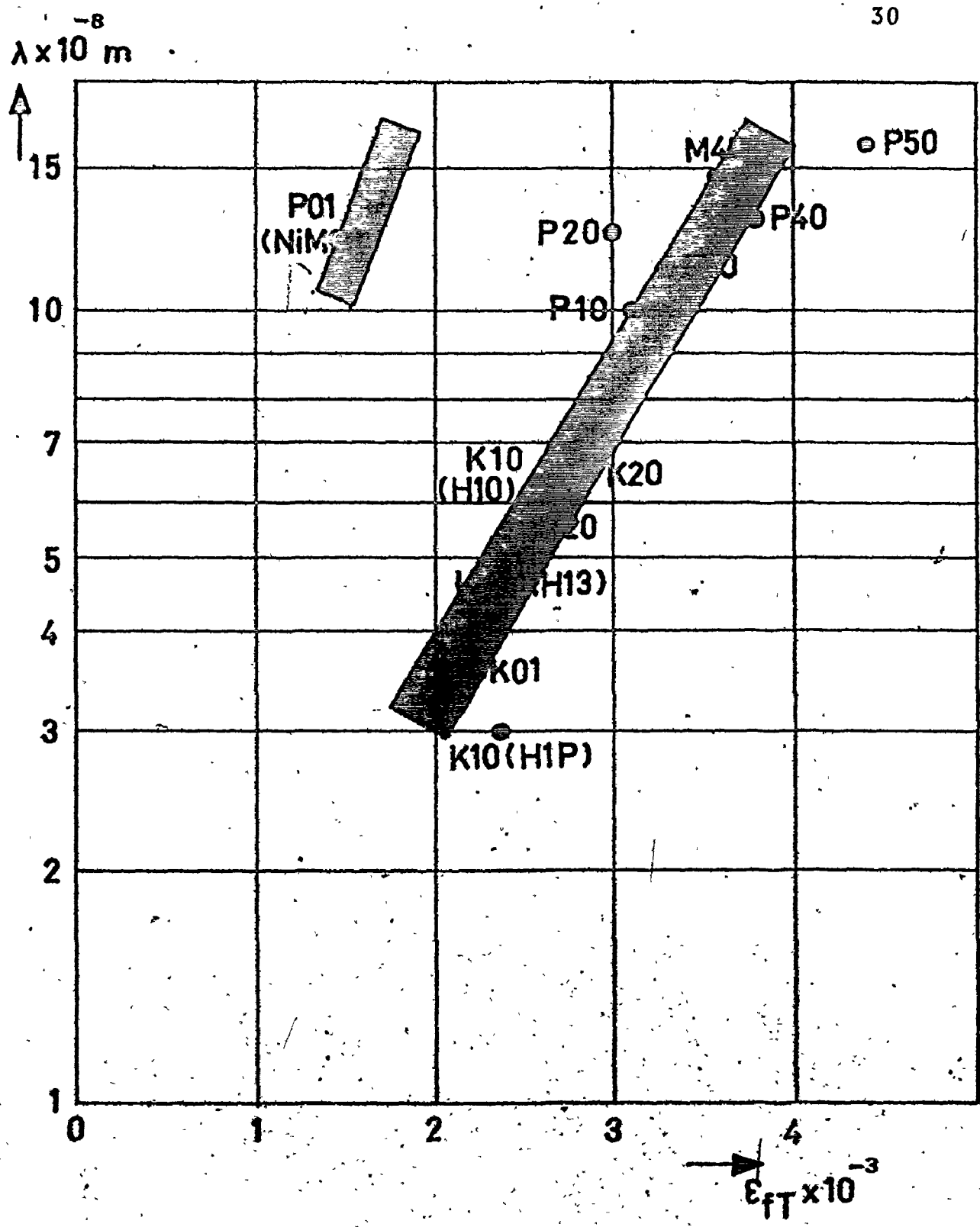


Figure 11. The Mean Free Path λ Versus Fracture
 Toughness ϵ_{fT} for a Number of Carbide
 Tool Materials.

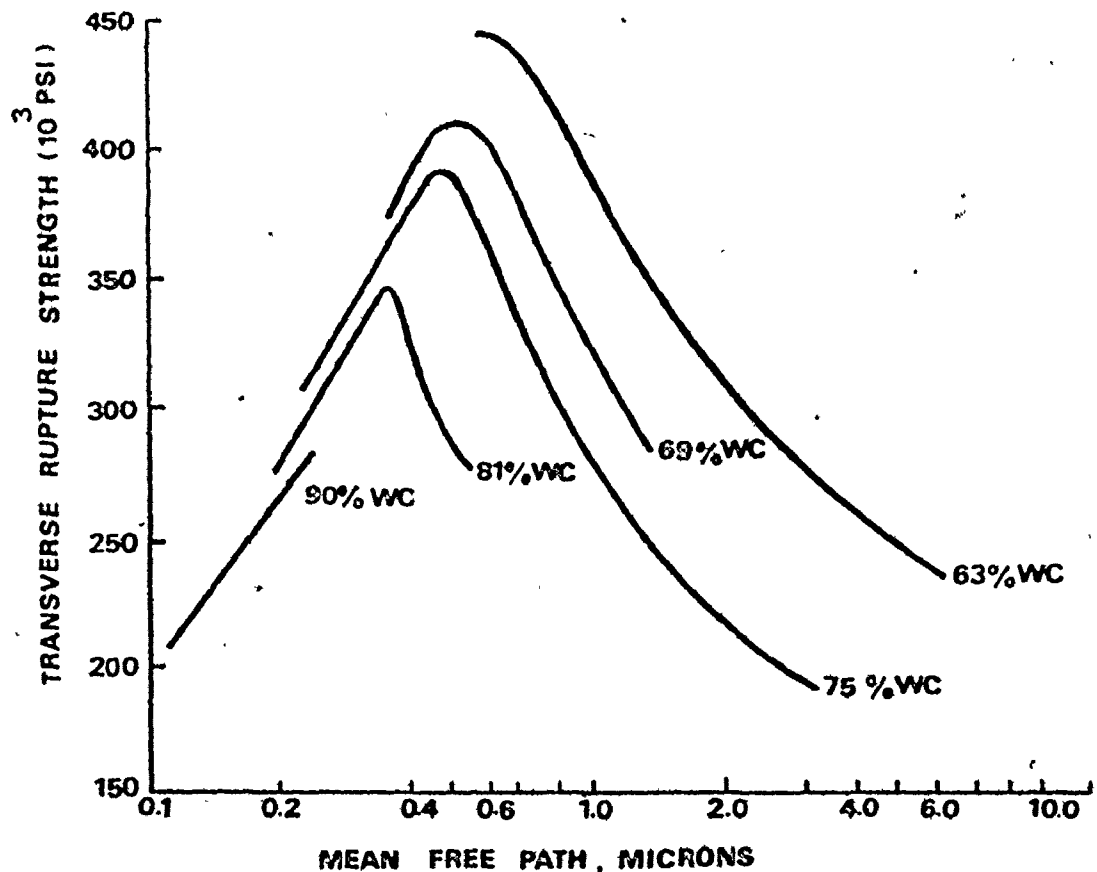


Figure 12. Transverse Rupture Strength (σ_{fT}) as a Function of Mean Free Path for Various Compositions.

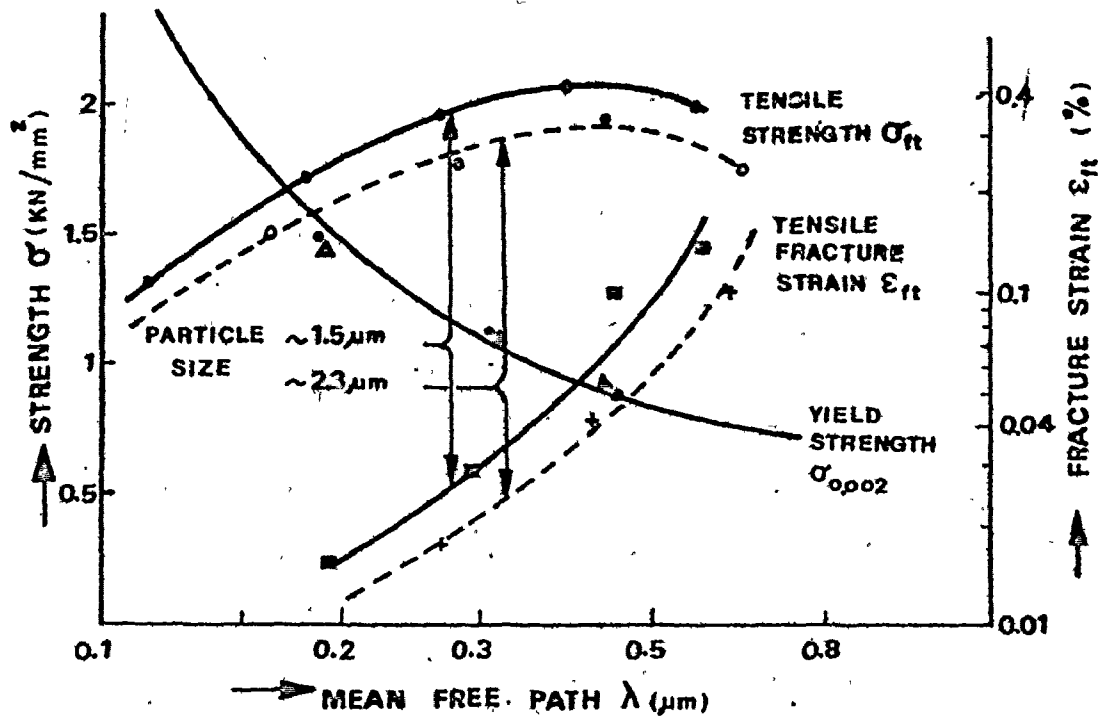


Figure 13. The Influence of Grain Size on Tensile Strength (σ_{fT}) and Fracture Strain (ϵ_{fT}) for Straight Carbides.

strength parameters exists, there remains the need for determining a generally applicable structural parameter which would uniquely quantify the fracture behaviour of cemented carbides. Bridgman [15] derived the relation

$$\frac{\bar{\sigma}}{\sigma_z} = C_B = \left[\left(1 + \frac{2h}{R} \right) \ln \left(1 + \frac{R}{2h} \right) \right]^{-1} \quad (2.7)$$

with applying the model of Figure 14-a which shows a toroidal-shaped reduction area characterized by the ratio $\frac{R}{h}$ and assuming a three-dimensional state of stress. This relationship explains the results of tensile tests at high strain values ($\bar{\sigma}$ stands for the effective stress, whilst σ_z represents the average value of the axial tensile stress related to the true area). The factor C_B is known as the Bridgman factor.

Close examination of the structure of cemented carbides was carried out by Kals and Gielisse [9]. This examination reveals, both on the surface and in the bulk (particularly in and around voids and pores) specific detail that is geometrically comparable to the tensile test situation of Figure 14-a. It seems therefore justified to adopt the analogue model of Figure 14-b, where it will be noticed that $d_{av}/2$ substitutes for R , whilst half the average value of the mean free path $\lambda_{av}/2$ represents a fair minimum value of the radius. Generally, the occurrence of intergranular voids is less frequent than is suggested in Figure 14-b. Putting the average effective distance between the voids equal to $K d_{av}$, an expression analogous to Equation (2.7) is

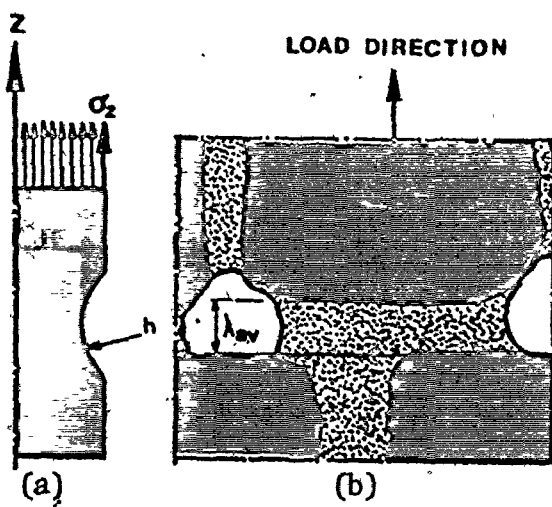


Figure 14. (a) Geometry of the Bridgman Model.
(b) Analogue for the Structure of
Cemented Carbides.

arrived at:

$$\left(\frac{\sigma}{\sigma_z}\right)_{z=0} = C = \left[\left(1 + \frac{2\lambda_{av}}{Kd_{av}} \ln \left(1 + \frac{Kd_{av}}{2/\lambda_{av}} \right) \right)^{-1} \right]^{-1} \quad (2.8)$$

The factor K depends upon the density of the voids. Its value will be largely determined by specific material processing conditions.

The ratio d_{av}/λ_{av} is a structural parameter and the potential significance of it to failure, in terms of the ultimate uniaxial strain is shown in Figures 15 and 16.

The use of tensile test analogue gives rise to the following five statements:

1. Necking phenomenon in a tensile specimen
2. Plastic flow in the carbide intergranular layer is localized and concentrated in the immediate vicinity of the voids.
3. The Bridgman factor has not been verified for values of R/h exceeding 10.
4. Maximum tensile stress occurs at the surface, so the test result depends very strongly on the surface roughness of the specimen.
5. Brittle fracture being a probabilistic feature, it depends strongly on the volume under stress, i.e., practically on the size of the specimen.

2.3.4 Standard Test Method for Measuring Material Properties

A proposal is found for the introduction of a new

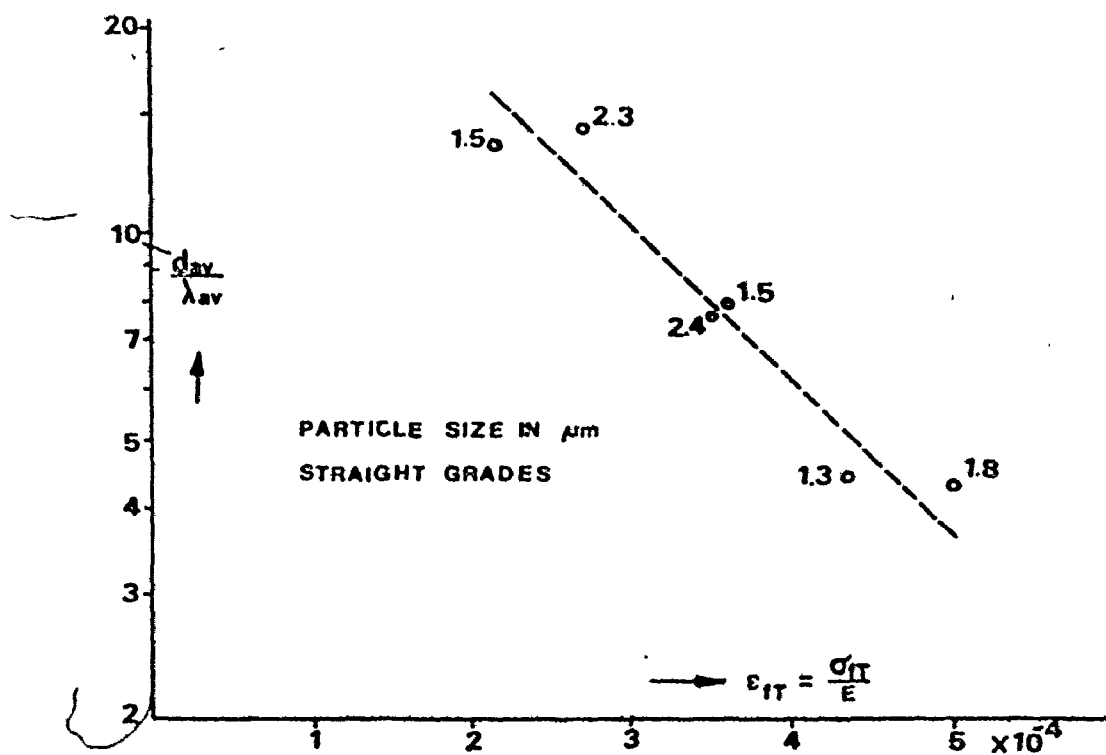


Figure 15. The Ultimate Uniaxial Strain (ϵ_{ft} , Tensile Test) as a Function of d_{av}/λ_{av} .

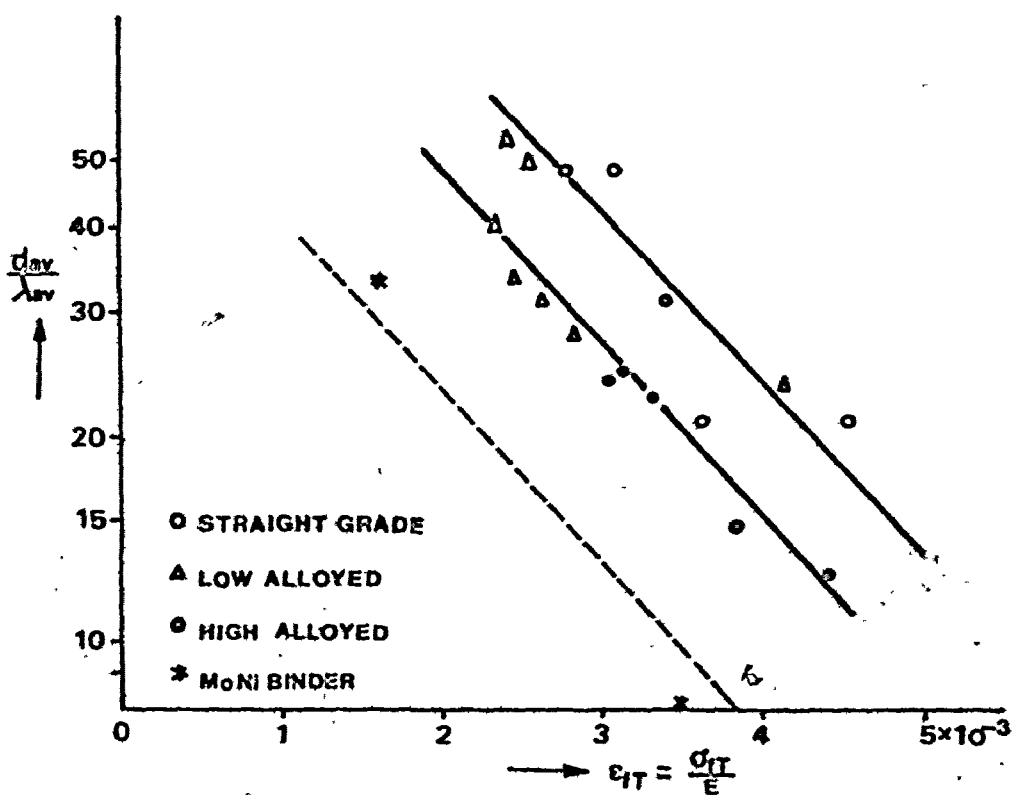


Figure 16. The Ultimate Uniaxial Strain (ϵ_{ft} , Bending Test) vs. the Ratio d_{av}/λ_{av} for a Number of Commercial Grades.

method for testing toughness of cemented carbides in which a disc-type specimen is compressed [7]. It is based upon the phenomenon that a tensile stress is acting across the loaded diameter of a diametrical loaded disc. Except for the regions quite near the strip loadings, this stress is uniformly distributed over the loaded diameter and is equal to

$$\sigma_3 = \frac{2F}{\pi dt} \quad (2.9)$$

where F = applied load
 d = diameter of the disc
 t = thickness of the disc

The stresses in such a case are shown to be as given in Figure 17.

In the region of the load the stress condition is biaxial compressive which means that the material there can resist much greater stresses. The fact that compression shows a minimum at the centre of the disc specimens may explain why the specimens rupture at the centre. Also, the volume under stress is rather well specified. For these reasons, this test may become more important than the classical test.

2.3.5 The Development of Test Method

The development of the test method based on the diametrical compression test was carried out by H. Kals and W. Nollet [16]. Square specimens are ground flat at the two diagonally opposed corners till the resulting faces

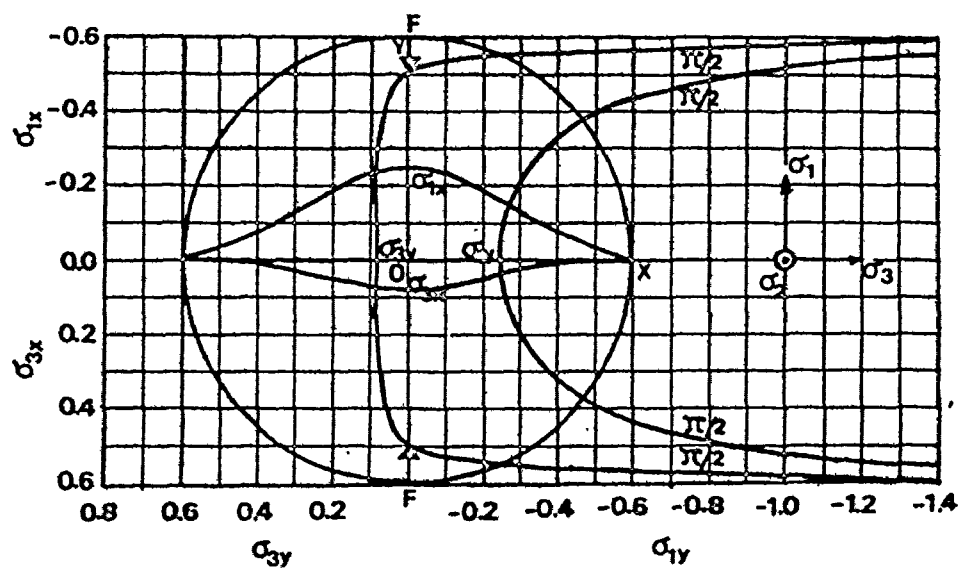


Figure 17. Distribution of Stresses of a Diametrical Loaded Circular Disk.

attain a length of $0.1 D$, where D is the length of the diagonal. The test specimen is placed upright, the two small faces touching between the dies or an adapted pillar die set. The results of stress analysis (plane stress) made with the aid of the finite element is given in Figure 18. Figure 18-a shows the principle stresses across the diagonals and Figure 18-b shows the mesh distribution in the quarter of the specimen.

2.3.6 Introduction of Tool Fracture Classification System

Keiji Okushima and Tetsutaro Hashi [17] classified the tool fractures into three major categories according primarily to the outside appearance and association with any preceding crack. They are:

Category 1 Chipping at low cutting speed.

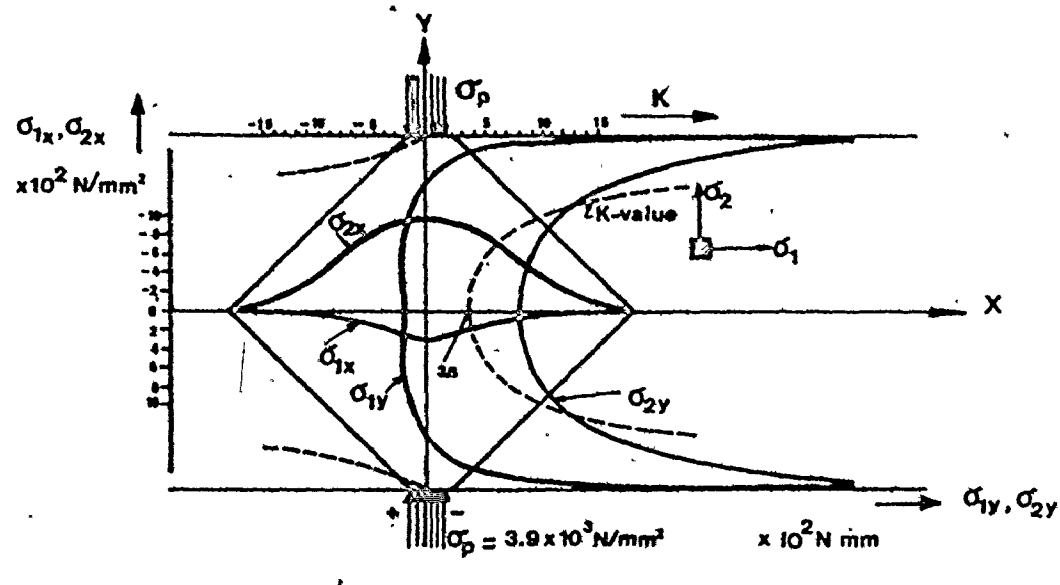
Category 2 Chipping of large size without a preceding crack.

Category 3 Fractures at high cutting speed:
it occurred as a result of fatigue damage to the tool tip.

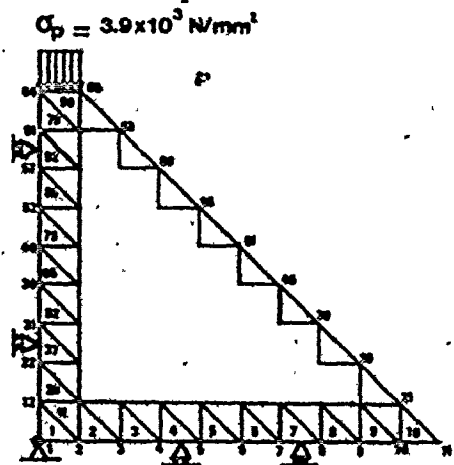
The tests were carried out in the face-milling operations on carbon steel work materials.

Features of Category 1 and Category 2

Category 1: The chipping occurred along the cutting edge, and the thickness of the fractured portion was rather small



(a)



(b)

Figure 18. Stress Distribution across the Diagonals of a Diagonally Loaded Square Specimen.

on the rake face but somewhat larger on the flank. No crack was inferred. This type of chipping occurred a short time after a new tool tip was put into operation. A tougher tool grade was safer from this type of chipping. Also it was commonly experienced that machining of a harder steel was accompanied by more danger due to this type of chipping. The experiments showed the chipping at low cutting speeds is caused by mechanical impacts of intermittent cutting and the brittleness of tool material when subjected to the impact loading (Figure 19).

Category 2: This is the fracture which occurs in a fairly large size. The fracture is supposed to start on the rake face and develop nearly parallel to the flank so that a large fracture is observed on the flank. No crack is precedingly recognized as causing the fracture. This breakage occurs occasionally at any early stage after a new tool is started.

Features of Category 3

This category is the most important one and it consists of several types of breakage which occur due to preceding cracks, therefore, they are fatigue fractures. Each type of fracture is caused by different types of cracks. They occur earlier at high cutting speeds. Fractures of this category are classified into five types. The first three types are most common in operations without cutting fluids.

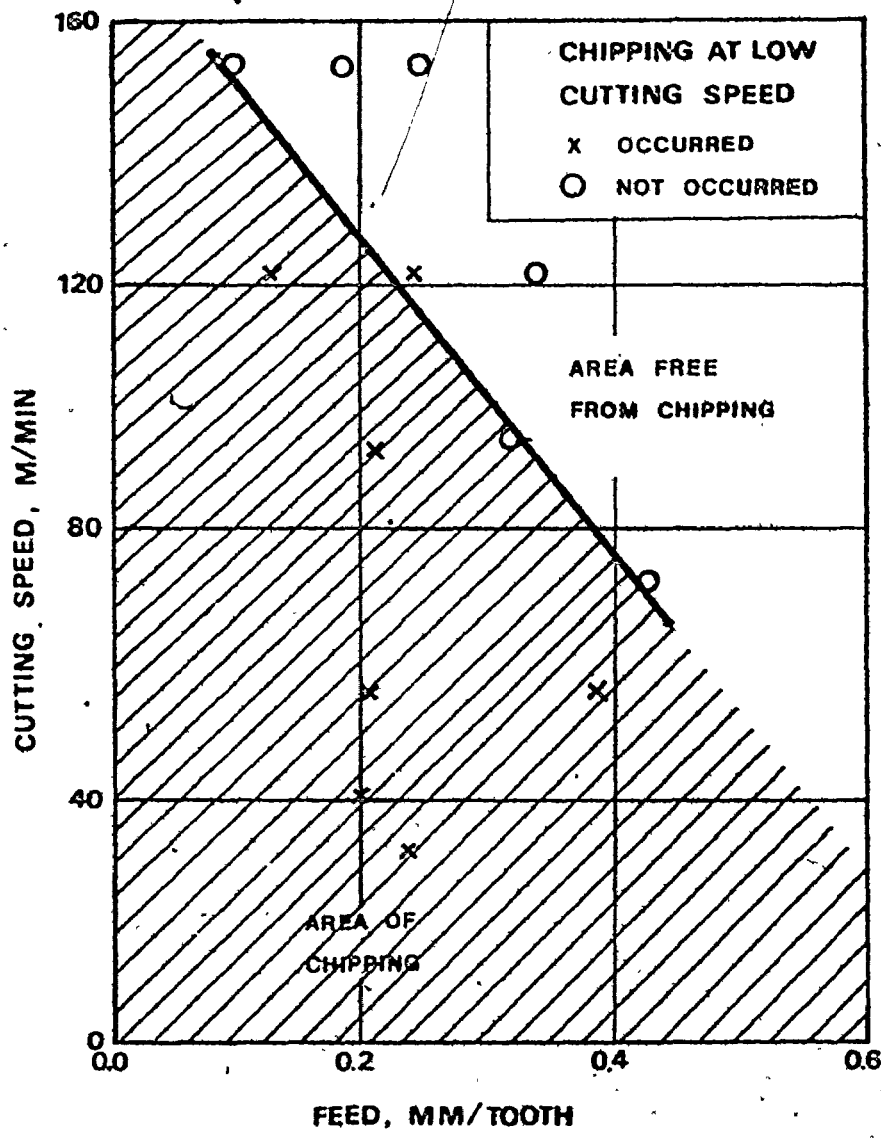


Figure 19. Safety Chart of the Chipping at Low Cutting Speed.

Fracture starting on the rake face is the first type and it is caused by cracks parallel to the cutting edge starting on the rake face. With repetition of the intermittent cutting, the crack gradually propagates into the tool material, nearly parallel to the flank surface and finally causes the breakage (Figure 20-I).

Fracture starting on the flank or land is the second type and it is caused by cross cracks starting on the flank or land (Figures 20-IIA, IIB).

The third type is fracture starting both on the rake face and on the flank and it is caused by combined propagation of the above two cracks (Figures 20-III A, B, C, D).

Figure 21 shows that the fracture starting on the flank occurs below a certain cutting speed and the chipping starting on the rake face occurs at high cutting speeds.

Breakage is a fourth type of fracture at high cutting speeds. This is a fracture caused by a crack in the direction nearly perpendicular to the cutting edge which propagates and finally splits the tool tip (Figure 22).

Occasionally, thermal cracks occur also in the direction parallel to the cutting edge.

Pitting is a fifth type of fracture at high cutting speeds. This is segregation of a thin layer of tool material from the localized portion of the tool chip contact area. Pitting occurs adjacent to thermal cracks both perpendicular and parallel to the cutting edge (Figure 20-IV).

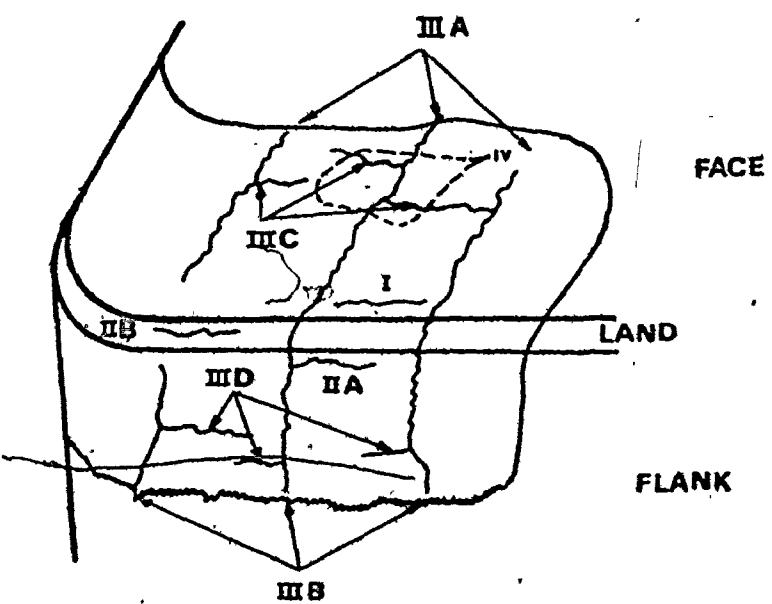


Figure 20. Typical Location and Appearance of Various Types of Fatigue Cracks.

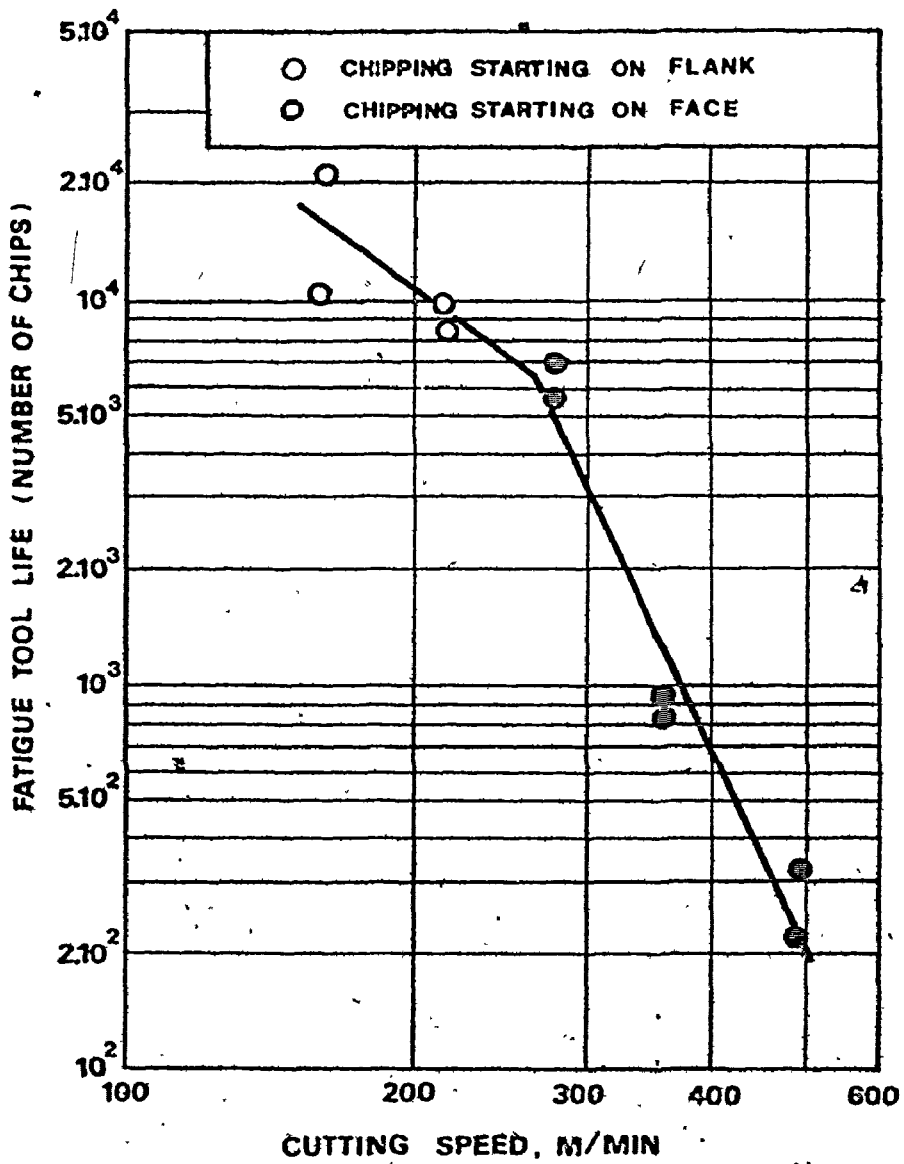


Figure 21. Fatigue Tool Life of P20 Tungsten Carbide Determined by the Chipping Starting on the Flank and/or the Chipping Starting on the Rake Face.



Figure 22. Example of Breakage. Tool Grade KZH, Rake Angle +ve 5°, Work Material Steel 4340 (217 BHN), Initial Diameter 3 inches, Depth of Cut 0.1 inch, Feed .035 inch/rev., Cutting Speed 250 ft./min.

CHAPTER 3

EXPERIMENTAL RESULTS

3.1 Introduction

Failures of tungsten and titanium carbide tools due to fracture of the cutting edge were investigated in turning operations using alloy steel 4340 for work material. The purpose was to classify what is generally called fracture of the tool edge into several definite types and to reveal the cause and mechanism of each type.

The study consisted of metal cutting tests in which tools were tested until they fail due to fracture. The fractured tool was inspected under a scanning electron microscope to analyze the location, size, direction and other characteristics of the fracture.

3.2 Test Equipment and Materials

3.2.1 Machine tool

All turning tests were performed on a Mazak-Rex heavy duty lathe rated at 25 HP of main motor. The spindle speed ranged from 12 to 1200 rev./min. (stepless speed drive) and the feed ranged from (0.0021 inch - 0.265 inch).

3.2.2 Tool

Tool holders for triangular negative rake inserts

and triangular positive rake inserts were used. They had 4.5 in. length, 3/4 in. x 3/4 in. cross section and 30° side cutting edge angle. Figure 23 shows the dimensions of the inserts used and mounted in the tool holder. They had negative 5° and positive 5° rake angles. Steel machining grades of tungsten-titanium carbide Kennametal K7H (93.5 R_WA) and K45 (92.5 R_WA) and Wickaloy WP6 (92.2 R_WA) and WP5 (91.0 R_WA) were used.

They have a three-phase structure as shown in Figures 24, 25, 26 and 27 showing the angular grey grains of tungsten carbide (WC), round dark grey grains of complex (WC + TiC + TaC) carbide and the white phase (Co).

The exact composition of the Kennametal grades was not available. Hardness and chemical composition of the Wickaloy grades (WP6 and WP5) are listed in Table 3.

Table 3

Grade	Chemical Composition				Hardness R _W A
	Co	WC	TiC	TaC	
WP5	8	72	9	11	91.0
WP6	4.5	71	12.5	12	92.2

3.2.3 Workpiece

Three kinds of steel were used: 4340 alloy steel normalized with hardness 217 BHN, 4340 hardened and tempered to about 380 BHN and 1040 carbon steel. Their compositions

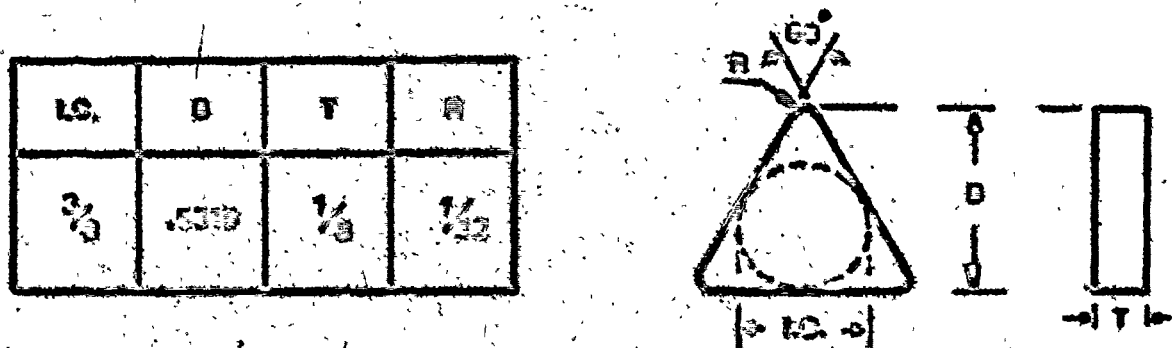


Figure 23: Dimensions of the tool.



Figure 24: Microstructure of K7H Carbide grade (X2000)

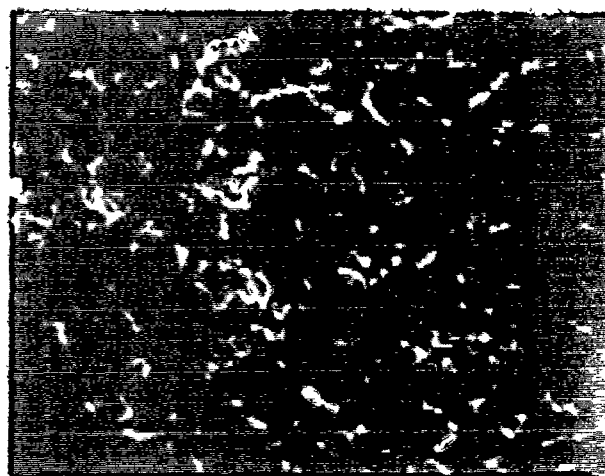


Figure 25: Microstructure of K45 Carbide grade (X2000)



Figure 26: Microstructure of WP5 Carbide grade (X2000)

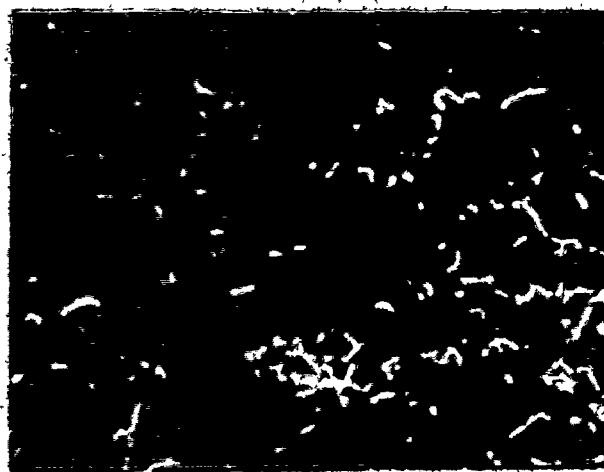


Figure 27: Microstructure of WP6 Carbide grade (X2000)

are listed in Table 4

Table 4

Steel	C	Mn	S	Si	Cr	Ni	Mo	P	Brinell Hardness BHN
4340	.4	.7	0.02	.25	.8	1.75	.25	0.04	217
1040	.4	.6-.7	0.04	-	-	-	-	0.04	210

3.3 Cutting Tests

Two types of cutting tests were carried out. The first type was continuous cutting, where K7H and K45 tool grades and the three kinds of steel workpieces were used. The second type was interrupted cutting. Tool grades WPS and WP6 and 4340 hardened and tempered steel workpiece were used.

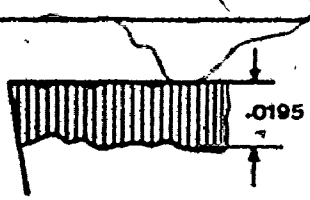
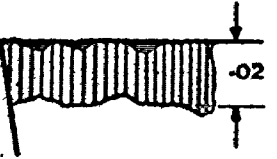
For every tool the test was carried out by increasing the feed in steps from 0.010 inch up to 0.043 inch and using 0.05 inch or 0.1 inch depth of cut. The cutting speed also changed due to the change in workpiece diameter starting from 250 ft./min. down to 100 ft./min.

The tests were periodically interrupted and the tools were examined using the tool maker's microscope. The test results of continuous cutting were recorded in Tables 5 to 18.

For interrupted cutting the test results were recorded in Tables 19, 20 and 21.

a. Continuous Cutting tests

Table 5 : Cutting test results using tool number (1-a)

Tool number (1)				
Cutting time (min.)	Cutting speed (ft/min.)	feed (in./rev.)	Sketch of the figure Shown under the microscope	Comment
1	260	.010		Flank wear
2	260	.010		Flank wear + chipping
3.5	250	.010		Flank wear + chipping
5.5	225	.018		Flank wear + chipping

Cont. Table 5

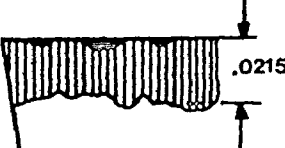
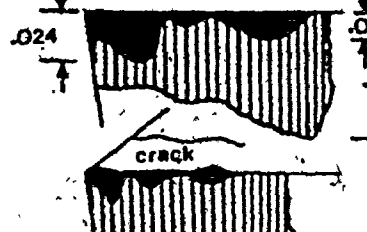
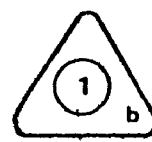
Cutting time (min.)	Cutting speed (ft/min.)	feed (in./rev.)	Sketch of the figure Shows under the microscope	Comment
8	190	.024		Flank wear + chipping
10	180	.024		Flank wear + chipping
12	160	.024		Flank wear + chipping
14	140	.024		Flank wear + large amount of chipping
16	120	.024		Flank wear + large amount of chipping
18	110	.024		Flank wear + large amount of chipping + crack

Table 6 : Cutting test results using tool number (1-b)

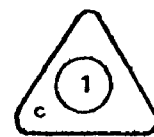
53

Tool Number 1-b.



Cutting time (min.)	Cutting speed (ft/min.)	feed (in./rev.)	Sketch of the figure Shown under the microscope	Comment
5.5	220	.010		Flank wear + chipping
9.5	160	.024		Flank wear + chipping
13	130	.027		Flank wear + chipping
15.5	110	.035		Flank wear + chipping
18	100	.035		The tool is broken

Tool Number 1-c



T min.	V ft/min	f in.	Sketch of the figure Shown under the microscope	Comment
1	110	.024		Flank wear + chipping
2.5	110	.024		Flank wear + chipping
5.5	100	.024		Flank wear + chipping
7.5	90	.032		Flank wear + chipping
9.0	90	.043		The tool is broken

Table 8 : Cutting test results using tool number (2)

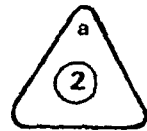
55

Tool number (2)

Tool material : K7H

Geometry of tool : positive 5° rake angleWorkpiece material : steel 4340, 217 HN, initial diameter 3.0 in.,
length 18.0 in.

Depth of cut : 0.05



Cutting time (min.)	Cutting speed (ft/min)	feed (in./rev.)	Sketch of the figure Shown under the microscope	Comment
.5	240	.027		The tool is broken

Tool number 2-b



10	240	.027		Flank wear
20	240	.027		Flank wear + chipping
30	240	.027		The tool is broken

Table 9 : Cutting test results using tool number (3)

56

Tool number (3)

Tool material : K7H

Geometry of tool : positive 5° rake angleWorkpiece material : steel 1040, 210 BHN, initial diameter 2.0 in.,
length 18.0 in.

Depth of cut : 0.05 in.



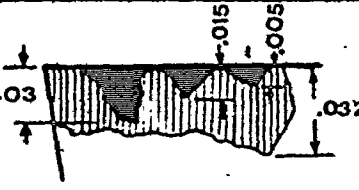
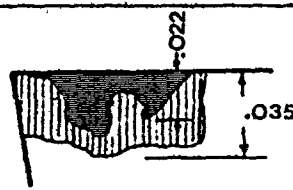
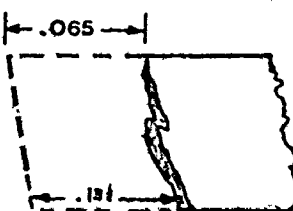
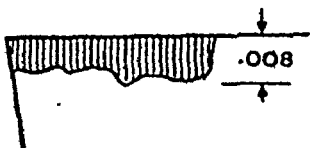
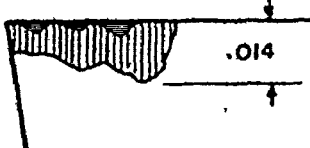
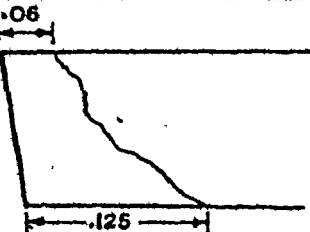
Cutting time (min.)	Cutting speed (ft/min)	feed (in./rev.)	Sketch of the figure Shown under the microscope	Comment
3	240	.027		Flank wear + chipping
6.5	240	.027		Flank wear + chipping
9.5	240	.027		The tool is broken

Table 10 : Cutting test results using tool number (4-a)

57

Tool number (4)				
Cutting time (min.)	Cutting speed (ft/min)	feed (in./rev.)	Sketch of the figure Shown under the microscope	Comment
1.5	250	.019		Flank wear
4.5	240	.035		Flank wear + chipping
5.5	230	.043		Crack

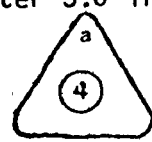


Table 11 : Cutting test results using tool number (4-b,c)

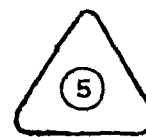
Tool number 4-b,c				
Cutting time (min.)	Cutting speed (ft/min)	feed (in./rev.)	Sketch of the figure Shown under the microscope	Comment
1.5	220	.019		Flank wear + chipping
4.5	200	.035		Flank wear + chipping
6	190	.043		The tool is broken

Table 12 : Cutting test results using tool number (5)

59

Tool number (5)

Tool material : K45
 Geometry of tool : positive 5° rake angle
 Workpiece material : steel 4340, 217 BHN, initial diameter 2.0 in.,
 length 18.0 in.
 Depth of cut : 0.05 in.



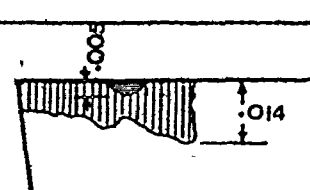
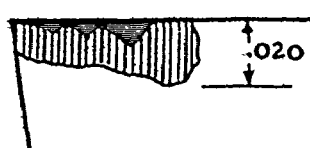
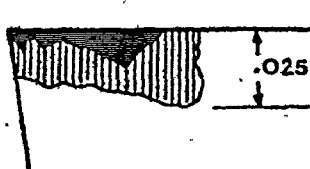
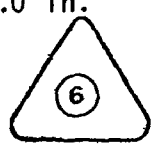
Cutting time (min.)	Cutting speed (ft/min.)	feed (in./rev.)	Sketch of the figure Shown under the microscope	Comment
3.5	240	.027		Flank wear + chipping
8.5	240	.027		Flank wear + chipping
13.5	220	.035		Flank wear + chipping

Table 13 : Cutting test results using tool number (6)

60

Tool number (6)

Tool material : K45
 Geometry of tool : negative 5° rake angle
 Workpiece material : 4340 steel hardened and tempered to 380 BHN,
 initial diameter 2.0 in., length 18.0 in.
 Depth of cut : 0.05 in.



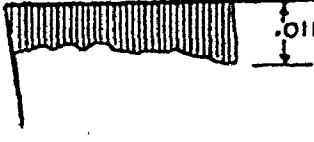
Cutting time (min.)	Cutting speed (ft/min.)	feed (in./rev.)	Sketch of the figure Shown under the microscope	Comment
1	250	.010		Flank wear
2	250	.024		Flank wear
3	250	.035		Plastic deformation

Table 14 : Cutting test results using tool number (7-a) 61

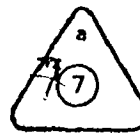
Tool number (7)

Tool material : K45

Geometry of tool : positive 5° rake angle

Workpiece material : 4340 steel hardened and tempered to 380 BHN, initial diameter 2.6 in., length 18.0 in.

Depth of cut : 0.1 in.

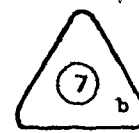


Cutting time (min.)	Cutting speed (ft/min.)	feed (in./rev.)	Sketch of the figure Shown under the microscope	Comment
1	160	.020.		Flank wear
2	160	.027		Flank wear + chipping
5	160	.038		The tool is broken

Table 15 : Cutting test results using tool number (7-b)

62

Tool number 7-b



Cutting time (min.)	Cutting speed (ft/min)	feed (in./rev.)	Sketch of the figure Shown under the microscope	Comment
1	150	.020		Flank wear
4	150	.030		Flank wear + chipping
7	150	.033		Flank wear + chipping
8	150	.033		The tool is broken



Table 16 : Cutting test results using tool number (8)

Tool number (8)

Tool material : K45

Geometry of tool : negative 5° rake angleWorkpiece material : steel 4340, 217 BHN, initial diameter 2.3 in.,
length 18.0 in.

Depth of cut : 0.1 in.



Cutting time (min.)	Cutting speed (ft/min.)	feed (in./rev.)	Sketch of the figure Shown under the microscope	Comment
2	250	.018	<p>A micrograph sketch showing a machined surface with a wavy profile. A vertical dimension line indicates a height of .005 inches from the base to the peak of the waviness.</p>	Flank wear
3.5	250	.024	<p>A micrograph sketch showing a machined surface with a wavy profile and some small, irregular chips or pits. A vertical dimension line indicates a height of .006 inches from the base to the peak of the waviness.</p>	Flank wear + chipping
4.5	250	.030	<p>A micrograph sketch showing a machined surface with a wavy profile and more pronounced chipping. A vertical dimension line indicates a height of .009 inches from the base to the peak of the waviness.</p>	Flank wear + chipping
5.5	200	.030	<p>A micrograph sketch showing a machined surface with a wavy profile and significant chipping. A vertical dimension line indicates a height of .013 inches from the base to the peak of the waviness.</p>	Flank wear + chipping
7.5	200		<p>A micrograph sketch showing a machined surface with a very wavy profile and extensive chipping. A vertical dimension line indicates a height of .016 inches from the base to the peak of the waviness.</p>	Flank wear + chipping

Cont. Table 16

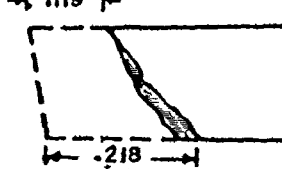
Cutting time (min.)	Cutting speed (ft/min)	feed (in.rev.)	Sketch of the figure Shown under the microscope	Comment
9.5	160			Flank wear + chipping
11.5	160			The tool is broken

Table 17 : Cutting test results using tool number (9)

65

Tool number (9)

Tool material : K45
 Geometry of tool : positive 5° rake angle
 Workpiece material : 4340 steel hardened and tempered to 380 BHN,
 initial diameter 1.5 in., length 20.0 in.
 Depth of cut : 0.1 in.

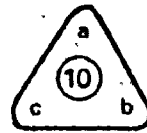


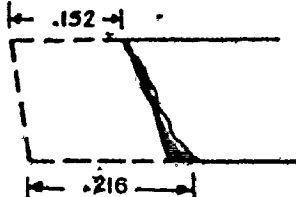
Cutting time (min.)	Cutting speed (ft/min.)	feed (in./rev.)	Sketch of the figure Shown under the microscope	Comment
.5	150	.033		The tool is broken
1	150	.03		The tool is broken
2	150	.02		Good example of chipping

Table 18 : Cutting test results using tools number (10,11)

Tool number (10)

Tool material : K45
 Geometry of tool : positive 5° rake angle
 Workpiece material : steel 4340, 217 BHN, initial diameter 2.0 in.,
 length 20.0 in.
 Depth of cut : 0.1 in.

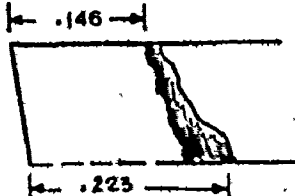


Cutting time (min.)	Cutting speed (ft/min.)	feed (in./rev.)	Sketch of the figure Shown under the microscope	Comment
1.0	250	.031		The tool is broken

Tool number (11)

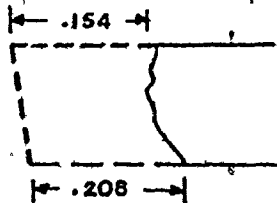
Tool material : K45
 Geometry of tool : positive 5° rake angle
 Workpiece material : steel 4340, 217 BHN, initial diameter 2.0 in.,
 length 20.0 in.
 Depth of cut : 0.1 in.



Cutting time (min.)	Cutting speed (ft/min.)	feed (in./rev.)	Sketch of the figure Shown under the microscope	Comment
1.0	250	.034		The tool is broken

b. Interrupted Cutting tests

Table 19 : Cutting test results using tool number (1)

Tool number (1)			
Cutting time (min.)	Cutting speed (ft/min.)	feed (in./rev.)	Sketch of the figure Shown under the microscope
.1	250	.020	 <p>The sketch shows a stepped profile. The top horizontal segment has a width of .154 indicated by arrows at the ends. The bottom horizontal segment is wider, indicated by arrows at the ends, and appears to be approximately .208 wide. A vertical dashed line connects the two segments.</p>



Comment

The tool is broken

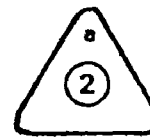
Table 20 : Cutting test results using tool number (2)

Tool number (2)

Tool material : WP5

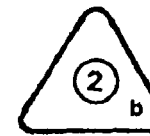
Geometry of tool : positive 5° rake angleWorkpiece material : steel 4340 hardened and tempered to 380 BHN,
initial diameter 3.5 in., length 25.0 in.

Depth of cut : 0.1 in.



Cutting time (min.)	Cutting speed (ft/min.)	feed (in./rev.)	Sketch of the figure Shown under the microscope	Comment
1.5	200	0.022		Breakage

Tool number 2-b



2	250	0.017		Chipping
5	250	0.017		Breakage

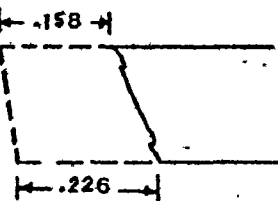
Table 21 : Cutting test results using tools number (3,4)

69

Tool number (3)

Tool material : WP6
 Geometry of tool : positive 5° rake angle
 Workpiece material : 4340 steel hardened and tempered to 380 BHN,
 initial diameter 3.0 in., length 25.0
 Depth of cut : 0.1 in.

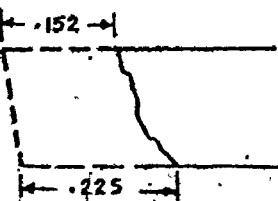


Cutting time (min.)	Cutting speed (ft/min)	feed (in./rev.)	Sketch of the figure Shown under the microscope	Comment
1.0	180	0.0155		The tool is broken

Tool number (4)

Tool material : WP6
 Geometry of tool : positive 5° rake angle
 Workpiece material : 4340 steel hardened and tempered to
 380 BHN, initial diameter 3.0 in.,
 length 25.0
 Depth of cut : 0.1 in.



Cutting time (min.)	Cutting speed (ft/min)	feed (in./rev.)	Sketch of the figure Shown under the microscope	Comment
1.0	200	0.022		The tool is broken

According to the preceding tables, the results of the tests conducted for both types of cutting are summarized in Tables 22 and 23:

From Table 22 one may conclude that:

1. Complete breakage of the tool occurred starting from a feed rate of 0.027 in./rev. In the case of tool 1-a the only observations were chipping and crack on the rake face at 0.024 in./rev. feed rate.
2. Breakage occurred at a higher feed rate (0.043 in./rev.) when using tools with negative rake angle (tools 4, 6 and 8), than with tools with positive rake angle.
3. An increase in the depth of the cut (0.1 in.) had a similar effect as an increase of feed; it lead to a breakage in a shorter cutting time.
4. For the same cutting conditions tool material and workpiece there was considerable scatter in the time of cutting before breakage. (Tool number 7 was broken after 4 minutes while tool number 9 was broken after 0.5 minute).
5. The difference in breakage observed in cutting the hardened steel (380 BHN) and non-hardened steel (217 BHN) was rather small.
6. In general breakage occurred at heavy loads on the tool tip, actually, when a load specified by feeds in the range of 0.027 inch to 0.043 inch at 0.05 and 0.1 inch width of cut was exceeded. Often, it occurred first after some amount of chipping had

Table (22) : Cutting test results in case of continuous cutting

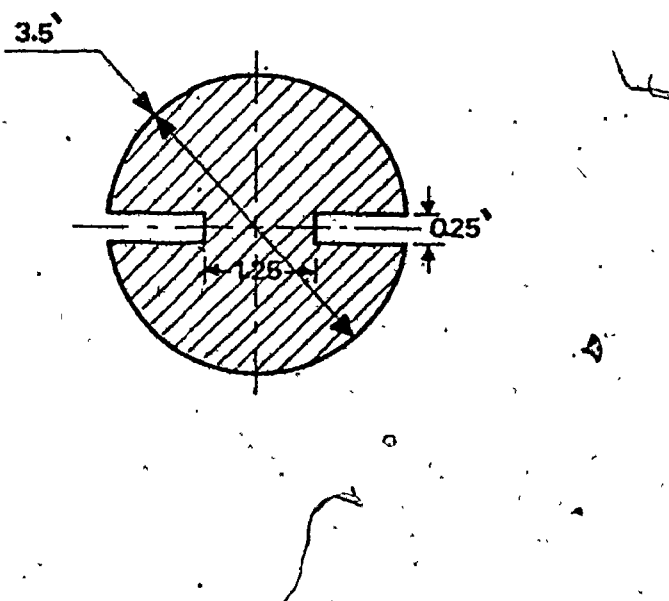
Tool		Work piece material	Cutting speed (ft/min)	Maximum feed (inch)	Depth of cut (inch)	Total time (min.)	Time at max. feed (min.)	Speed at max. feed (ft/min.)	Comment
No.	grade								
1-a	K7H	4340 STEEL 217 BHN	260	0.024	0.05	18	12.5	110	Chipping, crack
1-b	positive 5°		220	0.035	0.05	18	5	100	Chipping, break
1-c	RAKE ANGLE		110	0.043	0.05	9	1.5	90	Chipping, break
2-a	K7H	4340 STEEL 217 BHN	240	0.027	0.05	0.5	0.5	240	Break
2-b	positive 5° RAKE		240	0.027	0.05	9.5	9.5	240	Break
3	K7H +ve 5° RAKE	1040 STEEL 210 BHN	240	0.027	0.05	9.5	9.5	240	Break
4-a	K7H	4340 STEEL 217 BHN	250	0.043	0.05	5.5	1.0	230	Break
4-b,c	negative 5° RAKE		220	0.043	0.05	6	1.5	190	Break
5	K45 +ve 5° RAKE	4340 STEEL 217 BHN	240	0.036	0.05	13.5	5	220	Chipping

Cont. Table (22)

Tool		Work piece material	Cutting speed (ft/min)	Maximum feed (inch)	Depth of cut (inch)	Total time (min.)	Time at max. feed (min.)	Speed at max. feed (ft/min.)	Comment
No.	grade								
6	K45 -ve 5° RAKE	hardened 4340 380 BHN	250	0.035	0.05	3	1	250	Plastic deformation
7-a	K45 positive	hardened 4340 380 BHN	160	0.038	0.1	5	3	160	Break
7-b	5° RAKE	380 BHN	150	0.033	0.1	8	4	150	Break
8	K45 -ve 5° RAKE	4340 STEEL 217 BHN	250	0.03	0.1	11.5	8	160	Break
9-a	K45 positive	hardened 4340 STEEL	150	0.033	0.1	.5	.5	150	Break
9-b	5° RAKE	380 BHN	150	0.03	0.1	1.0	1.0	150	Break
9-c	ANGLE		150	0.02	0.1	2.0	2.0	150	Chipping
10 a,b,c	K45 +ve 5° RAKE	4340 STEEL 217 BHN	250	0.031	0.1	1.0	1.0	250	Break
11 a,b,c	K45 +ve 5° RAKE	4340 STEEL 217 BHN	250	0.039	0.1	1.0	1.0	250	Break

Table (23) : Cutting tests results in case of interrupted cutting

Tool		Work piece material	Cutting speed (ft/min)	Maximum feed (inch)	Depth of cut (inch)	Total time (min.)	Time at max. feed (min.)	Speed at max. feed (ft/min.)	Comment
No.	grade								
1	WP5 - ve 5° RAKE	HARDENED STEEL (380 BHN)	180	0.02	0.1	2.0	2.0	180	Break
2-a	WP5 - ve 5° RAKE		250	0.017	0.1	3.0	3.0	250	Break
2-b	WP5 - ve 5° RAKE		200	0.022	0.1	1.5	1.5	200	Break
3	WP6 - ve 5° RAKE		200	0.022	0.1	.5	.5	200	Break
4	WP6 - ve 5° RAKE		180	0.0155	0.1	0.5	0.5	180	Break



accumulated on the cutting edge (thus obviously contributing to the increase in the cutting force). Sometimes, however, it occurred after a very short time.

Comparing the results of tests carried out in interrupted cutting, Table 23 with those of continuous cutting the most significant difference is found in the fact that in interrupted cutting, complete breakage occurred at feeds of 0.015 inch to 0.022 inch at which it did not occur at all in the continuous cut. Again, the times before breakage were rather short.

The tests were carried out by turning a workpiece with two slots .25 inch wide as indicated by the diagram in Table 23. The side cutting edge angle of the tool was 30° . The diameter of the workpiece was about 3.5 inches and, on average, the spindle speed was about 220 r.p.m.

This means that the increased tendency to breakage in the interrupted cutting cannot be explained by fatigue because the number of impacts before breakage was between 100 and 400. Therefore, the reason should be related rather to either special loading conditions on the edge of the tool at the entrance or at the exit of the cut or to the interference of the chip adhering to the tool at the end of every cutting period. Thermal cycling is not a probable influence because the slots are rather narrow and the tool does not have enough time to cool down between the cutting periods.

3.4 Fractography

The study of fracture in sintered carbides on a microscope scale has been limited mainly to the optical examination of surface cracks on the intersections of fracture surfaces with polished surfaces. The large depth of focus of the scanning electron microscope has permitted the examination of fracture surfaces of many different materials. There appears, however, to have been few applications of the technique to the sintered carbides.

3.5 Fracture Mechanisms for Sintered Carbides

3.5.1 Transgranular Fracture

If the fracture through the tool followed a random surface, the fraction of the surface represented by transgranular fracture would be equal to the volume fraction of carbide in the tool. The actual fractions observed were always much smaller than expected on this basis [1].

Figure 28 shows a transgranular crack at a WC-15% Co specimen [2]. The fraction of transgranular fracture was found to depend on the grain size rather than the cobalt content.

Kreimer and Alekseyva [3] report that no fracture of grains smaller than $2 \mu\text{m}$ was observed in the cracked specimens.

3.5.2 Intergranular Fracture

The two types of intergranular fracture, namely ductile rupture of the cobalt (which means that the fracture



Figure 28: Optical micrograph showing a transgranular crack in one of the sides of a WC-15 wt%Co specimen. The trains transversed by the crack have been indicated by arrows [2].

occurs through the cobalt layer) and interfacial fracture (which means that the fracture occurs tangent to the grain boundaries) will be discussed together (Figure 29). The fraction of intergranular fracture area represented by interfacial fracture was found to correlate with the cobalt content of the tools but not with their grain size [1].

Figure 30 shows an intergranular crack of the same specimen as Figure 28 [2]. The interfacial fracture area decreased rapidly as the cobalt volume fraction increased from about .1 to .4 [1].

It is concluded, therefore, that intergranular fracture does not follow a random intergranular path and produce one or other mode of fracture according to the thickness of cobalt encountered locally.

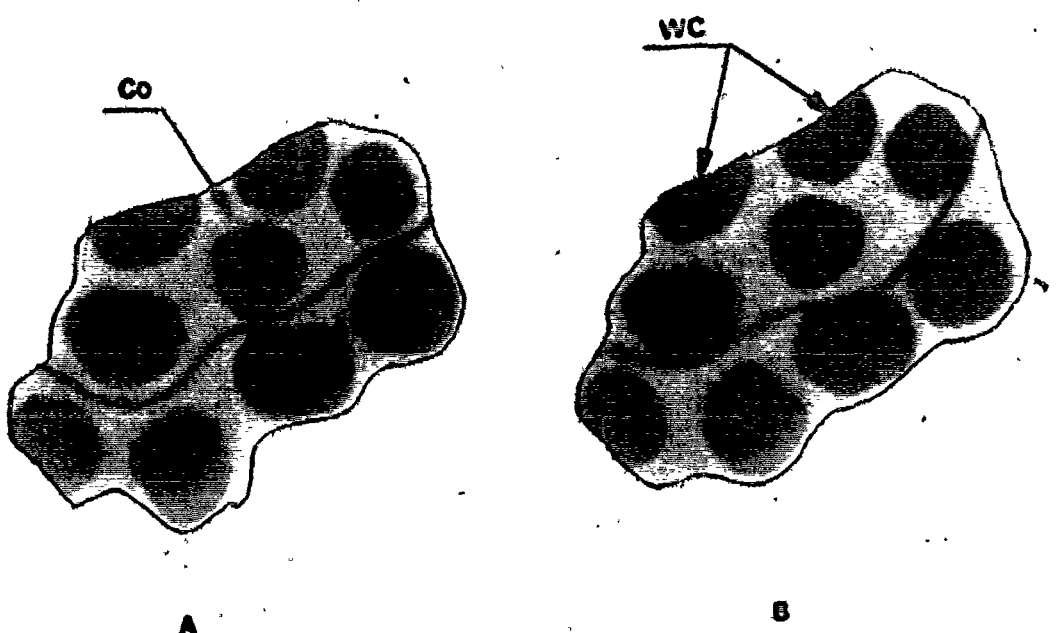


Figure 29: Types of intergranular fracture.

- A - Ductile rupture of carbide
- B - Interfacial fracture

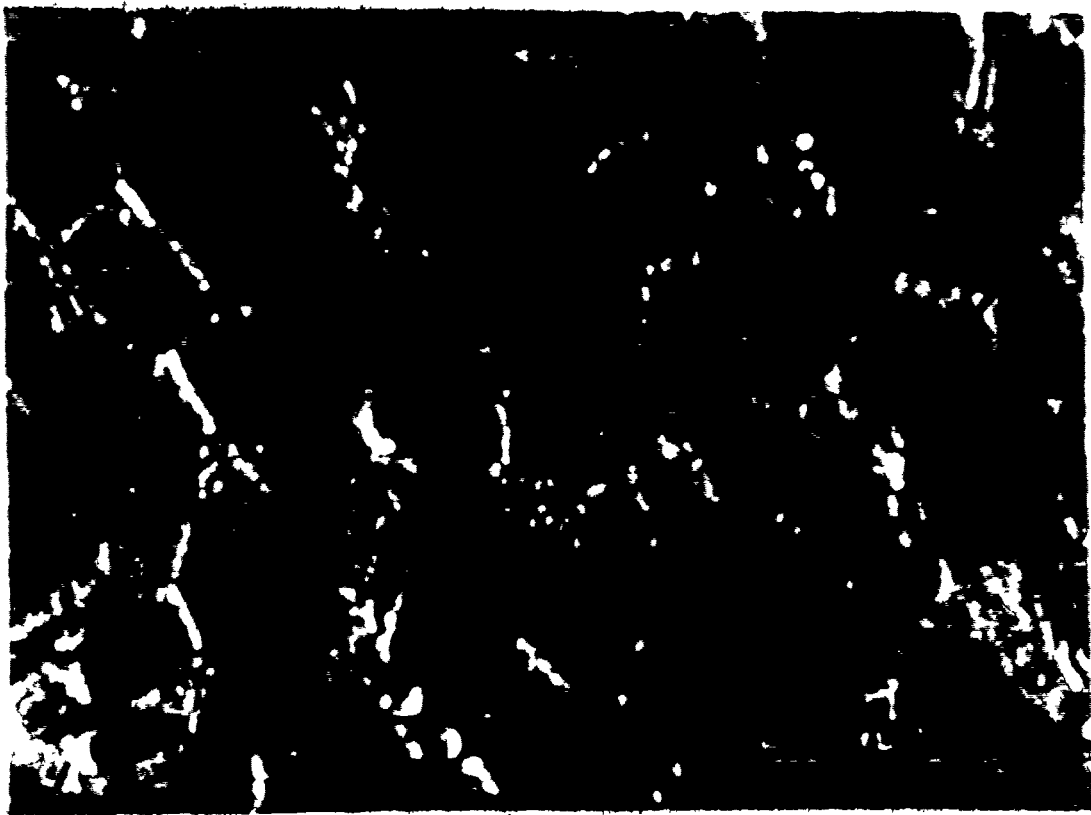


Figure 30: Optical micrograph showing an intergranular crack in one of the sides of the same specimen as figure 28.

3.6 Evaluation of Test Results

3.6.1 Type of Fracture

On a macroscopic scale, the fracture of all the tools tested had the characteristic features of brittle fracture except in the region where chipping occurred.

No reduction in thickness was observed, and the fragments into which the tools broke fitted one another exactly, so that they could be put together restoring the tools to their original shape and size.

The tool fractures were classified into two major categories according primarily to the outside appearance and the feature of the fracture. They are:

3.6.2 Chipping

Chipping occurs along the cutting edge. Figure 31 shows the chipping area with low magnification. The appearance of the chipped away surfaces makes it obvious that it occurred gradually. Due to the high temperature generated from the cutting operation, the binder (Cobalt) starts to lose a part of its strength which results in some plastic deformation.

Also a portion of the work metal could be adhered to the cutting edge. The tool edge was examined under the ESM using the X-ray to determine its composition. At the nose it is found that a steel layer is spread over the carbide grains (Figure 32-a). It is interesting to note that it is generally inclined at 45° to the rake face. At the area near the nose a small amount of iron was found (Figure 32-b).

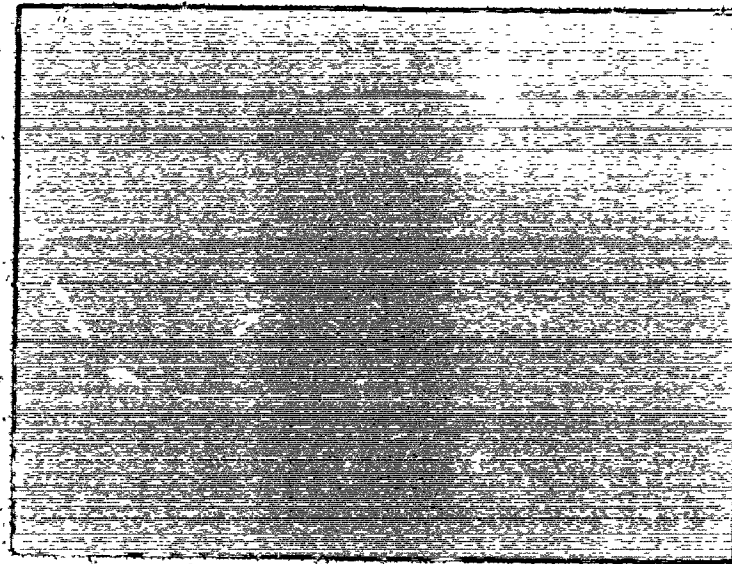
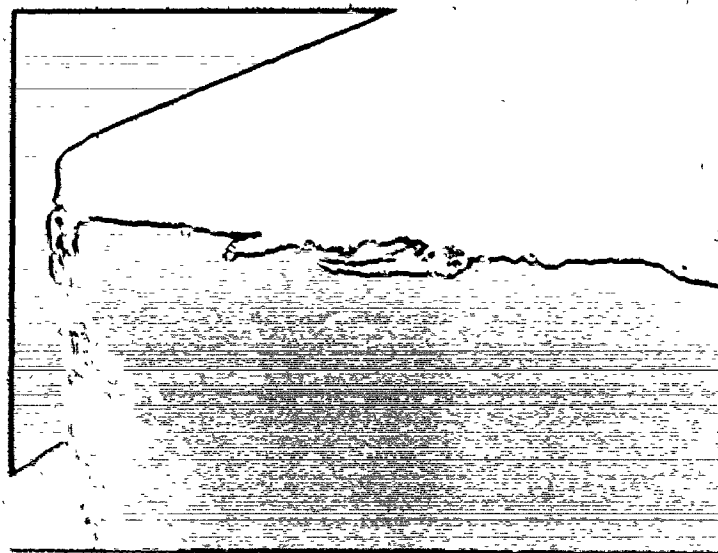


Figure 31: Chipping of the edge in continuous cutting using K45 carbide grade for machining 4340 steel hardened and tempered to 380 BHN (X65).

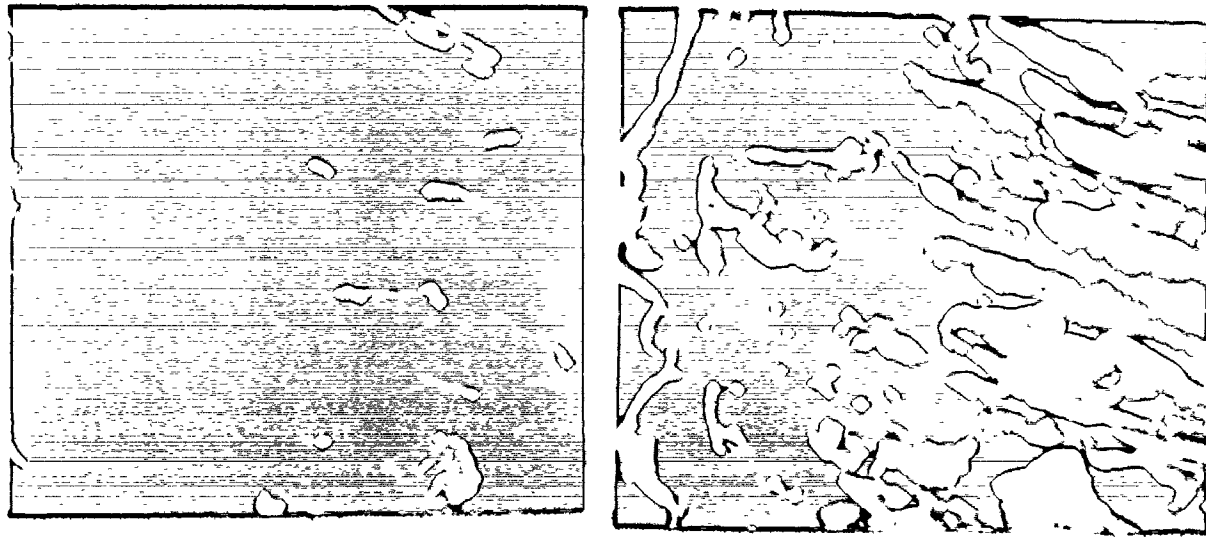


Figure 32-a: Stereo picture of chipping area covered with a steel layer at the tool nose in case of interrupted cutting using WP6 tool grade (X2200).

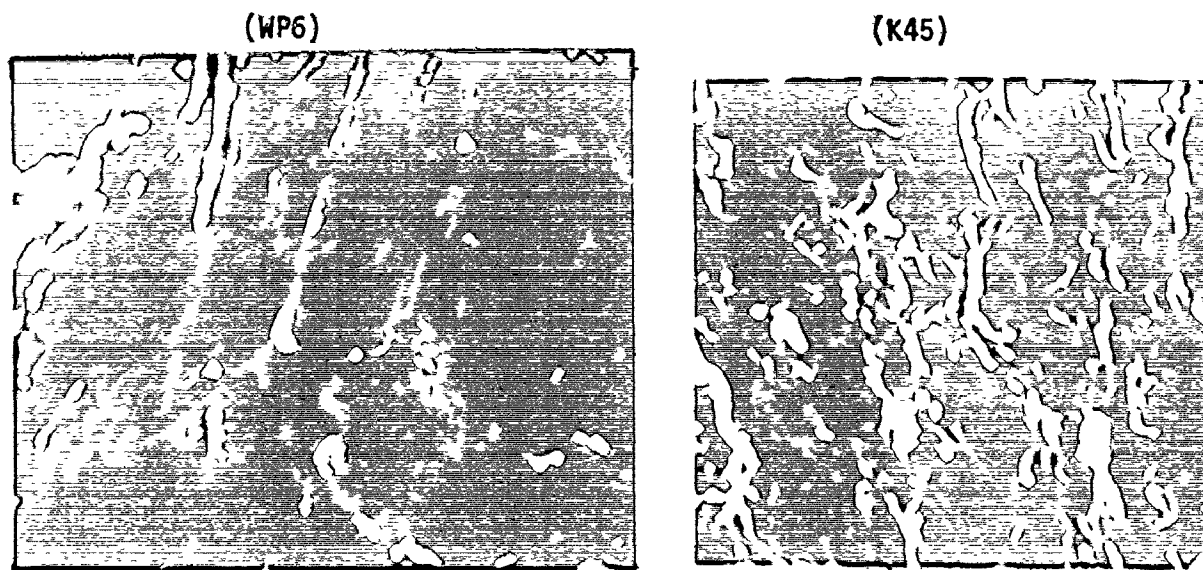


Figure 32-b: Chipping area near to the tool nose in case of interrupted cutting using WP6 tool grade and in case of continuous cutting using K45 grade for machining steel 4340 (380 BHN) (X2000).

Table 24 shows a typical composition of the etcher used to remove the steel.

Table 24

Component	Volume %
nitric acid	30
hyperchloride acid (HCl)	15
hyperfloride acid HF	10

Typical electro scanning micrographs of the chipped surfaces after etching away any steel coating and smears are shown in Figure 33-a for WP6 tool grade and in Figure 33-b for K45 tool grade at 2000 magnification.

3.6.3 Breakage

Breakage is the most dangerous type of fracture because in metal cutting, as mentioned before, it may lead to damage of the workpiece and/or the machine. It occurs due to preceding cracks. The direction of these cracks is nearly perpendicular to the cutting edge which propagates and finally splits the tool tip.

Figure 34 shows the crack which starts on the rake face and gradually propagates into the tool material nearly parallel to the flank surface.

Cracks running from the cutting edge were examined in the present work and found to be mainly intergranular fractures

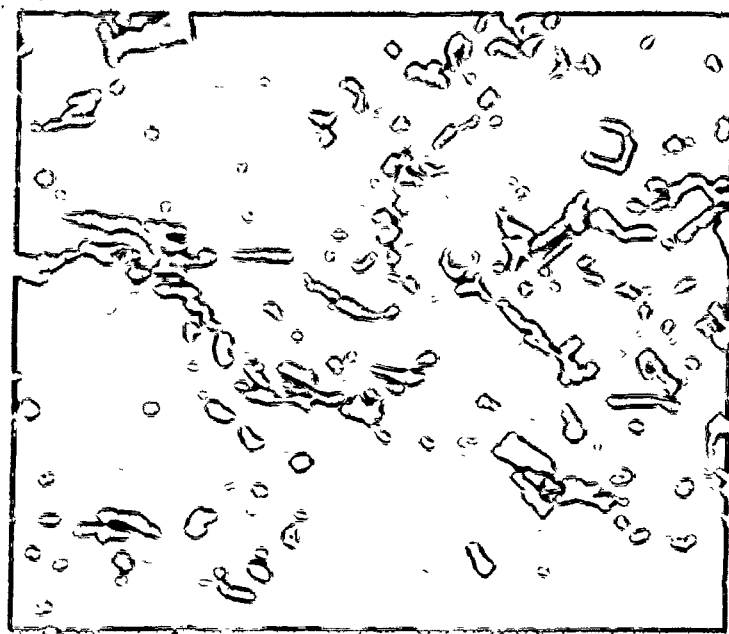


Figure 33-a: Chipping area after etching, WP6, (X2000).

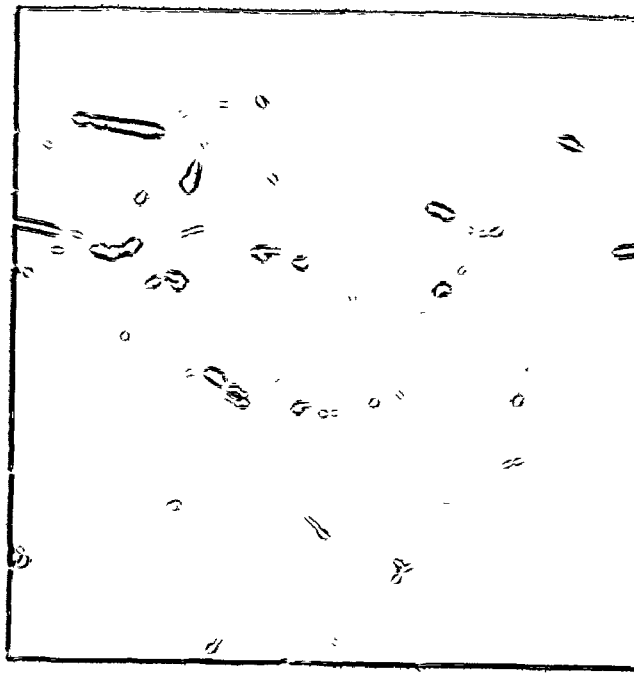


Figure 33-b: Chipping area after etching, K45, (X2000).

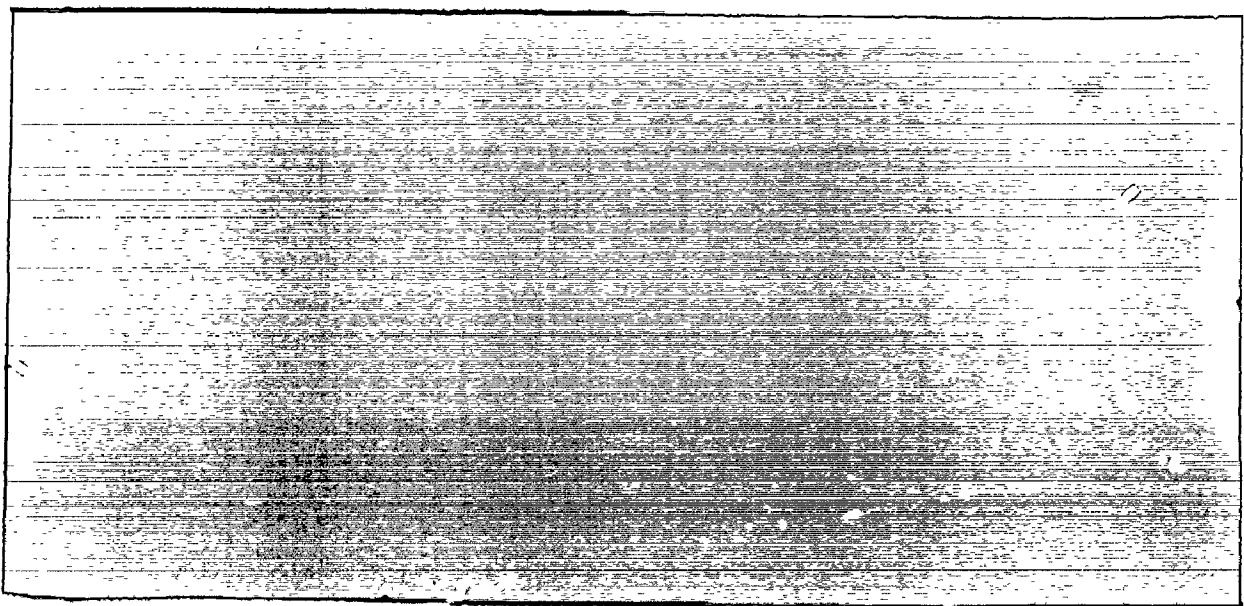


Figure 34-a: Crack on the rake face of K7H carbide grade tool used for machining 4340 steel (217 BHN), (X55).

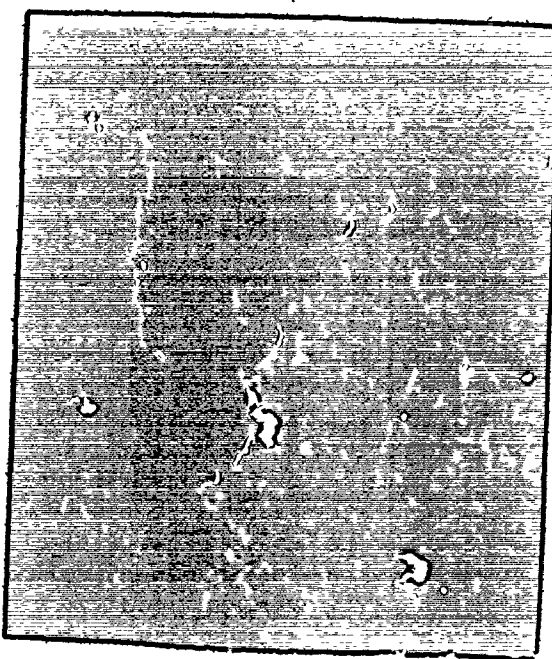


Figure 34-b: End of the same crack with high magnification (X550).

(Figure 35). Transgranular fracture was occasionally observed usually when a large carbide grain was situated across the path of the crack.

Figure 35-a shows the microcrack with low magnification and Figure 35-b shows a stereo view for the same microcrack with high magnification. Figure 36 shows another microcrack which was found in the same tool.

Breakages with high magnification are illustrated in the following photographs. Figure 37, 38, 39 and 40 are low magnification (X20) views of K7H tool grade and Figure 40 is a low magnification (X23) view of K45 tool grade. The broken surfaces have many sharp edges and other cleavage fracture features of brittle materials. Figures 41 and 42 show the fractured surface of K45 tool grade at high magnification. Figure 43 shows the fractured surface of WP6 tool grade at a 1300 magnification and the same spot again at 2700 magnification. Figure 44 shows the fractured surface of another WP6 tool at 1700 magnification. Figure 45 shows the fractured surface of ~~WP5~~ tool grade at 1700 magnification and the same spot again at 3300 magnification.

In all these micrographs sharp contours of individual carbide grains are visible. The large grain in the centre of Figure 43 shows ridge markings of intergranular fracture.

Comparing the fracture surfaces in the case of breakage (Figures 44 and 45) with those obtained in the case of chipping (Figures 33), it is seen that there is a significant difference between the two cases.

In the case of breakage it is found that the particles



Figure 35-a: Microcrack on the rake face of K45 carbide grade tool used for machining 4340 steel hardened and tempered to 380 BHN, (X2300).

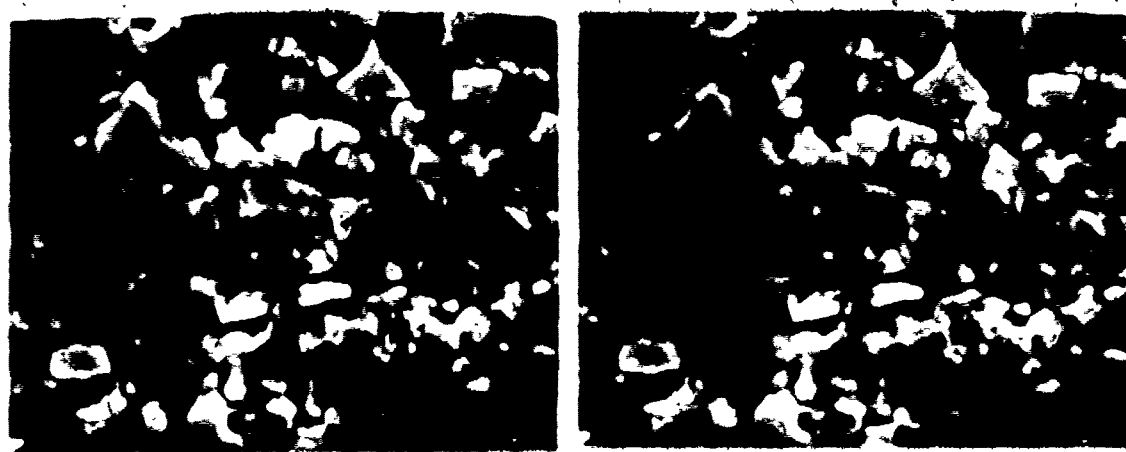


Figure 35-b: Stereo view of the same microcrack as figure 35-a, (X5300).



Figure 36-a: Microcrack on the rake face of the same tool as figure 35, (X2300).

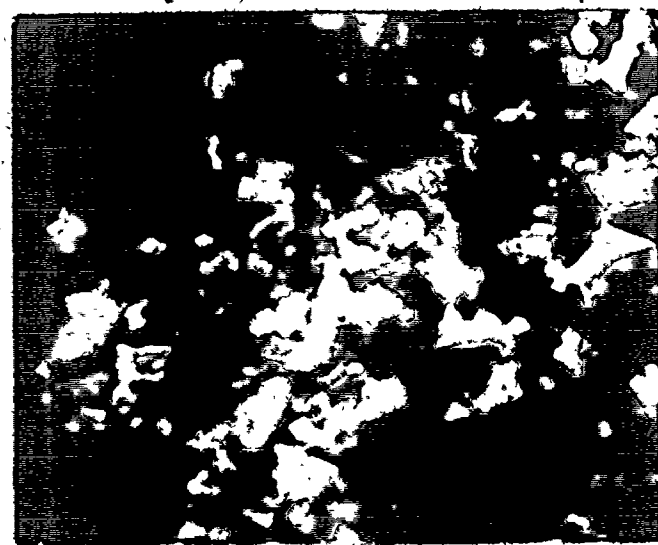


Figure 36-b: Microcrack with high magnification, (X5300).



Figure 37: Fracture surface of K7H carbide grade tool used for machining 4340 steel (217 BHN), (X20).



Figure 38: Fracture surface of the same tool as figure 37 taken from another view, (X20).



Figure 39: Fracture surface of K7H carbide grade tool used for machining 4340 hardened and tempered to 380 BHN, (X30).



Figure 40: Fracture surface of K45 carbide grade tool used for machining 4340 hardened and tempered to 380 BHN, (X23).

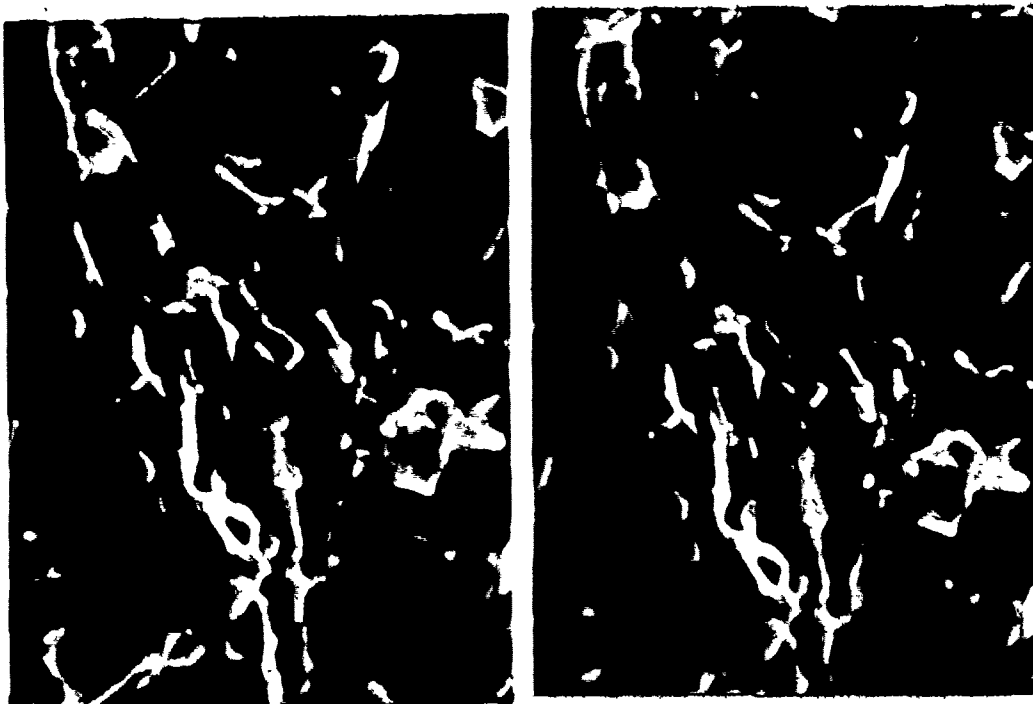


Figure 41: Stereo picture of fracture surface of K45 carbide grade tool used for machining 4340 steel (217 BHN), (X5900).

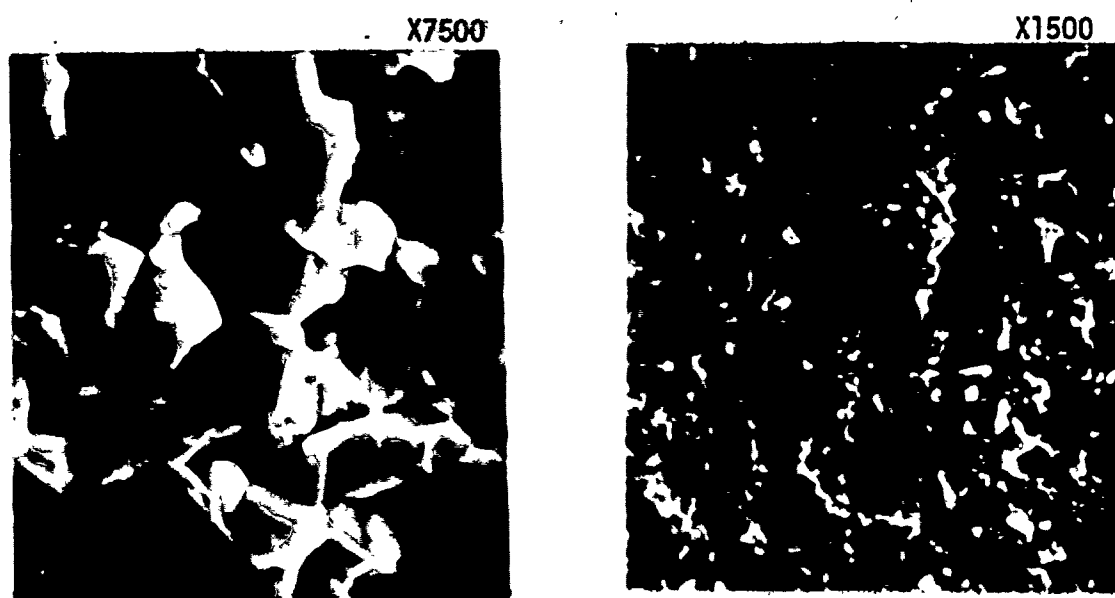


Figure 42: Fracture surface of K45 carbide grade tool used for machining 4340 steel hardened and tempered to 380 BHN.

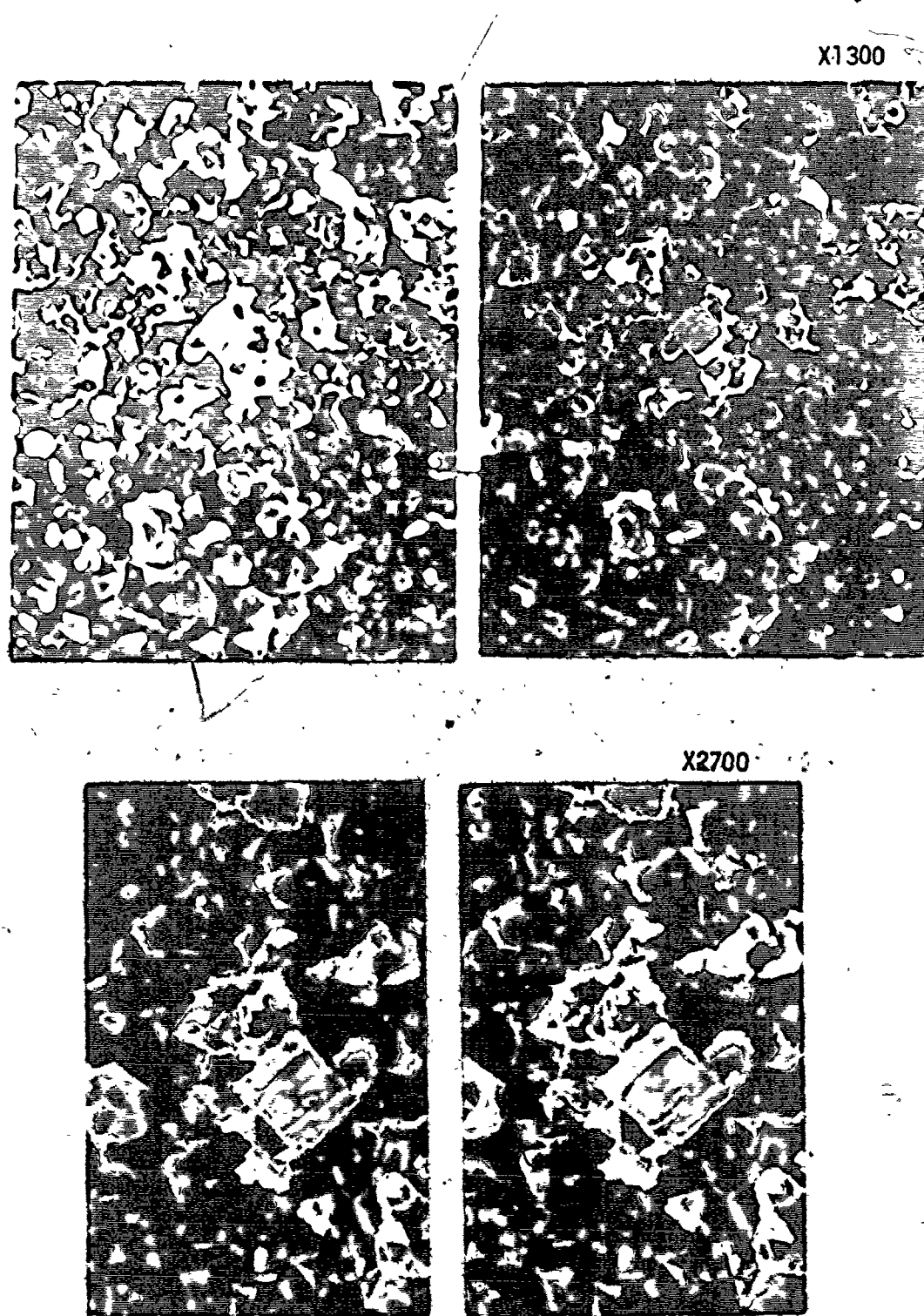


Figure 43: Stereo picture of fracture surface of KPS carbide tool used for machining 4340 steel hardened and tempered to 380 BHN (interrupted cutting case).

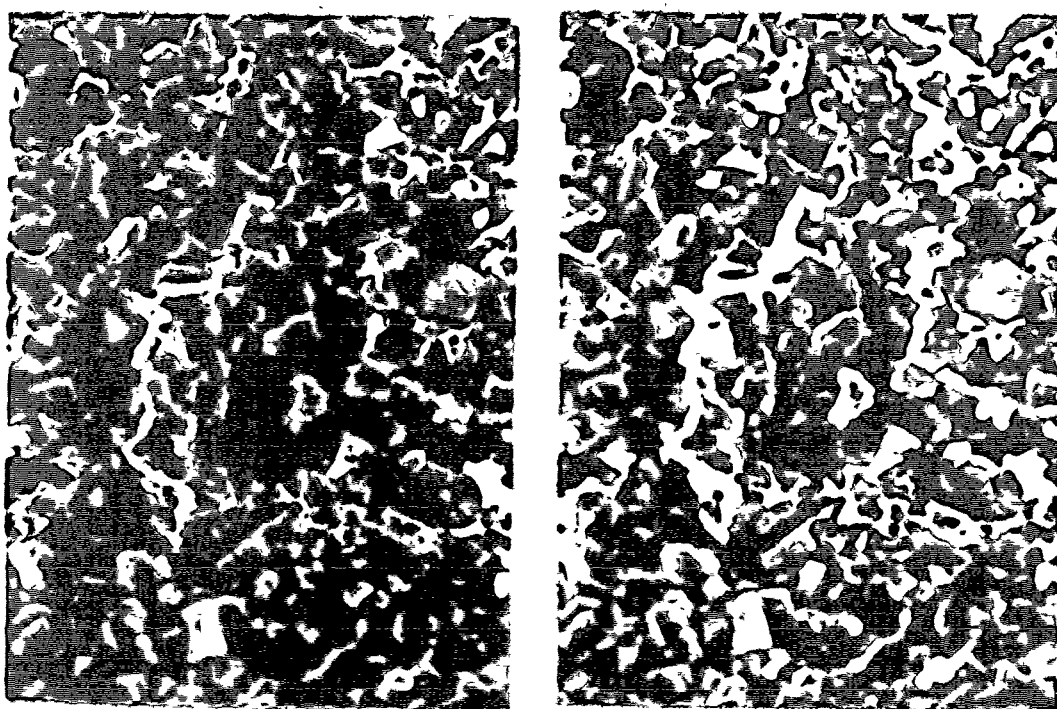


Figure 44: Stereo view of fracture surface of WPG carbide grade used for machining 4340 steel hardened and tempered to 350 BHN X17C (interrupted cutting case).

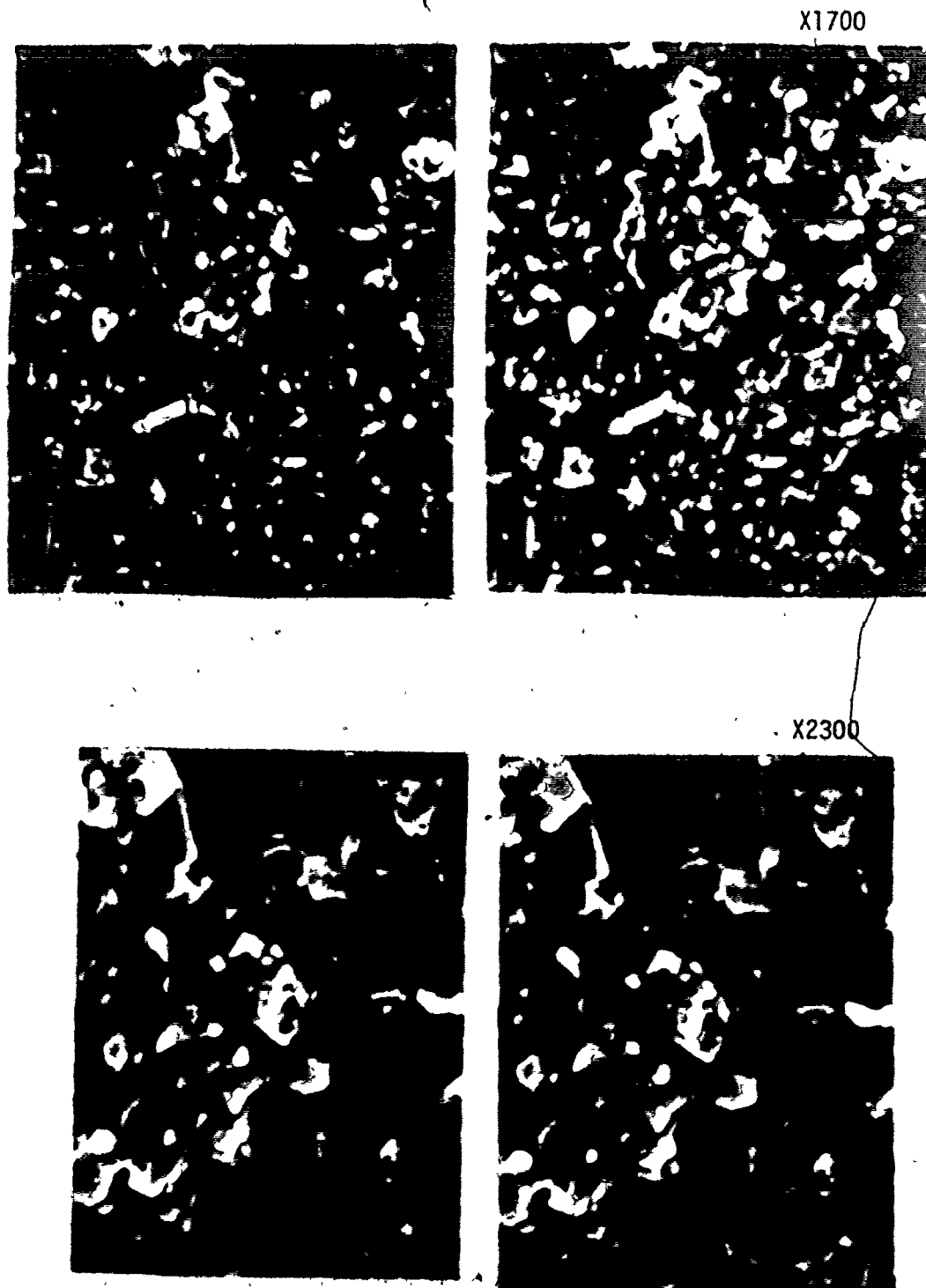


Figure 45: Stereo view of fracture surface of WP5 carbide grade used for machining 4340 steel hardened and tempered to 380 BHN (interrupted cutting case).

are standing out of the surface and one could easily distinguish between individual grains. But in the case of chipping the fracture surface looks more smooth and it could be considered as a shear mode of failure. However it is obvious that one had to deal with a brittle fracture in the case of breakage and a ductile fracture in the case of chipping.

CHAPTER 4

ANALYSIS OF STRESSES

4.1 Introduction

The finite element method has been used to solve many varied and complex engineering problems. By this method a continuous body is idealized by a number of discrete elements, continuous forces are discretized and the problem is then solved by the methods of structural analysis.

The method is especially useful for stress analysis problems which cannot be solved by classical theory. One such problem which is of special interest in this report concerns the analysis of local stresses in the tool wedge.

4.2 Definition of the Problem

Using the findings of Primus [8] about the actual load distribution on the tip of a cutting tool it should be possible to utilize recent developments in finite elements computing methods to determine stresses in the tool wedge for various geometries and assuming various loadings under various cutting conditions. The case represents a three-dimensional problem due to the rather short length of the loaded edge and to the load on the tip. However for simplifying the computations, a plane strain (2-dimensional) case was assumed. This assumption is considered justifiable in about the middle of the width of

the cut, assuming rather large width to thickness ratio of the chip. This ratio may often in practice be between 10 and 20. At this stage no temperature induced stresses are considered.

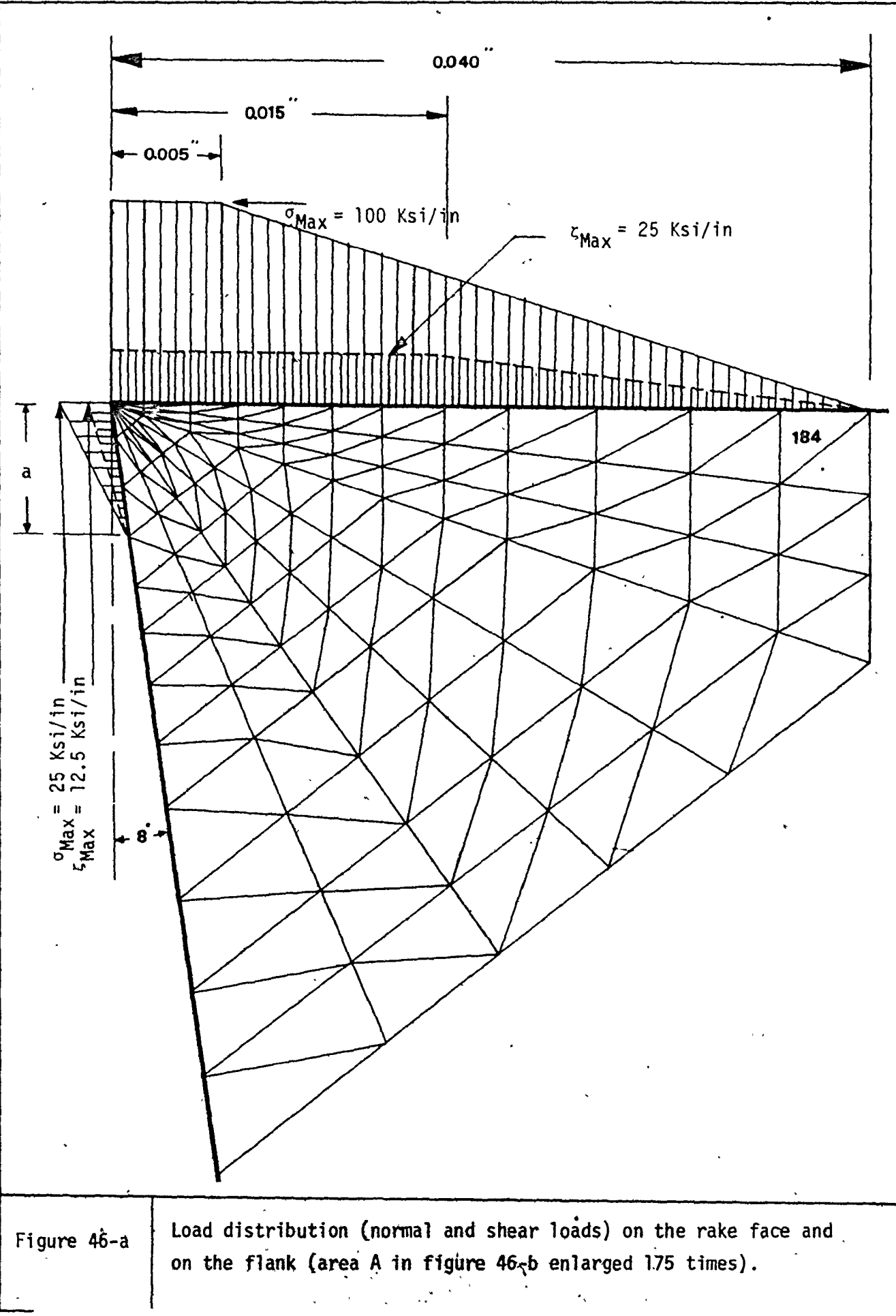
Figure 46-a shows the load distribution of normal and shear loads on the rake and on the flank. The length of contact of the chip with the rake face is .040 in. and the length of contact on the flank (a) is taken as 0.0, 0.006 in. and 0.015 in.

Both normal and frictional loads are maximum at the tip of the tool and are assumed to decrease linearly towards the end of the contact area with the exception of the normal force on the rake face which differs slightly by being constant over the distance of half of the undeformed chip thickness.

The size of the insert considered was .5625 in. length and .125 in. thickness. The width may be assumed of any large dimension.

The computation work has been carried out for various tool geometries: zero rake angle, positive 5° rake angle, and negative 5° rake angle, with 8° relief angle in all cases.

Two different methods were used. Figures 46-a and 46-b show the mesh used in the first method. The main characteristic of this method is that the mesh is getting finer the closer it approaches the cutting edge at which the load is concentrated on a small area. Computation of stresses is based on one single large stiffness matrix encompassing the whole tool. This method will be henceforth referred to as "the single step method". A detailed explanation of this method is found in Appendices A and B.



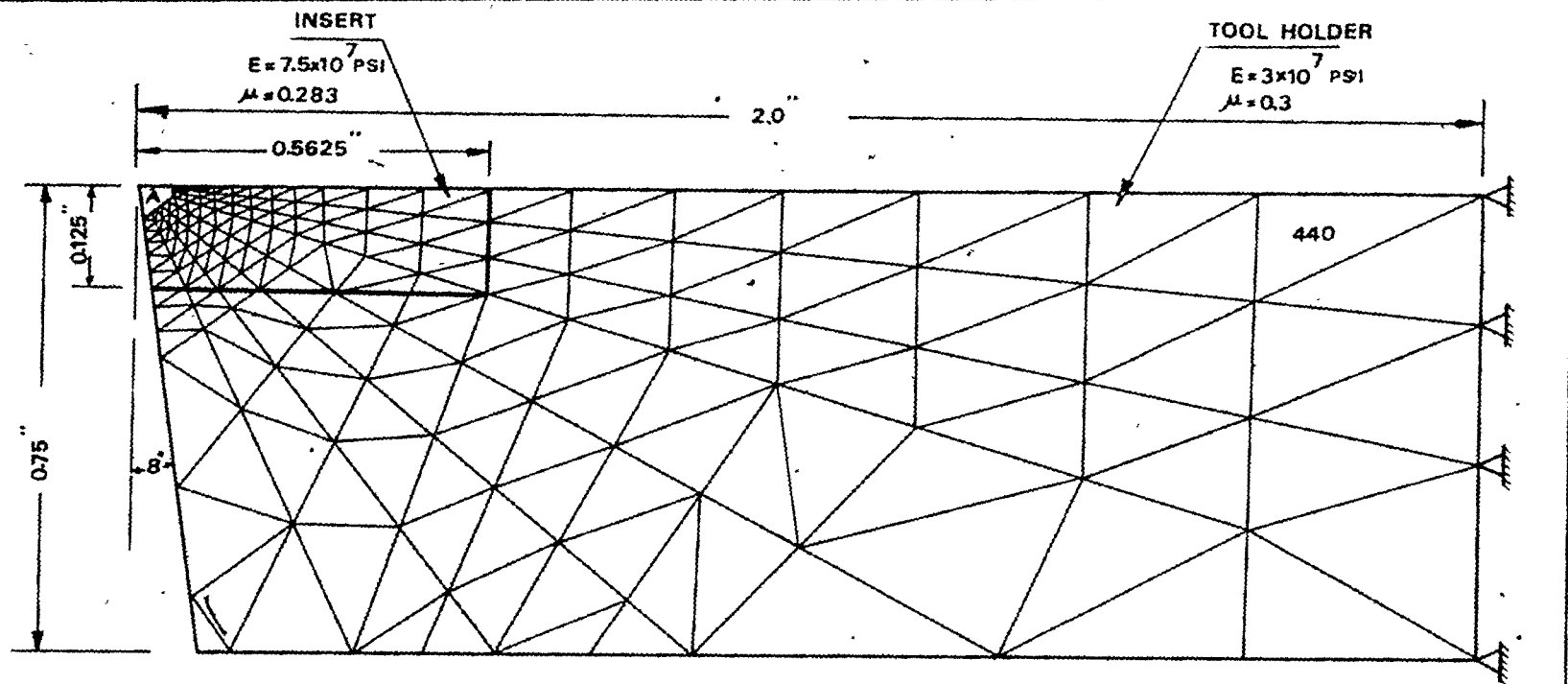


Figure 46-b. Mesh used in finite element computation (single step method).

In this method it is known that the region of high stress gradients necessitates a finer finite element mesh than the other regions of the tool. This gives rise to the following two major difficulties:

- i) there will be a great variation in element size resulting in great variations in the terms of the stiffness matrix. This causes computational errors such as rounding errors.
- ii) because of limitations on computer memory size the mesh cannot be made as fine as desired.

It is possible to use methods with uniform mesh such that repeatedly, stepwise smaller and smaller areas are considered and mesh refined.

Considering the structure in Figure 47 as a diagrammatical representation of the problem investigated in the present work, the total structure is considered consisting of two areas: A (large) and B (small). The load is concentrated on a part of area B which is the area of interest in which a detailed stress analysis is required. This diagram will represent one step in the gradual narrowing down and refining of a small part of the structure.

The most straightforward of such methods is the one described by Mahomed [18]. For example, in Figure 47 the governing matrix equation for the analysis of the structure (A + B) without imposing the boundary conditions is:

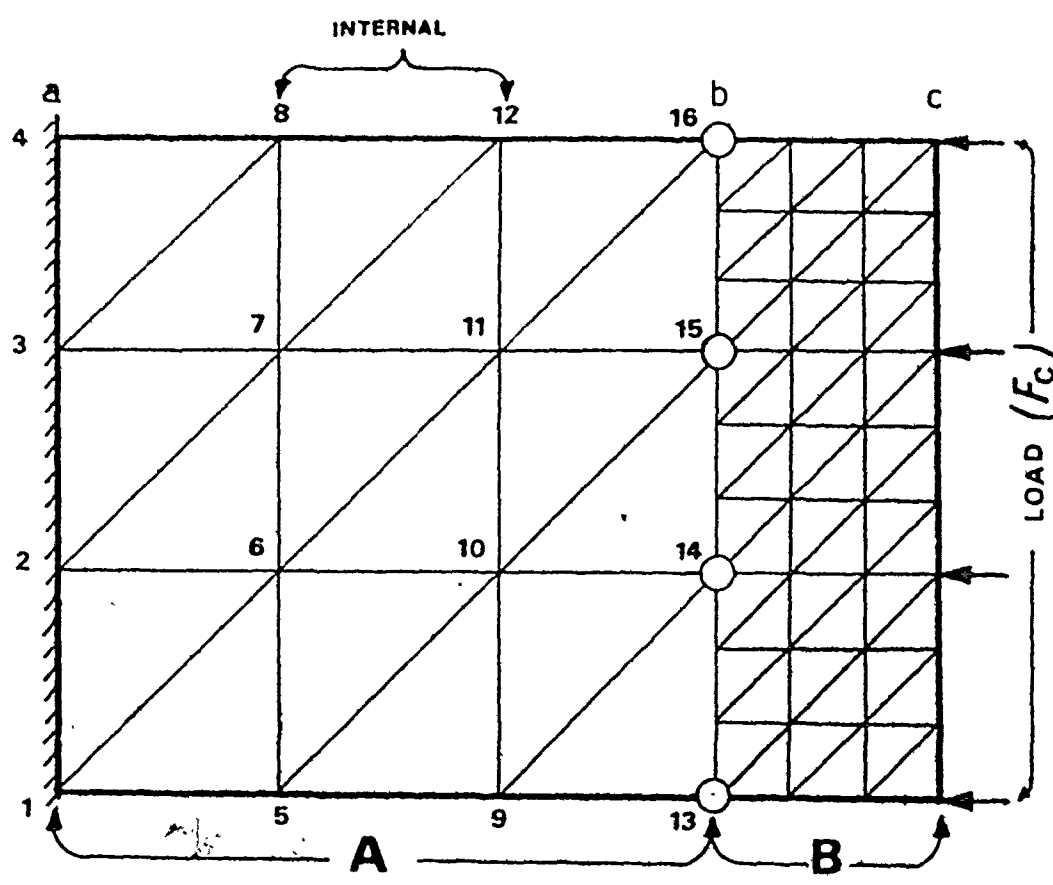


Figure 47. Diagrammatical representation of the problem.

$$\left[\begin{array}{c} K_a \\ \vdots \\ K_{(A+B)} \\ \vdots \end{array} \right]_{40 \times 40} = \left\{ \begin{array}{c} \delta_a \\ \vdots \\ \delta \\ \vdots \end{array} \right\}_{40 \times 1} = \left\{ \begin{array}{c} F_a \\ \vdots \\ F \\ \vdots \end{array} \right\}_{40 \times 1} \quad (4.1)$$

Figure 47 shows that the structure has imposed boundary conditions on α but these are zero displacements (boundary α is fixed). Because the primary interest is in the analysis of stresses not of the forces, Equation (4.1) can be reduced to Equation (4.2).

$$\left[\begin{array}{c} K_{(A+B)} \text{ less } K_a \\ \hline 32 \times 32 \end{array} \right] \left\{ \begin{array}{c} \delta \\ \text{less} \\ \delta_a \end{array} \right\}_{32 \times 1} = \left\{ \begin{array}{c} 0 \\ 0 \\ 0 \\ \hline F_c \end{array} \right\}_{32 \times 1} \quad (4.2)$$

So, in all the following the structure $(A+B)$ without the terms relating to the boundary a is considered.

In reference [18] a first approximation is made by performing a coarse analysis of the structure (A+B) without particular attention to the mesh size of the region of interest B and solving for the displacements δ_b between A and B.

$$[K_{A+B}] \cdot \{\delta_{A+B}\} = \{F_{A+B}\},$$

i.e., in more detail:

$$\begin{bmatrix} K_{AA} & K_{AB} \\ K_{BA} & \begin{matrix} K_{bb} & K_{bc} \\ K_{cb} & K_{cc} \end{matrix} \end{bmatrix}_{32 \times 32} \cdot \begin{Bmatrix} \delta \\ \delta_b \end{Bmatrix}_{32 \times 1} = \begin{Bmatrix} 0 \\ 0 \\ 0 \\ 0 \\ 0 \\ F_c \end{Bmatrix}_{32 \times 1} \quad (4.3)$$

where K_{bb} and K_{cc} are sub-matrices representing direct stiffness on boundary b and on the loading nodes c respectively.

The region B is then isolated from the main structure (A+B) and a refined mesh (e.g., three times) applied to this isolated region which is termed a "sub-region". The sub-region B is now treated as a separate problem and the displacements δ_b obtained in the previous step are imposed as displacement conditions on the part B of the outer boundary (Figure 48). The load may now be more uniformly distributed accordingly:

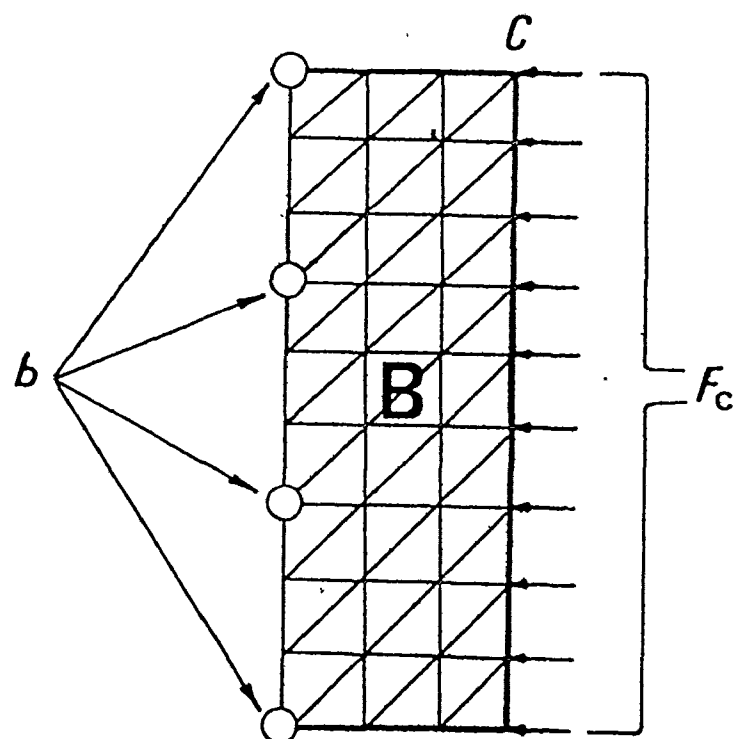


Figure 48. The area of interest (B) with refined mesh and imposed the displacement boundary conditions (δ_b).

$$\begin{bmatrix} K_{bb} \\ & \ddots \\ & & K_B \\ & & & \ddots \\ & & & & K_{cc} \end{bmatrix}_{80 \times 80} \begin{Bmatrix} \delta_b \\ \vdots \\ \delta \end{Bmatrix}_{80 \times 1} = \begin{Bmatrix} 0 \\ 0 \\ 0 \\ 0 \\ \vdots \\ 0 \\ F_c \end{Bmatrix}_{80 \times 1} \quad (4.4)$$

This has now to be solved for displacements δ , and further for strains and stresses with δ_b imposed as boundary conditions. This needs a special computational technique described in [18].

The refined analysis gives a more detailed picture of the stress distribution in the area under special consideration. If the solution by the first sub-region is not as detailed as desired, a second sub-region can be isolated from the first sub-region. A number of sub-regions may be isolated successively in this manner until convergence occurs or until a desired accuracy is attained.

A similar method was proposed by Emery [22]. He wanted to use package programs for stress analysis which, however, do not provide for imposed displacement boundary conditions. Therefore he used a technique which amounts to the same purpose but is formally different.

The first step in the solution is identical with that

in the preceding method [18]; the total structure A and B (B is the part to be subsequently refined in mesh and it contains all the external forces) was solved with coarse mesh for displacements.

Subsequently, as shown in Figure 49, part B is solved with a refined mesh while attaching springs at the original boundary b which are very stiff (several orders stiffer than the elements of the stiffness matrix) and adding external forces at the same boundary b which would give the displacements δ_b as calculated in the first step. These added springs and forces, actually, enforce displacements δ_b with a very good approximation (due to the very high stiffness of the springs). The problem now looks formally different from the preceding one:

$$\begin{bmatrix} K_{bb} + k_b & \\ \vdots & \end{bmatrix} \begin{bmatrix} \delta \\ \vdots \end{bmatrix} = \begin{bmatrix} B_b \\ \vdots \\ F_c \\ \vdots \end{bmatrix} \quad (4.5)$$

K_B

K_{cc}

80x80 80x1 80x1

In both previous methods all steps will have to be repeated for the same structure if the loading is changed. However, the problem investigated in the present work is such that while the region of loading remains confined to always

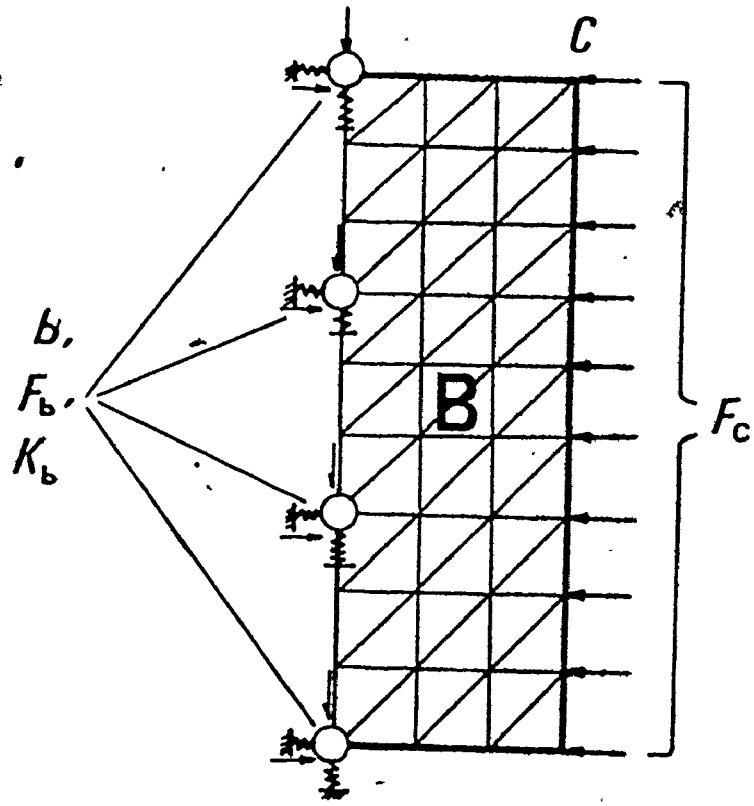


Figure 49. The area of interest (B) with refined mesh and imposed very stiff springs (K_b) and external force (F_b) on boundary b.

the same rather small part of the structure, the actual load distribution varies with cutting conditions. Therefore another method was proposed by Tlusty [23] in which all but the last step may be carried out once only for all the various loadings.

In this method already the first step is different from that in the two previous methods.

Referring to Figure 47 in the first step only part A of the structure is considered and such a structure is sought which would replace A by giving the same relationship between displacements and forces on the boundary b but be much simpler. In other words, the whole structure is considered as a sum of two substructures A and B (Figure 50). The original internal boundary b is split into an external boundary b_A on part A and an external boundary b_B on part B. The original "internal" forces on b may be considered as external forces F_{bA} and F_{bB} acting on these new boundaries. In this way the original structure is a sum of A and B, while

$$\delta_{bA} = \delta_{bB} \text{ and } F_{bA} = F_{bB}$$

The task is now to formulate a stiffness matrix K_A^* which would replace the stiffness matrix K_A and be much smaller while it would still give the same relationships between forces F_{bA} and displacements δ_{bA} :

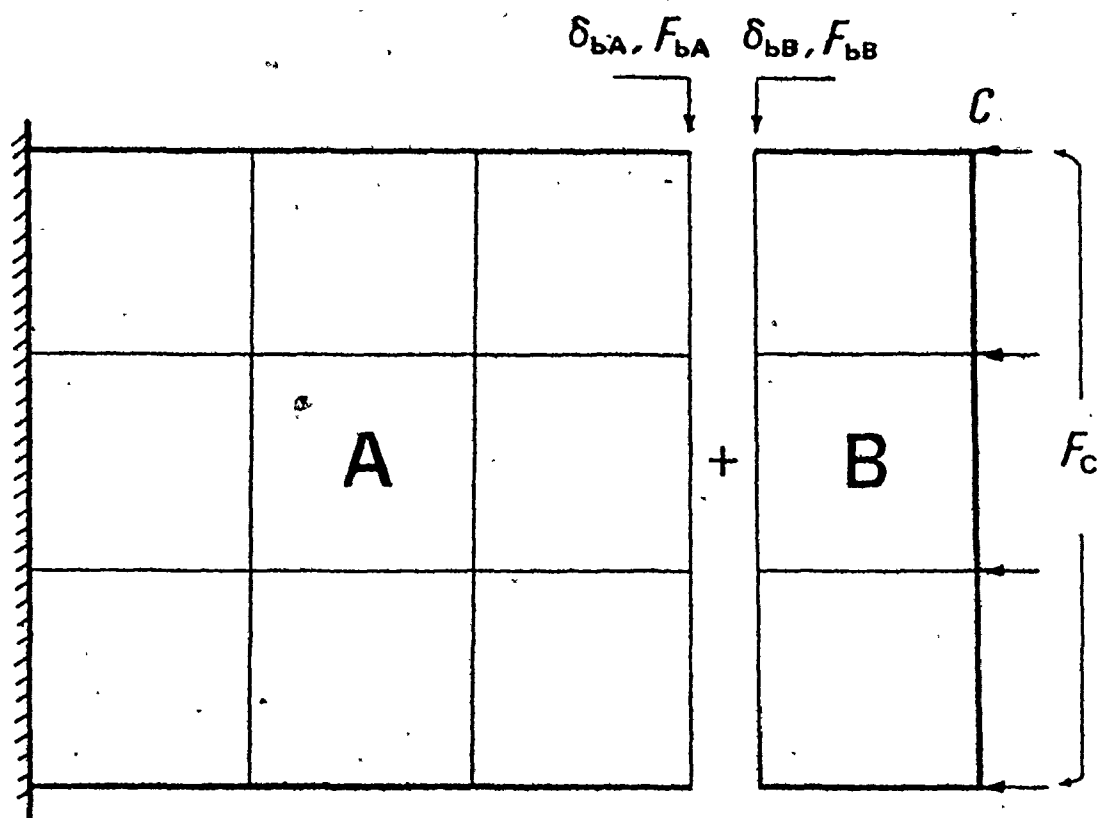


Figure 50. Substructures A and B

$$\begin{bmatrix}
 K_{\alpha\alpha} & K_{\alpha b} \\
 K_A & \\
 \hline
 K_{b\alpha} & K_{bb} \\
 8 \times 10 & 8 \times 8
 \end{bmatrix}_{18 \times 18} = \begin{bmatrix}
 \dots \\
 \delta_b \\
 \dots
 \end{bmatrix}_{18 \times 1} = \begin{bmatrix}
 0 \\
 F_b
 \end{bmatrix}_{18 \times 1}$$

$$[K_A^*]_{8 \times 8} \{\delta_b\}_{8 \times 1} = \{F_b\}_{8 \times 1} \quad (4.6)$$

Actually, as shown in Appendix B, such a replacement matrix can be determined which will have a size of the original K_{bbA} of Equation (4.6), eg., for example in Figure 47 it will be 8×8 only instead of 32×32 . Practically, of course, the saving is much bigger because the number of the boundary nodes is much smaller than the total number of nodes in structure A.

In the next step, solving for part B only, a refined K_B matrix is formulated and combined with the replacement matrix K_A^* . As a result, the displacements could be obtained from Equation (4.7), and accordingly the strains and stresses.

$$\left[\begin{array}{c} [K_A^*] + \\ \vdots \end{array} \right] + K_{BB} \left[\begin{array}{c} \vdots \\ \vdots \end{array} \right] \cdot \left\{ \begin{array}{c} \delta \\ \vdots \end{array} \right\} = \left\{ \begin{array}{c} 0 \\ \vdots \\ F_C \end{array} \right\}$$

(4.7)

In this method again, the refining of the mesh could be carried out in a number of steps.

Applying this method to the problem investigated in the present work, the computations were carried out in a number of steps. Referring to Figure 51, excluding the area ABC which includes the loading region JKC, a large mesh was used. Accordingly, the corresponding stiffness matrix was calculated using a mathematical technique which is explained in detail in Appendix C.

As a result, the effect of both the remaining part of the tool and the tool holder on the region ABC could be found. Proceeding with the same technique and taking into consideration the effect of the previous step, a smaller mesh was used for the area ABED and its effect on the remaining region DEC was calculated.

The same technique is repeatedly used until a very fine mesh is reached for the loading region.

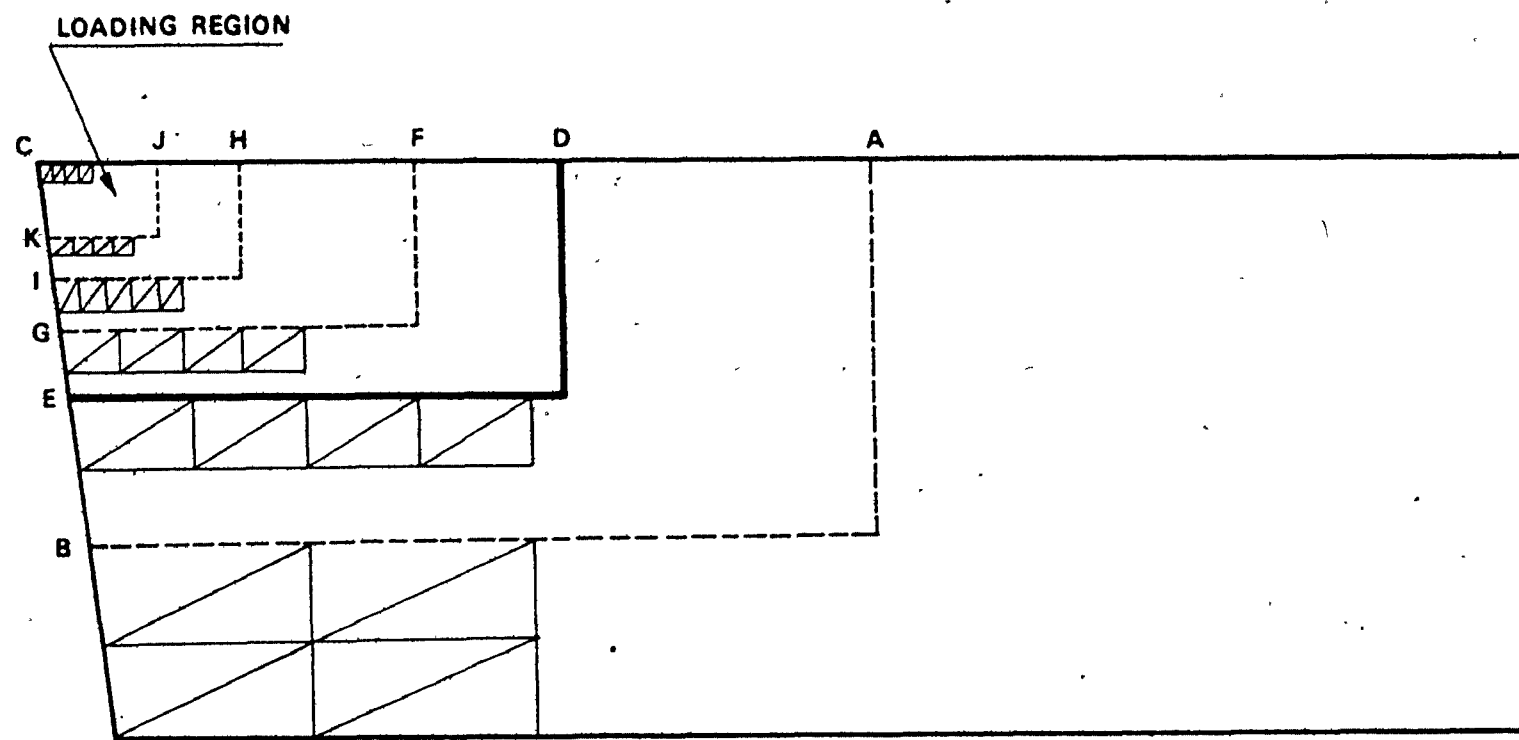


Figure 51. Stepwise and subdividing and refining method.

The stiffness matrix replacing the area KJHI and, in this way replacing all the remaining part of the structure outside of the area of consideration is independent of loading as long as loading is confined to the area of consideration. Once this replacement matrix is derived and combined with the refined matrix of area CJK it may be repeatedly used in the various cases of loading as they correspond to the various combinations of cutting conditions.

4.3 Stress Analysis of the Tool

4.3.1 Solution Using Elementary Beam Theory (Cantilever Beam in Bending)

The tool and tool holder were treated as a square section cantilever of 2 inches length and 0.75 inch in depth. A concentrated normal load of 2250 pounds acting at the tip of the free end, which is equivalent to the load acting on the tool tip, was considered.

Figures 52-a, 52-b, 52-c, 52-d and 52-e show the contours of normal stresses (σ_x), the contours of maximum principal stress, the contours of minimum principal stress, the contours of maximum shear stress and the direction of maximum principal and shear stresses respectively.

This approximation cannot, of course, solve the local stresses in the loading region (the tip of the tool). From Figures 52, this analysis would lead to a conclusion that as the tip of the tool is approached, both principal stresses and also the maximum shear stress are all approaching zero and this is obviously incorrect. On the other hand, in regions

2250 IB/IN.

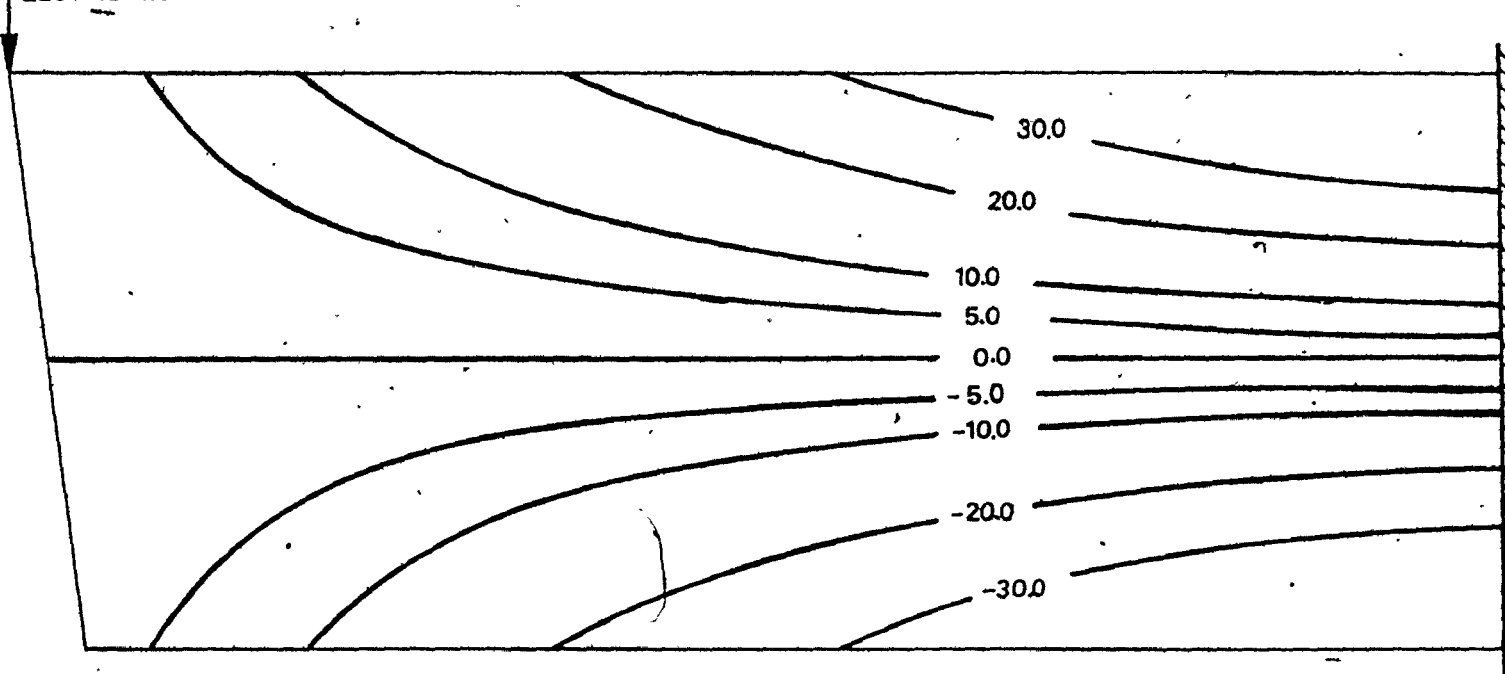


Figure 52-a. Normal stress contours using the classical solution (σ_x ksi).

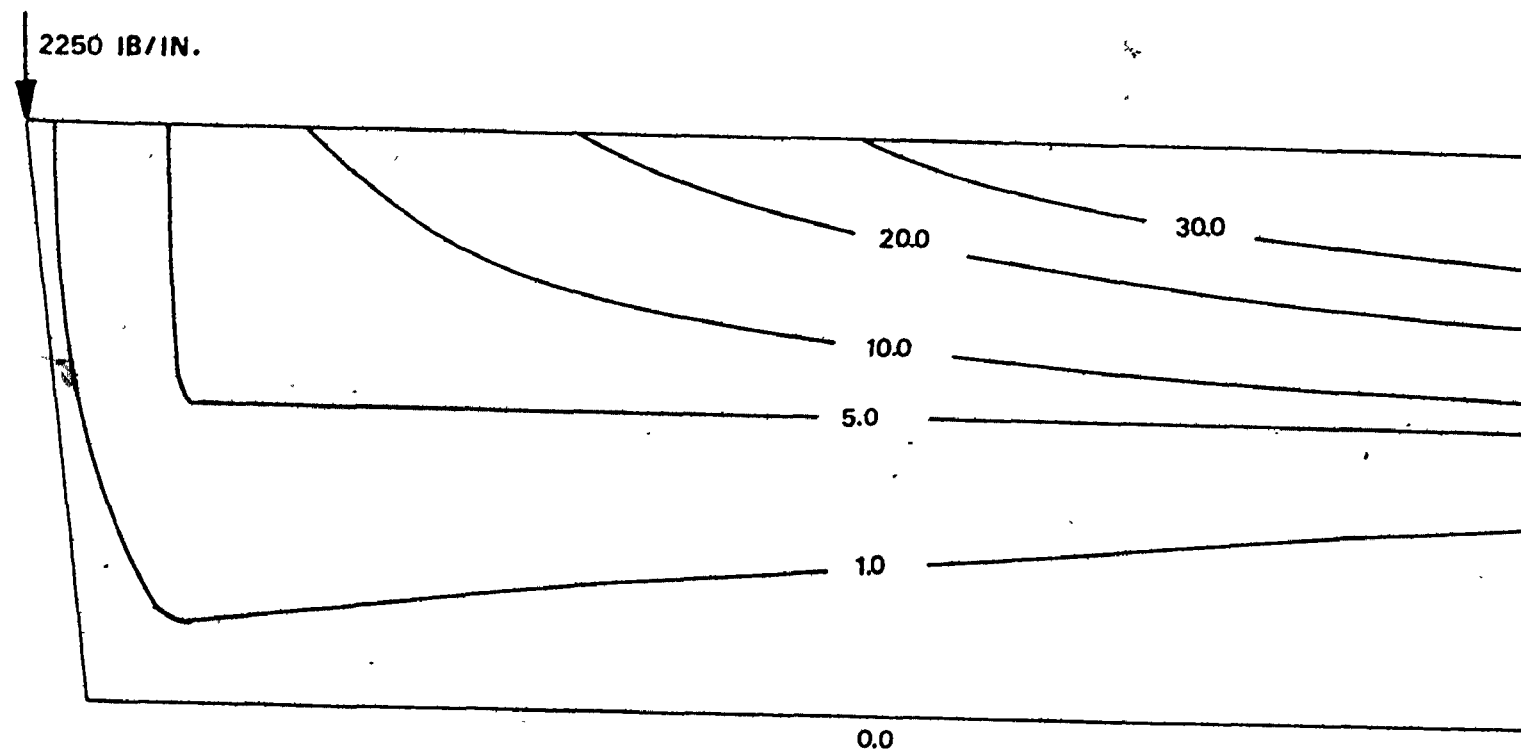


Figure 52-b. Maximum principal stress contours using the classical solution (σ_1 ksi).

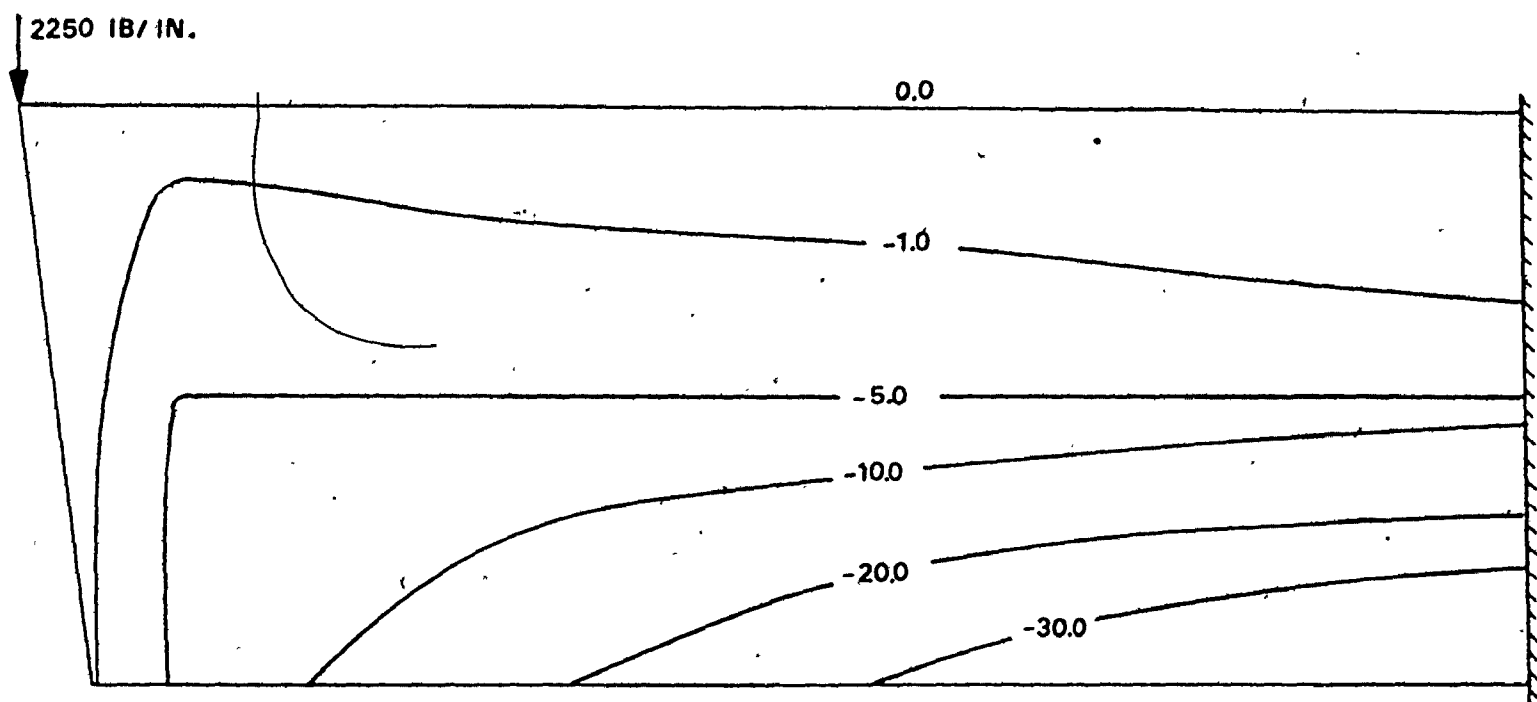


Figure 52-c. Minimum principal stress contours using the classical solution (σ_2 ksi).

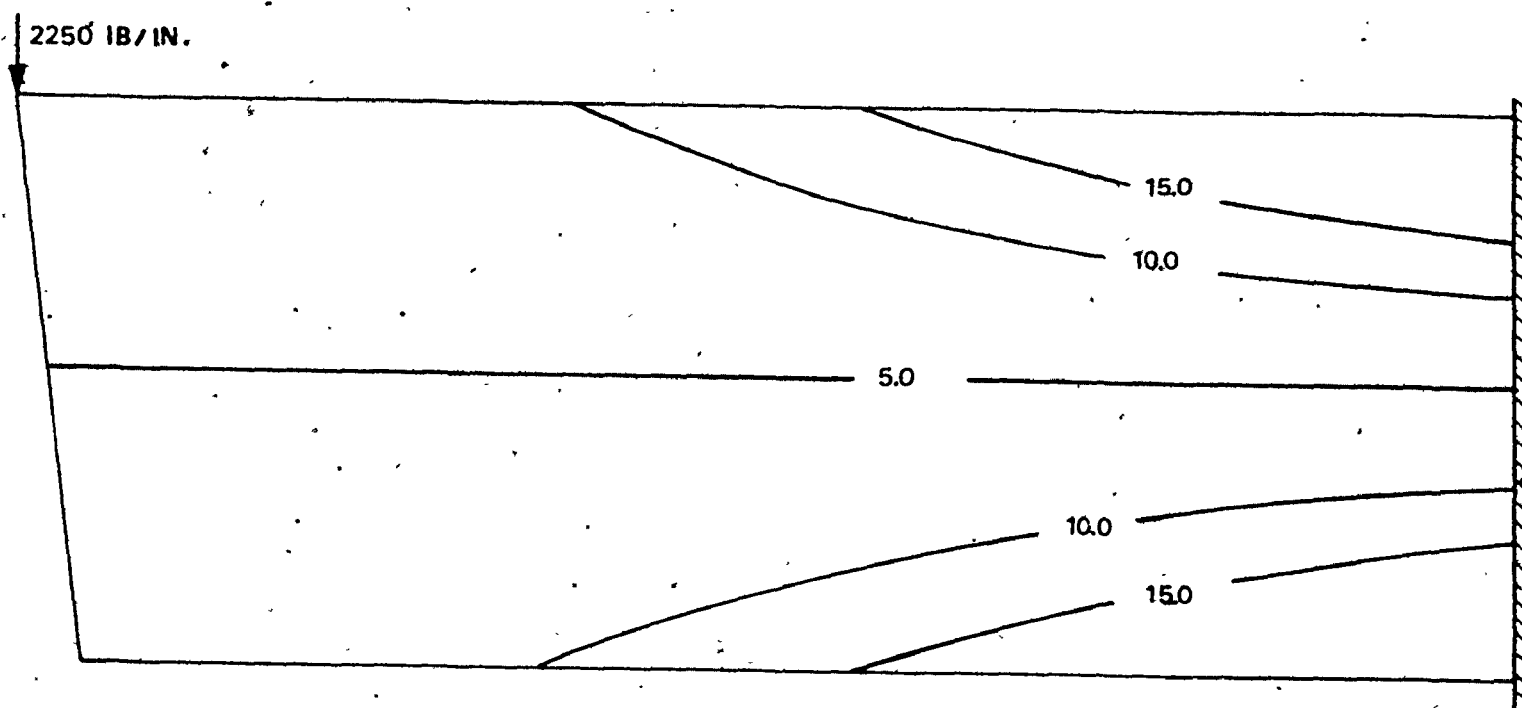


Figure 52-d. Maximum shear stress contours using the classical solution (τ_{Max} ksi).

→ Direction of σ_1
--- Direction of τ_{Max}

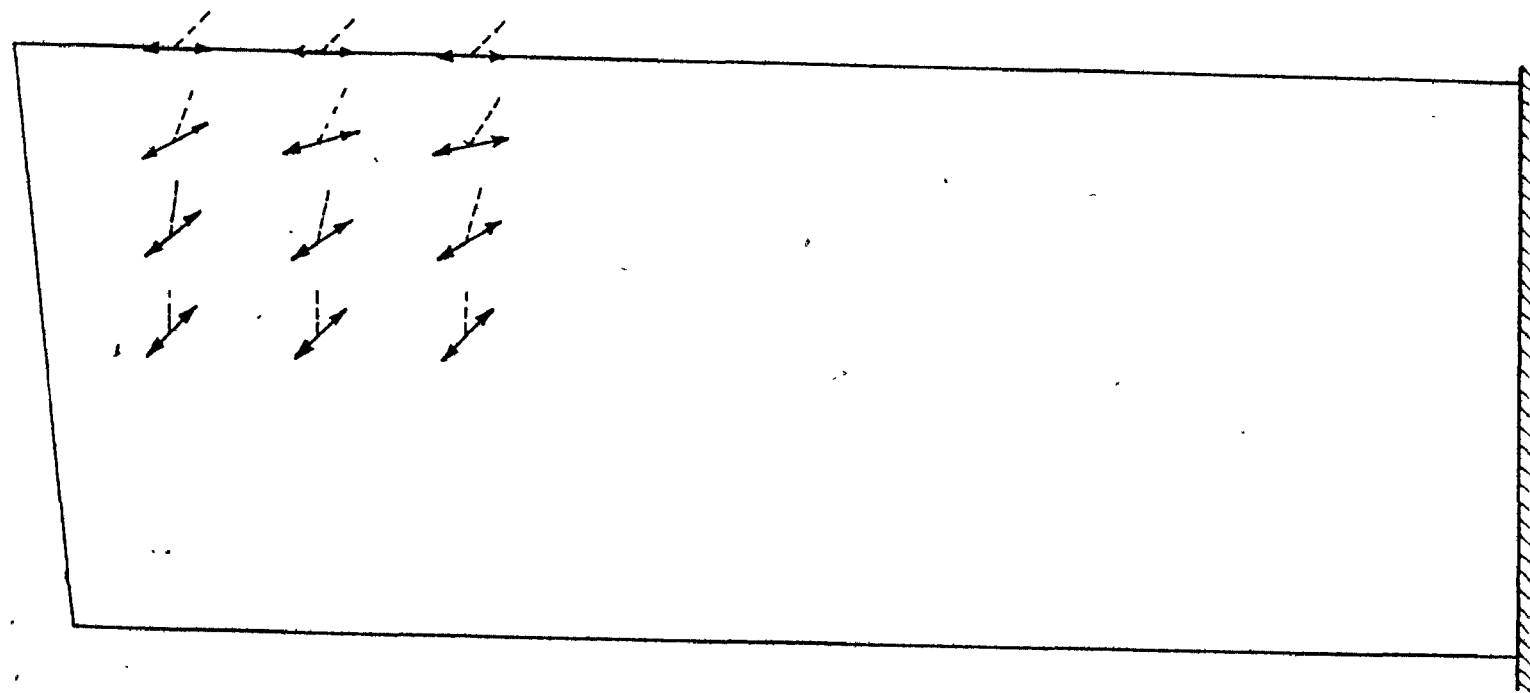


Figure 52-e. Directions of maximum principal stresses (σ_1) and of maximum shear stresses (τ_{Max}) using the classical solution

remote from the load the stress distribution obtained in this way should approach the actual one. Therefore it will be possible to use these regions for comparing the results obtained by the finite element technique with this classical solution.

4.3.2 Solutions Using the Finite Element Technique

A. Single Step Method

The computations have been carried out for various tool geometries. Three different cases were considered: zero rake angle, positive 5° rake angle and negative 5° rake angle.

The flank wear is considered one of the important failure mechanisms and accordingly in each of the previously mentioned cases three different values of flank wear width "a" were considered: $a = 0.0$ inch, $a = 0.006$ inch and $a = 0.015$ inch, and the corresponding maximum and minimum principal stresses as well as the maximum shear stress were plotted.

The discussion of the results will include the effect of rake angle and the effect of flank wear on the distribution of stresses in the tool with special interest in the tool wedge.

The effect of rake angle:

In the case of zero rake angle ($\alpha = 0^{\circ}$) with no flank wear, the contours of principal stresses and of maximum shear stress are shown in Figures 53, 54 and 55 respectively.

By inspecting the maximum principal stress contours it can be seen that there are no tensile stresses in the immediate loading area (close to the cutting edge) Figure 53-a.

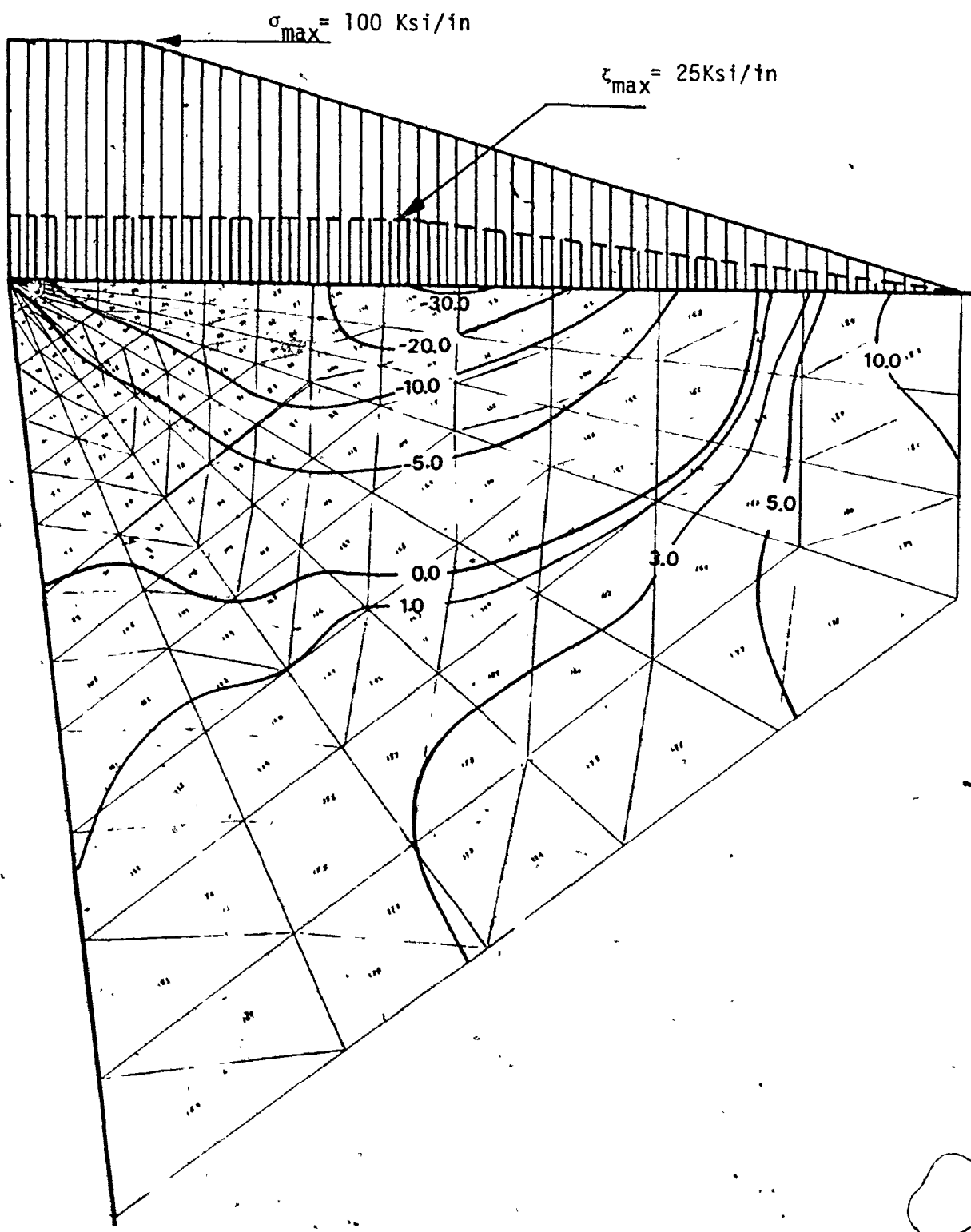


Figure 53-a

Maximum principal stress contours in
the loading region (σ_1 Ksi).

$\alpha = 0^\circ$
 $a = 0.0 \text{ inch}$

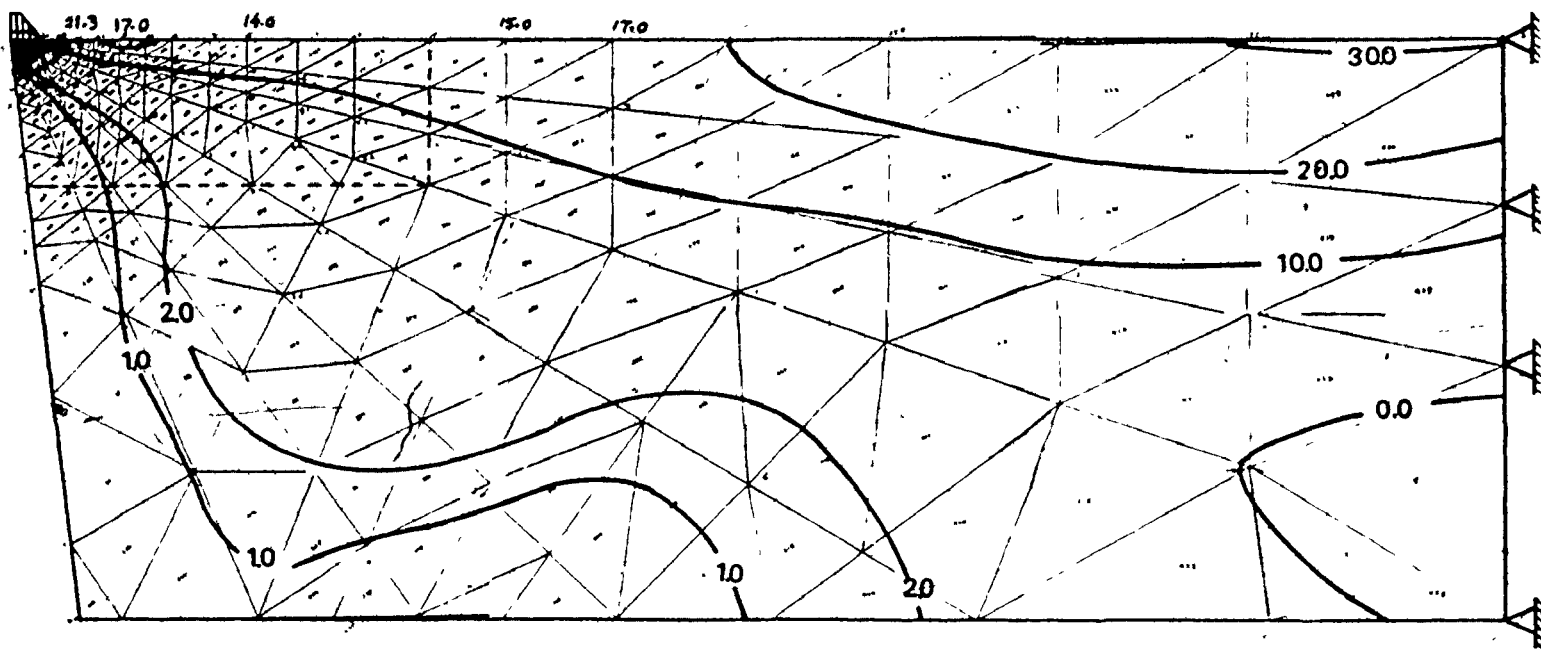


Figure 53-b. Maximum principal stress contours in the tool and tool holder (σ_1 , Ksf).

$$\alpha = 0^0$$

$$a = 0.0 \text{ inch}$$

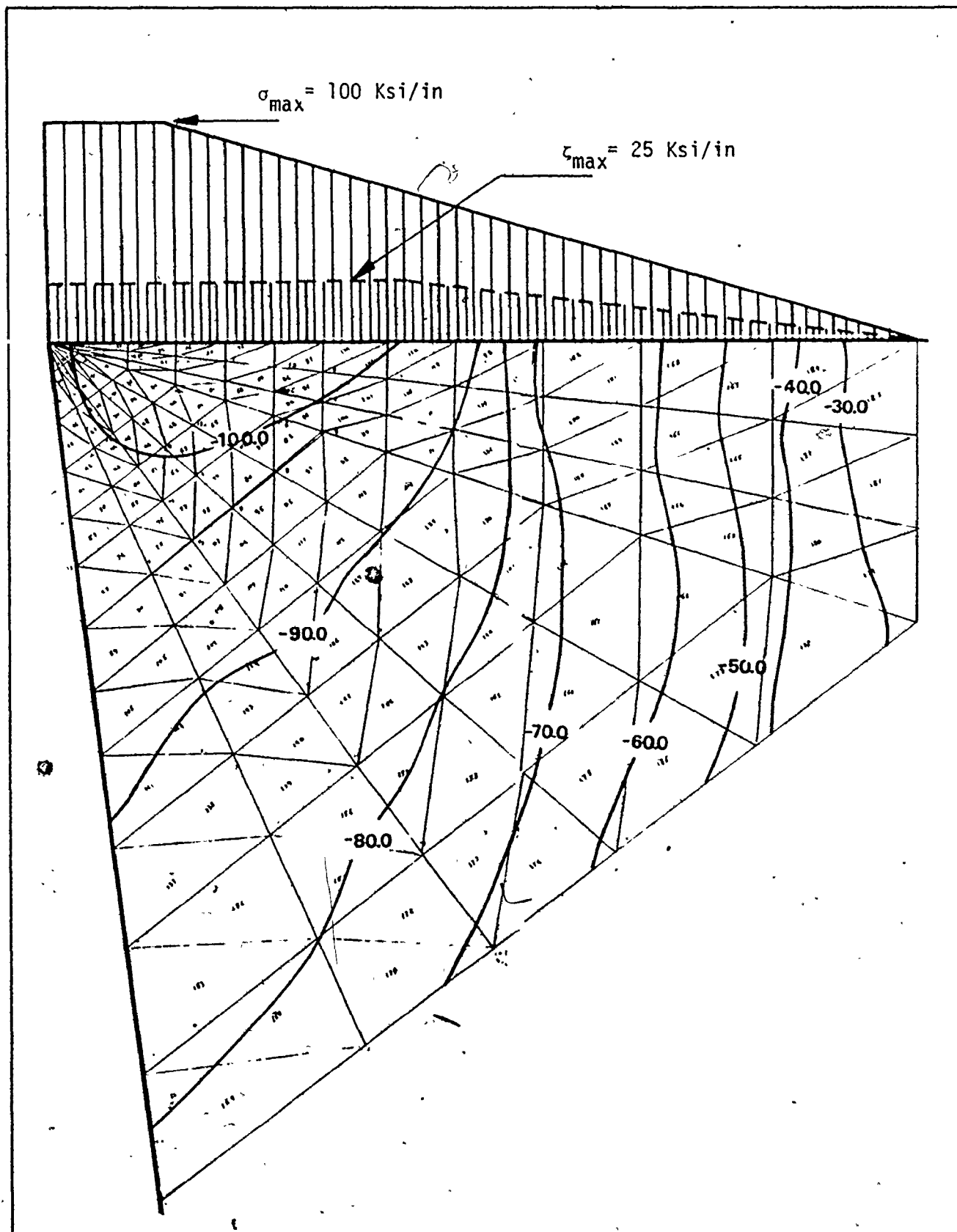
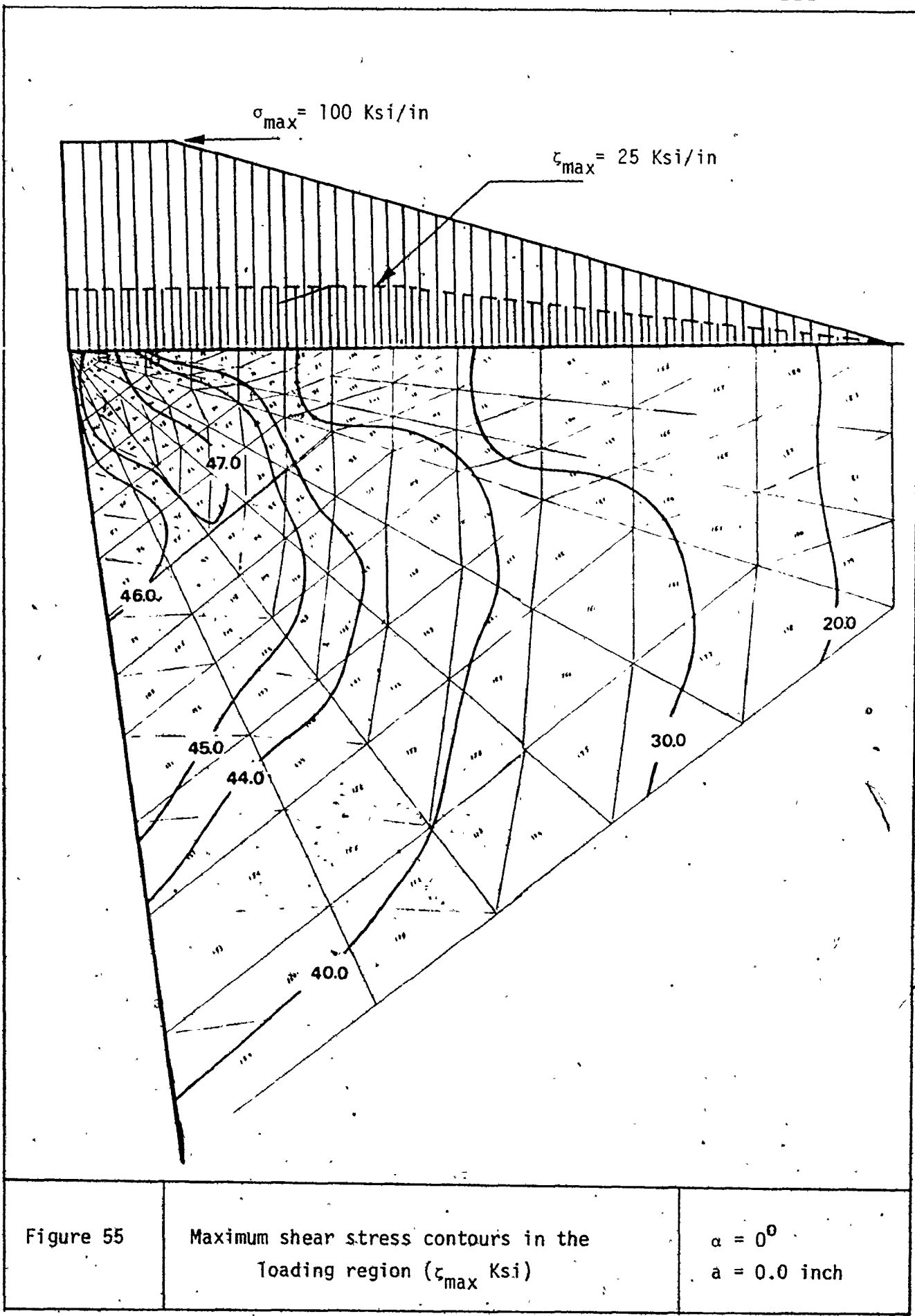


Figure 54

Minimum principal stress contours in the
loading region (σ_2 ksi).

$\alpha = 0^\circ$
 $a = 0.0 \text{ inch}$



Checking with Figure 53-b it is seen that a local maximum of tensile stress in the carbide insert occurred at the rake face at a distance from the tip slightly greater than two times the length of chip contact, which agrees rather well with the results obtained by Loladze [6].

The value of the local maximum tensile stress is 21.3 ksi and it starts to decrease moving away from the tool tip and starts to increase again in the tool holder and reaches the maximum value of about 30 ksi near the fixed end. The area of the local maximum tensile stress is rather small and it is confined to the immediate vicinity of the rake face. From there into the insert the stress decreases rapidly.

The values of the local maximum tensile stress in the insert are rather small. The usual values of the transverse rupture strength of carbides are between 100 ksi and 400 ksi. The feed assumed in calculating the forces on the tip of the tool was 0.010 in./rev. In the cutting tests no breakage of the tool was obtained at this feed. The tools were broken at the values of feeds between 0.030 in./rev. and 0.043 in./rev. which are larger by about four times than those used in the computations. For these feeds the computation would give a maximum tensile stress on the rake face of the insert of about 85 ksi. The difference between this value and the transverse rupture strength may be due to the simplification of the computations to a two-dimensional case. Actually, this value would be expected to be higher if the computations were carried out as a three-dimensional finite element problem which would

better express the real case. Also, in the computations, a homogeneous and isotropic material was assumed. However, actually, in the case of sintered material (carbide), the structure is anisotropic and not homogeneous. The structure consists of two or three phases (Figures 25, 27). Local stresses in such a structure may be much higher than those computed above and this would further account for the discrepancy between computation and experiment. It is however very important that the computations show the location of the point of the highest tensile stress on the rake face of the tool (Figures 53-b, 63-b and 66-b) and this location agrees with the location of breakages found experimentally (Tables 14, 15 and 16).

The point of highest tensile stress found in the computations was at a distance from the tip of between 0.1 inch and 0.13 inch and the distance of breakage from the tip was found to be about 0.15 inch in the cutting tests.

These findings may interpret the breakage of the tool as a brittle fracture phenomenon but in the case of chipping of the edge, these could not explain the chipping phenomenon as caused by tensile stresses because no tensile stresses were found close to the edge of the tool.

Figure 54 shows the contours of the minimum principal stress at the cutting edge. It is seen that high compressive stresses were found with a maximum value of 100 ksi close to the tip of the tool and they decrease when moving from the tip.

From Figure 55, which shows the contours of the maximum shear stress, it is found that the shear stress increases as

we move towards the tool wedge with a maximum value of 47 ksi.

These high values of shear stress especially when combined with high temperatures in this area resulting from the cutting operation (400°C), could be the possible cause of chipping as a ductile failure in a shear flow mode. The strength of cobalt starts decreasing to some extent and its ductility increases. The cobalt deforms plastically and spreads over the carbide grains. These results agree with those obtained experimentally. Figures 32, 33 show this kind of fracture and the direction of shear flow of the cobalt matrix is shown too.

There are several other aspects to consider regarding chipping of the edge. One of them is that often the sintering process will not have the same result at the edge as in the bulk of the insert and the edge itself has lower strength. Hence, the purpose of honing the edge. Another one is the opinion that chipping is due to the mechanism of adhesion between the tool and the workpiece material [4].

Figure 56 shows the direction of maximum principal stresses and the maximum shear stresses (the lines with arrows represent the direction of the maximum principal stresses while the simple lines represent the direction of the maximum shear stresses). Comparing these directions with those shown in the photomicrographs of breakage (Figures 37, 40), it is seen that the direction of breakage in the cutting tests was rather the same as the normal to the directions of maximum tensile stresses obtained from the computations. This agrees with the

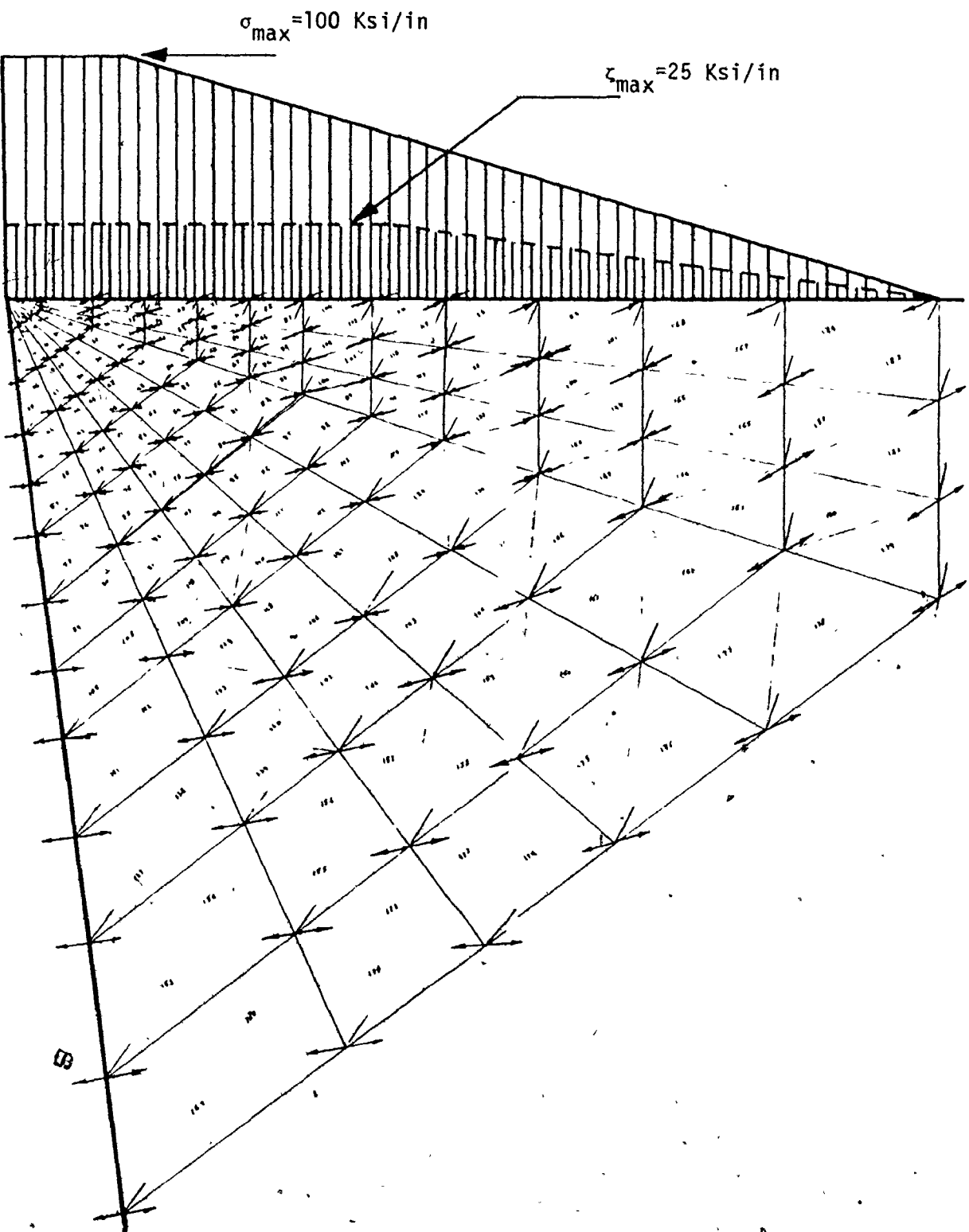


Figure 56-a

Directions of maximum principal stress and
of maximum shear stress in the loading region

→ Direction of σ_1 — Direction of τ_{\max}

$$\alpha = 0^\circ$$

$$a = 0.0 \text{ inch}$$

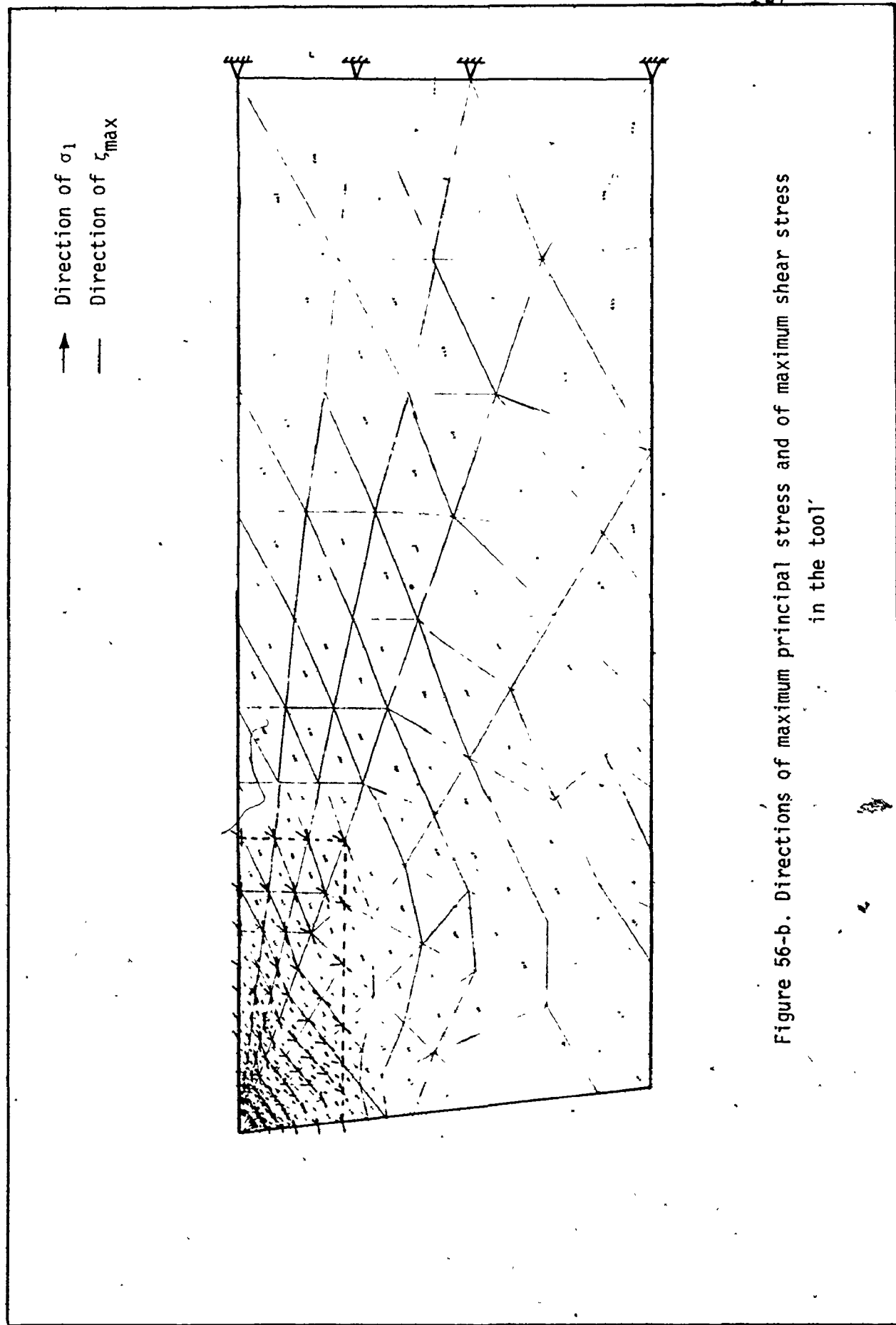


Figure 56-b. Directions of maximum principal stress and of maximum shear stress in the tool

assumption of brittle fracture phenomenon which means that the breakage initiates by crack starts and propagates at the point of maximum tensile stresses and at the direction normal to these stresses.

Comparing the stresses obtained by the classical solution with those resulting from using the finite element technique, a strong difference at the tip of the tool was found. In Figure 53-a a compressive stress area was shown close to the tip when using the finite element method while zero stresses were found at the same area when using the classical solution (Figure 52-b).

Some differences were also found at the fixed boundary. A maximum tensile stress (30 ksi) was found very close to the top by using the finite element method, but the location of this value using the classical solution was at a distance from the top. Also the end of the stress contours are different in both methods. These differences are understood because the classical solution, similarly to the area under the external load, cannot express the local effects of the fixed boundary reaction stresses.

The contours of 20 ksi, 10 ksi and 5 ksi are almost identical in values and locations but at the area near to the bottom of the tool holder, there are some differences at very low stress values and these can be neglected.

Comparing the contours of the minimum principal stress resulted from both methods, tensile stresses were found in the area close to the top of the fixed end when using the finite

element method (Figure 53-b). The values of these stresses are from 1 ksi to 3 ksi. In Figure 52-c it is seen that there are no tensile stresses when using the classical solution.

In the other regions the values of the compressive stress are almost the same in both solutions and it reaches the maximum (30 ksi) in the area near to the bottom of the fixed end.

Figures 55 and 52-d show the contours of the maximum shear stress resulting from the solution using the above mentioned two methods. The maximum values of shear stress were found in both solutions at the area near to the top and bottom of the fixed end. These values are smaller in the solution using the finite element method in the area near to the upper fixed end than those obtained by using the classical solution. This is mainly due to the difference between the values of the minimum principal stress which were obtained by the finite element method and those of the classical solution.

It is shown that the value of the shear stress is 5.0 ksi in the middle of the tool holder using the classical solution. This value is the same and approximately at the same area with using the finite element method. The other values of the shear stress are the same in both solutions.

From the above discussion it can be concluded that a comparison of the finite element results with those obtained by the classical method verifies that the finite element results are correct since they agree in general with those obtained from the classical solution in areas remote from

localized stresses.

From investigating the resulting stresses in the case of zero rake angle and comparing with those obtained in the case of -5° and $+5^{\circ}$ rake angles, it can be concluded that there is no significant difference in the values of stresses of the three cases.

Figures 53-a, 57 and 60 show the maximum principal stress contours at the tool wedge for the cases of $\alpha = 0^{\circ}$, $\alpha = +5^{\circ}$ and $\alpha = -5^{\circ}$ respectively (with flank wear $a = 0.0$). In all these three cases there are practically no tensile stresses in the vicinity of the tip of the tool.

The value of the maximum compressive stress is almost the same (100 ksi) and it decreases when moving from the tool wedge in all three cases (Figures 54, 58 and 61). The contours of the maximum shear stress at the tool wedge in the case of $\alpha = 0^{\circ}$, $\alpha = 5^{\circ}$ and $\alpha = -5^{\circ}$ with no flank wear ($a = 0.0$) are shown in Figures 55, 59 and 62 respectively. The maximum value of the shear stress is 46 ksi in the case of $\alpha = 5^{\circ}$, 47 ksi in the case of $\alpha = 0^{\circ}$ and 48 ksi in the case of $\alpha = +5^{\circ}$. The maximum shear stress increases slightly with decreasing the tool wedge angle but the difference between these values is only about 4%.

The results obtained by using the finite element technique are in agreement with the results obtained from the experimental work in both $+5^{\circ}$ and -5° rake angle tests. In Table 22, it is seen that in both $+5^{\circ}$ and -5° rake angles tools and for the same cutting conditions, the breakage occurred approximately at the same cutting time in both tools.

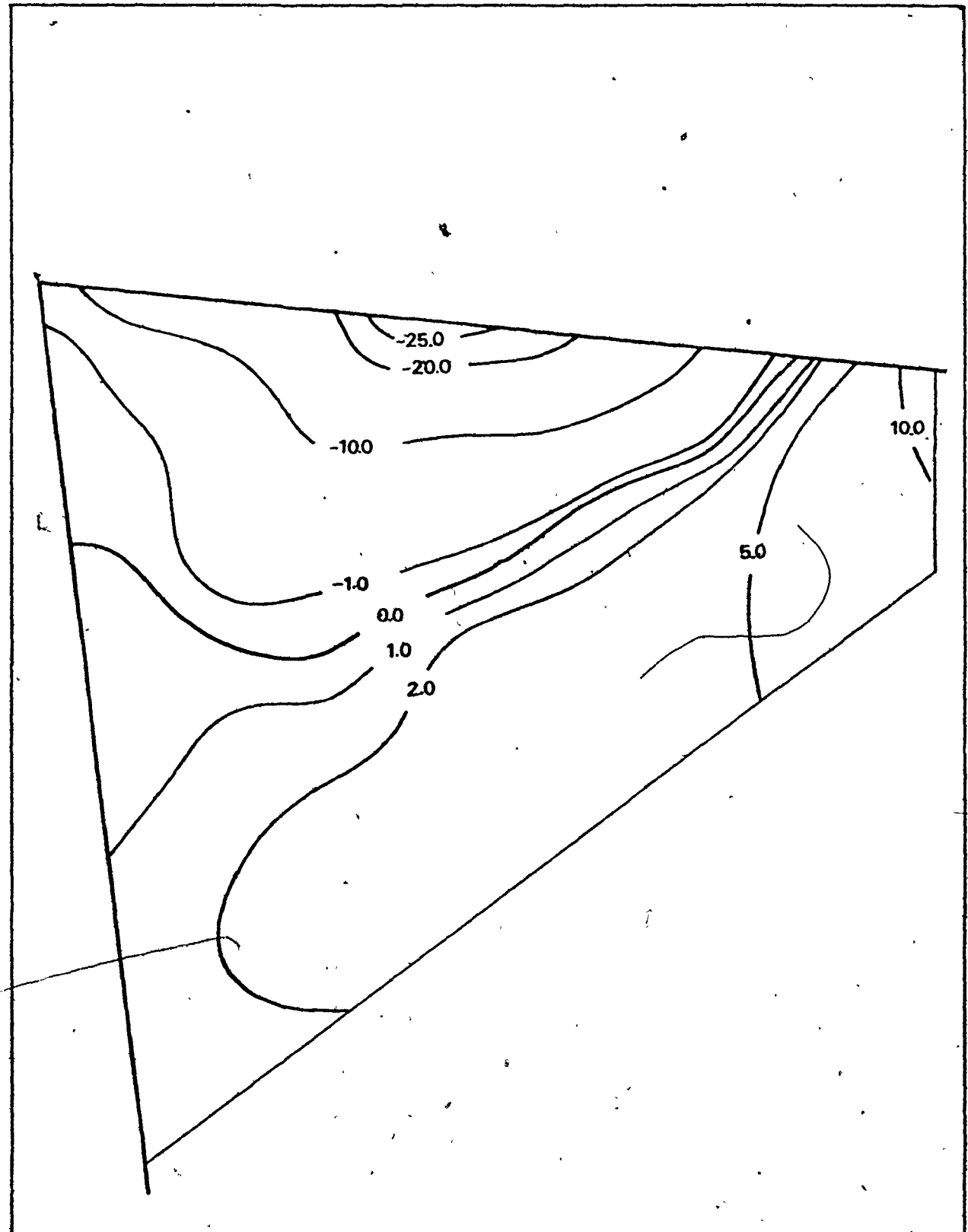


Figure 57

Maximum principal stress contours in the loading region (σ_1 ksi).

$$\alpha = +50$$

a = 0.0 inch

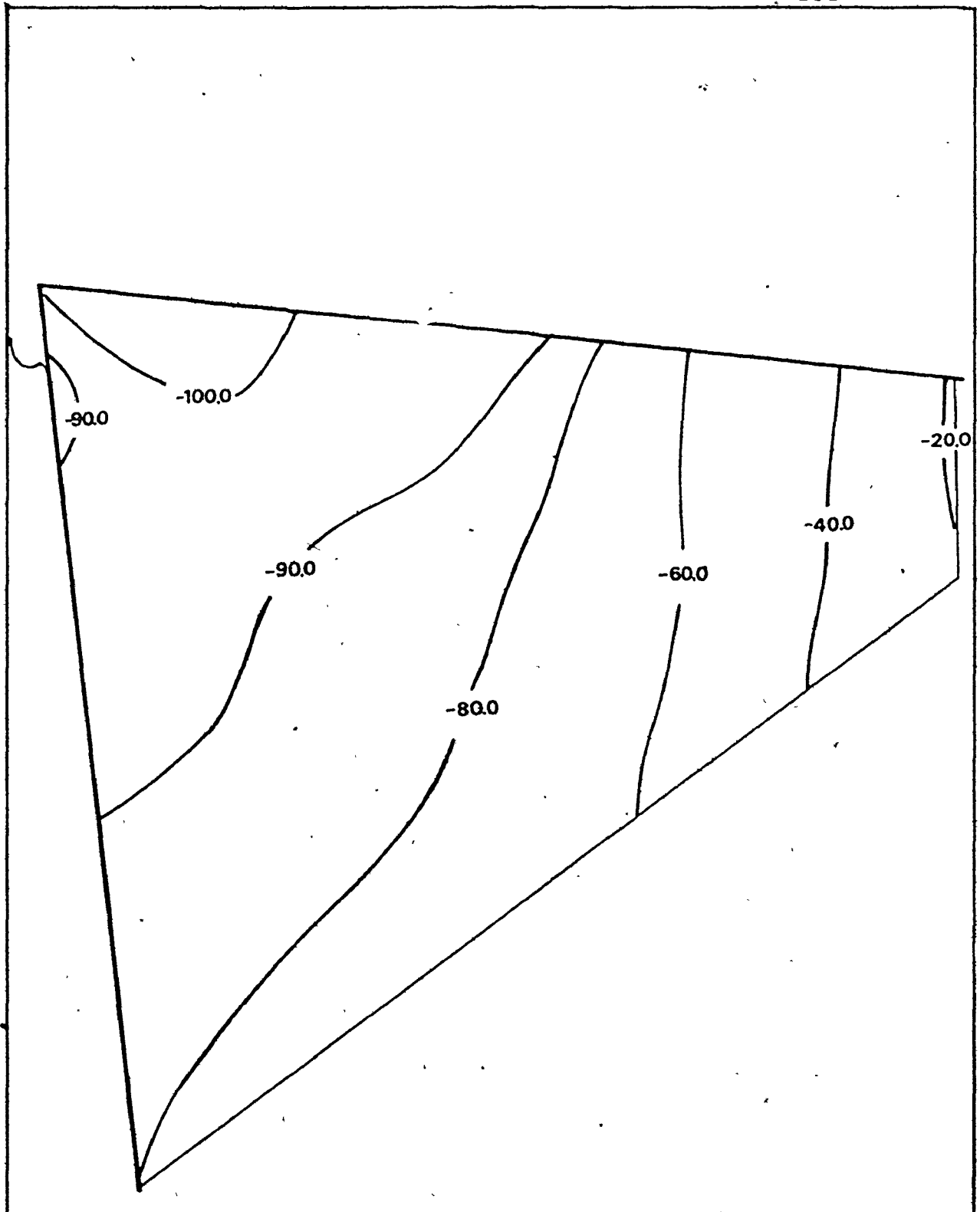
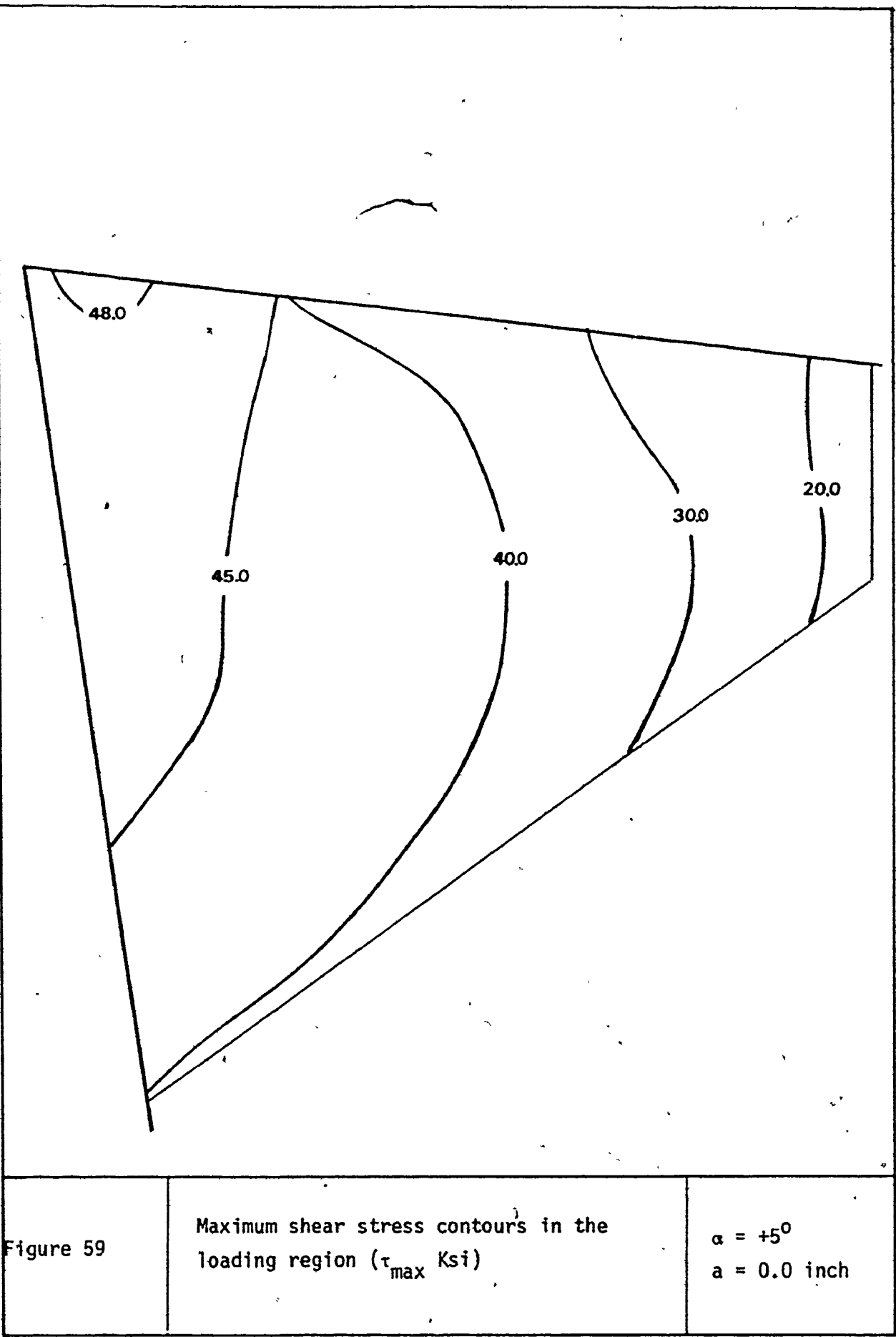
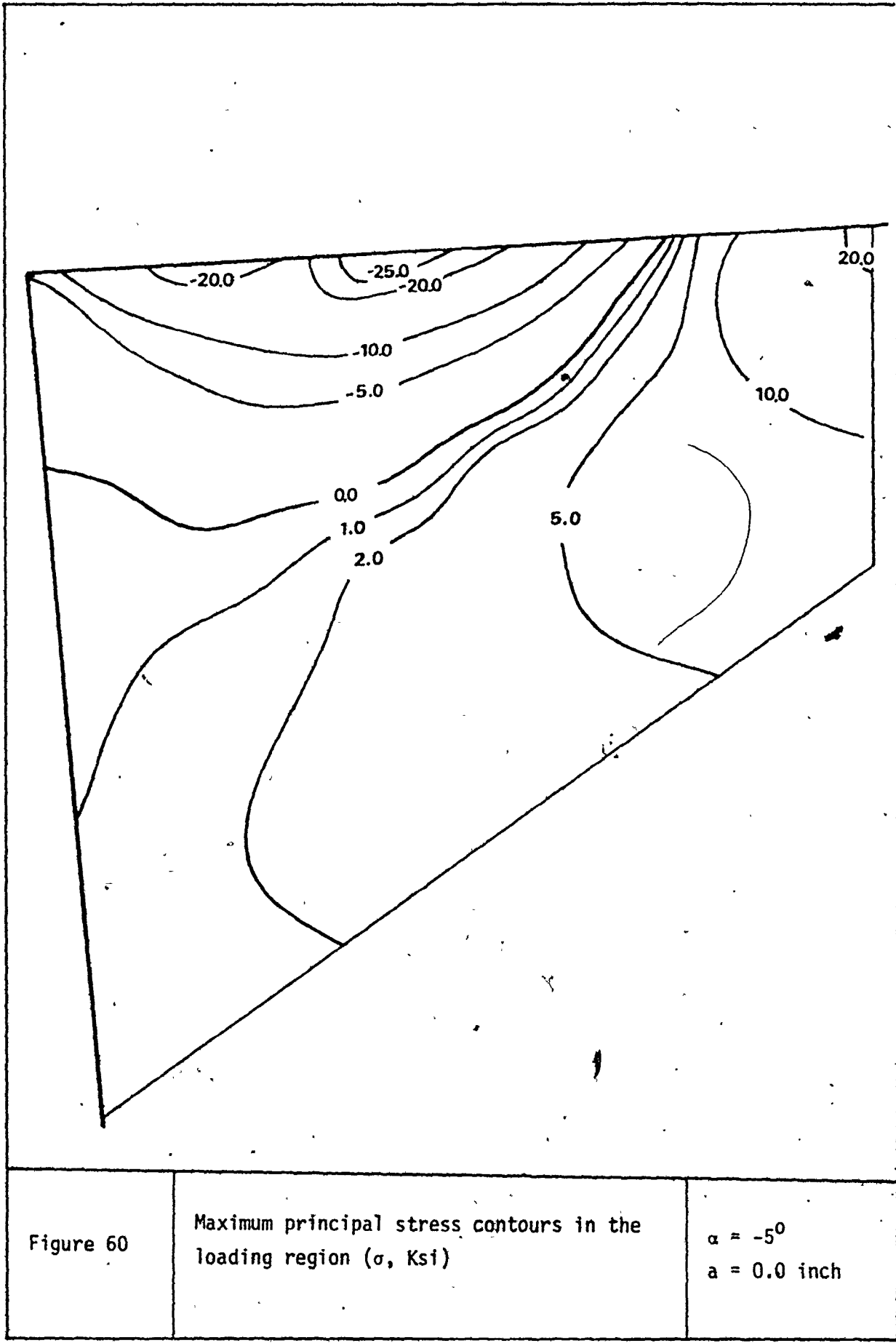


Figure 58

Minimum principal stress contours in the
loading region (σ_2 ksi)

$\alpha = +50^\circ$
 $a = 0.0$ inch





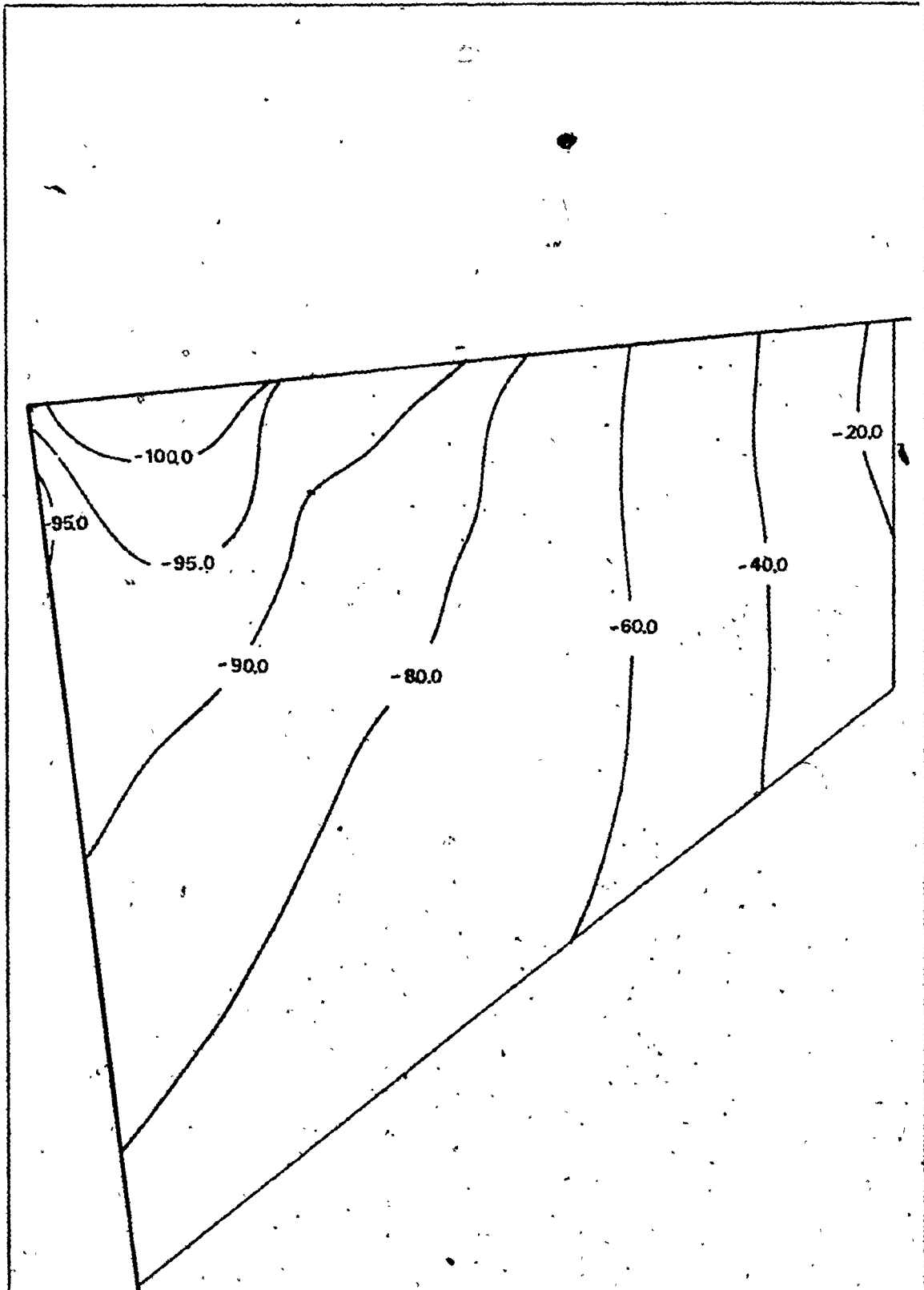


Figure 61

Minimum principal stress contours in the
loading region (σ_2 Ksf)

$\alpha = -5^\circ$
 $a = 0.9$ inch

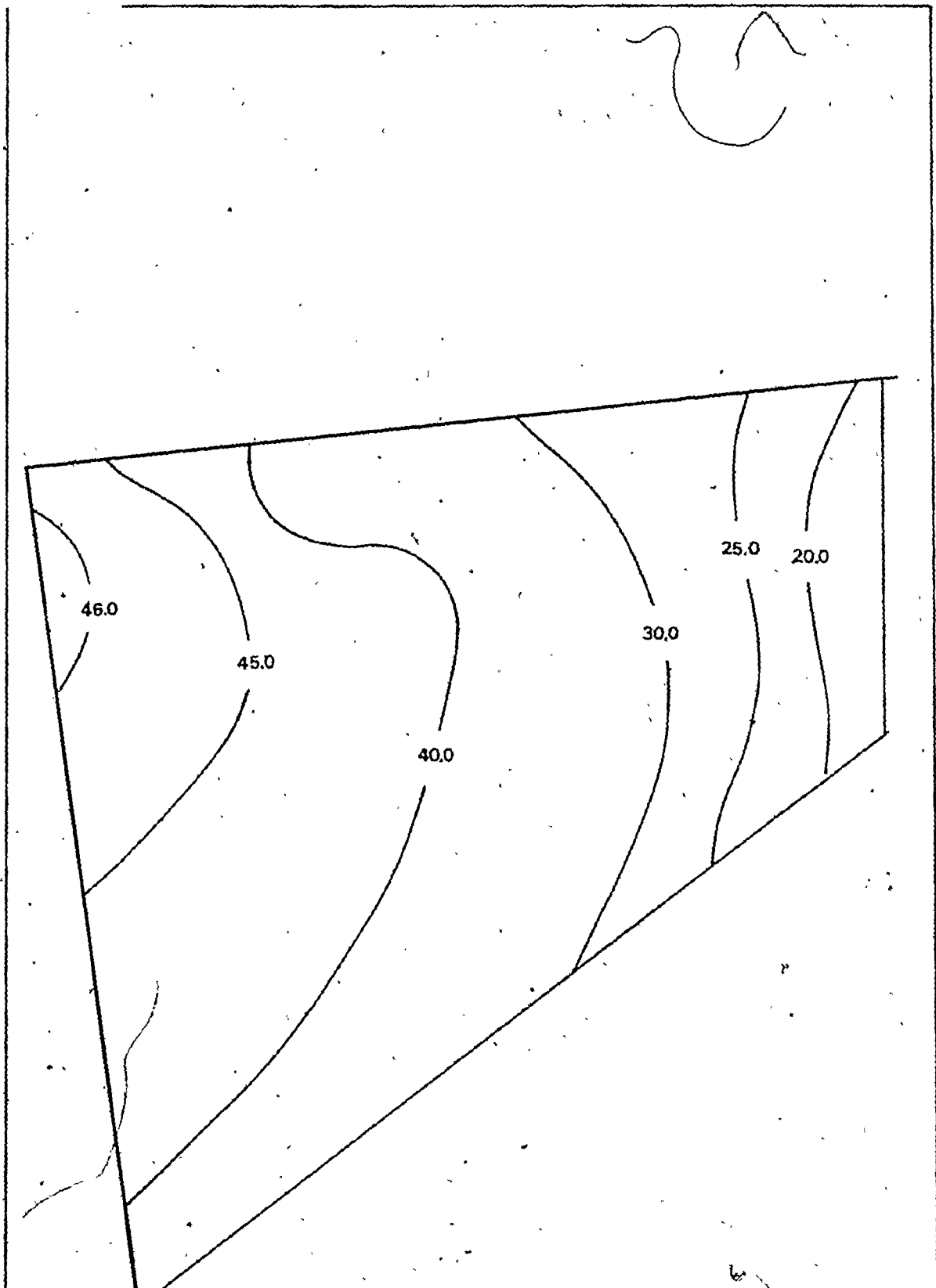


Figure 62

Maximum shear stress contours in the
loading region (τ_{\max} ksi)

$\alpha = -5^\circ$
 $a = 0.0$ inch

Effect of the flank wear:

The discussion of the effect of flank wear will be restricted to the case of zero rake angle.

From Figures 53, 63 and 66 which represent the contours of the maximum principal stress in the three cases of flank wear ($a = 0.0$, $a = 0.006$ inch and $a = 0.015$ inch) respectively, it can be seen that as the flank wear increases the friction load will increase too and consequently the area of the minor compressive stresses at the tool wedge increases (Figures 53-a, 63-a and 66-a).

The value of the local maximum tensile stress in the case of $a = 0.0$ is 21.3 ksi and it decreases to 18 ksi and 17 ksi as the flank wear increases (Figures 53-b, 63-b and 66-b).

Figures 54, 64 and 67 illustrate the contours of the minimum principal stress of the three values of flank wear width respectively. In these figures there is not any recognizable change in the values of the stress with flank wear growth.

A slight difference in values of the maximum shear stress was found when comparing the three cases of flank wear. It is seen that as the flank wear increases, the shear stress slightly decreases (Figures 55, 65, 68). Its value is 47 ksi in the case of no flank wear ($a = 0.0$) and 45 ksi in the case of flank wear width $a = 0.015$ inch.

This is mainly so because of the increase in compressive stress in the horizontal direction due to the increasing normal load on the flank which, to some extent,

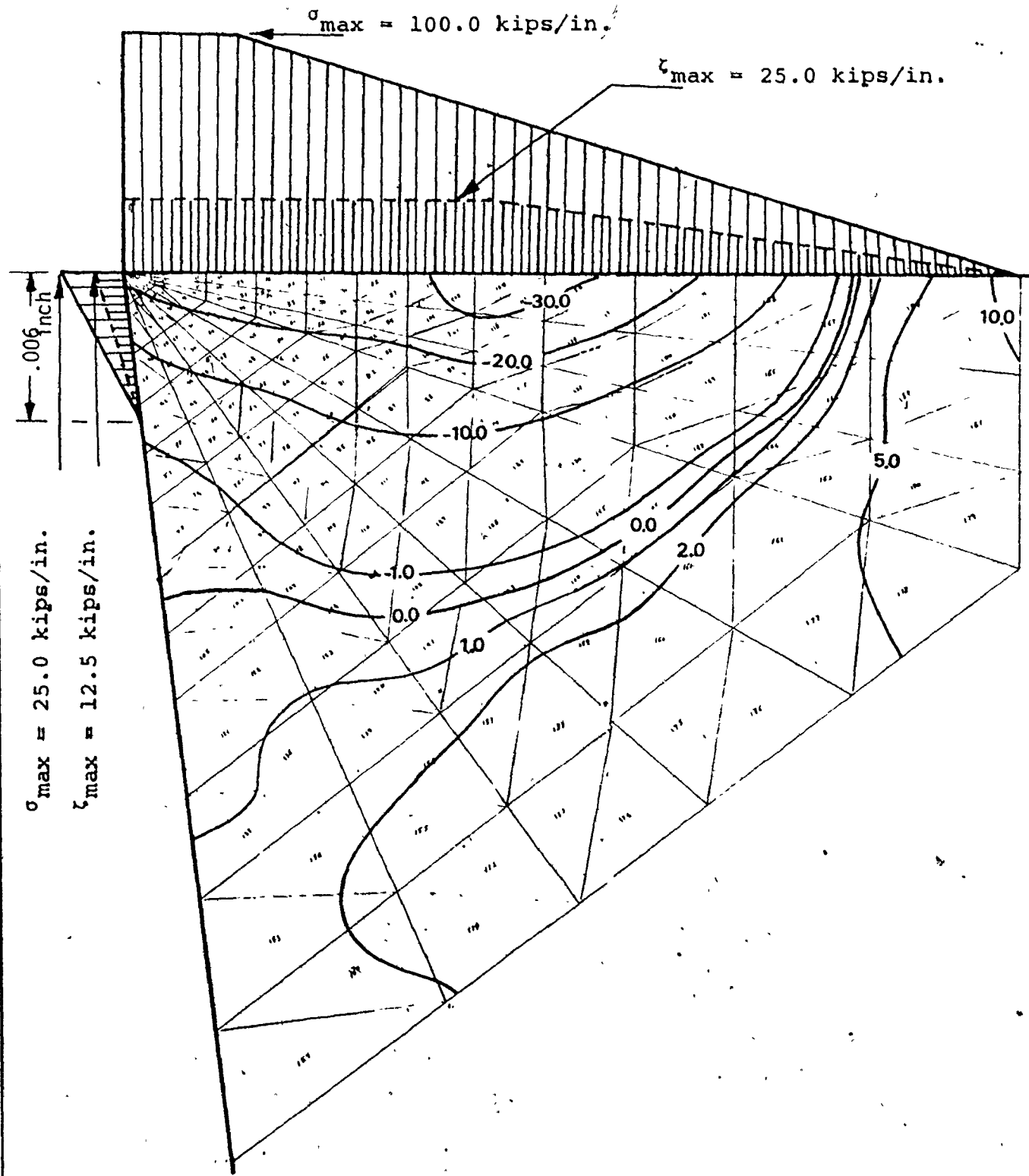


Figure 63a

Maximum principal stress contours in the
loading region (σ , ksi)

$$\alpha = 0^\circ$$

$$a = 0.006 \text{ inch}$$

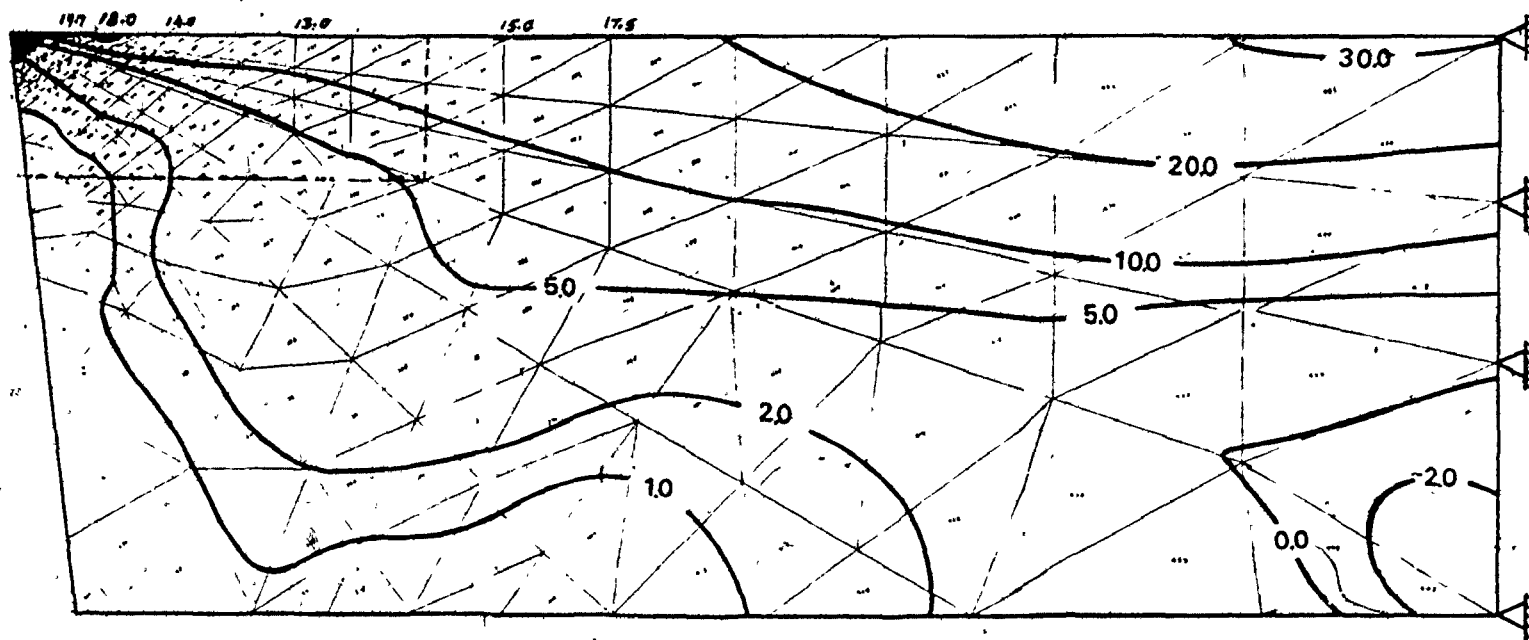


Figure 63b. Maximum principal stress contours in the tool and tool holder (σ_1 ksi) $\alpha = 0^\circ$
 $a = 0.006$ inch

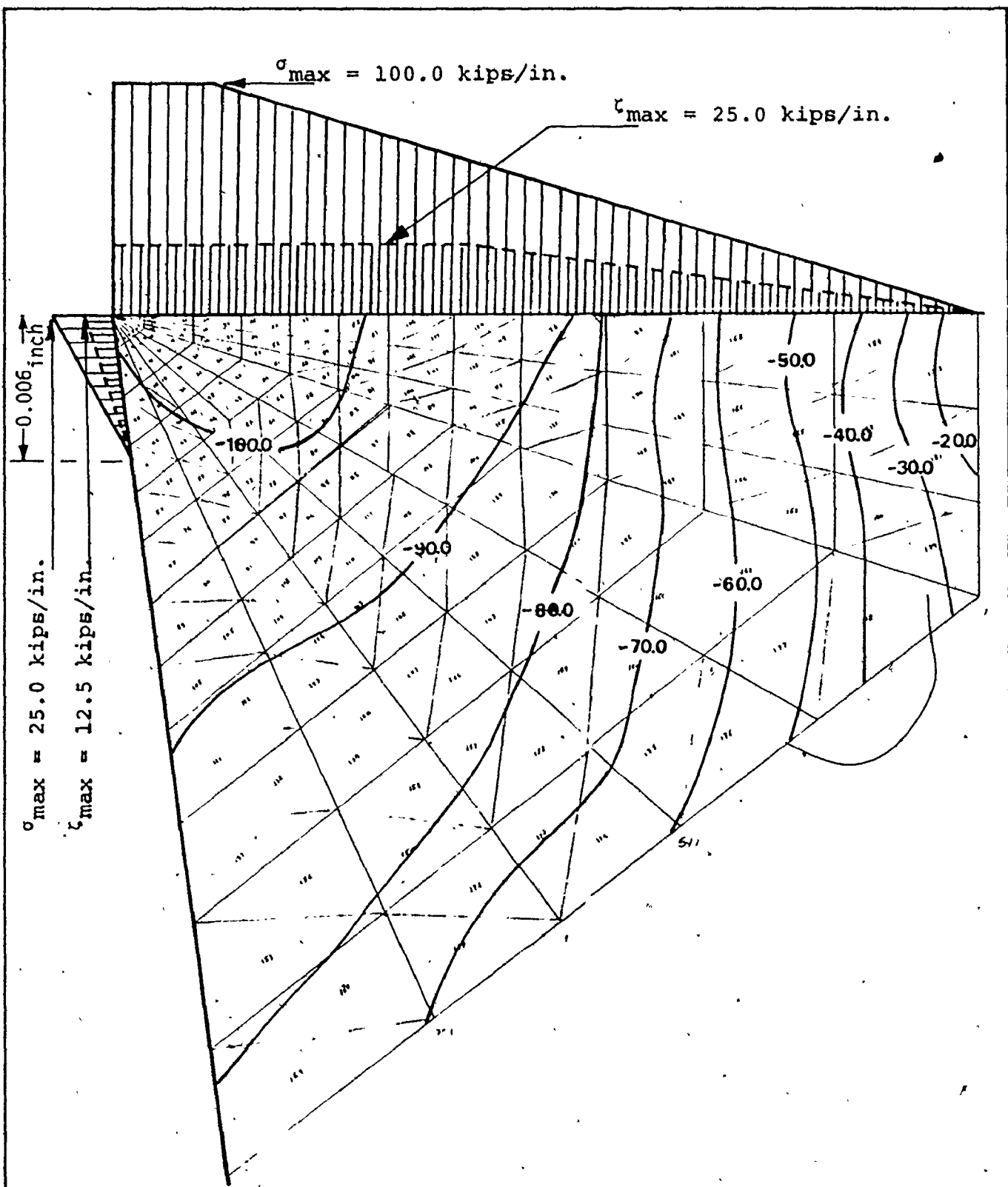


Figure 64

Minimum principal stress contours in the loading region (σ_2 Ksi)

$$\alpha = 0^{\circ}$$

$$a = 0.006 \text{ inch}$$

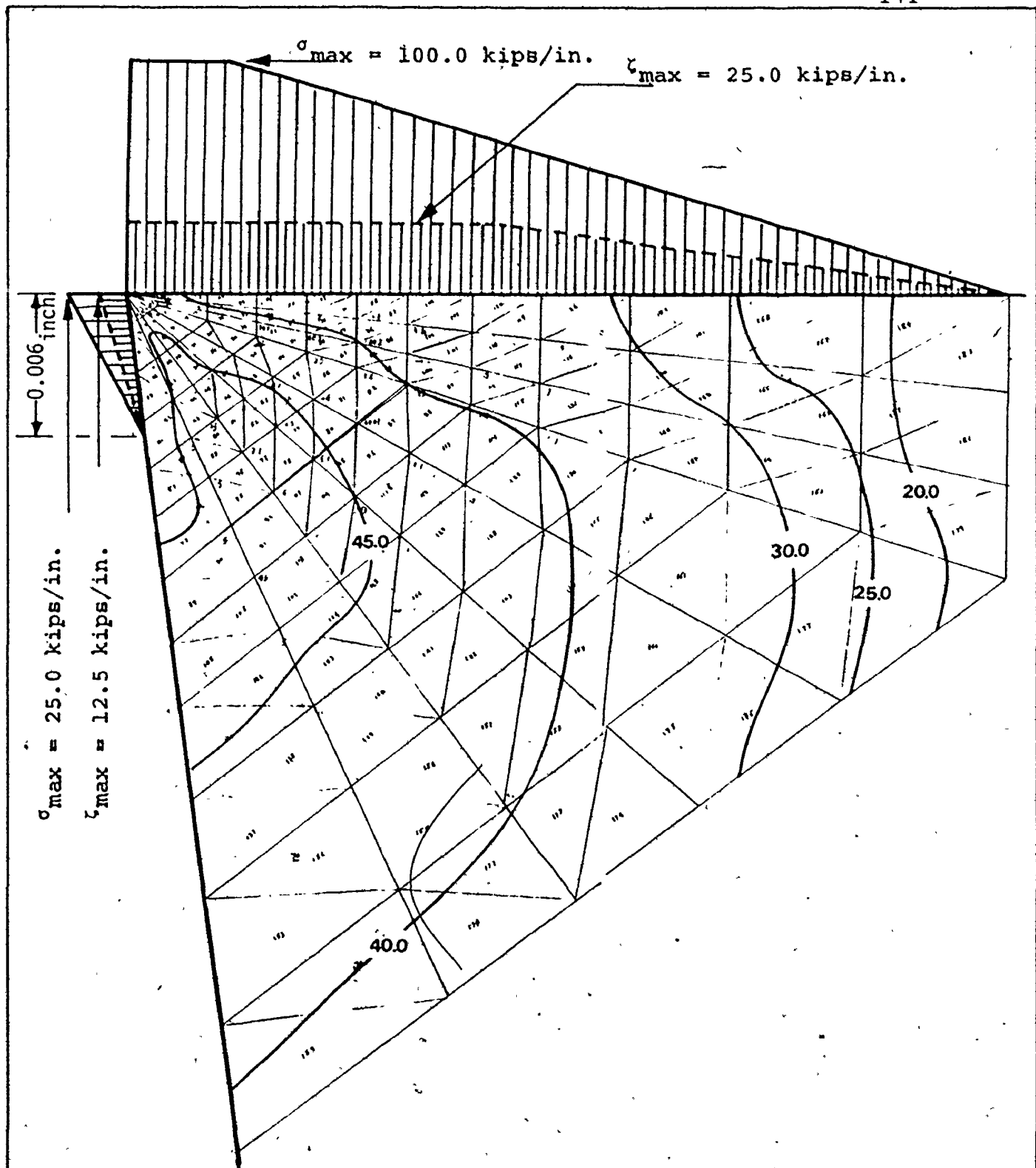


Figure 65	Maximum shear stress contours in the loading region (τ_{max} ksi)	$\alpha = 0^{\circ}$ $a = 0.006 \text{ inch}$
-----------	---	--

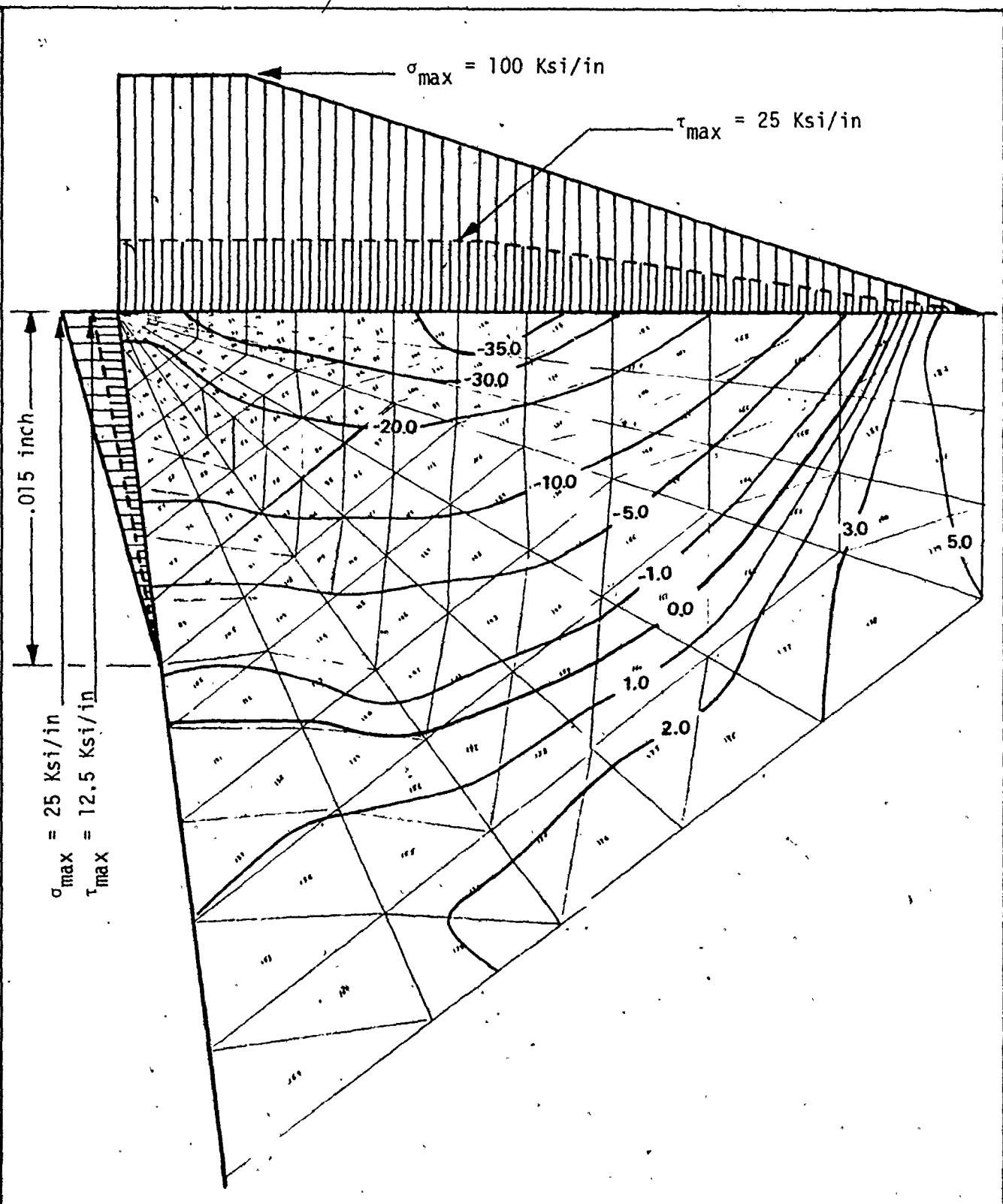
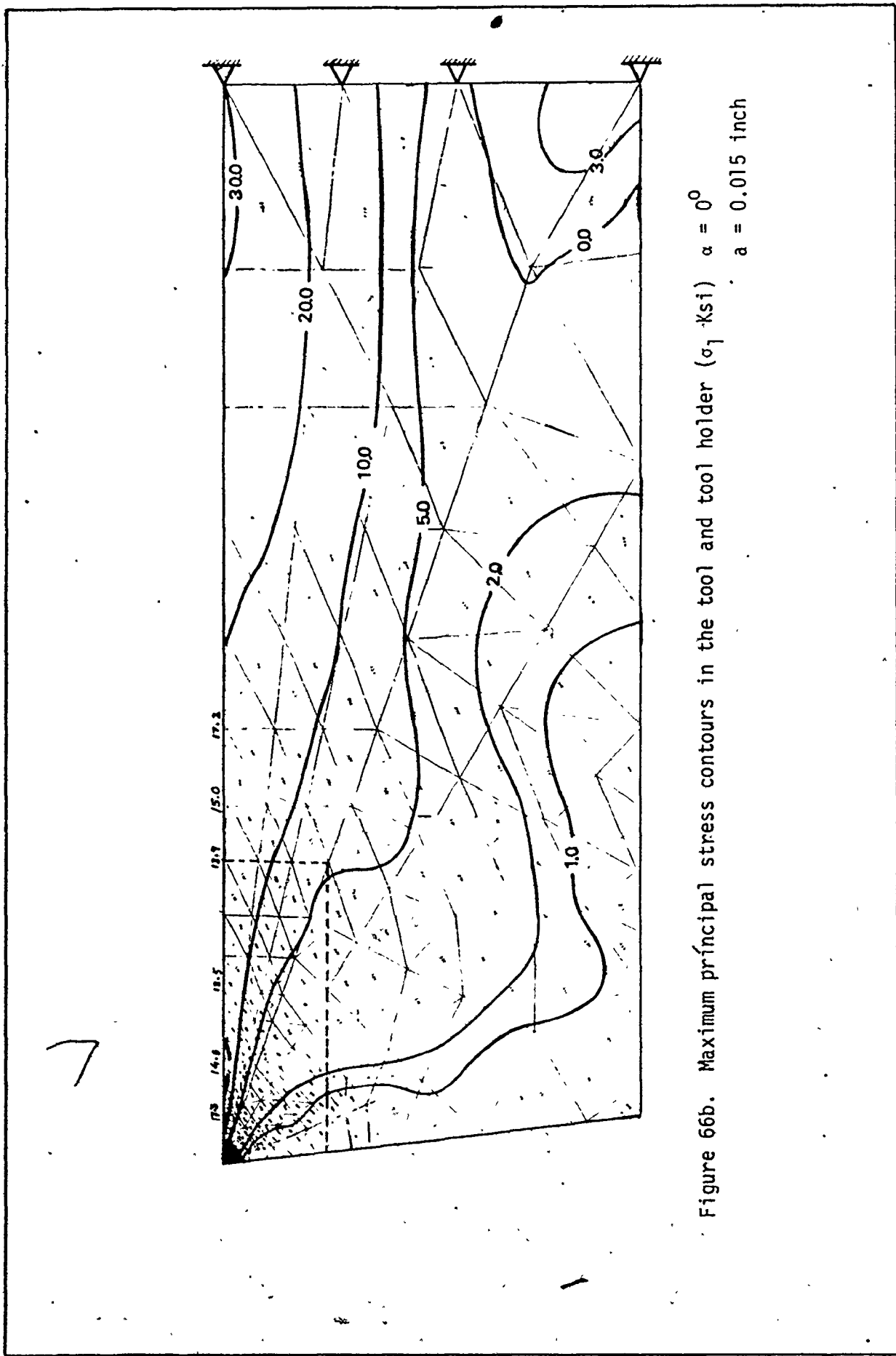


Figure 66a

Maximum principal stress contours in the loading region (σ_1 , Ksi)

$\alpha = 0^\circ$
 $a = 0.015 \text{ inch}$



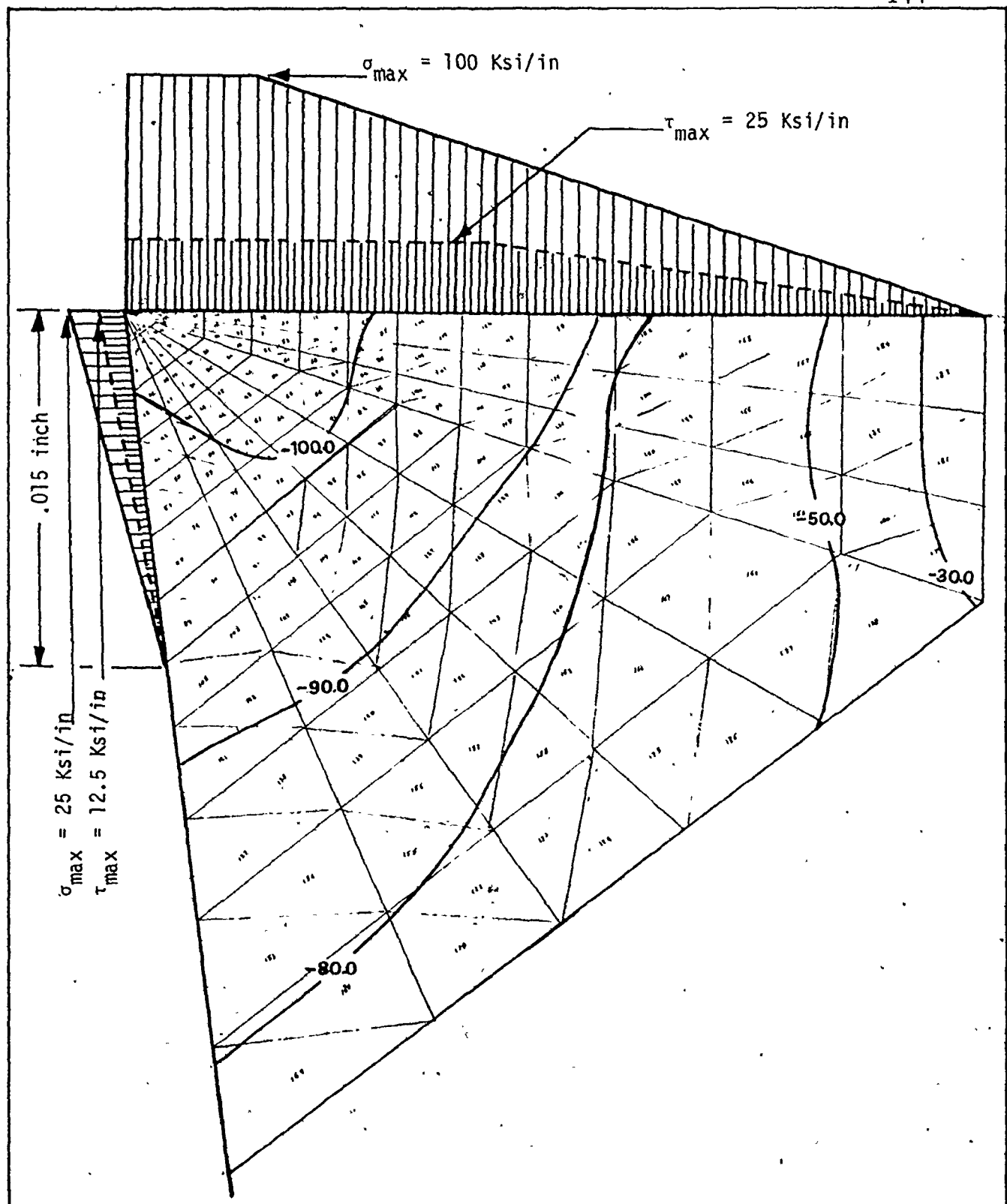


Figure 67

Minimum principal stress contours in the
loading region (σ_2 KSI)

$\alpha = 0^\circ$
 $a = 0.015$ inch

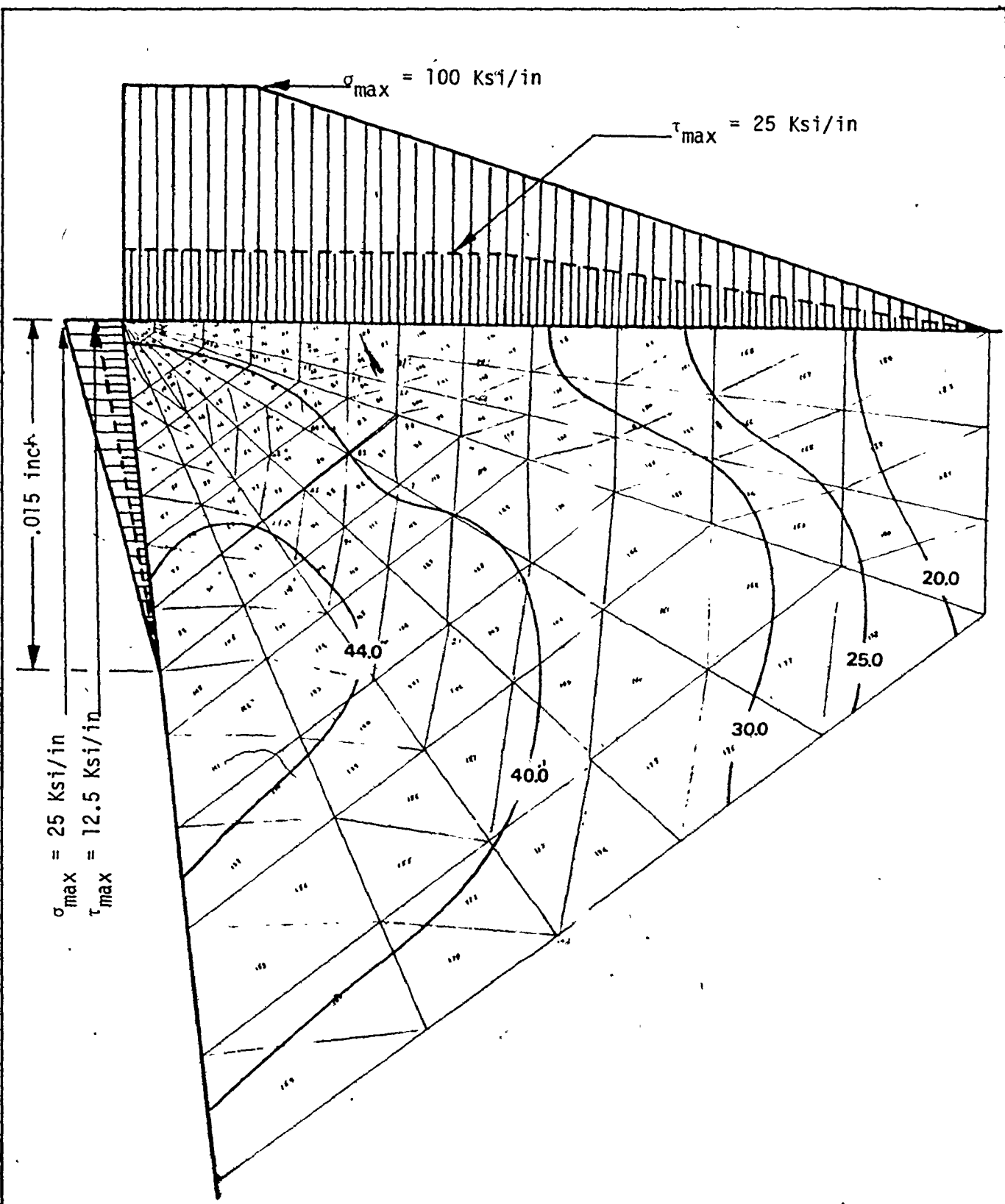


Figure 68

Maximum shear stress contours in the loading
region (τ_{max} ksi)

$$\alpha = 0^\circ$$

$$a = 0.015 \text{ inch}$$

"supports" the edge against being sheared off by the effect of normal force acting on the rake face.

In reality, however, an increase of edge wear leads to more chipping and eventually breakage. This is because the initial chipping of the normal load on the rake face increases further with increased chipping, etc. This aspect was not considered in the computations just described where normal load on the rake face was kept constant and independent of the wear on the flank.

B. Stepwise Sub-dividing and Refining Method

The computation work was carried out in five steps using the method suggested by Tlusty [23] for the case of zero rake angle with no flank wear ($a = 0.0$ inch) and with flank wear width $a = 0.006$ inch. Figure 69 shows the dimensions of the fifth step (loading region) using the same load values as in the single step method. The area considered in detail overlaps with only a part of the area considered in the preceding, the latter one is shown in a broken line.

The contours of the principal stresses and the maximum shear stresses at the tool edge (loading region) in the case of no flank wear are next shown in Figures 70, 71 and 72.

Figure 70 shows the maximum principal stress contours at the tip of the tool. The stresses were shown in great detail and it is seen that the stresses in this area are compressive stresses. These results agree with those obtained from the single step method (Figure 53-a).

The contours of the minimum principal stress are

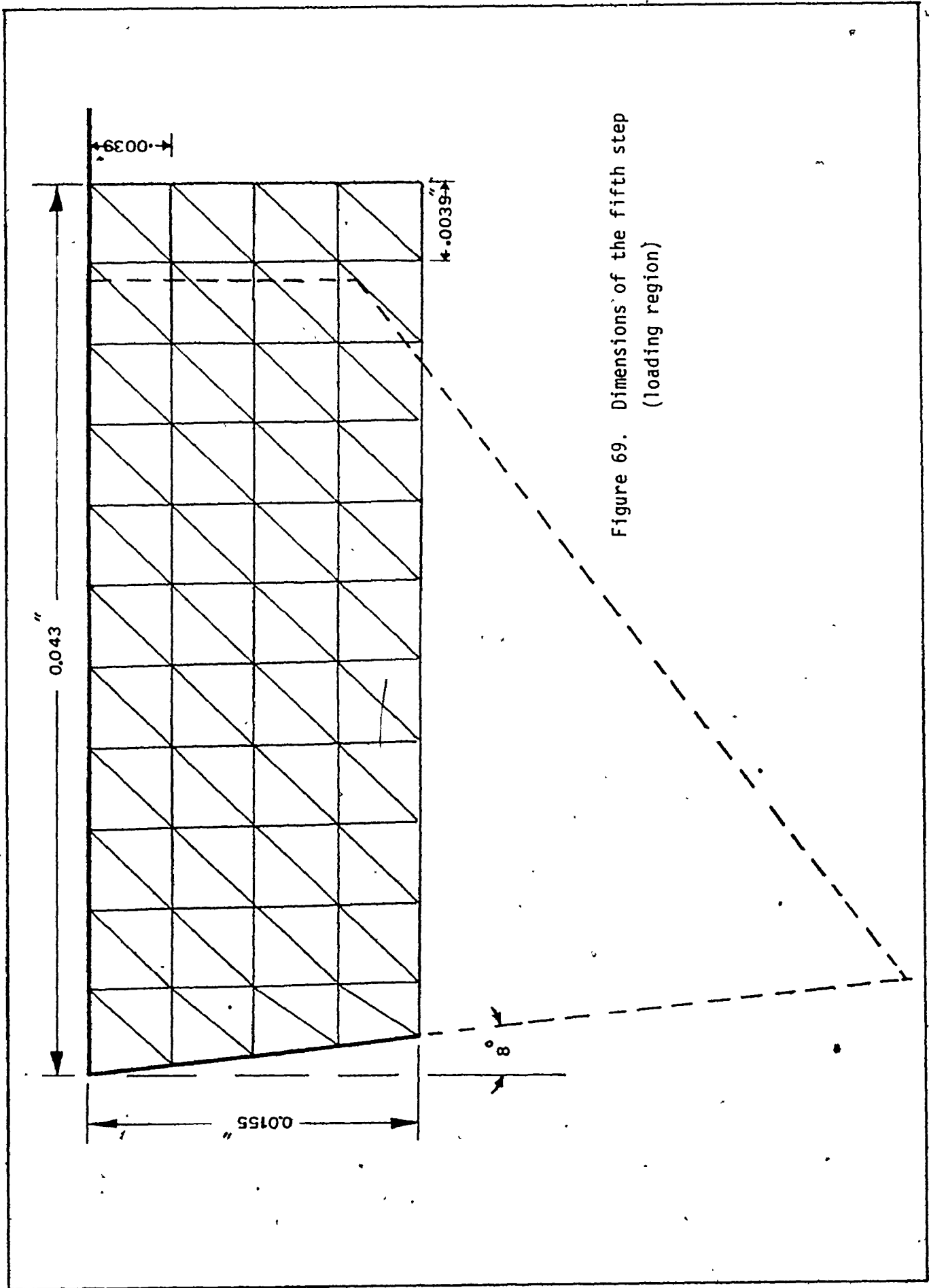


Figure 69. Dimensions of the fifth step
(loading region)

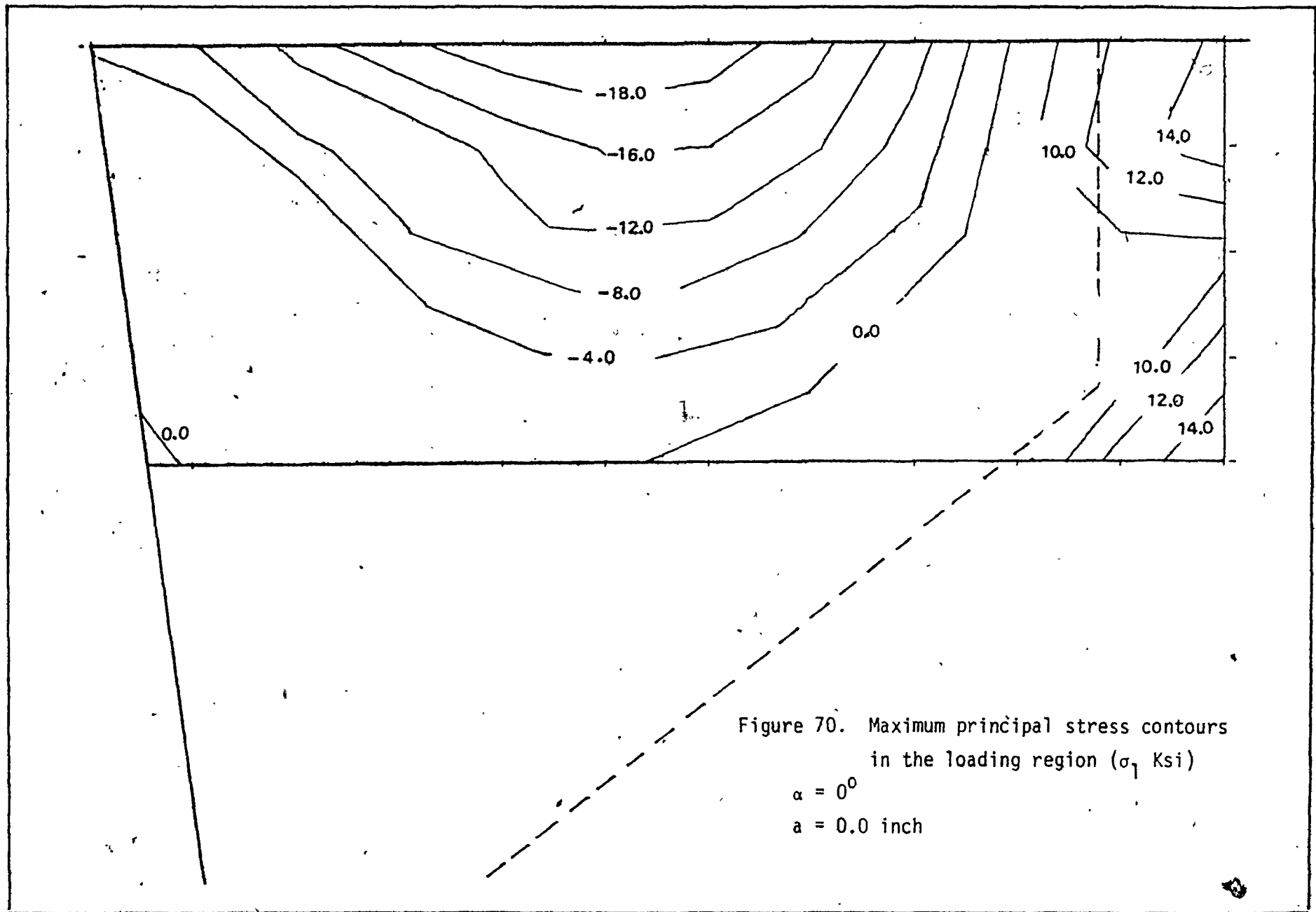


Figure 70. Maximum principal stress contours
in the loading region (σ_1 Ksi)

$$\alpha = 0^\circ$$

$$a = 0.0 \text{ inch}$$

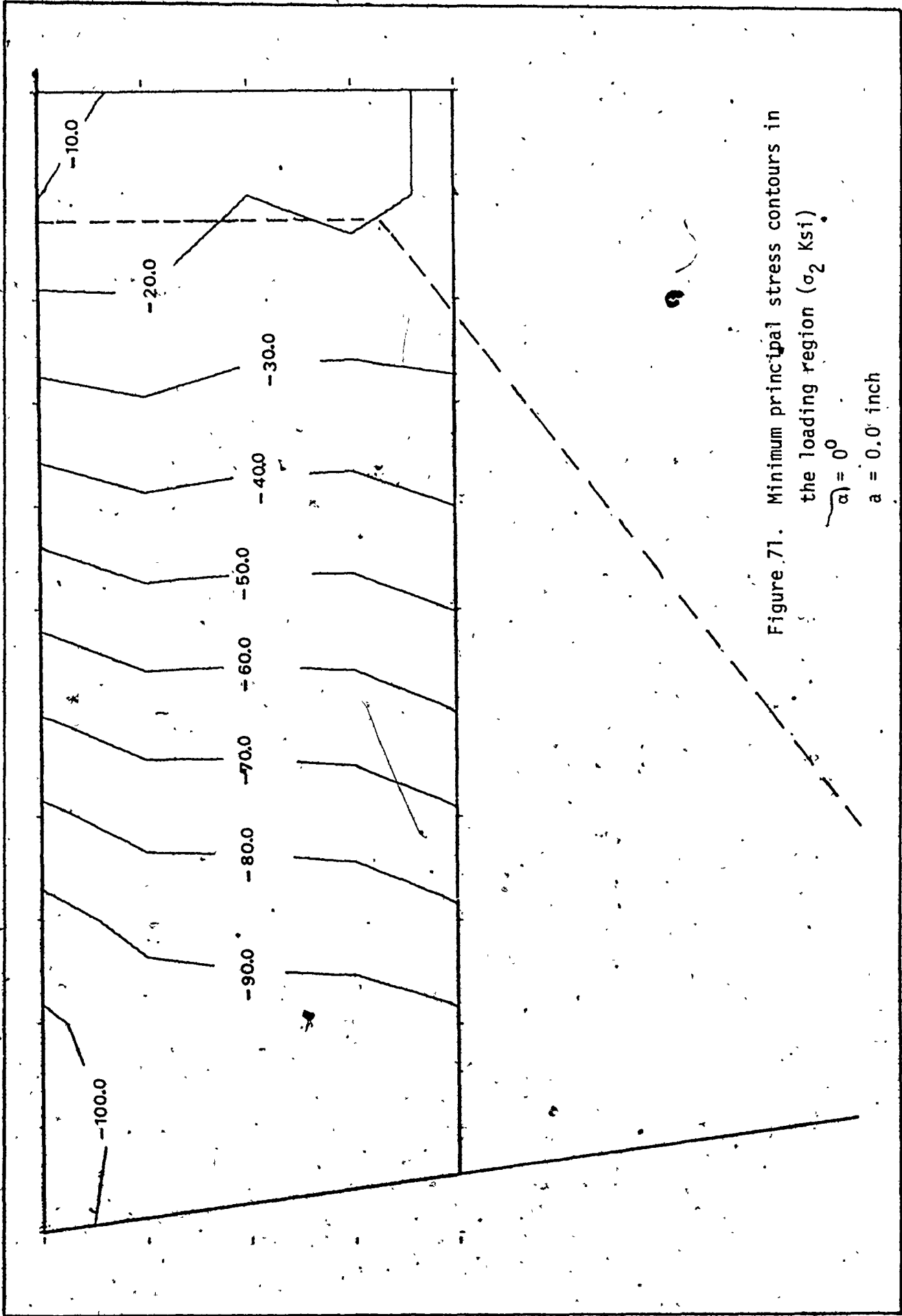
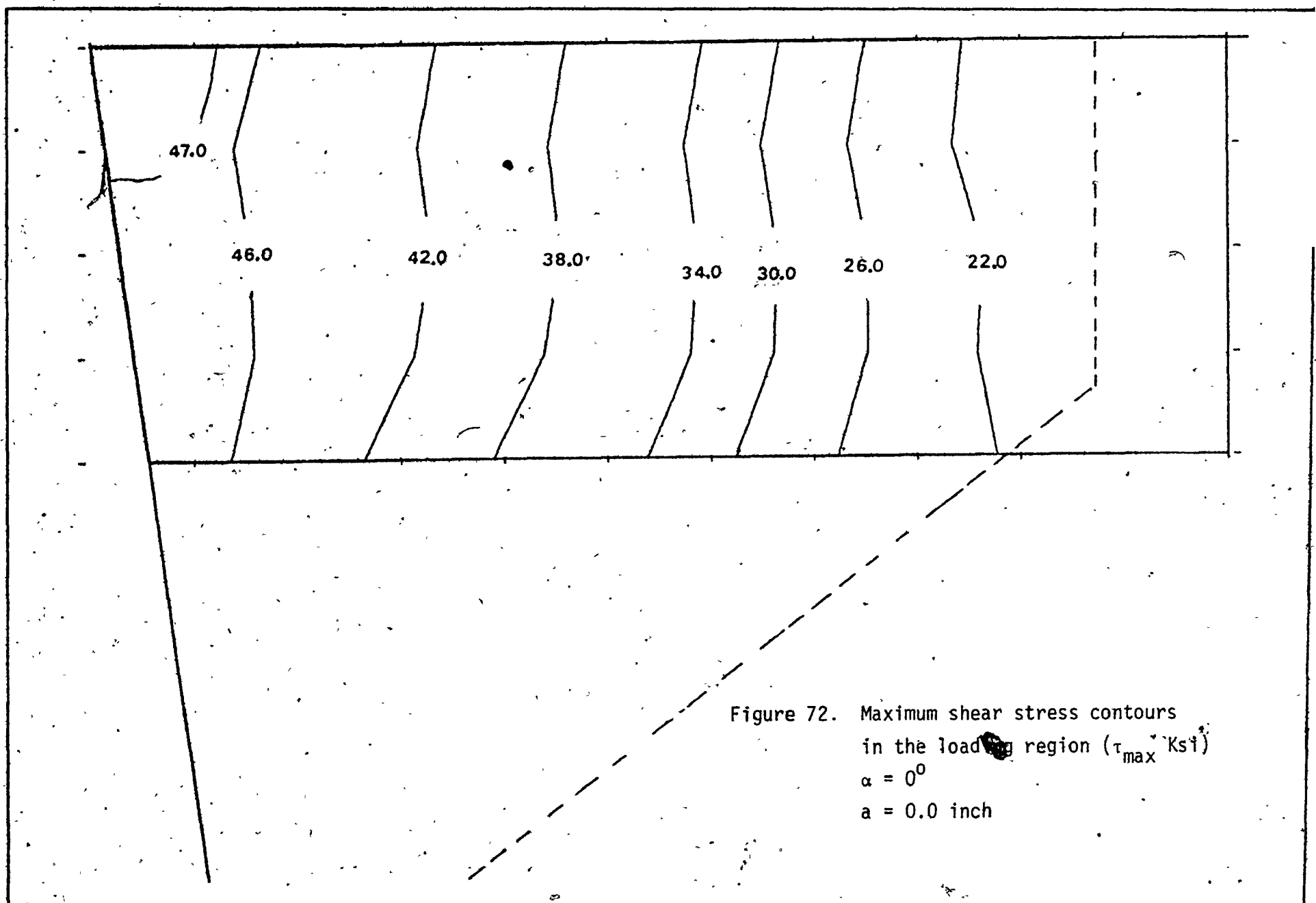


Figure 71. Minimum principal stress contours in
the loading region (σ_2 KSI)
 $\alpha_1 = 0^\circ$
 $a = 0.0$ inch



shown in Figure 71 for the same area. The maximum value of the compressive stress is 100 ksi which agrees with the results obtained when using the single step method (Figure 54).

The maximum value of the shear stress is 46 ksi (Figure 72) and the difference between this value and the value obtained by using the finite element method is very small and is equal to 1 ksi (Figure 55).

In the case of $a = 0.006$ inch, only the load values of the preceding case were changed and the computation work was carried out for the fifth step only (the loading region).

Figures 73, 74 and 75 show the contours of the principal stresses and the maximum shear stresses resulting in the case of zero rake angle with 0.006 inch flank wear width.

Figure 73 shows the contours of the maximum principal stress (minor compressive stress). It is seen that the stresses near the flank are increased by about 1.5 times the case of no flank wear ($a = 0.0$). This, actually, is due to increasing the load values resulting from the present flank wear, $a = .006$ inch.

Comparing these results with those obtained by using the single step method, it is seen that there is no significant difference between the values of the stresses in the case of no flank wear ($a = 0.0$) and those in the case of $a = .006$ inch (Figures 53-a, 63-a).

From Figure 74 it is seen that the maximum value of the compressive stress is 100 ksi which agrees with the value

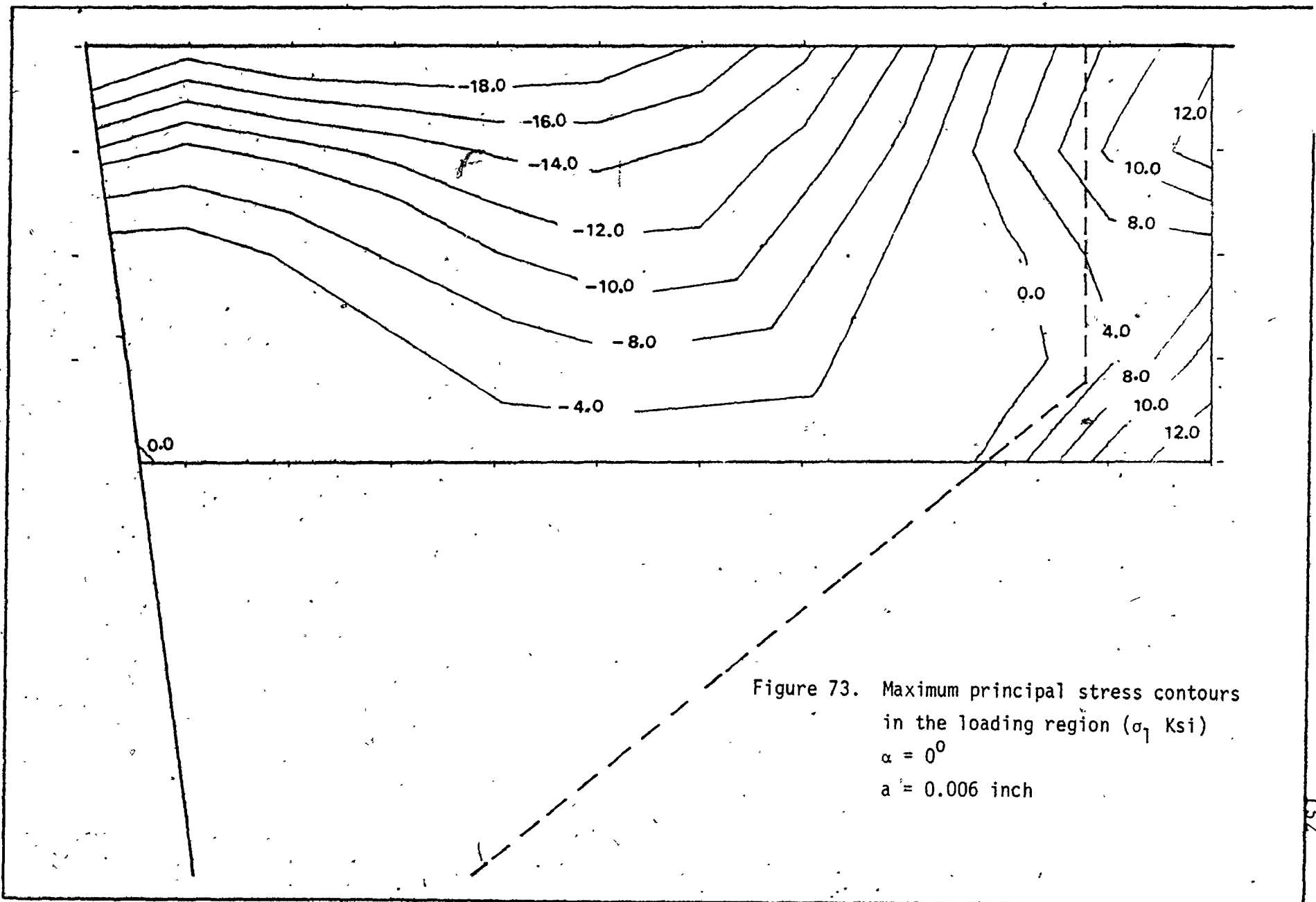


Figure 73. Maximum principal stress contours
in the loading region (σ_1 ksi)
 $\alpha = 0^0$
 $a = 0.006$ inch

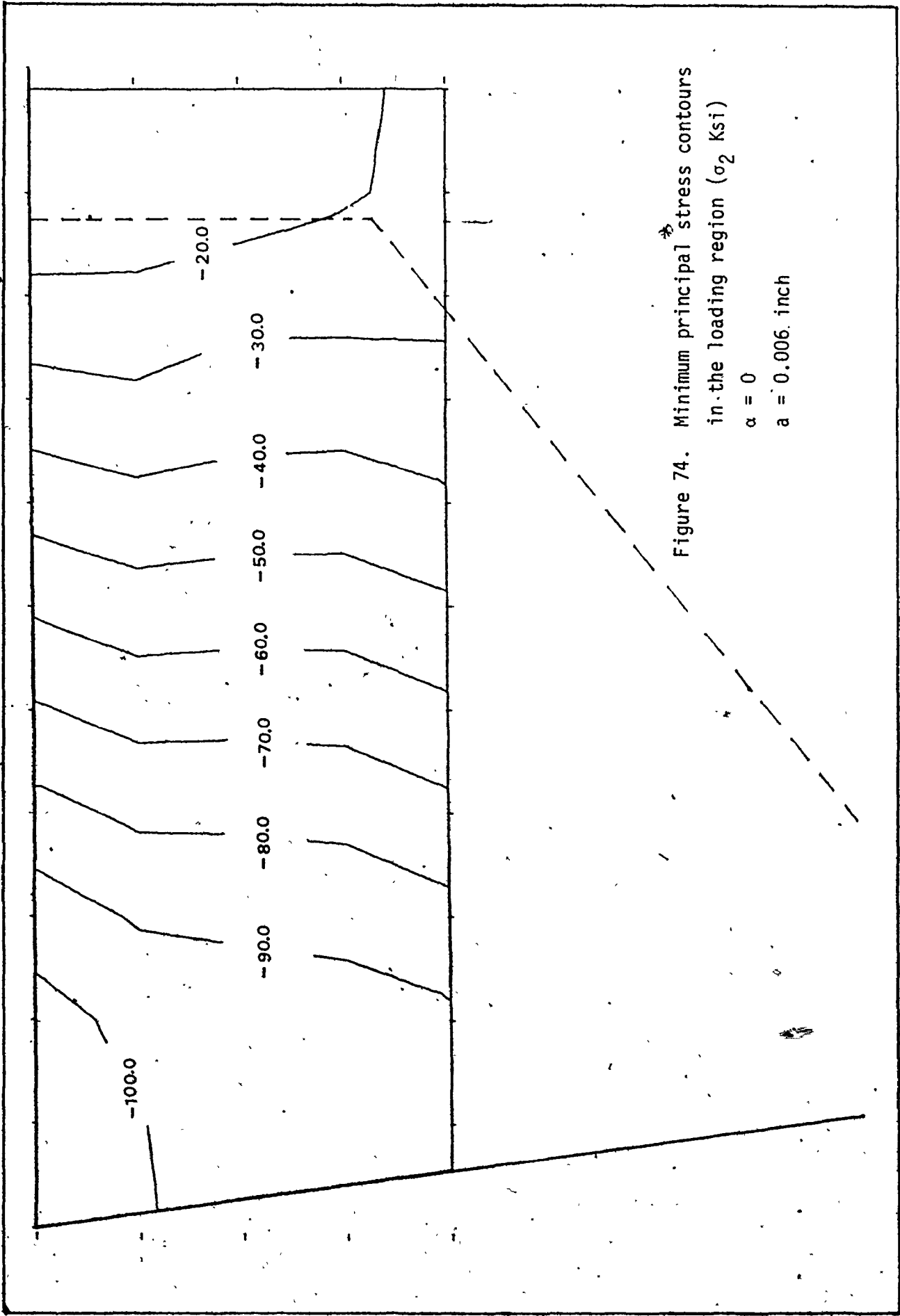
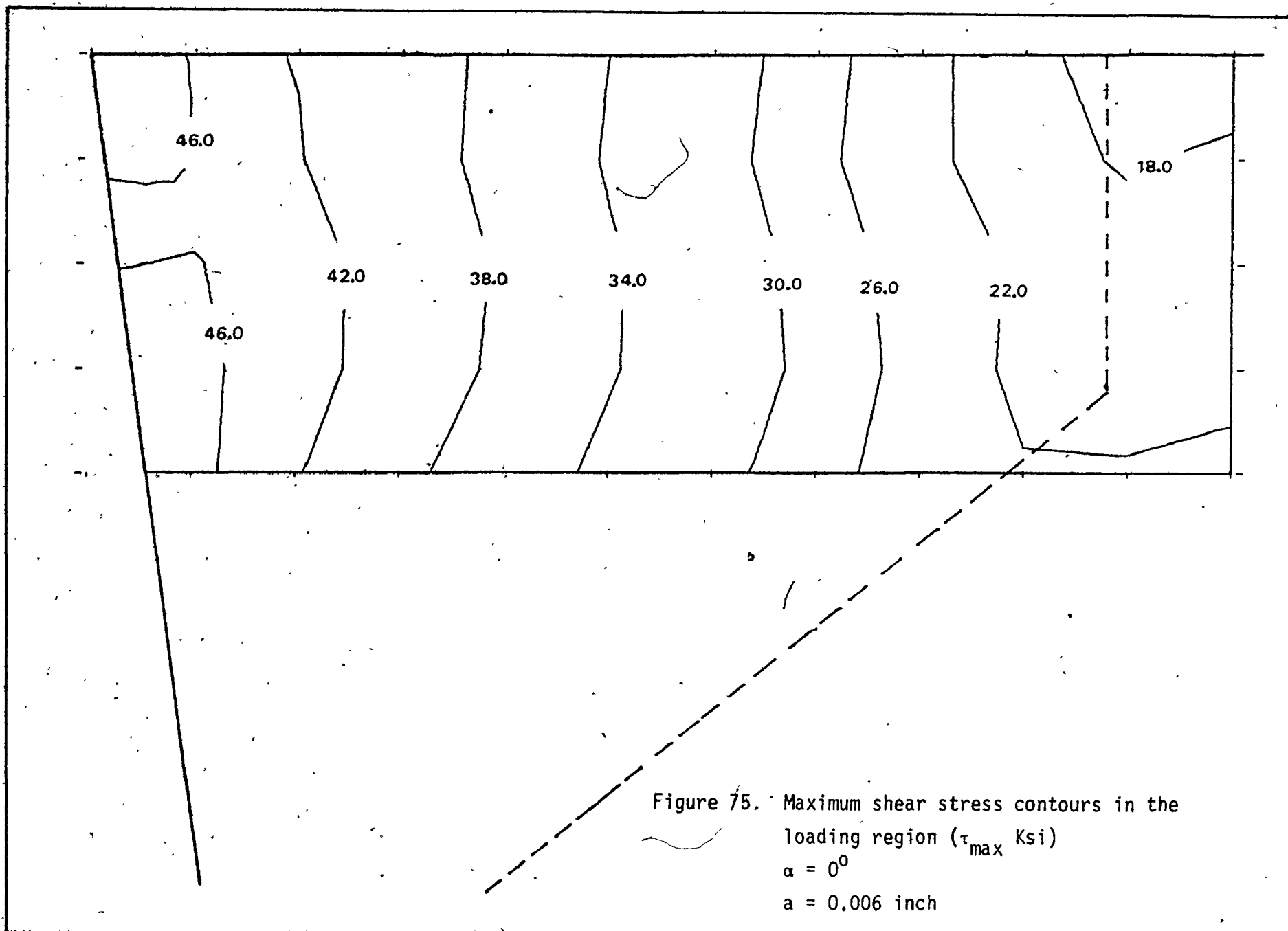


Figure 74. Minimum principal stress contours
in the loading region (σ_2 ksi)
 $\alpha = 0$
 $a = 0.006$ inch



obtained when using the single step method (Figure 58).

The shear stress has a maximum value of 46 ksi which occurred close to the flank (Figure 75). These results too agree with those obtained by using the single step method (Figure 10-b).

From the preceding discussion, it can be concluded that comparing the results obtained by using the stepwise method, a negligible difference was found. This difference may be due to variations in grid distribution.

CHAPTER 5

CONCLUSIONS

The investigation concentrated on chipping (gradual damage to the cutting edge) and on breakage (fracture of a rather large portion of the tool wedge) of carbide tools.

Experiments conducted by turning 1040, 4340/217 BHN, and 4340/380 BHN in continuous and interrupted cutting, the latter with very short interruptions so as not to induce cyclic thermal stresses have confirmed general experience in that chipping was observed at medium feeds of .012 to .024 in./rev. and breakage at heavy feeds of .027 to .043 in./rev. in continuous cutting. Breakage occurred either after some accumulation of chipping (and consequent increase of cutting force) or outright after a very short cutting time. In interrupted cutting breakage occurred at lower feeds about 0.02 inch after very short cutting times. Therefore, fatigue was excluded as an explanation. Occurrence of breakage at lower feeds in interrupted cutting is believed to be due to a change in the loading mode (shock wave at the exit of the cut or chip interference at the entrance into the cut). The nature of this change was not investigated. Both the above mentioned types of fractured surfaces were inspected under a scanning electron microscope. The chipped surfaces appear to have failed in the middle of the cobalt layer and the failure was accompanied by an amount of plastic flow. The broken surfaces

appear as brittle fractures occurring at the cobalt carbide interfaces as a result of tensile stresses.

Stress analysis simplified to a two-dimensional plane strain problem confirmed these conclusions. A local maximum of tensile stress was identified on the rake face at a distance between .08 to .15 inch from the cutting edge which coincides with the origin of the observed brittle fracture. The level of the stress roughly corresponds to the TRS of the sintered carbide. Shear stress maxima were found close to the cutting edge at levels corresponding to the shear flow strength of the sintered carbide.

Although all three modes of investigation, experimental, fractographic and stress analysis lead to the same conclusion, explaining breakage as brittle failure and chipping as ductile failure it is necessary to be very cautious in accepting these conclusions as absolute. Too many aspects were neglected like thermally induced stresses, anisotropy and nonhomogeneity of the sintered carbide and the three-dimensional nature of the stresses. It is quite possible that on a microscopic scale when considering the individual grains as distinct from the binder, tensile stresses could be found at the cutting edge. As well, adhesive forces could produce tensile stresses at the cutting edge. A large amount of work based on a multifaceted effort will be necessary to really clarify these phenomena. However, the conclusion presented here may remain valid to a good degree.

On the side of methodology an efficient method was presented in applying finite element analysis to a problem with various loads concentrated to one small area of the body.

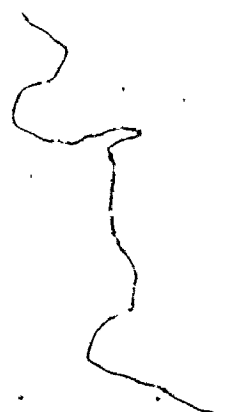
REFERENCES

1. H.L. Patts, "Understanding Micrograin Cemented Carbides", Proceedings of the 7th Carbide Cutting and Forming Seminar, McMaster University, Hamilton, Canada, June 1975.
2. H.S. Kalish, "Some Plain Talk about Carbides", Proceedings of the 7th Carbide Cutting and Forming Seminar, McMaster University, Hamilton, Canada, June 1975.
3. I.D. Murray, "The Titanium Carbide Coating Concept", Proceedings of the 7th Carbide Cutting and Forming Seminar, McMaster University, Hamilton, Canada, June 1975.
4. J. Tlusty, "Breakage of Carbide Tools", Proceedings of the 7th Carbide Cutting and Forming Seminar, McMaster University, Hamilton, Canada, June 1975.
5. G.S. Kreimer, "Strength of Hard Alloys", Scientific Research Institute for Hard Alloys, Moscow, translated from Russian, Consultants Bureau, New York, 1968.
6. T.N. LoLadze, "Requirements of Tool Materials", Proceedings of the 9th M.T.D.R. Conference, Manchester, England, 1968, Pergamon Press, Oxford.
7. Kals, H.J.J. and P.C. Veenstra, "Proposal for Cooperative Research on Testing and Classification of Cemented Carbide tool materials", Report WT0333, Eindhoven University of Technology, Presented at the meeting of the STC - 'Toughness', C.I.R.P., Kyoto, Japan, Aug. 1974.
8. I.F. Primus, "Beitrag zur Kenntnis der Spannungsverteilungen in den Kontaktzonen von Drehwerkzeugen", Dr.-Ing Dissertation, Tech. University Aachen, W. Germany, November, 1969.
9. Kals, H.J.J., Gielisse, P.J., 'The significance of structure parameters in failure of cemented carbides', Report WT0347, Eindhoven University of Technology, Published in the Annals of C.I.R.P. Vol. 24 (1975).
10. Shaw, M.C., Braiden, P.M., DeSalvo, G.J., ASME Paper No. 73-Wa/Prod-17 (1973).
11. Liebowitz, H., "Fracture", Vol. III Academic Press (1972).
12. Hatano, T., Int. J. of Fracture Mechanics, Vol. 5, 1 (1969) 73.

13. Brandes, M., Int. J. of Fracture Mechanics, Vol. 1, 1(1965)56.
14. Doi H. Fujiwara, Y., Oosawa, Y., Proc. of the Int. Conf. on Mech. Behaviour of Materials, Kyoto, Vol. V (1972)209.
15. Bridgman, P.W., Trans. Am. Soc. Metals, 32 (1943)553.
16. Kals, H.J.J. Nollet, W.A., "The Testing of Cemented Carbide Tools", Report WT0372, Eindhoven University of Technology, Presented at the meeting of the STC-subgroup "Toughness of tool materials", C.I.R.P., January 1976.
17. Okushima, K., Tetsutarō, H., 'Tool Fracture in Face-milling Operation", Kyoto University, Annals of the C.I.R.P. Vol. XV pp. 309-329 (1967).
18. M. Mahomed, M.Eng. Thesis "The finite element method used for the stress analysis of a diamond impregnated circular saw blade", McMaster University, July 1971.
19. A. Mason and P. Kenny, "The structure and fractography of cemented tungsten carbide", Metallurgia, December 1970.
20. S.B. Luyckx, "Microscopic aspects of fracture in WC-Co alloys", Department of Physics, University of the Witwatersrand, Johannesburg, South Africa, ACTA Metallurgica, Vol. 16, April 1968.
21. G.S. Kreimer and N.A. Alekseyeva, "Mechanism of fracture in sintered tungsten-cobalt carbides", Phys. of Metal and Metallography, 13, 117-121, 1962.
22. J.J. Emery, Associate Professor of Civil Engineering and Engineering Mechanics, McMaster University, Personal Communication, 1975.
23. J. Tlusty, MWRG Memorandum of December, 1975.
24. O.C. Zienkiewicz, "The Finite Element Method in Engineering Science", McGraw-Hill, 2nd Edition, 1971

APPENDIX A

ANALYSIS OF STRESSES USING THE
SINGLE STEP METHOD



APPENDIX A

The analysis of the problem by using the finite element technique will follow the following logic [24]:

1. The idealization of the structure is shown in Figure 46. Four hundred and forty triangular elements and two hundred and fifty four nodes are used for the mesh generation.
2. The geometric dimensions and elastic properties of the tool and tool holder are shown in Figure 46-b.
3. The boundary condition is defined by the fixity of the side which has nodes number 251, 252, 253 and 254. Therefore, the displacements of these nodes are zero.
4. This is a plane strain analysis problem. The elements used are constant-strain triangles.
5. The governing matrix equation for the analysis of this problem is given by:

$$[K] \{ \delta \} = \{ F \} \quad (A-1)$$

where the stiffness matrix $[K]$ is defined by the equation:

$$[K] = \sum_{e=1}^n [K]_e \quad (A-2)$$

The expression which defines the element stiffness matrix $[K]_e$ is given by the expression:

$$[K]_e = (\text{Area})_e \cdot (\text{thickness})_e \cdot \{B\}_e^T \cdot [D]_e \cdot \{B\}_e \quad (A-3)$$

The displacement strain matrix $\{B\}$ is defined by Equation (A-4). For a triangular element defined by the nodes i, j, m , the general matrix $\{B\}_e$ is written as:

$$\{B\}_e = \{C\} [A^{-1}] \quad (A-4)$$

where

$$\{C\} = \begin{bmatrix} 0 & 1 & 0 & 0 & 0 & 0 \\ 0 & 0 & -1 & 0 & 0 & 1 \\ 0 & 0 & 1 & 0 & 1 & 0 \end{bmatrix} \quad (A-5)$$

and

$$[A] = \begin{bmatrix} 1 & x_i & y_i & 0 & 0 & 0 \\ 1 & x_j & y_j & 0 & 0 & 0 \\ 1 & x_m & y_m & 0 & 0 & 0 \\ 0 & 0 & 0 & 1 & x_i & y_i \\ 0 & 0 & 0 & 1 & x_j & x_j \\ 0 & 0 & 0 & 1 & x_m & y_m \end{bmatrix} \quad (A-6)$$

and the inversion of $[A]$ is:

$$[A^{-1}] = \frac{1}{|A|} \begin{bmatrix} (x_j y_m - x_m y_j) & (x_m y_i - x_i y_m) & (x_i y_j - x_j y_i) & 0 & 0 & 0 \\ (y_i - y_m) & (y_m - y_i) & (y_i - y_j) & 0 & 0 & 0 \\ (x_m - x_j) & (x_i - x_m) & (x_j - x_i) & 0 & 0 & 0 \\ 0 & 0 & 0 & (x_j y_m - x_m y_j) & (x_m y_i - x_i y_m) & (x_i y_j - x_j y_i) \\ 0 & 0 & 0 & (y_j - y_m) & (y_m - y_i) & (y_i - y_j) \\ 0 & 0 & 0 & (x_m - x_j) & (x_i - x_m) & (x_j - x_i) \end{bmatrix}$$
(A-7)

and

$$|A| = |2 \text{ times the area of the element}|$$

$$= x_i(y_j - y_m) + x_j(y_m - y_i) + x_m(y_i - y_j) \quad (A-8)$$

The elasticity matrix for plane strain analysis problems is given by the expression:

$$[D_e]_e = \frac{E}{(1+\mu)(1-2\mu)} \begin{bmatrix} (1-\mu) & \mu & 0 \\ \mu & (1-\mu) & 0 \\ 0 & 0 & \frac{1-2\mu}{2} \end{bmatrix} \quad (A-9)$$

where E = Modulus of elasticity

μ = Poisson's ratio

The general nodal displacement matrix for this particular problem can be written as follows:

$$\{s\} = \begin{Bmatrix} u_1 \\ u_2 \\ \vdots \\ u_{254} \\ v_1 \\ v_2 \\ \vdots \\ v_{254} \end{Bmatrix} \quad (A-10)$$

The diagram shows a wavy line representing a tool profile. Nodes are marked along the profile at various points, with specific node numbers labeled: 1, 10, 19, 28, 37, 46, 55, 64, 73, 82, 91, and 109. The nodes are distributed such that they are concentrated at the peaks and troughs of the wave.

The external loads are applied only at the tip of the tool at nodes 1, 10, 19, 28, 37, 46, 55, 64, 73, 82, 91, 100 and 109 after calculation of the equivalent loads from the distributed load and these external loads are illustrated by the following matrix:

F_{x1}	19 0.0 " " "	node 1
F_{x10}	46.9 0.0 " " "	node 2
F_{x19}	56.0 0.0	node 19

$$\{F\} = \{ \quad , \quad \}, \quad (A-11)$$

F_{y1}	-75.0 0.0 " " "	node 1
F_{y10}	-187.5 0.0 " " "	node 10
F_{y19}	-225.0 0.0	node 19

6. The total stiffness matrix for the tool and tool holder is obtained by the superposition of the element stiffness matrices. The general form of the total matrix will be in the following form:

$$[K]_{\text{total}} = \begin{bmatrix} \Sigma K_{11} & \Sigma K_{1,254} & \Sigma K_{11} & \Sigma K_{1,254} \\ \Sigma K_{2,1} & \Sigma K_{22} & | & | \\ | & | & | & | \\ K_{UU} & | & | & K_{UV} \\ | & | & | & | \\ \Sigma K_{254,1} & \Sigma K_{254,254} & | & | \\ \Sigma K_{11} & \Sigma K_{1,254} & \Sigma K_{11} & | \\ \Sigma K_{21} & | & | & K_{VW} \\ | & | & | & | \\ K_{VU} & | & | & K_{VW} \\ | & | & | & | \\ \Sigma K_{2541} & | & | & \Sigma K_{254,254} \end{bmatrix} \quad (A-12)$$

508x508

7. The computation of the nodal displacement $\{\delta\}$ is based on the general equation:

$$\{\delta\} = [K^{-1}] \{F\} \quad (A-13)$$

The displacement matrix $\{\delta\}$ has 508 possible elements in which the elements $u_{251}, v_{251}, u_{252}, v_{252}, u_{253}, v_{253}, u_{254}$ and v_{254} are zero, due to the fixed boundary condition at

nodes 251, 252, 253 and 254 respectively. This will reduce the stiffness matrix [K] to 500 x 500 instead of 508 x 508. The remaining unknown displacements are computed by the use of Equation (A-13).

8. The calculation of the element strains are performed by the use of the equation:

$$\{\epsilon\} = [B]\{\delta\} \quad (A-14)$$

which relate strains to displacement.

9. The calculation of the element stresses are performed by the use of the equation:

$$\{\sigma\} = [D]\{\epsilon\} \quad (A-15)$$

Since all the values of the matrices are located at the right-hand side of the above equation, the stresses are readily obtained. The computations are done for each element.

The principal stresses and maximum shear stresses are also readily computed using expressions (A-16), (A-17) and (A-18).

$$\sigma_{\max} = \frac{\sigma_x + \sigma_y}{2} + \sqrt{\left(\frac{\sigma_x - \sigma_y}{2}\right)^2 + \tau_{xy}^2} \quad (A-16)$$

$$\sigma_{\min} = \frac{\sigma_x + \sigma_y}{2} - \sqrt{\left(\frac{\sigma_x - \sigma_y}{2}\right)^2 + \tau_{xy}^2} \quad (A-17)$$

$$\tau_{\max} = \frac{\sigma_{\max} - \sigma_{\min}}{2} \quad (A-18)$$

and the direction of principal stresses is given by the equation:

$$\tan 2\theta = \frac{-\tau_{xy}}{(\sigma_x - \sigma_y)/2} \quad (A-19)$$

APPENDIX B

RESULTING STRESSES IN THE CASE OF ZERO
RAKE ANGLE AND NO FLANK WEAR ($a=0.0$)

FIRST LINE FOR EACH NODE GIVES INCREMENT, SECOND GIVES TOTAL

NO.	X STRESS	Y STRESS	XY STRESS	MAX STRESS	MIN STRESS	MAX SH-STR	DIRECTION
1	-9147.0779	-94346.7912	18509.5098	-9207.6933	-98220.1821	40479.2444	11.1311
2	-9147.0779	-94346.7975	18509.50698	-9207.6933	-98220.1821	40479.2144	11.1017
3	-3013.0338	-91772.9476	13427.6978	-1026.9350	-93759.8428	40366.4249	0.4170
4	-3013.0338	-91772.9476	13427.6978	-1026.9350	-93759.8455	40366.4249	0.4170
5	-3090.0163	-94143.0366	14727.0360	-774.9184	-96460.1344	40845.6080	0.9308
6	-3090.0163	-94143.0366	14727.0360	-774.9184	-96460.1344	40845.6080	0.9308
7	-5526.8243	-94547.6655	17016.9029	-2386.0511	-97690.4387	47652.1933	10.4020
8	-5526.8243	-94547.6655	17016.9029	-2386.0511	-97690.4387	47652.1938	10.4020
9	-8213.4478	-95231.6117	18667.7599	-4377.7785	-99067.2810	47344.7512	11.6110
10	-8213.4478	-95231.6117	18667.7599	-4377.7785	-99067.2810	47344.7512	11.6110
11	-8744.1374	-97142.2567	19979.5807	-4438.1404	-101448.2936	48505.0566	12.1023
12	-8744.1374	-97142.2567	19979.5807	-4438.1404	-101448.2535	48505.0565	12.1023
13	-12374.4088	-97866.4757	20542.6966	-7694.4393	-102546.4452	47426.0030	12.6339
14	-12374.4088	-97866.4757	20542.6966	-7694.4393	-102546.4452	47426.0030	12.6339
15	-14566.6923	-98928.0907	21883.7917	-9246.6748	-104268.1083	47510.7168	13.7132
16	-14566.6923	-98928.0907	21883.7917	-9246.6748	-104268.1083	47510.7163	13.7132
17	-15780.7754	-98833.5916	22656.9963	-10001.9824	-104612.3846	47305.2011	14.3065
18	-15780.7754	-98833.5916	22656.9963	-10001.9824	-104612.3846	47305.2011	14.3065
19	-15822.1593	-99046.4812	23496.2427	-9646.8181	-105221.8224	47767.5022	14.7296
20	-15822.1593	-99046.4812	23496.2427	-9646.8181	-105221.8224	47767.5022	14.7296
21	-1959.9962	-89249.6701	12038.9187	-330.0369	-90879.6314	4274.7973	1.7104
22	-1959.9962	-89249.6701	12038.9187	-330.0369	-90879.6314	4274.7973	1.7104
23	-2290.3463	-94052.1666	13592.3070	-325.1889	-96023.3259	47843.0685	3.2515
24	-2290.3463	-94052.1666	13592.3070	-325.1889	-96023.3259	47843.0682	3.2515
25	-3716.8303	-98515.4746	16019.4486	-1082.9767	-101149.3262	50033.1737	9.3308
26	-3716.8303	-98515.4746	16019.4486	-1082.9787	-101149.3262	50033.1737	9.3308
27	-5948.6244	-97990.9507	17044.3646	-2893.7463	-101045.8288	49076.0412	10.1013
28	-5948.6244	-97990.9507	17044.3646	-2893.7463	-101045.8288	49076.0412	10.1013
29	-10400.3743	-99019.3249	16802.4174	-6976.0725	-102843.6268	48133.7771	11.4908
30	-10400.3743	-99019.3249	16802.4174	-6976.0725	-102843.6268	48133.7771	11.4908
31	-15831.2167	-98816.3982	20766.7045	-10924.5499	-103723.0650	40399.2576	13.2936
32	-15831.2167	-98816.3982	20766.7045	-10924.5499	-103723.0660	40399.2576	13.2936
33	-18361.2317	-99385.2366	22983.3851	-12295.7897	-105450.6760	46577.4445	14.7036
34	-18361.2317	-99385.2366	22983.3851	-12295.7897	-105450.6760	46577.4445	14.7036
35	-21160.9644	-99549.9506	23302.3246	-14447.6214	-106263.2935	42907.8361	15.8002
36	-21160.9644	-99549.9506	23302.3246	-14447.6214	-106263.2935	42907.8361	15.8002
37	-22454.4034	-100265.4492	25273.0602	-14966.3029	-107753.5497	46393.6234	16.5039
38	-22454.4034	-100265.4492	25273.0602	-14966.3029	-107753.5497	46393.6234	16.5039
39	-1780.5063	-86778.3508	11264.7857	-312.9209	-86245.9361	43966.5076	7.4227
40	-1780.5063	-86778.3508	11264.7857	-312.9209	-86245.9361	43966.5076	7.4227
41	-2060.0275	-89439.9447	12457.8136	-326.4603	-91181.5119	42427.5258	1.9502
42	-2060.0275	-89439.9447	12457.8136	-326.4603	-91181.5119	42427.5258	1.9502
43	-3577.9227	-98818.9892	14174.0026	-1513.2717	-100883.6402	49665.1042	8.2877
44	-3577.9227	-98818.9892	14174.0026	-1513.2717	-100883.6402	49665.1042	8.2877
45	-7232.1635	-99190.4422	14395.6970	-5031.2515	-101391.3542	46180.0013	5.6925
46	-7232.1635	-99190.4422	14395.6970	-5031.2515	-101391.3542	46180.0013	5.6925
47	-11540.4436	-99262.8451	18532.3051	-7790.5781	-103018.7106	47614.0562	11.4949
48	-11540.4436	-99262.8451	18532.3051	-7790.5781	-103018.7106	47614.0562	11.4949

25	-16969.4185	-99267.9618	20625.4353	-12089.6652	-104147.7151	40029.0250	13.3100
26	-20590.0831	-99415.8384	22525.2503	-14016.2004	-105399.2212	42391.3004	14.075
27	-24733.4581	-99683.6153	23749.0407	-14616.5004	-105399.2212	42391.3004	14.075
28	-27071.1516	-100384.4283	25269.9802	-17841.9000	-106575.1734	44366.6367	15.1318
	-27071.1516	-100384.4283	25269.9802	-19204.9752	-108250.6047	44522.8148	17.2300
29	-4753.5346	-88319.7105	10606.6152	-474.8643	-89600.3008	44502.7583	0.0047
30	-1753.2346	-88319.7105	10606.6152	-474.8643	-89600.3008	44502.7583	0.0047
31	-2440.3081	-90124.2559	11285.7567	-1010.2736	-91554.2905	42272.0004	1.2136
32	-3260.9403	-94410.8418	11572.0826	-1840.1369	-95857.0452	41008.7242	1.1200
33	-3260.9403	-94410.8416	11572.0826	-1840.1369	-95857.0452	41008.7242	1.1200
34	-6660.9653	-97923.8536	15286.4648	-4167.9267	-100416.8962	46124.4857	9.2015
35	-6660.9653	-97923.8540	15286.4648	-4107.9267	-100416.8962	46124.4857	9.2015
36	-11389.5997	-98297.1733	18009.2949	-7774.7751	-101911.9979	47068.6114	11.3007
	-11389.5997	-98297.1733	18009.2949	-7774.7751	-101911.9979	47068.6114	11.3007
37	-17391.4601	-97426.0587	21013.0932	-12209.5584	-102607.9624	42159.2030	13.6924
38	-22232.8469	-98582.7079	22485.2602	-16103.0079	-104712.5469	43304.7099	13.2432
39	-22232.8469	-98582.7079	22485.2602	-16103.0079	-104712.5469	43304.7099	13.2432
40	-26603.3908	-99294.0158	22943.9267	-19467.0338	-105934.7720	42963.2693	15.1307
41	-26603.3908	-99294.0158	22943.9267	-19467.0338	-105934.7728	42963.2693	15.1307
42	-29996.8342	-100261.7347	24901.7544	-22066.6970	-106191.6718	43062.5874	17.0644
43	-29996.8342	-100261.7347	24901.7544	-22066.6970	-108141.6718	43062.5874	17.0644
44	-1278.0185	-90005.1274	10388.3747	-77.9548	-91205.1911	45563.6181	0.5096
	-1278.0185	-40005.1274	10388.3747	-77.9548	-91205.1911	45563.6181	0.5096
45	-1777.0679	-91124.3477	11009.1562	-440.5387	-92460.8770	46010.1692	0.9219
46	-1777.0679	-91124.3477	11009.1562	-440.5387	-92460.8770	46010.1692	0.9219
47	-2773.4213	-94402.3899	12344.7214	-1139.4165	-96036.3947	47448.4891	1.6401
48	-2773.4213	-94402.3899	12344.7214	-1139.4165	-96036.3947	47448.4891	1.6401
49	-6156.4245	-95849.3053	15189.6197	-3653.8653	-98351.8645	47348.9990	3.3557
50	-6156.4245	-95849.3053	15189.6197	-3653.8653	-98351.8645	47348.9990	3.3557
51	-11236.2612	-95613.3558	18327.6850	-7427.2264	-99422.3906	45997.5821	11.7406
	-11236.2612	-95613.3558	18327.6850	-7427.2264	-99422.3906	45997.5821	11.7406
52	-17633.5850	-92334.1602	21457.4138	-12095.4499	-98072.3033	42986.4267	1.4.917
53	-17633.5850	-92334.1602	21457.4138	-12095.4499	-98072.3033	42986.4267	1.4.917
54	-22627.5737	-93105.1403	24247.1415	-15091.4144	-100641.2997	42774.9420	17.2026
55	-22627.5737	-93105.1403	24247.1415	-15091.4144	-100641.2997	42774.9420	17.2026
56	-28600.8660	-94275.9216	26370.1804	-19328.5379	-103554.2497	42112.6559	19.3344
57	-28600.8660	-94275.9216	26370.1804	-19328.5379	-103554.2497	42112.6559	19.3344
58	-32245.5676	-100994.2754	26333.7921	-23317.9030	-109921.9400	43302.0185	13.1210
	-32245.5676	-100994.2754	26333.7921	-23317.9030	-109921.9400	43302.0185	13.1210
59	-1086.4066	-91206.9997	10465.0649	112.8679	-92406.2742	40254.5110	0.0315
60	-1086.4066	-91206.9997	10465.0649	112.8679	-92406.2742	40254.5110	0.0315
61	-1477.5654	-91190.0998	11014.1965	-145.1188	-92522.5464	40188.7138	0.0315
62	-1477.5654	-91190.0998	11014.1965	-145.1188	-92522.5464	40188.7138	0.0315
63	-2672.2600	-93305.8886	12562.1160	-963.3322	-95014.8163	47025.7420	2.7409
64	-2672.2600	-93305.8886	12562.1160	-963.3322	-95014.8163	47025.7420	2.7409
65	-5741.2780	-93451.4848	15370.0635	-3125.8644	-96066.8964	46470.5170	9.6211
	-5741.2780	-93451.4848	15370.0635	-3125.8644	-96066.8964	46470.5170	9.6211
66	-11099.1706	-91609.5330	18319.0687	-7126.8955	-95581.8061	44227.4563	12.2343
67	-11099.1706	-91609.5330	18319.0687	-7126.8955	-95581.8061	44227.4563	12.2343

52	-16281.0988	-81087.4144	17949.9146	-11990.6423	-41377.8708	39693.6143	13.4420
53	-20361.3902	-84506.5530	18755.7848	-15279.8340	-89588.1092	37154.1376	13.1594
54	-20361.3902	-84506.5530	18755.7848	-15279.8340	-89588.1092	37154.1376	13.1394
54	-24160.3078	-80602.4451	19320.0225	-18198.8676	-86683.8853	34192.5069	11.2024
54	-24160.3078	-80602.4451	19320.0225	-18198.8676	-86683.8853	34192.5069	11.2024
55	-28481.6190	-80196.2474	23616.9448	-19319.4989	-89358.3675	3019.4343	21.2036
56	-28481.6190	-80196.2474	23616.9448	-19319.4989	-89358.3675	3019.4343	21.2036
56	-971.5564	-91534.3871	10676.9778	270.1884	-92776.1319	40523.1001	0.6338
56	-971.5564	-91534.3871	10676.9778	270.1884	-92776.1319	40523.1001	0.6330
57	-1167.5833	-90584.9020	11207.9610	215.8075	-91968.3526	40092.1101	1.0301
57	-1167.5833	-90584.9020	11207.9610	215.8075	-91968.3526	40092.1101	1.0307
58	-2487.4462	-91470.4907	12607.9073	-680.6095	-93277.3274	40298.3589	3.0298
58	-2487.4462	-91470.4907	12607.9073	-680.6095	-93277.3274	40298.3589	3.0296
59	-5182.7023	-90373.0592	15420.1693	-2474.7061	-93081.0554	42303.1740	3.9523
60	-5182.7023	-90373.0592	15420.1693	-2474.7061	-93081.0554	42303.1740	3.9523
60	-9587.5880	-87734.6675	16915.6822	-6083.1779	-91239.0776	42577.9499	11.703
61	-14470.2884	-87830.8888	17828.2084	-10367.1430	-91934.0343	40783.4456	12.9008
61	-14470.2884	-87830.8888	17828.2084	-10367.1430	-91934.0343	40783.4456	12.9609
62	-20775.7806	-89503.1879	17474.0776	-16588.1222	-93690.8463	38551.3020	13.4706
62	-20775.7806	-89503.1879	17474.0776	-16588.1222	-93690.8463	38551.3020	13.4706
63	-28866.5870	-90695.3775	17202.1645	-24421.5509	-95160.4056	35364.4234	14.2207
63	-28866.5870	-90695.3775	17202.1645	-24421.5509	-95160.4056	35364.4234	14.2207
64	-32009.9404	-87958.3763	15030.1700	-20227.6536	-91740.4629	31756.3046	14.123
64	-32009.9404	-87958.3763	15030.1700	-20227.6536	-91740.4629	31756.3046	14.123
65	-816.2174	-90538.5819	11106.2757	536.1204	-91892.9277	40215.5260	0.9920
65	-816.2174	-90538.5819	11106.2757	536.1204	-91892.9277	40215.5260	0.9920
66	-800.4517	-88966.3903	11664.9952	710.9013	-90483.7434	45597.3224	7.4113
66	-800.4517	-88966.3903	11664.9952	710.9013	-90483.7434	45597.3224	7.4113
67	-2057.0296	-88930.1699	13249.5304	-81.2041	-90902.9954	42412.3957	0.4817
67	-2057.0296	-88930.1699	13249.5304	-81.2041	-90902.9954	42412.3957	0.4817
68	-3653.0641	-86769.8660	15707.0000	-97.4.052	-89643.5249	44334.0550	10.3744
68	-3653.0641	-86769.8660	15707.0000	-97.4.052	-89643.5249	44334.0550	10.3744
69	-7489.9796	-85324.5765	17654.6996	-3289.6834	-89224.8727	42617.5947	12.3225
69	-7489.9796	-85324.5765	17654.6996	-3289.6834	-89224.8727	42617.5947	12.3225
70	-11937.7870	-81019.2639	21416.5301	-5837.0396	-87120.0113	40641.4653	13.9002
70	-11937.7870	-81019.2639	21416.5301	-5837.0396	-87120.0113	40641.4653	13.9002
71	-17669.6421	-82758.2026	21356.3367	-11288.2324	-89139.6090	30925.7887	10.630
71	-17669.6421	-82758.2026	21356.3367	-11288.2324	-89139.6090	30925.7887	10.630
72	-26677.0251	-83769.5844	20955.8599	-19811.6262	-90635.7833	32412.0783	10.1414
72	-26677.0251	-83769.5844	20955.8599	-19811.6262	-90635.7833	32412.0783	10.1414
73	-37336.3032	-90526.5220	22460.3677	-20784.9524	-94074.8728	35147.4602	20.4124
73	-37336.3032	-90526.5220	22460.3677	-20784.9524	-94074.8728	35147.4602	20.4124
74	-641.7088	-88316.9650	11871.7822	933.4349	-89896.1059	42414.7719	1.5708
74	-641.7088	-88316.9650	11871.7822	933.4349	-89896.1059	42414.7719	1.5708
75	-430.2071	-86132.5204	12533.3420	1365.0302	-87927.8295	44646.4329	8.1517
75	-430.2071	-86132.5204	12533.3420	1365.0302	-87927.8295	44646.4329	8.1517
76	-1380.2901	-84961.6470	14266.6261	986.2520	-87336.4861	44161.5205	9.4318
76	-1380.2901	-84961.6470	14266.6261	986.2520	-87336.4861	44161.5205	9.4318
77	-2219.1349	-81632.0260	12344.4470	1116.3426	-85267.5055	43191.9241	11.0301
77	-2219.1349	-81632.0260	12344.4470	1116.3426	-85267.5055	43191.9241	11.0301
78	-5022.7203	-77456.5779	20659.5020	-219.1941	-83090.1041	41435.4550	13.1133
78	-5022.7203	-77456.5779	20659.5020	-219.1941	-83090.1041	41435.4550	13.1133

79	-9372.3246	-67743.1813	23750.7179	-929.4946	-76186.0113	37628.2583	19.5641
80	-14973.2700	-69104.6995	22794.0386	-6053.4037	-77424.5658	33365.5610	20.0518
81	-14973.2700	-69104.6995	22794.0386	-6653.4037	-77424.5658	33365.5610	20.4218
	-21063.4089	-68671.2160	20686.3064	-13329.5280	-76403.0969	31537.7044	20.4912
82	-30752.6895	-74600.8427	21487.7856	-21978.5652	-83375.1670	30698.3009	22.2122
	-30752.6895	-74600.8427	21487.7856	-21978.5652	-83375.1670	30698.3009	22.2122
83	-777.0160	-84955.2246	12782.7567	1121.2821	-86853.5227	43467.4024	0.4433
84	-331.9847	-82219.3245	13639.2114	1860.0193	-84431.3260	43155.6740	0.2120
	-331.9847	-82219.3245	13639.2114	1860.0193	-84431.3260	43155.6740	0.2120
85	-1076.6129	-79749.1847	15817.4841	1984.4619	-82810.2592	42397.3607	10.9728
86	-1076.6129	-79749.1847	15817.4841	1984.4619	-82810.2592	42397.3607	10.9728
87	-2025.4912	-74326.2976	19531.5129	2913.4166	-79262.2074	41089.3130	14.1306
	-2025.4912	-74326.2976	19531.5129	2913.4166	-79265.2074	41089.3130	14.1306
88	-486.4652	-66267.0675	22921.2078	2746.0909	-73879.0230	33313.8273	10.3723
	-486.4652	-66267.0675	22921.2078	2748.0909	-73879.0230	33313.8273	10.3723
89	-6909.5370	-52280.7180	24299.3807	3047.8595	-52838.1109	33242.9830	23.4830
	-6909.5370	-52280.7180	24299.3807	3047.8595	-52838.1109	33242.9830	23.4830
90	-9899.2975	-52036.7045	22598.9077	96.6401	-61832.9421	30964.7911	23.4329
	-9899.2975	-52036.7045	22598.9077	96.6401	-61832.9421	30964.7911	23.4329
91	-13406.4159	-52226.5764	19135.6148	-5259.8826	-60073.1095	27256.6133	22.2900
	-13406.4159	-52226.5764	19135.6148	-5259.8826	-60073.1095	27256.6133	22.2900
92	-19113.3738	-57270.7837	18363.3361	-11711.7258	-64672.4317	20460.03530	21.9221
	-19113.3738	-57270.7837	18363.3361	-11711.7258	-64672.4317	20460.03530	21.9221
93	-1126.6715	-80157.1737	13670.5866	1171.2333	-82455.0765	41813.1559	3.4417
	-1126.6715	-80157.1737	13670.5866	1171.2333	-82455.0765	41813.1559	3.4417
94	-233.6033	-77205.3576	14956.3145	2522.0391	-60011.0549	41266.5392	10.0240
	-233.6033	-77205.3576	14956.3145	2522.0391	-60011.0549	41266.5392	10.0240
95	-902.0506	-73144.8265	14426.0539	3081.9592	-7128.8364	40102.3370	12.0714
	-902.0506	-73144.8265	14426.0539	3081.9592	-7128.8364	40102.3370	12.0714
96	-2072.4102	-65017.4102	21074.1950	4331.7311	-71421.5514	31876.6112	10.9035
	-2072.4102	-65017.4102	21074.1950	4331.7311	-71421.5514	31876.6112	10.9035
97	-4734.6369	-53365.0756	23402.1675	4645.9975	-62805.7120	33122.8947	21.9056
	-4734.6369	-53365.0756	23402.1675	4645.9975	-62805.7120	33122.8947	21.9056
98	-5001.0780	-34291.5502	22431.0210	5401.036	-16063.0317	26035.6117	20.0636
	-5001.0780	-34291.5502	22431.0210	5401.036	-16063.0317	26035.6117	20.0636
99	-5206.2420	-32177.4586	21299.0349	6436.1124	-43882.3129	27224.4621	20.0311
	-5206.2420	-32177.4586	21299.0349	6436.1124	-43882.3129	27224.4621	20.0311
100	-2221.8426	-31134.0041	10245.4962	6600.3155	-34950.1621	23278.2368	2.0049
	-2221.8426	-31134.0041	10245.4962	6600.3155	-34950.1621	23278.2368	2.0049
101	-4160.4383	-38343.9248	15722.5034	1900.0323	-74470.3954	23221.2133	21.3014
	-4160.4383	-38343.9248	15722.5034	1900.0323	-74470.3954	23221.2133	21.3014
102	-2332.8551	-75123.9886	14022.5510	275.0295	-77731.08734	39003.4515	10.5314
	-2332.8551	-75123.9886	14022.5510	275.0295	-77731.08734	39003.4515	10.5314
103	-1423.1051	-71216.9674	15586.0933	1899.6844	-74539.7569	30219.7206	12.0341
	-1423.1051	-71216.9674	15586.0933	1899.6844	-74539.7569	30219.7206	12.0341
104	-1839.2538	-63480.5775	18487.5339	3260.3416	-68600.1731	32940.2274	10.4755
	-1839.2538	-63480.5775	18487.5339	3260.3416	-68600.1731	32940.2274	10.4755
105	-3646.6947	-50858.1380	20671.3505	4257.0061	-56761.8387	31509.4224	20.410
	-3646.6947	-50858.1380	20671.3505	4257.0061	-56761.8387	31509.4224	20.410
106	-5662.9741	-35574.4901	20620.0913	4854.7022	-46092.1664	29473.4343	21.0236
	-5662.9741	-35574.4901	20620.0913	4854.7022	-46092.1664	29473.4343	21.0236

106	-2210.5256	-16980.3513	15017.4983	7139.0203	-26330.4972	16735.0583	31.90/1
107	-2210.5256	-16980.3513	15017.4983	7139.0203	-26330.4972	16735.0588	31.90/1
108	-2210.5256	-12684.1865	13028.4777	8848.5152	-20567.1375	14707.8263	31.1702
109	-2210.5256	-12684.1865	13028.4777	8848.5152	-20567.1375	14707.8263	31.1702
110	-2210.5256	-10014.0971	10555.0425	11893.4386	-15099.5126	13496.4757	22.7247
111	-2210.5256	-10014.0971	10555.0425	11893.4386	-15099.5126	13496.4757	22.7247
112	-2210.5256	-12625.7208	9796.2743	15041.9831	-16094.2771	15568.1301	19.4975
113	-2210.5256	-12625.7208	9796.2743	15041.9831	-16094.2771	15568.1301	19.4975
114	-2210.5256	-65446.2479	12334.8930	-380.8265	-67784.6572	33701.9153	10.7346
115	-2210.5256	-65446.2479	12334.8930	-380.8265	-67784.6572	33701.9153	10.7346
116	-3258.3754	-62017.2835	15346.5239	508.3355	-65783.9423	33146.1629	13.7403
117	-3258.3754	-62017.2835	15346.5239	508.3355	-65783.9423	33146.1523	13.7403
118	-4435.4220	-47195.1111	17987.4492	2124.7779	-53755.3110	24940.0445	20.0314
119	-4435.4220	-47195.1111	17987.4492	2124.7779	-53755.3110	24940.0445	20.0314
120	-5683.2550	-34048.0422	16595.0043	3521.1901	-43252.4674	23388.6368	22.0314
121	-5683.2550	-34048.0422	16595.0043	3521.1901	-43252.4674	23388.6368	22.0314
122	-4973.7968	-19616.7725	15104.8150	4490.4122	-29080.9815	15765.6968	332.0700
123	-4973.7968	-19616.7725	15104.8150	4490.4122	-29080.9815	15765.6968	332.0700
124	1732.1639	-7926.2221	7680.0173	5975.1135	-12164.1717	4042.1426	23.9192
125	1732.1639	-7926.2221	7680.0173	5975.1135	-12164.1717	4042.1426	23.9192
126	6777.5911	-4508.1825	4945.4985	6638.0454	-6368.6367	7030.3411	20.6179
127	6777.5911	-4508.1825	4945.4985	6638.0454	-6368.6367	7030.3411	20.6179
128	13497.2857	-2647.4180	2761.6670	13956.6265	-3106.7588	6531.6926	3.4433
129	13497.2857	-2647.4180	2761.6670	13956.6265	-3106.7588	6531.6926	3.4433
130	19157.6121	-1359.7006	76.2397	19157.8954	-1359.9639	10258.9397	2129
131	19157.6121	-1359.7006	76.2397	19157.8954	-1359.9639	10258.9397	2129
132	-1868.9007	-51175.0693	10540.6837	289.9635	-53333.9334	20811.9484	11.5718
133	-1868.9007	-51175.0693	10540.6837	289.9635	-53333.9334	20811.9484	11.5718
134	-3404.4847	-48084.2947	13695.9704	4599.6360	-151948.4154	26204.0257	13.1720
135	-3404.4847	-48084.2947	13695.9704	4599.6360	-151948.4154	26204.0257	13.1720
136	-5299.9358	-34735.7045	16054.4328	1765.6943	-41601.3346	21783.5145	23.7419
137	-5299.9358	-34735.7045	16054.4328	1765.6943	-41601.3346	21783.5145	23.7419
138	-6210.4346	-22761.7536	14956.2176	2607.0327	-31579.2209	17093.1209	30.5215
139	-6210.4346	-22761.7536	14956.2176	2607.0327	-31579.2209	17093.1209	30.5215
140	-3397.2299	-10442.4941	9912.8012	3600.2409	-17439.9649	10520.1029	3.2103
141	-3397.2299	-10442.4941	9912.8012	3600.2409	-17439.9649	10520.1029	3.2103
142	3295.6787	-3411.9731	3878.1707	5069.0700	-5185.3644	5127.2172	24.0734
143	3295.6787	-3411.9731	3878.1707	5069.0700	-5185.3644	5127.2172	24.0734
144	8573.2557	-1670.3532	1223.8396	6717.4426	-1814.5400	5269.9913	0.0193
145	8573.2557	-1670.3532	1223.8396	6717.4426	-1814.5400	5265.9913	0.0193
146	15319.8817	-692.5558	227.8126	15323.1222	-695.7963	8009.4593	0.0193
147	15319.8817	-692.5558	227.8126	15323.1222	-695.7963	8009.4593	0.0193
148	21175.0396	258.7009	-1578.1955	21293.4465	140.2920	10576.5763	-4.2307
149	21175.0396	258.7009	-1578.1955	21293.4465	140.2920	10576.5763	-4.2307
150	-2120.9243	-40983.3601	9280.4142	-18.5153	-43085.7991	21533.6119	12.0707
151	-2120.9243	-40983.3601	9280.4142	-18.5153	-43085.7991	21533.6119	12.0707
152	-3348.1773	-37418.7246	12094.2926	508.4724	-41275.3142	20691.9233	17.0566
153	-3348.1773	-37418.7246	12094.2926	508.4724	-41275.3142	20891.9233	17.0566
154	-5517.1509	-25818.1804	13462.9014	1193.0163	-32528.3490	15830.6540	20.4422
155	-5517.1509	-25818.1804	13462.9014	1193.0163	-32528.3490	15830.6540	20.4422

131	-5664.7037	-14883.1947	11522.1005	2160.3161	-22713.2145	12436.7053	34.1234
132	-2285.5763	-5808.4508	6777.9411	2950.1160	-11050.1432	1003.1290	37.712
133	-2285.5763	-5808.4508	6777.9411	2950.1160	-11050.1432	1003.1290	37.712
134	3187.8060	-1056.6855	2442.2045	4722.7429	-2991.6224	3657.1829	20.9481
135	3187.8060	-1666.6855	2442.2045	4722.7429	-2991.6224	3657.1525	20.9481
136	8019.1180	-576.8754	256.4006	8026.2047	-584.0221	605.1+34	1.2302
137	8019.1180	-576.8754	256.4006	8026.2047	-584.0221	605.1454	1.2302
138	14212.6566	-204.8750	341.1922	14220.7284	-212.9447	216.8360	-1.3249
139	14212.6566	-204.8750	341.1922	14220.7284	-212.9449	216.8360	-1.3249
140	19317.5411	317.4746	-1316.0574	19406.2659	226.7498	3590.7560	-3.9+35
141	19317.5411	317.4746	-1316.0574	19406.2659	226.7498	3590.7560	-3.9+35
142	-1472.6037	-32387.5965	7715.1233	345.6278	-34206.0260	17275.8273	13.2024
143	-1472.6037	-32387.5965	7715.1233	345.6278	-34206.0260	17275.8274	13.2024
144	-3466.0469	-29161.3842	10041.2156	-25.5031	-32621.9330	16298.2149	19.0117
145	-3466.0469	-29161.3842	10041.2156	-25.5031	-32621.9330	16298.2149	19.0117
146	-5530.2161	-18272.7939	11196.4488	960.7987	-24783.8108	12062.3047	30.1741
147	-5530.2161	-18272.7939	11196.4488	960.7987	-24783.8108	12062.3047	30.1741
148	-5124.6465	-9843.3634	9208.4185	2021.7079	-16969.9678	5505.8370	37.0116
149	-5124.6465	-9843.3634	9208.4185	2021.7079	-16969.9678	5505.8370	37.0116
150	-5124.6465	-9843.3634	9208.4185	2021.7079	-16969.9678	5505.8370	37.0116
151	-1896.2347	-3992.8490	5337.0826	2614.6750	-8303.7602	5459.2160	30.9266
152	-1896.2347	-3992.8490	5337.0826	2614.6750	-8303.7602	5459.2160	30.9266
153	-925.6719	-925.7832	1681.7579	4919.3469	-1535.4582	3227.4026	17.0305
154	-925.6719	-925.7832	1681.7579	4919.3469	-1535.4582	3227.4026	17.0305
155	8751.0459	-192.9180	189.2819	0755.0499	-196.9220	4475.9859	1.2118
156	8751.0459	-192.9180	189.2819	0755.0499	-196.9220	4475.9859	1.2118
157	13048.9132	-84.9953	-273.1786	13054.5906	-95.6721	5575.1310	-1.1906
158	13048.9132	-84.9953	-273.1786	13054.5906	-95.6721	5575.1310	-1.1906
159	16914.4378	141.5827	-919.1202	16964.6534	91.3670	8430.6432	-5.122
160	16914.4378	141.5827	-919.1202	16964.6534	91.3670	8430.6432	-5.122
161	-575.0068	-24113.1054	6558.5553	1034.8060	-25823.7801	13429.2930	14.6117
162	-575.0068	-24113.1054	6558.5553	1034.8060	-25823.7801	13429.2930	14.6117
163	-2021.4506	-21598.1988	6357.6467	1061.1700	-24680.8202	12670.9950	23.2429
164	-2021.4506	-21598.1988	6357.6467	1061.1700	-24680.8202	12670.9950	23.2429
165	-4663.9011	-13068.6229	9562.4084	1438.9700	-19371.5020	10405.2400	33.3901
166	-4663.9011	-13068.6229	9562.4084	1438.9700	-19371.5020	10405.2400	33.3901
167	-4622.5283	-6971.9053	7614.7415	2110.2633	-13704.6974	907.4006	40.7264
168	-4622.5283	-6971.9053	7614.7415	2110.2633	-13704.6974	907.4006	40.7264
169	-940.1814	-2606.5737	4266.6569	2825.2964	-6378.0515	601.6739	39.6031
170	-940.1814	-2606.5737	4266.6569	2825.2964	-6378.0515	601.6739	39.6031
171	4147.9717	-388.2473	1702.3255	4115.7453	-956.0206	2635.6031	10.4410
172	4147.9717	-388.2473	1702.3255	4115.7453	-956.0206	2635.6031	10.4410
173	8585.7331	82.6218	176.8764	8589.4108	78.9441	4255.2333	1.1911
174	8585.7331	82.6218	176.8764	8589.4108	78.9441	4255.2333	1.1911
175	12296.7738	3.0640	-190.5524	12299.7266	1112	6149.8077	-0.0618
176	12296.7738	3.0640	-190.5524	12299.7266	1112	6149.8077	-0.0618
177	15560.5247	179.5067	-504.0277	15566.6602	157.3732	1112.6435	-2.1705
178	15560.5247	179.5067	-504.0277	15566.6602	157.3732	1112.6435	-2.1705
179	-2735.7450	-18623.9715	5699.3549	-957.1235	-20462.5430	972.7347	17.0750
180	-2735.7450	-18623.9715	5699.3549	-957.1235	-20462.5430	972.7347	17.0750
181	-2223.9240	-15030.8519	7126.4303	573.0686	-16928.4444	971.0.056+	23.0099
182	-2223.9240	-15030.8519	7126.4303	573.0686	-16928.4444	971.0.0564	23.0099
183	-4554.0044	-9853.1299	8251.4992	1593.9804	-15801.1147	6697.5716	33.1024
184	-4554.0044	-9853.1299	8251.4992	1593.9804	-15801.1147	6697.5716	33.1024

156	-4093.6899	-5499.3333	6662.3889	1922.7336	-11515.7606	9719.2472	41.9500
157	-4093.6899	-5499.3333	6662.3889	1922.7336	-11515.7606	6719.2472	41.9500
158	-671.3600	-2024.0597	4071.0465	2779.3969	-547.6166	4121.5061	70.2012
159	-671.3600	-2024.0597	4071.0465	2779.3969	-547.6166	4121.5061	70.2012
160	4133.3465	-235.2740	1690.9326	4713.1564	-813.0634	2113.1212	10.0000
161	4133.3465	-235.2740	1690.9326	4713.1564	-813.0634	2113.1212	10.0000
162	6070.4819	7.5657	390.4676	6089.3472	-11.2996	4050.3234	2.0012
163	6070.4819	7.5657	390.4676	6089.3472	-11.2996	30.0.3234	2.0012
164	11792.4311	-104.0598	-37.5765	11792.5468	-104.0598	3540.0.641	-1.0010
165	11792.4311	-104.0598	-37.5765	11792.5468	-104.0598	3540.0.641	-1.0010
166	14285.8271	16.0.3243	-49.4.1944	14602.7440	151.4122	222.6660	-1.9001
167	1445.6639	-14633.0322	4629.4135	17.2102	-1609.9096	8055.0.5000	1.0.5303
168	1445.6639	-14633.0322	4629.4135	17.2102	-1609.9096	8055.0.5000	1.0.5303
169	-2754.2470	-13093.9855	5874.2167	-96.9010	-15749.3315	7822.2112	24.3240
170	-2754.2470	-13093.9855	5874.2167	-96.9010	-15749.3315	8025.2152	24.3240
171	-4278.3481	-8102.9883	6664.4618	935.1864	-13316.5228	7125.8940	37.2105
172	-4278.3481	-8102.9883	6664.4618	935.1864	-13316.5228	1125.8940	37.2105
173	-4142.5469	-4092.8130	5714.9934	1597.3672	-9832.2118	2715.0410	4.0.1210
174	-4142.5469	-4092.8130	5714.9934	1597.3672	-9832.2118	2715.0410	4.0.1210
175	-911.0745	-1817.8205	3654.7669	2318.3324	-5047.224	3682.7.49	41.0.643
176	-911.0745	-1817.8205	3654.7669	2318.3324	-5047.2274	3682.7.49	41.0.643
177	4013.6151	-2.2560	1955.0603	4808.7481	-797.3909	2803.0.0695	22.1230
178	4013.6151	-2.2560	1955.0603	4808.7481	-797.3909	2803.0.0695	22.1230
179	7828.2326	116.4413	781.1293	7906.5579	38.1160	3934.2209	2.0.1230
180	7828.2326	116.4413	781.1293	7906.5579	38.1160	3934.2209	2.0.1230
181	11428.5017	-74.6.6802	338.4582	11438.4515	-84.6.6300	5761.5408	1.0.639
182	11428.5017	-74.6.6802	338.4582	11438.4515	-84.6.6300	5761.5408	1.0.639
183	13970.2142	155.2711	-187.7873	13972.7663	152.7190	6910.0237	-0.700
184	13970.2142	155.2711	-187.7873	13972.7663	152.7190	6910.0237	-0.700
185	-1003.4282	-10299.9731	3979.9974	467.6797	-11771.0610	6119.3803	20.2006
186	-1003.4282	-10299.9731	3979.9974	467.6797	-11771.0610	119.3803	20.2006
187	-2074.0537	-9885.3400	5265.0.909	576.3347	-12532.7284	056.0.315	20.1175
188	-2074.0537	-9885.3400	5265.0.909	576.3347	-12532.7284	556.0.315	20.1175
189	-3385.9639	-6414.3822	6210.7264	1492.4752	-11292.8213	6392.6462	33.1431
190	-3385.9639	-6414.3822	6210.7264	1492.4752	-11292.8213	2392.6462	33.1431
191	-3733.8005	-3152.3227	5141.4387	1706.5910	-8592.7141	5149.6526	40.0.102
192	-3733.8005	-3152.3227	5141.4387	1706.5910	-8592.7141	5149.6526	40.0.102
193	-603.6401	-548.1693	3259.4838	2566.0811	-3937.8905	3261.9858	40.1221
194	-603.6401	-548.1693	3259.4838	2566.0811	-3937.8905	3261.9858	40.1221
195	3609.8378	-220.1178	2278.8725	4669.9719	-1280.2515	2975.1115	2.0.9071
196	3609.8378	-220.1178	2278.8725	4669.9715	-1280.2515	2975.1115	2.0.9071
197	7840.1119	-120.9779	1060.2519	7782.3475	-263.2135	4022.7803	7.0.6408
198	7840.1119	-120.9779	1060.2519	7782.3475	-263.2135	4022.7803	7.0.6408
199	11300.1400	-200.5826	551.1961	11326.4966	-226.9393	776.7181	2.0.377
200	11300.1400	-200.5826	551.1961	11326.4966	-226.9395	776.7181	2.0.377
201	14042.8349	117.6841	-20.4958	14042.8665	117.6525	0962.6070	-0.004
202	14042.8349	117.6841	-20.4958	14042.8665	117.6525	0962.6070	-0.004
203	-1170.9387	-5112.9072	2849.4149	322.7480	-6606.5939	3464.6709	27.0.034
204	-1170.9387	-5112.9072	2049.4149	322.7480	-6606.5939	3464.6709	27.0.034
205	-1600.6254	-5761.8466	4479.5700	1215.3887	-8637.8526	4926.6167	32.0.016
206	-1600.6254	-5761.8466	4479.5700	1215.3887	-8637.8526	4926.6167	32.0.016
207	-2741.4406	-3935.5756	5184.0509	2476.2777	-9153.2941	2814.7659	42.0.032
208	-2741.4406	-3935.5756	5184.0509	2476.2777	-9153.2941	2814.7659	42.0.032
209	-2725.7262	-2100.2171	5370.3514	2966.4790	-7792.4223	2379.4507	40.0.605
210	-2725.7262	-2100.2171	5370.3514	2966.4790	-7792.4223	2379.4507	40.0.605

186	-1051.9176	-775.7938	3801.0985	2840.3488	-4716.0603	3804.2046	40.0334
187	4051.7476	-353.1754	2204.3279	4968.8460	-1270.3239	3119.0100	22.5446
188	7700.7049	-165.2873	1142.4865	7877.5120	-342.0944	4104.8032	8.4331
189	7700.7049	-165.2873	1142.4865	7877.5120	-342.0944	4104.8032	8.4331
190	11438.5414	-186.3696	675.3980	11537.4504	-225.2766	2881.3049	3.2311
191	11439.5414	-186.3696	675.3980	11537.4504	-225.2766	2881.3045	3.2311
192	14210.0567	96.4834	64.4251	14210.3508	96.1893	7057.0008	2017
193	14210.0567	96.4834	64.4251	14210.3508	96.1893	7057.0008	2017
194	-862.4774	-1378.2966	1338.6711	242.9023	-2483.6764	1363.2693	34.2416
195	-862.4774	-1378.2968	1338.6711	242.9023	-2483.6764	1363.2693	34.2416
196	-2073.2341	-1808.6363	2887.2876	946.9973	-4833.8678	2690.4325	40.3305
197	-2073.2341	-1808.6363	2887.2876	946.9973	-4833.8678	2690.4325	40.3305
198	-3057.3398	-1728.1445	5213.2910	2862.7372	-7648.2265	3255.4813	43.0324
199	-2541.7589	-1031.7298	5362.1009	3628.2567	-7201.7455	2415.0011	43.0014
200	-2541.7589	-1031.7298	5362.1009	3628.2567	-7201.7455	2415.0011	43.0014
201	-690.6318	-779.9081	4561.7941	3726.6001	-5397.4000	4562.1300	42.3470
202	-690.6318	-779.9081	4561.7941	3726.6001	-5397.4000	4562.1300	42.3470
203	1697.2521	-388.6890	3084.6466	3904.1637	-2602.5962	3255.0801	32.6017
204	1697.2521	-388.6890	3084.6466	3904.1637	-2602.5962	3255.0801	32.6017
205	5089.3723	-797.7520	2358.0979	5917.4390	-1025.8167	3771.6268	19.3432
206	5089.3723	-797.7520	2358.0979	5917.4390	-1025.8167	3771.6268	19.3432
207	8041.0488	-699.9433	1354.5799	8247.6362	-9005.5308	577.0535	3.4400
208	8041.0488	-699.9433	1354.5799	8247.6362	-9005.5308	577.0535	3.4400
209	11611.7529	-681.8954	680.9055	11048.7019	-918.9044	223.8332	3.1107
210	11611.7529	-681.8954	680.9055	11048.7019	-918.9044	223.8332	3.1107
211	14568.2376	56.2276	60.7956	14508.4923	59.9729	7256.2551	2400
212	14568.2376	56.2276	60.7956	14508.4923	59.9729	7256.2297	2400
213	-2089.1000	-1193.7003	779.5594	0000	-1702.6003	851.4002	35.1470
214	-2089.1000	-1193.7003	779.5594	0000	-1702.6003	851.4002	35.1470
215	-674.8756	-653.8590	1191.4420	327.1159	-2052.6607	1191.4063	52.2525
216	-674.8756	-653.8590	1191.4420	327.1159	-2052.6607	1191.4063	52.2525
217	-853.8690	1191.4420	327.1159	-2055.6607	1191.4883	42.2225	
218	-4265.4953	-445.5267	2363.7925	699.0752	-5410.0952	3054.5812	64.3515
219	-4265.4953	-445.5267	2383.7925	699.0752	-5410.0952	3054.5812	64.3515
220	-4240.6027	-459.9827	4080.4847	2060.2006	-7066.7660	4563.4933	50.2937
221	-4240.6027	-459.9827	4080.4847	2060.2006	-7066.7660	4563.4933	50.2937
222	-3314.0975	-344.2839	5312.4031	3666.6382	-7345.2196	2516.0269	32.6053
223	-3314.0975	-344.2839	5312.4031	3666.6382	-7345.2196	2516.0269	32.6053
224	-495.8499	616.1562	4849.1346	4339.2705	-5361.2765	4850.2746	52.0003
225	-495.8499	616.1562	4849.1346	4339.2705	-5361.2765	4850.2746	52.0003
226	-616.1562	4849.1346	4339.2705	-5361.2765	4850.2746	52.0003	
227	-194.4938	3097.3814	5321.5252	-1933.7503	3627.6377	23.3133	
228	-194.4938	3097.3814	5321.5252	-1933.7503	3627.6377	23.3133	
229	8371.8441	-290.1229	1710.5488	8697.4039	-615.6827	4656.5433	10.7759
230	8371.8441	-290.1229	1710.5488	8697.4039	-615.6827	4656.5433	10.7759
231	12033.9758	-445.2303	644.9626	12090.9307	-502.1852	0296.5560	3.6501
232	12033.9758	-445.2303	644.9626	12090.9307	-502.1852	0296.5560	3.6501
233	14602.0227	-97.4922	34.6159	14002.1039	-97.5764	7375.8401	1.34
234	14602.0227	-97.4922	34.6159	14002.1039	-97.5764	7375.8401	1.34
235	-7172.4288	-300.3709	2001.0459	260.7828	-7756.2062	4018.6857	74.0111
236	-7172.4288	-300.3709	2001.0459	260.7828	-7756.2062	4018.6857	74.0111
237	-1009.4439	-199.8214	2499.353	925.0678	-8194.9331	4560.3005	59.4541
238	-1009.4439	-199.8214	2499.353	925.0678	-8194.9331	4560.3005	59.4541

213	-5122.3478	86.5943	4697.3605	2845.5070	-7911.2605	376.3837	54.5730
214	-1112.564	-273.2648	5132.7374	4456.4075	-2842.8241	2149.8263	53.5730
215	-1112.5264	-273.2646	5132.7374	4456.4075	-2842.8241	2149.8263	41.3313
216	4000.3551	351.9110	3089.0747	6476.6104	-2118.3435	4297.4769	32.4100
217	4000.3551	351.9110	3089.0747	6476.6104	-2118.3435	4297.4769	32.4100
218	8561.0935	473.6421	2264.5565	9154.4288	-119.7233	4637.0910	14.0011
219	8561.0935	473.6421	2264.5565	9154.4288	-119.7233	4637.0910	14.0011
220	12952.2462	173.6385	1294.8957	13083.1365	42.7462	6520.1442	5.7499
221	12952.2462	173.6385	1294.8957	13083.1365	42.7462	6520.1442	5.7499
222	15649.9813	1143.7323	311.1863	12056.6538	1137.0599	7259.7970	1.2233
223	15649.9813	1143.7323	311.1863	12056.6538	1137.0599	7259.7970	1.2233
224	-10467.2285	-167.8898	2288.4209	317.6072	-10452.8052	5635.2463	73.8292
225	-10467.2285	-167.8898	2288.4209	317.6072	-10452.8052	5635.2463	73.8292
226	-6436.5886	170.5937	3992.7868	1467.3752	-9783.3701	2625.3721	70.1234
227	-6436.5886	170.5937	3992.7868	1467.3752	-9783.3701	2625.3721	70.1234
228	-3102.5488	122.0954	4903.4792	3671.5260	-6651.9749	5161.7227	54.1007
229	-3102.5488	122.0954	4903.4792	3671.5260	-6651.9749	5161.7227	54.1007
230	3100.3869	446.794	4500.3633	6712.4913	-2785.2044	4749.0461	32.0041
231	3460.3869	446.794	4500.3633	6712.4913	-2785.2044	4749.0461	32.0041
232	9050.7662	288.4751	3283.7600	1010.1942	-804.9529	2477.5732	13.4167
233	9050.7662	288.4751	3283.7600	1010.1942	-804.9529	2477.5732	13.4167
234	14350.5565	-280.0081	2078.1337	14647.6290	-569.3066	1600.2366	1.6923
235	14350.5565	-280.0081	2078.1337	14647.6290	-569.3066	1600.2366	1.6923
236	17739.6076	294.8911	828.6066	17776.8172	255.6215	6761.6279	2.7133
237	17739.6076	294.8911	828.6066	17776.8172	255.6215	6761.6279	2.7133
238	-15112.0532	32.8173	1804.9345	247.9052	-1324.1411	7786.3231	85.2952
239	-15112.0532	32.8173	1804.9345	247.9052	-1324.1411	7786.3231	85.2952
240	-12840.3661	-121.6669	2000.2720	307.2535	-13407.4057	5897.3395	13.4231
241	-4091.4858	-506.1323	4322.2619	1316.2925	-10914.2136	5112.4030	57.2916
242	-4091.4858	-506.1323	4322.2619	1316.2925	-10914.2136	5112.4030	57.2916
243	-9091.4858	-506.1323	4322.2619	1316.2925	-10914.2136	5112.4030	57.2916
244	263.3349	-215.4855	4051.1328	4800.9660	-4813.1360	4837.0613	43.5812
245	263.3349	-215.4855	4051.1328	4800.9660	-4813.1360	4837.0613	43.5812
246	8921.0495	-382.0905	3749.2736	10275.4419	-1730.4828	0005.9023	13.0205
247	8921.0495	-382.0905	3749.2736	10275.4419	-1730.4828	0005.9023	13.0205
248	15949.5651	-674.4049	2612.2259	16350.3764	-1075.2161	8712.7362	0.1232
249	15949.5651	-674.4049	2612.2259	16350.3764	-1075.2161	8712.7362	0.1232
250	20515.6564	163.7958	1140.8664	20579.4103	100.0419	10239.6842	3.1935
251	20515.6564	163.7958	1140.8664	20579.4103	100.0419	10239.6842	3.1935
252	-16595.6733	71.9409	2610.7138	533.1582	-17050.8905	8795.0243	80.6812
253	-16595.6733	71.9409	2610.7138	533.1582	-17056.8905	8795.0243	80.6812
254	-13424.3703	-769.7604	3351.3140	62.9691	-14257.0999	7160.0345	70.0428
255	-13424.3703	-769.7604	3351.3140	62.9691	-14257.0999	7160.0345	70.0428
256	-3400.0748	-134.6902	4132.3119	2675.7792	-6210.5441	4443.1617	22.7738
257	-3400.0748	-134.6902	4132.3119	2675.7792	-6210.5441	4443.1617	22.7738
258	8000.5380	-484.5610	3976.2319	9572.5949	-2056.6178	2814.6064	21.5720
259	8000.5380	-484.5610	3976.2319	9572.5949	-2056.6178	2814.6064	21.5720
260	17530.3273	-830.8651	2878.4205	1970.9915	-1271.5293	9621.2604	0.1000
261	17530.3273	-830.8651	2878.4205	1970.9915	-1271.5293	9621.2604	0.1000
262	23724.4285	231.8926	1144.6107	23780.0648	176.2563	11801.9043	2.7828
263	23724.4285	231.8926	1144.6107	23780.0648	176.2563	11801.9043	2.7828
264	-23628.1089	1045.8849	1521.4840	1139.3508	-23721.5748	12430.4628	80.4047
265	-23628.1089	1045.8849	1521.4840	1139.3508	-23721.5748	12430.4628	80.4047
266	-16667.6185	-654.9618	2275.8593	-293.8465	-19028.7338	3367.4437	62.0116
267	-16667.6185	-654.9618	2275.8593	-293.8465	-19028.7338	3367.4437	62.0116

241	-10770.6991	-569.2537	4051.1513	843.7936	-12183.7464	5513.7700	70.711
	-10770.6991	-569.2537	4051.1513	843.7938	-12183.7464	5513.7700	70.711
242	5756.5294	-379.1364	4623.1155	8237.1013	-2859.7083	5548.4048	20.2161
	5756.5294	-379.1364	4623.1155	8237.1013	-2859.7083	5548.4048	20.2161
243	18919.3086	-977.7600	3306.2197	19454.3054	-1212.7567	10463.5311	9.1917
	18919.3086	-977.7600	3306.2197	19454.3054	-1212.7567	10463.5311	9.1917
244	27153.4168	443.7936	1247.5312	27211.5609	385.6515	13412.9247	2.6614
	27153.4168	443.7936	1247.5312	27211.5609	385.6515	13412.9247	2.6614
245	-25084.9084	1985.4542	2952.2883	2303.6890	-25403.1433	13853.4161	63.6477
	-25084.9084	1985.4542	2952.2883	2303.6890	-25403.1433	13853.4161	63.6477
246	-21793.2524	-692.0553	3367.1558	-167.7784	-22317.5293	11074.8755	81.1499
	-21793.2524	-692.0553	3367.1558	-167.7784	-22317.5293	11074.8755	81.1499
247	480.9741	-349.4526	4166.8397	4253.2368	-4121.7152	4187.4760	2.1247
	480.9741	-349.4526	4166.8397	4253.2368	-4121.7152	4187.4760	2.1247
248	19134.9538	1341.8552	3746.8378	19891.7657	585.0432	9653.3612	11.4133
	19134.9538	1341.8552	3746.8378	19891.7657	585.0432	9653.3612	11.4133
249	30403.6998	393.0876	1305.4666	30460.3809	336.4064	15061.9872	2.4861
	30403.6998	393.0876	1305.4666	30460.3809	336.4064	15061.9872	2.4861
250	-36062.9651	1967.4811	2127.6461	2086.1441	-36181.6281	19133.8661	80.0318
	-36062.9651	1967.4811	2127.6461	2086.1441	-36181.6281	19133.8661	80.0318
251	-30376.8108	-4961.5803	3612.8033	-4457.9946	-30880.3966	13211.2010	82.0647
	-30376.8108	-4961.5803	3612.8033	-4457.9946	-30880.3966	13211.2010	82.0647
252	-6531.2784	-2819.7066	5237.4599	289.9495	-11640.9346	5962.4421	59.3009
	-6531.2784	-2819.7066	5237.4599	289.9495	-11640.9346	5962.4421	59.3009
253	11726.9221	3564.8521	5325.7143	14355.4385	936.3358	8709.5513	20.2667
	11726.9221	3564.8521	5325.7143	14355.4385	936.3358	8709.5513	20.2667
254	29588.8415	6106.4814	3891.0817	30216.8096	5478.5133	12369.1462	9.1077
	29588.8415	6106.4814	3891.0817	30216.8096	5478.5133	12369.1462	9.1077

APPENDIX C

**DERIVATION OF THE REPLACEMENT MATRIX USED
IN THE METHOD SUGGESTED BY TLUSTY**

C. Stepwise Sub-dividing and Refining
Method (Tlusty's Method)

The purpose of the problem of stepwise sub-dividing and refining of a structure with loading concentrated on a small part of the outer boundary is to investigate stresses in greater detail in the vicinity of the concentrated load.

In this method, if there is a structure "A and B", Figure 47, where B is the part in which all external loads are applied and which has to be subsequently refined in mesh. Such a structure is sought which would replace A by giving the same relationship between displacements and forces on boundary b but be much simpler. Actually the size of the stiffness matrix of this replacement structure would be $2n \times 2n$ where n is the number of nodes on boundary b, irrespectively of the number of nodes of the original structure A.

As an example, in Figure 47 part A is originally represented by a 24×24 stiffness matrix. There are no external forces acting on internal nodal points of A; all external forces are concentrated on boundaries a and b. In addition to this simplification, boundary a is fixed.

It can be shown that under these conditions part A can be replaced by another structure A^* with a stiffness matrix 8×8 only.

The stiffness matrix K_A of the original A structure may be partitioned:

$$\left[\begin{array}{|c|} \hline K_A \\ \hline 24 \times 24 \\ \hline \end{array} \right] \cdot \left\{ \begin{array}{l} \delta_{int} \\ \hline \delta_b \\ \hline 24.1 \end{array} \right\} = \left\{ \begin{array}{l} 0 \\ \hline F_b \\ \hline 24.1 \end{array} \right\}$$

(C-1)

$$\left[\begin{array}{|c|c|} \hline P & Q \\ \hline \cdots & \cdots \\ \hline 16 \times 16 & 16 \times 8 \\ \hline R & S \\ \hline 8 \times 16 & 8 \times 8 \\ \hline \end{array} \right] \cdot \left\{ \begin{array}{l} \delta_{int} \\ \hline \delta_b \\ \hline \end{array} \right\} = \left\{ \begin{array}{l} 0 \\ \hline F_b \\ \hline \end{array} \right\}$$

(C-2)

From (C-2)

$$[P] \{\delta_{int}\} + [Q] \{\delta_b\} = 0 \quad (C-3)$$

and

$$[R] \{\delta_{int}\} + [S] \{\delta_b\} = \{F_b\} \quad (C-4)$$

From (C-3) and (C-4)

$$[\delta_{int}] = -[P]^{-1} [Q] \{\delta_b\}$$

$$[S] - [R][P]^{-1}[Q] \{\delta_b\} = \{F_b\} \quad (C-5)$$

From (C-5) we can see that

$$[K_A^*] = [S] - [R][P]^{-1}[Q] \quad (C-6)$$

where K_A^* is the stiffness matrix of the replacement structure and it is 8×8 .

So now the stiffness matrix of the total original structure $(A+B)$ is replaced by a sum:

$$\left(\begin{bmatrix} K_A^* \\ 8 \times 8 \end{bmatrix} + \begin{bmatrix} K_B \\ 16 \times 16 \end{bmatrix} \right) \begin{Bmatrix} \delta_b \\ \delta_c \end{Bmatrix} = \begin{Bmatrix} 0 \\ F_c \end{Bmatrix}$$

(C-7)

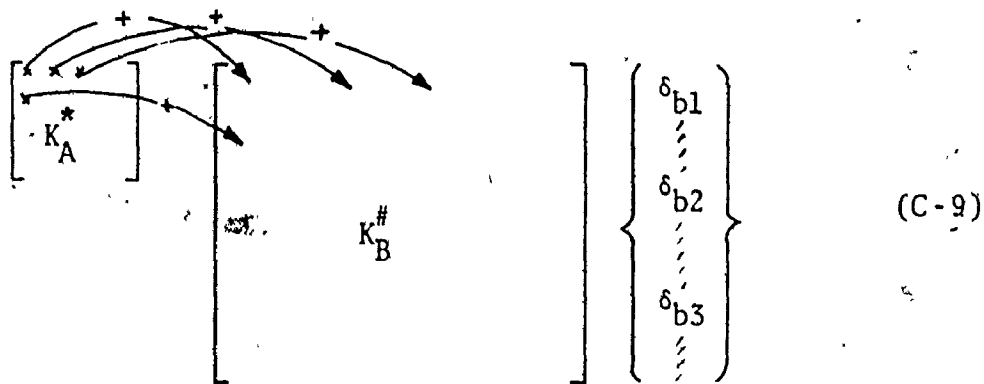
In the next step, area B may be covered by a finer mesh expressed by a corresponding stiffness matrix $K_B^\#$. Now,

- 1.) either $K_B^\#$ is arranged so that the points of the original boundary are partitioned:

$$\left[\begin{bmatrix} K_A^* \\ \vdots \end{bmatrix} + \begin{bmatrix} \vdots & \vdots \\ \vdots & K_B^\# \\ \vdots & \vdots \end{bmatrix} \right] \begin{Bmatrix} \delta_b \\ \vdots \end{Bmatrix} = \begin{Bmatrix} 0 \\ \vdots \end{Bmatrix}$$

(C-8)

- 2.) or the nodes of the original boundary b are interspersed in $K_B^\#$



In both cases, the band width of $K_B^{\#}$ is increased, so generally boundaries b between the parts A and B of a structure would have more than 4 nodes. It will be necessary to do the refining of the mesh in steps in order to keep the band width of a reasonable size.

APPENDIX D

**COMPUTER PROGRAM USED FOR CALCULATION OF
THE REPLACEMENT MATRIX IN THE FIRST STEP**

PLANE STRAIN FINITE ELEMENT PROGRAM BY HASOON Z.

SMM IS THE TOTAL STIFFNESS MATRIX

BBA TWISE AREA OF ELEMENT

NI,NJ,NK NUMBER OF NODES OF ELEMENT IN ANTICLOCKWISE DIRECTION
E MODULUS OF ELASTICITY

U POSITION RATIO

UW SPECIFIC WEIGHT OF ELEMENT

ARRWT OWN WEIGHT OF ELEMENT

T IS ELEMENT STIFFNESS MATRIX

X,Y ARE COORDINATES OF NODES

NN NUMBER OF NODES

NE NUMBER OF ELEMENTS

NLC NUMBER OF LOAD CASES

NU NUMBER OF UNKNOWNS

```

COMMON BBA(100),NI(96),NJ(96),E(100),U(100)
$,ARR(100),T(100,6,6),SMM(108,108),MP(100,6),X(65),Y(65)
COMMON CC(100,100),NI(100)
COMMON ND(65,2),FF(2),S(6,6),R(6,6),F(160),SB(6),FN(3),NPN(3),P(
$100,6,6)
WRITE(6,1)
1 FORMAT(1H1,30X,*FINITE ELEMENT PROGRAM FOR SOLVING STRESSES ON
SCARBIDE TOOL*,//)
READ(5,3) NN,NE,NLC
READ(5,3) NU
3 FORMAT(3I6)
WRITE(6,4)
4 FORMAT(1X,4H NO.,4H NI,4H NJ,4H NK,5H XI,5H XJ,5H XK,
15H YI,5H YJ,5H YK,18H CODE NUMBERS ,6H AREA,12H
2 E,6H U,6H UNHT)
DO 19 I=1,NN
READ(5,2) NM,ND(I,1),ND(I,2),X(I),Y(I)
2 FORMAT(3I6,2F8.0)
19 CONTINUE
ARRT=0.0
N8=0
C
DO 11 J=1,NE
READ(5,724) NI(J),NJ(J),NK(J),E(J),U(J)
724 FORMAT(3I6,2F12.0)

```

CALCULATION OF CODE NUMBERS

```
MP(J,1)=ND(NI(J),1)
MP(J,2)=ND(NJ(J),1)
MP(J,3)=ND(NK(J),1)
MP(J,4)=ND(NI(J),2)
MP(J,5)=ND(NJ(J),2)
MP(J,6)=ND(NK(J),2)
```

CALCULATION OF BAND WIDTH

```
MAX=0
MIN=3000
DO 27 II=1,6
IF(MP(J,II).EQ.0) GO TO 27
IF(MP(J,II)-MAX) 28,28,29
29 MAX=MP(J,II)
28 IF(MP(J,II)-MIN) 30,27,27
30 MIN=MP(J,II)
27 CONTINUE
NB1=MAX-MIN
IF(NB1.GT.NB) NB=NB1
DO 15 II=1,6
DO15 JJ=1,6
P(J,II,JJ)=0.0
15 CONTINUE
```

CALCULATION OF ELEMENT STIFFNESS MATRIX

```
XI=X(NI(J))
XJ=X(NJ(J))
XK=X(NK(J))
YI=Y(NI(J))
YJ=Y(NJ(J))
YK=Y(NK(J))
P(J,1,1)=XJ*YK-XK*YJ
P(J,1,2)=XK*YI-XI*YK
P(J,1,3)=XI*YJ-XJ*YI
P(J,2,1)=YJ-YK
P(J,2,2)=YK-YI
P(J,2,3)=YI-YJ
P(J,3,1)=XK-XJ
P(J,3,2)=XI-XK
P(J,3,3)=XJ-XI
P(J,4,4)=P(J,1,1)
P(J,4,5)=P(J,1,2)
P(J,4,6)=P(J,1,3)
P(J,5,4)=P(J,2,1)
P(J,5,5)=P(J,2,2)
P(J,5,6)=P(J,2,3)
P(J,6,4)=P(J,3,1)
P(J,6,5)=P(J,3,2)
P(J,6,6)=P(J,3,3)
BBA(J)=((XI-XJ)*(YI-YK)-(XI-XK)*(YI-YJ))
ARR(J)=ABS(BBA(J)/2.)
WRITE(6,31) J,NI(J),NJ(J),NK(J),XI,XJ,XK,YI,YJ,YK,(MP(J,I),I=1,6),
ARR(J),E(J),U(J)
31 FORMAT(1X,4I4,6F7.5,6I3,1F9.6,1E10.3,1FS.3)
11 CONTINUE
```

```

NB=NB+1
WRITE(6,34) NN,NE,NB
34 FORMAT(1H1,3X,14HNO OF NODES IS,I4,3X,17HNO OF ELEMENTS IS,I4,3X,
18HHALF BAND WIDTH IS,I4/)
NV=NB*NU
DO 7 IG=1,NU
F(IG)=0.0
7 CONTINUE
N81=NB-1
READ(5,3) MX,NX,LX
DO 90 NIS=1,NLC
DO 888 JJ=1,MX
DO 888 II=1,MX
SMH(JJ,II)=0.0
888 CONTINUE
DO 37 L=1,NE
WRITE(6,681) L
681 FORMAT(//,* STIFFNESS MATRIX FOR ELEMENT *,I6,/*)
DO 16 II=1,6
DO 16 JJ=1,6
S(II,JJ)=0.0
16 CONTINUE
EU=E(L)/((1.+U(L))*(1.-2.*U(L)))
S(2,2)=EU*(1.-U(L))
S(2,6)=EU*U(L)
S(3,3)=EU*(1.-2.*U(L))/2.
S(3,5)=S(3,3)
S(5,3)=S(3,3)
S(5,5)=S(3,3)
S(6,2)=S(2,6)
S(6,6)=S(2,2)
DO 21 JA=1,6
DO 21 IA=1,6
R(JA,IA)=0.0
DO 21 KK=1,6
R(JA,IA)=R(JA,IA)+S(JA,KK)*P(L,KK,IA)
21 CONTINUE
DO 22 JJ=1,6
DO 22 II=1,6
T(L,JJ,II)=0.0
DO 22 KK=1,6
T(L,JJ,II)=T(L,JJ,II)+P(L,KK,JJ)*R(KK,II)/(4.*ARR(L))
22 CONTINUE
DO 641 JJ=1,6
WRITE(6,642) (T(L,JJ,II),II=1,6)
CONTINUE
FORMAT(1X,6E10.2)
*****CALCULATION OF TOTAL STIFFNESS MATRIX*****
*****DO 522 KK=1,6
IF(MP(L,KK).EQ.0) GO TO 522
IS=MP(L,KK)
DO 523 KJ=1,6
IF(MP(L,KJ).EQ.0) GO TO 523
NS=4P(L,KJ)

```

```

SMM(IS,NS)=SMM(IS,NS)+T(L,KK,KJ)
523 CONTINUE
522 CONTINUE
37 CONTINUE
WRITE(6,654)
654 FORMAT(1H1)
90 CONTINUE
DO 201 I=1,NX
DO 201 J=1,NX
CC(I,J)=SMM(I,J)
201 CONTINUE
ZERO=1.E-06
CALL INVMAT(CC,100,100,ZERO,IERR,N1)
DO 261 I=1,NX
DO 261 J=1,LX
JJ=NX+J
SMM(I,J)=0.0
DO 261 K=1,NX
SMM(I,J)=SMM(I,J)+SMM(JJ,K)*CC(K,I)
261 CONTINUE
DO 262 I=1,LX
DO 262 J=1,LX
JJ=NX+J
CC(I,J)=CC(I,J)+SPM(I,K)*SHH(K,JJ)
262 CONTINUE
DO 263 I=1,LX
II=I+NX
DO 263 J=1,LX
JJ=J+NX
SMM(I,J)=SHH(II,JJ)-CC(I,J)
263 CONTINUE
DO 264 I=1,LX
WRITE(6,650)(SMM(I,J),J=1,LX)*
WRITE(7,231)(SMM(I,J),J=1,LX)
264 CONTINUE
650 FORMAT(8(1X,E10.4),/)
231 FORMAT(8E10.4)
997 STOP
END

```

* 6400 END OF RECORD

	61	92	1	
108				
1	0	00.0	0.0	
2	0	00.0	0.125	
3	0	00.0	0.25	
4	0	00.0	0.375	
5	0	00.0	0.5	
6	0	00.0	0.625	
7	0	00.0	0.75	
8	1	21.905	0.0	
9	3	41.75	0.0	
10	5	61.5	0.0	
11	7	81.25	0.0	
12	9	101.0	0.0	
13	11	120.75	0.0	
14	13	140.5	0.0	
15	15	160.25	0.0	
16	17	180.25	0.125	
17	19	200.25	0.25	
18	21	220.25	0.375	

CDTOT 376

APPENDIX E
COMPUTER PROGRAM FOR THE CALCULATION
OF THE STRESSES IN THE FIFTH STEP

PLANE STRAIN FINITE ELEMENT PROGRAM BY MASOOD Z.

SMM IS THE TOTAL STIFFNESS MATRIX

BBA TWISE AREA OF ELEMENT

NI,NJ,NK NUMBER OF NODES OF ELEMENT IN ANTICLOCKWISE DIRECTION

E' MODULUS OF ELASTICITY

U POSSESSION RATIO

UW SPECIFIC WEIGHT OF ELEMENT

ARRWT OWN WEIGHT OF ELEMENT

T IS ELEMENT STIFFNESS MATRIX

X, Y ARE COORDINATES

NN NUMBER OF NODES

THE NUMBER OF ELEMENTS

NLC NUMBER OF LOAD CASES

NU NUMBER OF UNKNOWNS

```

COMMON SM(5500),BBA(88),NI(88),NJ(88),NK(88),E(88),U(88)
$,ARR(88),T(88,6,6),SMH(120,120),MP(88,6),X(60),Y(60),EQUV(28,28)
COMMON ND(60,2),FF(2),S(6,6),R(6,6),F(160),SB(6),FN(3),NPN(3),P(
$88,6,6)
UDFTC 1

```

```
1      WRITE(6,1)
1      FORMAT(1H1,30X,*FINITE ELEMENT PROGRAM FOR SOLVING STRESSES ON
$CARBIDE TOOL*,//)
1      READ(5,3) NN,NE,NIC
```

READ(5,3) NU

3 FORMAT(3I6)
4 WRITE(6,4)
4 FORMAT(1X,4H NO.,4H NI,4H NJ,4H NK,5H XI,5H XJ,5H XK,
15H YI,5H YJ,5H YK,18H CODE NUMBERS ,6H AREA,12H
2 F,6H I,6H LIN4T//

```
DO 19 I=1,NN  
READ(5,2)NM,ND(I,1),ND(I,2),X(I),Y(I)  
FORMAT(3T6.2E8.0)
```

19 FORTNIGHTS CONTINUE

ARRT=0.
NP=8

9

READ (5,724)

724 FORMAT(3I6,2F12.0)

G CALCULATION OF CODE NUMBERS

```
MP(J,1)=ND(NI(J),1)
MP(J,2)=ND(NJ(J),1)
MP(J,3)=ND(NK(J),1)
MP(J,4)=ND(NI(J),2)
MP(J,5)=ND(NJ(J),2)
MP(J,6)=ND(NK(J),2)
```

C CALCULATION OF BAND WIDTH

```
MAX=0
MIN=3000
DO 27 II=1,6
IF(MP(J,II).EQ.0) GO TO 27
IF(MP(J,II)-MAX) 28,28,29
29 MAX=MP(J,II)
28 IF(MP(J,II)-MIN) 30,27,27
30 MIN=MP(J,II)
27 CONTINUE
NB1=MAX-MIN
IF(NB1.GT.NB) NB=NB1
DO 15 II=1,6
DO15 JJ=1,6
P(J,II,JJ)=0.0
15 CONTINUE
```

C CALCULATION OF ELEMENT STIFFNESS MATRIX

```
XI=X(NI(J))
XJ=X(NJ(J))
XK=X(NK(J))
YI=Y(NI(J))
YJ=Y(NJ(J))
YK=Y(NK(J))
P(J,1,1)=XJ*YK-XK*YJ
P(J,1,2)=XK*YI-XI*YK
P(J,1,3)=XI*YJ-XJ*YI
P(J,2,1)=YJ-YK
P(J,2,2)=YK-YI
P(J,2,3)=YI-YJ
P(J,3,1)=XK-XJ
P(J,3,2)=XI-XK
P(J,3,3)=XJ-XI
P(J,4,4)=P(J,1,1)
P(J,4,5)=P(J,1,2)
P(J,4,6)=P(J,1,3)
P(J,5,4)=P(J,2,1)
P(J,5,5)=P(J,2,2)
P(J,5,6)=P(J,2,3)
P(J,6,4)=P(J,3,1)
P(J,6,5)=P(J,3,2)
P(J,6,6)=P(J,3,3)
BBA(J)=((XI-XJ)*(YI-YK)-(XI-XK)*(YI-YJ))
ARR(J)=ABS(BBA(J)/2.)
WRITE(6,31) J,NI(J),NJ(J),NK(J),XI,XJ,XK,YI,YJ,YK,(MP(J,I),I=1,6),
ARR(J),E(J),U(J)
31    1X,4I4,6F7.5,6I3,1F8.6,1E10.3,1F6.3
```

```

34 WRITE(6,34) NN,NE,NB
      FORMAT(1H1,3X,14HNO OF NODES IS,I4,3X,17HNO OF ELEMENTS IS,I4,3X,1
     18HHALF BAND WIDTH IS,I4/)
      NV=NB*NU
      DO 7 IG=1,NU
      F(IG)=0.0
7 CONTINUE
      NB1=NB -1
      DO 90 NIS=1,NLC
      DO 888 JJ=1,120
      DO 888 II=1,120
      SMM(JJ,II)=0.0
888 CONTINUE
      DO 37 L=1,NE
      WRITE(6,681) L
681 FORMAT(//,* STIFFNESS MATRIX FOR ELEMENT *,I6,//)
      DO 16 II=1,6
      DO 16 JJ=1,6
      S(II,JJ)=0.0
16 CONTINUE
      EU=E(L)/(1.+U(L))*(1.-2.*U(L))
      S(2,2)=EU*(1.-U(L))
      S(2,6)=EU*U(L)
      S(3,3)=EU*(1.-2.*U(L))/2.
      S(3,5)=S(3,3)
      S(5,3)=S(3,3)
      S(5,5)=S(3,3)
      S(6,2)=S(2,6)
      S(6,6)=S(2,2)
      DO 21 JA=1,6
      DO 21 IA=1,6
      R(JA,IA)=0.0
      DO 21 KK=1,6
      R(JA,IA)=R(JA,IA)+S(JA,KK)*P(L,KK,IA)
21 CONTINUE
      DO 22 JJ=1,6
      DO 22 II=1,6
      T(L,JJ,II)=0.0
      DO 22 KK=1,6
      T(L,JJ,II)=T(L,JJ,II)+P(L,KK,JJ)*R(KK,II)/(4.*ARR(L))
22 CONTINUE
      DO 641 JJ=1,6
      WRITE(6,642) (T(L,JJ,II) ,II=1,6)
641 CONTINUE
642 FORMAT(1X,6E10.2)
*****CALCULATION OF TOTAL STIFFNESS MATRIX*****
*****CALCULATION OF TOTAL STIFFNESS MATRIX*****
DO 522 KK=1,6
IF(MP(L,KK).EQ.0) GO TO 522
IS=MP(L,KK)
DO 523 KJ=1,6
IF(MP(L,KJ).EQ.0) GO TO 523
NS=MP(L,KJ)
SMM(IS,NS)=SMM(IS,NS)+T(L,KK,KJ)
523 CONTINUE

```

```

522 CONTINUE
37 CONTINUE
DO 271 I=1,28
READ(5,272)(EQUV(I,J),J=1,28)
271 CONTINUE
272 FORMAT(8E10.4)
DO 273 I=1,28
DO 273 J=1,28
SMM(I,J)=SMM(I,J)+EQUV(I,J)
273 CONTINUE
WRITE(6,654)
654 FORMAT(1H1)
DO 36 KK=1,5000
SH(KK)=0.0
36 CONTINUE
NBB=NB
DO 5555 I=1,NU
DO 5556 J=I,NBB
IF(I-1) 151,151,152
152 NA =I-1
K= NA*NB+J-NA
GO TO 153
151 K=J
153 SM(K)= SMM(J,I)
5556 CONTINUE
NBB= NBB+1
5555 CONTINUE
WRITE(6,92)NIS
92 FORMAT(1X,30HNDAL LOADS FOR LOAD CASE NO.,I4//1X,30HNODE NO.
$X FORCE Y FORCE/)
READ(5,3)NNL
DO 47 J=1,NNL
READ(5,48)JNU,FF(1),FF(2)
DO 50 L=1,2
IF(ND(JNU,L).EQ.0) GO TO 50
IK=ND(JNU,L)
F(IK)=F(IK)+FF(L)
50 CONTINUE
47 CONTINUE
DO 93 II=1,NN
IF(ND(II,1).NE.0) GO TO 94
FX=0.0
GO TO 95
94 IK=ND(II,1)
FX=F(IK)
95 CONTINUE
IF(ND(II,2))NE.0) GO TO 96
FY=0.0
GO TO 97
96 IK=ND(II,2)
FY=F(IK)
97 CONTINUE
WRITE(6,98)II,FX,FY
98 FORMAT(1X,1I6,2F11.1)
93 CONTINUE
ccc      CALCULATION OF DISPLACEMENT
DET=1.E-8
CALL BAND(SM,F,NU,NB,1,DET)

```

```

56 IF(DET)56,57,58
56 WRITE(6,59)DET
59 FORMAT(1X,34HMATRIX SM IS NOT POSITIVF-DEFINITE/6H DET= ,E15.7)
GO TO 997
57 WRITE(6,60)DET
60 FORMAT(1X,19HDETERMINANT IS ZERO/6H DET= ,E15.7)
GO TO 997
58 CONTINUE
DO 3336 KKL=1,5000
SM(KKL)=0.0
3336 CONTINUE
WRITE(6,121)NIS
121 FORMAT(1H1,1X,38HNODAL DISPLACEMENTS FOR LOAD CASE NO.,I4//1X,40
$HNODE NO. X DEFLECTION Y DEFLECTION//)
DO 61 K=1,NN
IF(ND(K,1).NE.0) GO TO 62
DX=G.0
GO TO 63
62 IK=ND(K,1)
DX=F(IK)
63 CONTINUE
IF(ND(K,2).NE.0) GO TO 64
DY=G.0
GO TO 67
64 IK=ND(K,2)
DY=F(IK)
67 SM(K)=DX
SM(K+500)=DY
WRITE(6,65)K,DX,DY
65 FORMAT(1X,1I8,2(1PE16.5))
61 CONTINUE

```

C
C CALCULATION OF STRAINS AND STRESS FOR ELEMENTS

```

C
C      WRITE(6,132)NIS
132 FORMAT(1H1,1X,47HELEMENT STRAINS AND STRESSES FOR LOAD CADE NO.,I4
1//)
C      WRITE(6,777)
777 FORMAT(1X,3HNO.,4X,8HX STRAIN,4X,8HY STRAIN,3X,9HXY STRAIN,8X,8HX
1STRESS,8X,8HY STRESS,7X,9HXY STRESS//)
DO 68 L=1,NE
DO 69 JJ=1,6
SB(JJ)=0.0
LL=MP(L,JJ)
IF(LL.EQ.0) GO TO 69
SB(JJ)=F(LL)
69 CONTINUE
RS=(SB(1)*P(L,2,1)+SB(2)*P(L,2,2)+SB(3)*P(L,2,3))/BBA(L)
SHS=(SB(1)*P(L,3,1)+SB(2)*P(L,3,2)+SB(3)*P(L,3,3)+SB(4)*P(L,2,1)+$ SB(5)*P(L,2,2)+SB(6)*P(L,2,3))/BBA(L)
VS=(SB(4)*P(L,3,1)+SB(5)*P(L,3,2)+SB(6)*P(L,3,3))/BBA(L)
EU=E(L)/((1.+U(L))*(1.-2.*U(L)))
SIGR=EU*((1.-U(L))*RS+U(L)*VS)
SIGS=EU*((1.-2.*U(L))/2.)*SHS)
SIGV=EU*(U(L)*RS+(1.-U(L))*VS)
WRITE(6,81) L,RS,VS,SHS,SIGR ,SIGV ,SIGS
81 FORMAT(1X,I3,3E12.3,3E16.6)

```

C
C CALCULATION OF STRESS AT NODES

```

NPN(1)=NI(L)
NPN(2)=NJ(L)
NPN(3)=NK(L)
FN(1)=SIGR
FN(2)=SIGV
FN(3)=SIGS
DO 75 NMM=1,3
IEC=10*NPN(NMM)-9+1000
SM(IEC)=SM(IEC)+1.
DO 75 MNN=1,3
ICC=IEC+MNN
SM(ICC)=SM(ICC)+FN(MNN)
75 CONTINUE
68 CONTINUE
WRITE(6,144) NIS
144 FORMAT(1H1,1X,33HNODAL STRESSES FOR LOAD CASE NO.,I4//)
WRITE(6,1442)
$11HMAX. STRESS,5X,11HMIN. STRESS,2X,14HMAX.S. STRESS,8X,4HDIR.///
1442 FORMAT(1X,3HNO.,8X,8HX STRESS,8X,8HY STRESS,7X,9HXY STRESS,5X,
DO 76 KKZ=1,NN
IDC=10*KKZ-9+1000
SIGNR=SM(IDC+1)/SM(IDC)
SIGNV=SM(IDC+2)/SM(IDC)
SIGNS=SM(IDC+3)/SM(IDC)
STMAX=.5*((SIGNR+SIGNV)+SQRT((SIGNR-SIGNV)**2+4.*SIGNS**2))
STMIN=.5*((SIGNR+SIGNV)-SQRT((SIGNR-SIGNV)**2+4.*SIGNS**2))
SSMN=.5*(STMAX-STMIN)
RESN=ABS(STMAX-STMIN)
IF(RESN.GT.0.001) GO TO 141
DIRRN=999.
GO TO 142
141 DIRRN=ATAN2(2.*SIGNS,SIGNR-SIGNV)
DIRRN=(.5/.0174533)*DIRRN
142 WRITE(6,83)KKZ,SIGNR,SIGNV,SIGNS,STMAX,STMIN,SSMN,BIRRN
WRITE(7,84)STMAX
WRITE(7,84)STMIN
WRITE(7,84)SSMN
84 FORMAT(E16.6)
83 FORMAT(1X,I3,7E16.6)
48 FORMAT(I6,2F10.0)
76 CONTINUE
90 CONTINUE
997 STOP
END
SUBROUTINE BAND(A,B,N,M,LT,DET)
DIMENSION A(1),B(1)
MM=M-1
NM=N*M
NM1=NM-MM
IF (LT.NE.1) GO TO 55
MP=M+1
KK=2
FAC=DET
A(1)=1./SQRT(A(1))
BIGL=A(1)
SML=A(1)
A(2)=A(2)*A(1)
A(HP)=1./SQRT(A(MP)-A(2)*A(2))
IF(A(HP).GT.BIGL)BIGL=A(HP)
IF(A(HP).LT.SML)SML=A(HP)

```

194

BNDF0010
BNDF0020
BNDF0030
BNDF0040
BNDF0050
BNDF0060
BNDF0070
BNDF0080
BNDF0090
BNDF0100
BNDF0110
BNDF0120
BNDF0130
BNDF0140
BNDF0150
BNDF0160

```

MP=MP+M          BNDFO170
DO 62 J=MP,NM1,M BNDFO180
JP=J-MM          BNDFO190
MZC=0            BNDFO200
IF(KK.GE.M) GO TO 1 BNDFO210
KK=KK+1          BNDFO220
II=1              BNDFO230
JC=1              BNDFO240
GO TO 2          BNDFO250
1                 BNDFO260
KK=KK+M          BNDFO270
II=KK-MM         BNDFO280
JC=KK-MM         BNDFO290
2                 BNDFO300
DO 65 I=KK,JP,MH BNDFO310
IF(A(I).EQ.0.)GO TO 64 BNDFO320
GO TO 66          BNDFO330
64                BNDFO340
65                BNDFO350
ASUM1=0.          BNDFO360
GO TO 61          BNDFO370
66                BNDFO380
MMZC=MM*MZC      BNDFO390
II=II+MZC         BNDFO400
KM=KK+MMZC        BNDFO410
A(KM)=A(KM)*A(JC) BNDFO420
IF(KM.GE.JP)GO TO 6 BNDFO430
KJ=KM+MM          BNDFO440
DO 5   I=KJ,JP,MH BNDFO450
ASUM2=0.          BNDFO460
IM=I-MM           BNDFO470
II=II+1           BNDFO480
KI=II+MMZC        BNDFO490
DO 7   K=KM,IM,MH BNDFO500
ASUM2=ASUM2+A(KI)*A(K) BNDFO510
KI=KI+MM          BNDFO520
A(I)=(A(I)-ASUM2)+A(KI) BNDFO530
CONTINUE          BNDFO540
ASUM1=0.          BNDFO550
DO 4   K=KM,JP,MH BNDFO560
ASUM1=ASUM1+A(K)*A(K) BNDFO570
61                BNDFO580
S=A(J)-ASUM1      BNDFO590
IF(S.LT.0.)DET=S  BNDFO600
IF(S.EQ.0.)DET=0.  BNDFO610
IF(S.GT.0.)GO TO 63 BNDFO620
NROW=(J+MM)/M    BNDFO630
WRITE(6,99) NROW  BNDFO640
99                BNDFO650
FORMAT(35H0ERROR CONDIONTERED IN ROW,I6) BNDFO660
RETURN             BNDFO670
63                BNDFO680
A(J)=1./SORT(S)  BNDFO690
IF(A(J).GT.BIGL)BIGL=A(J) BNDFO700
IF(A(J).LT.SML)SML=A(J) BNDFO710
62                BNDFO720
CONTINUE          BNDFO730
IF(SML.LE.FAC*BIGL) GO TO 54 BNDFO740
GO TO 53          BNDFO750
54                BNDFO760
DET=0.             BNDFO770
RETURN             BNDFO780
53                BNDFO790
DET=SML/BIGL     BNDFO800
55                BNDFO810
B(1)=B(1)*A(1)   BNDFO820
KK=1               BNDFO830
K1=1               BNDFO840
J=1               BNDFO850
DO 8   L=2,N       BNDFO860

```

```

BSUM1=0.
LM=L-1
J=J+M
IF(KK.GE.M) GO TO 12
KK=KK+1
GO TO 13
12 KK=KK+M
K1=K1+1
13 JK=KK
DO 9 K=K1,LH
BSUM1=BSUM1+A(JK)*B(K)
JK=JK+MM
9 CONTINUE
8 B(L)=(B(L)-BSUM1)*A(J)
B(N)=B(N)*A(NM1)
NMH=NM1
NN=N-1
ND=N
DO 10 L=1,NN
BSUM2=0.
NL=N-L
NL1=N-L+1
NMH=NMH-M
NJ1=NMH
IF(L.GE.M) NO=NO-1
DO 11 K=NL1,NO
NJ1=NJ1+1
BSUM2=BSUM2+A(NJ1)*B(K)
11 CONTINUE
10 B(NL)=(B(NL)-BSUM2)*A(NMH)
RETURN
END

```

* 6400 END OF RECORD

60	88	1
120		
1	1	2.04468 .0
2	3	4.04297 .0
3	5	6.03906 .0
4	7	8.03515 .0
5	9	10.03124 .0
6	11	12.02733 .0
7	13	14.02343 .0
8	15	16.01951 .0
9	17	18.01562 .0
10	19	20.011715 .0
11	21	22.00781 .0
12	23	24.00391 .0
13	25	26.00391 .00781
14	27	28.00391 .01562
15	29	30.00391 .00391
16	31	32.00391 .011715
17	33	34.00781 .00391
18	35	36.04523 .00391
19	37	38.04297 .00391
20	39	40.03906 .00391
21	41	42.03515 .00391
22	43	44.03124 .00391
23	45	46.02733 .00391
24	47	48.02343 .00391
25	49	50.01951 .00391

BNDFO770
BNDFO780
BNDFO790
BNDFO800
BNDFO810
BNDFO820
BNDFO830
BNDFO840
BNDFO850
BNDFO860
BNDFO870
BNDFO880
BNDFO890
BNDFO900
BNDFO910
BNDFO920
BNDFO930
BNDFO940
BNDFO950
BNDFO960
BNDFO970
BNDFO980
BNDFO990
BNDF1000
BNDF1010
BNDF1020
BNDF1030
BNDF1040
BNDF1050
BNDF1060
BNDF1070
BNDF1080

26	51	52.011562	.00391
27	53	54.011715	.00391
28	55	56.00781	.00781
29	57	58.00781	.011715
30	61	60.00781	.01562
31	63	62.011715	.00781
32	65	64.011715	.011715
33	67	66.04578	.00781
34	69	68.04297	.00781
35	71	70.03906	.00781
36	73	72.03515	.00781
37	75	74.03124	.00781
38	77	76.02733	.00781
39	79	78.02343	.00781
40	81	80.01951	.00781
41	83	82.01562	.00781
42	85	84.01562	.011715
43	87	86.011715	.01562
44	89	88.01562	.01562
45	91	90.01951	.011715
46	93	92.04633	.011715
47	95	94.04297	.011715
48	97	96.03906	.011715
49	99	98.03515	.011715
50	101	100.03124	.011715
51	103	102.02733	.011715
52	105	104.02343	.011715
53	107	106.02343	.01562
54	109	108.02234	.01562
55	111	110.03124	.01562
56	113	112.03515	.01562
57	115	114.03515	.01562
58	117	116.03906	.01562
59	119	118.04297	.01562
60	11	120.04686	.01562
61	11	157500000000	.283
62	17	177500000000	.283
63	28	137500000000	.283
64	28	287500000000	.283
65	29	167500000000	.283
66	29	297500000000	.283
67	10	147500000000	.283
68	10	307500000000	.283
69	27	177500000000	.283
70	27	277500000000	.283
71	31	287500000000	.283
72	31	317500000000	.283
73	32	327500000000	.283
74	31	307500000000	.283
75	31	437500000000	.283
76	32	277500000000	.283
77	99	267500000000	.283
78	99	317500000000	.283
79	41	417500000000	.283
80	41	327500000000	.283
81	42	427500000000	.283
82	42	437500000000	.283
83	8	447500000000	.283
84		267500000000	.283

47	33	4675000000.	283
46	46	5975000000.	283
		6075000000.	283
$ \begin{aligned} & 2703E+09 \cdot 1143E+08 \cdot 2279E+09 \cdot 7631E+07 \cdot 8140E-09 \cdot 1032E-09 \cdot 2002E-09 \cdot 2046E-10 \\ & -4653E-10 \cdot 2697E-12 \cdot 2465E-10 \cdot 1933E-10 \cdot 1333E-10 \cdot 1833E-10 \cdot 1136E-10 \cdot 1959E-10 \\ & -1136E-07 \cdot 1365E-08 \cdot 8003E-08 \cdot 6663E-10 \cdot 5522E-08 \cdot 3299E-09 \cdot 3920E-08 \cdot 3217E-09 \\ & -1955E-08 \cdot 2007E-09 \cdot 1288E-08 \cdot 1372E-09 \\ & -1143E+08 \cdot 7035E+08 \cdot 3186E+07 \cdot 6689E+08 \cdot 1247E-09 \cdot 1561E-10 \cdot 3066E-10 \cdot 3133E-11 \\ & -7043E-11 \cdot 4142E-13 \cdot 3775E-11 \cdot 2348E-11 \cdot 2041E-11 \cdot 2807E-11 \cdot 1739E-11 \cdot 3000E-11 \\ & -1488E-08 \cdot 6956E-08 \cdot 5027E-09 \cdot 1928E-08 \cdot 7808E-10 \cdot 5236E-09 \cdot 2008E-09 \cdot 1243E-09 \\ & -3155E-09 \cdot 1126E-10 \cdot 2042E-09 \cdot 1635E-10 \\ & -2279E+09 \cdot 3186E+07 \cdot 3347E+09 \cdot 1143E+08 \cdot 9645E+08 \cdot 1461E+08 \cdot 4060E-09 \cdot 4149E-10 \\ & -9334E-10 \cdot 5491E-12 \cdot 4999E-10 \cdot 3110E-10 \cdot 2703E-10 \cdot 3717E-10 \cdot 2304E-10 \cdot 3973E-10 \\ & -2889E-08 \cdot 4033E-09 \cdot 2987E-08 \cdot 1874E-09 \cdot 3527E-08 \cdot 7539E-10 \cdot 4622E-08 \cdot 1069E-09 \\ & -4255E-08 \cdot 5715E-10 \cdot 2737E-08 \cdot 1946E-09 \\ & -7631E+07 \cdot 6689E+08 \cdot 1143E+08 \cdot 1305E+09 \cdot 1906E+08 \cdot 2919E+08 \cdot 6889E-10 \cdot 7022E-11 \\ & -1584E-10 \cdot 8669E-13 \cdot 8479E-11 \cdot 5261E-11 \cdot 4575E-11 \cdot 6286E-11 \cdot 3889E-11 \cdot 6716E-11 \\ & -2893E-09 \cdot 1519E-10 \cdot 2027E-09 \cdot 8409E-10 \cdot 1168E-09 \cdot 3086E-09 \cdot 7004E-10 \cdot 1082E-08 \\ & -1591E-09 \cdot 1066E-08 \cdot 8671E-10 \cdot 2857E-09 \\ & -6140E-09 \cdot 1247E-09 \cdot 9645E+08 \cdot 1906E+08 \cdot 2075E+09 \cdot 3367E+08 \cdot 9645E+08 \cdot 1461E+08 \\ & -3009E-09 \cdot 2650E-11 \cdot 1617E-09 \cdot 1024E-09 \cdot 8874E-10 \cdot 1228E-09 \cdot 7694E-10 \cdot 1318E-09 \\ & -8054E-09 \cdot 1058E-09 \cdot 8211E-09 \cdot 6009E-10 \cdot 9550E-09 \cdot 5714E-10 \cdot 1225E-08 \cdot 1013E-09 \\ & -2621E-08 \cdot 5074E-10 \cdot 3992E-08 \cdot 1433E-09 \\ & -1032E-09 \cdot 1561E-10 \cdot 1461E+08 \cdot 2919E+08 \cdot 3367E+08 \cdot 1067E+09 \cdot 1906E+08 \cdot 2919E+08 \\ & -6030E-10 \cdot 1813E-11 \cdot 3119E-10 \cdot 1496E-10 \cdot 1366E-10 \cdot 1679E-10 \cdot 8412E-11 \cdot 1676E-10 \\ & -1032E-09 \cdot 1326E-10 \cdot 1039E-09 \cdot 7785E-11 \cdot 1204E-09 \cdot 8027E-11 \cdot 1538E-09 \cdot 1569E-10 \\ & -977E-10 \cdot 2755E-09 \cdot 1027E-09 \cdot 9919E-09 \\ & -2032E-09 \cdot 3066E-10 \cdot 4060E-09 \cdot 6889E-10 \cdot 9645E+08 \cdot 1906E+08 \cdot 2075E+09 \cdot 3367E+08 \\ & -9545E+08 \cdot 1461E+08 \cdot 8418E-09 \cdot 5390E-09 \cdot 4550E-09 \cdot 6482E-09 \cdot 3726E-09 \cdot 6855E-09 \\ & -1581E-09 \cdot 2600E-10 \cdot 2019E-09 \cdot 1480E-10 \cdot 2348E-09 \cdot 1415E-10 \cdot 3010E-09 \cdot 2526E-10 \\ & -6163E-09 \cdot 4506E-10 \cdot 9083E-09 \cdot 8704E-10 \\ & -2046E-10 \cdot 3133E-11 \cdot 4149E-10 \cdot 7022E-11 \cdot 1461E+08 \cdot 2919E+08 \cdot 3367E+08 \cdot 1067E+09 \\ & -1906E+08 \cdot 2919E+08 \cdot 2242E-09 \cdot 4321E-09 \cdot 2619E-09 \cdot 5572E-09 \cdot 3360E-09 \cdot 5238E-09 \\ & -2024E-10 \cdot 2657E-11 \cdot 2063E-10 \cdot 1512E-11 \cdot 2399E-10 \cdot 1445E-11 \cdot 3076E-10 \cdot 2576E-11 \\ & -6337E-10 \cdot 4153E-11 \cdot 9383E-10 \cdot 7201E-11 \\ & -4603E-10 \cdot 7048E-11 \cdot 9334E-10 \cdot 1584E-10 \cdot 3009E-09 \cdot 6090E-10 \cdot 9645E+08 \cdot 1906E+08 \\ & -2075E+09 \cdot 3367E+08 \cdot 9645E+08 \cdot 1461E+08 \cdot 4734E-09 \cdot 5277E-10 \cdot 1629E-09 \cdot 8047E-11 \\ & -4554E-10 \cdot 5978E-11 \cdot 4642E-10 \cdot 3403E-11 \cdot 5398E-10 \cdot 3253E-11 \cdot 6921E-10 \cdot 5807E-11 \\ & -1517E-09 \cdot 1039E-10 \cdot 2087E-09 \cdot 2014E-10 \\ & -2697E-12 \cdot 4142E-13 \cdot 5491E-12 \cdot 8569E-13 \cdot 2650E-11 \cdot 1813E-11 \cdot 1461E+08 \cdot 2919E+08 \\ & -3367E+08 \cdot 1067E+09 \cdot 1906E+08 \cdot 2919E+08 \cdot 1119E-09 \cdot 2155E-08 \cdot 1648E-10 \cdot 1988E-08 \\ & -2669E-12 \cdot 3512E-13 \cdot 2722E-12 \cdot 1984E-13 \cdot 3167E-12 \cdot 1859E-13 \cdot 4064E-12 \cdot 3232E-13 \\ & -9710E-12 \cdot 1006E-12 \cdot 1588E-11 \cdot 4882E-12 \\ & -2455E-10 \cdot 3775E-11 \cdot 4999E-10 \cdot 8479E-11 \cdot 1617E-09 \cdot 3119E-10 \cdot 8418E-09 \cdot 2242E-09 \\ & -9645E+08 \cdot 1906E+08 \cdot 2075E+09 \cdot 3367E+08 \cdot 9645E+08 \cdot 1461E+08 \cdot 1050E-08 \cdot 5193E-09 \\ & -2439E-10 \cdot 3201E-11 \cdot 2486E-10 \cdot 1822E-11 \cdot 2891E-10 \cdot 1742E-11 \cdot 3707E-10 \cdot 3109E-11 \\ & -7596E-10 \cdot 5461E-11 \cdot 1120E-09 \cdot 1039E-10 \\ & -1533E-10 \cdot 2348E-11 \cdot 3110E-10 \cdot 5261E-11 \cdot 1024E-09 \cdot 1496E-10 \cdot 5390E-09 \cdot 4321E-09 \\ & -1461E+08 \cdot 2919E+08 \cdot 3367E+08 \cdot 1067E+09 \cdot 1906E+08 \cdot 2919E+08 \cdot 1581E-11 \cdot 5388E-08 \\ & -1517E-10 \cdot 1991E-11 \cdot 1546E-10 \cdot 1133E-11 \cdot 1798E-10 \cdot 1083E-11 \cdot 2306E-10 \cdot 1930E-11 \\ & -4754E-10 \cdot 3066E-11 \cdot 7043E-10 \cdot 5220E-11 \\ & -1333E-10 \cdot 2041E-11 \cdot 2703E-10 \cdot 4575E-11 \cdot 8874E-10 \cdot 1366E-10 \cdot 4550E-09 \cdot 2619E-09 \\ & -4734E-09 \cdot 1119E-09 \cdot 9645E+08 \cdot 1906E+08 \cdot 2075E+09 \cdot 3367E+08 \cdot 9645E+08 \cdot 1461E+08 \\ & -1319E-10 \cdot 1731E-11 \cdot 1344E-10 \cdot 9851E-12 \cdot 1563E-10 \cdot 9411E-12 \cdot 2004E-10 \cdot 1678E-11 \\ & -4127E-10 \cdot 2714E-11 \cdot 6110E-10 \cdot 4722E-11 \\ & -1833E-10 \cdot 2807E-11 \cdot 3717E-10 \cdot 6286E-11 \cdot 1228E-09 \cdot 1679E-10 \cdot 6482E-09 \cdot 5572E-09 \\ & -5277E-10 \cdot 2155E-08 \cdot 1461E+08 \cdot 2919E+08 \cdot 3367E+08 \cdot 1067E+09 \cdot 1906E+08 \cdot 2919E+08 \\ & -1813E-10 \cdot 2380E-11 \cdot 1848E-10 \cdot 1355E-11 \cdot 2150E-10 \cdot 1294E-11 \cdot 2756E-10 \cdot 2306E-11 \\ & -5689E-10 \cdot 3583E-11 \cdot 8436E-10 \cdot 5935E-11 \\ & -1136E-10 \cdot 1739E-11 \cdot 2304E-10 \cdot 3889E-11 \cdot 7694E-10 \cdot 8412E-11 \cdot 3726E-09 \cdot 3360E-09 \end{aligned} $			

+ 1629E-09 - 1648E-10 - 1050E-08 - 1581E-11 - 9645E+08 - 1906E+08 . 2075E+09 . 3367E+08
 - 23045E+08 - 1461E+08 - 1145E-10 - 8393E-12 - 1332E-10 - 8013E-12 - 1708E-10 - 1428E-11
 - 3033AE-10 - 2072E-11 - 5261E-10 - 3121E-11
 - 1959E-10 . 3000E-11 . 3973E-10 . 6716E-11 . 1318E-09 . 1676E-10 . 6855E-09 - 6238E-09
 - 8347E-11 . 1988E-08 . 5193E-09 . 5388E-08 - 1461E+08 - 2919E+08 . 3367E+08 . 1067E+09
 - 1966E+08 - 2919E+08 . 1976E-10 . 1448E-11 . 2298E-10 . 1383E-11 . 2946E-10 . 2464E-11
 - 6089E-10 . 3742E-11 . 9038E-10 . 6013E-11
 - 1166E-07 . 1488E-08 - 2889E-08 - 2899E-09 - 8054E-09 - 1020E-09 - 1981E-09 - 2024E-10
 - 4554E-10 . 2669E-12 - 2439E-10 . 1517E-10 - 1319E-10 . 1813E-10 - 9645E+08 - 1906E+08
 - 2075E+09 . 3367E+08 - 9645E+08 - 1461E+08 - 5798E-08 - 3499E-09 - 4034E-08 - 3331E-09
 - 1936E-08 - 1958E-09 - 1275E-08 - 1351E-09
 - 1365E-08 - 6956E-08 - 4033E-09 . 1519E-10 - 1058E-09 - 1326E-10 - 2600E-10 - 2657E-11
 - 5978E-11 . 3512E-13 - 3201E-11 . 1991E-11 - 1731E-11 . 2380E-11 - 1461E+08 - 2919E+08
 - 3367E+08 - 1067E+09 - 1905E+08 - 2919E+08 - 2575E-10 - 7501E-09 - 2198E-09 - 1915E-09
 - 2266E-09 - 1149E-10 - 1725E-09 - 1433E-10
 - 8063E-08 . 5027E-09 - 2987E-08 - 2027E-09 - 8211E-09 - 1038E-09 - 2019E-09 - 2063E-10
 - 4642E-10 . 2722E-12 - 2486E-10 . 1546E-10 - 1344E-10 . 1848E-10 - 1145E-10 . 1976E-10
 - 9645E+08 - 1906E+08 . 2069E+08 . 3367E+08 - 9572E+08 - 1461E+08 - 5222E-08 - 3203E-09
 - 1994E-08 - 1748E-09 - 1309E-08 - 1318E-09
 - 6663E-10 - 1928E-08 - 1874E-09 - 8409E-10 - 6009E-10 - 7785E-11 - 1480E-10 - 1512E-11
 - 3463E-11 . 1984E-13 - 1822E-11 . 1133E-11 - 9851E-12 . 1355E-11 - 8393E-12 . 1448E-11
 - 1461E+08 - 2919E+08 . 3367E+08 - 1067E+09 - 1906E+08 - 2897E+08 - 4024E-10 - 8556E-09
 - 1308E-09 . 3130E-10 - 8934E-10 - 1408E-10
 - 5222E-08 . 7808E-10 - 3527E-08 - 1168E-09 - 9550E-09 - 1204E-09 - 2348E-09 - 2399E-10
 - 5398E-10 . 3167E-12 - 2891E-10 . 1798E-10 - 1563E-10 . 2150E-10 - 1332E-10 . 2298E-10
 - 5798E-08 - 2575E-10 - 9572E+08 - 1906E+08 . 2075E+09 . 3367E+08 - 9720E+08 - 1461E+08
 - 2346E-08 - 1716E-09 - 1533E-08 - 1457E-09
 - 3259E-09 - 5236E-09 - 7539E-10 - 3086E-09 - 5714E-10 - 8027E-11 - 1415E-10 - 1445E-11
 - 3253E-11 . 1859E-13 - 1742E-11 . 1083E-11 - 9411E-12 . 1294E-11 - 8013E-12 . 1383E-11
 - 3499E-09 - 7501E-09 - 1461E+08 - 2897E+08 . 3367E+08 - 1067E+09 - 1906E+08 - 2942E+08
 - 7417E-10 - 9086E-10 - 6361E-10 - 2804E-10
 - 3920E-08 - 2008E-09 - 4622E-08 - 7004E-10 - 1225E-08 - 1538E-09 - 3010E-09 - 3076E-10
 - 6921E-10 - 4064E-12 - 3707E-10 . 2306E-10 - 2604E-10 - 2756E-10 - 1708E-10 . 2946E-10
 - 4033E-08 - 2198E-09 - 5222E-08 - 4024E-10 - 9720E+08 - 1906E+08 . 3120E+09 . 3367E+08
 - 7316E+07 - 1461E+08 - 1987E-08 - 1727E-09
 - 3217E-09 - 1243E-09 - 1869E-09 - 1082E-08 - 1013E-09 - 1569E-10 - 2526E-10 - 2576E-11
 - 5807E-11 . 3232E-13 - 3109E-11 - 1930E-11 - 1678E-11 . 2306E-11 - 1428E-11 . 2464E-11
 - 3331E-09 - 1915E-09 - 3203E-09 - 2556E-09 - 1461E+08 - 2942E+08 . 3367E+08 - 1601E+09
 - 1906E+08 - 2417E+08 - 6284E-10 - 8398E-10
 - 1955E-08 - 3155E-09 - 4255E-08 - 1591E-09 - 2621E-08 - 9747E-10 - 6163E-09 - 6337E-10
 - 1417E-09 - 9710E-12 - 7596E-10 - 4754E-10 - 4127E-10 . 5689E-10 - 3538E-10 . 6089E-10
 - 1936E-08 - 2660E-09 - 1994E-08 - 1308E-09 - 2346E-08 - 7417E-10 - 7316E+07 - 1906E+08
 - 2075E+09 . 3367E+08 - 7316E+07 - 1461E+08
 - 2007E-09 - 1126E-10 - 5715E-10 - 1066E-08 - 5074E-10 - 2755E-09 - 4506E-10 - 4153E-11
 - 1039E-10 - 1006E-12 - 5461E-11 . 3066E-11 - 2714E-11 . 3583E-11 - 2072E-11 . 3742E-11
 - 1958E-09 - 1149E-10 - 1748E-09 - 3130E-10 - 1716E-09 - 9086E-10 - 1461E+08 - 2417E+08
 - 3367E+08 - 1067E+08 - 1906E+08 - 2417E+08
 - 1288E-08 - 2042E-09 - 2737E-08 - 8671E-10 - 3992E-08 . 1027E-09 - 9083E-09 - 9383E-10
 - 2037E-09 . 1588E-11 - 1120E-09 . 7043E-10 - 6110E-10 . 8436E-10 - 5261E-10 . 9038E-10
 - 1275E-08 - 1725E-09 - 1309E-08 - 8934E-10 - 1533E-08 - 6361E-10 - 1987E-08 - 6284E-10
 - 7316E+07 - 1906E+08 . 1038E+09 - 3367E+08
 - 1372E-09 - 1635E-10 - 1946E-09 - 2857E-09 - 1433E-09 - 9919E-09 - 8704E-10 - 7201E-11
 - 2014E-10 - 4882E-12 - 1039E-10 . 5220E-11 - 4722E-11 . 5935E-11 - 3121E-11 . 6013E-11
 - 1311E-09 - 1433E-10 - 1318E-09 - 1408E-10 - 1457E-09 - 2804E-10 - 1727E-09 - 8398E-10
 - 1461E+08 - 2417E+08 . 3367E+08 . 5337E+08

12
 30 -2.0 -7.0
 43-11.0 -44.0
 44-22.25 -89.0
 46-35.0 -8.75

CDTOT 728

0
0 0 0 0 0 0 0 0
134 0
1627 2 0 0 0 0 0
1227 1 0 0 0 0 0
1227 3 0 0 0 0 0
- - - - - - - - - -

8 175
3 56 0 540
3 456 0 0 400 0 0
- 1 67 94 0 0 0 0
3 456 7 94 0 0 0 0
5 557 5 8 1 9 0 0 0
5 557 5 8 1 9 0 0 0
6 0